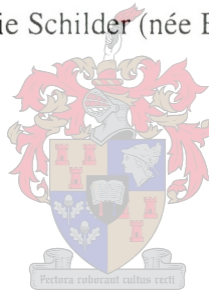# Wideband Modelling of Capacitive Voltage Sensors for Open-Air Transmission Line Applications

Melanie Schilder (née Botha)

Dissertation presented for the Degree of Doctor of Philosophy (Electrical Engineering) at the University of Stellenbosch.

Promoter: Dr. H.J. Vermeulen

September 2002

Declaration of Own Work

I, the undersigned, hereby declare that the work contained in this dissertation is my own original work and has not previously in its entirety or in part been submitted at any university for a degree.

Melanie Schilder (née Botha)

Abstract

This dissertation considers the wideband modelling of capacitive voltage sensors for open-air transmission line applications. Two novel topologies were introduced, namely a differential parallel plate sensor with a floating faraday cage for the interface instrumentation and a coaxial sensor mounted around the earth conductor with a faraday cage connected to the earth conductor. The modelling and analysis procedures included the derivation of equivalent circuit models in order to simulate the calibration factor, the loading effect of the interface instrumentation and the effect of leakage to ground, both in the time- and frequency domain.

In order to obtain a flat frequency response from very low frequencies (less than 5 Hz) to very high frequencies (several MHz) it is important that the interface instrumentation have a high input impedance and galvanic isolation be maintained. This was achieved by developing interface instrumentation with a fibre-optic link operated from battery power. The instrumentation represents a fairly unique approach in that the data is digitised before transmission across the serial fibre-optical link, where-as conventional interfaces use analogue optical technology. Despite the added complexity and high power requirements introduced by the digitising process, the improved versatility is expected to yield a superior interface solution. The instrumentation has a bandwidth of approximately 6 MHz, with an optional anti-aliasing filter at 1 MHz.

Special consideration should be given to the support structure as any unbalanced leakage to ground will introduce variations in the frequency response towards the low-frequency end. Leakage of a 100 MΩ was found to influence the frequency response of the circuit up to frequencies of 1 kHz.

Extensive simulation studies were conducted to obtain qualitative and quantitative insight into the differential sensor topology and the associated electric fields. The improvement of a differential plate sensor over the traditional single element plate sensor was demonstrated using two-dimensional simulations. Further simulations with a three-dimensional package showed that the two-dimensional simulations are insufficient, because the boundary conditions and end effects have a great influence on the calibration factor of the sensor.

Extensive laboratory tests were also undertaken to evaluate the sensor topology as well as the effects of the interface instrumentation and leakage to ground. Excellent correlation were found between the measured and simulated waveforms, both in the time- and frequency domains regarding the calibration factor as well as the added poles or zeros at low frequencies. It can therefore be deduced that a valid circuit model was suggested for these sensor topologies in the frequency range from 10 Hz to 1 MHz.

Keywords: Capacitive sensors, Open-air voltage sensors

Opsomming

Hierdie verhandeling beskou die wyeband modellering van kapasitiewe spanningsensors vir ope-lug transmissie lyn toepassings. Twee oorspronklike topologieë is voorgestel, naamlik 'n differensiële parallel plaat sensor met 'n aparte faraday hok vir die koppelvlak instrumentasie en 'n koaksiale sensor wat rondom die aardgeleier monteer word met die faraday hok ook aan die aardgeleier gekoppel. Die modellerings en analise prosedures het ingesluit die afleiding van ekwivalente stroombaanmodelle vir simulasie van die kalibrasiefaktor asook die belasingseffek van die koppelvlak instrumentasie en lekweerstand na grond in beide die tyd- en frekwensie gebiede.

Om 'n plat frekwensieweergawe te verkry vanaf baie lae frekwensies (laer as 5 Hz) tot by baie hoë frekwensies ('n paar MHz), is dit belangrik dat die koppelvlak instrumentasie 'n hoë intree-impedansie het en galvaniese isolasie verseker word. Dit was bereik deur koppelvlak instrumentasie te ontwikkel met 'n optiese vesel koppeling wat met battery krag aangedryf word. Die instrumentasie verskaf 'n redelik unieke aanslag in die opsig dat die data gemonster word voordat dit oor die seriële optiese vesel skakel gestuur word, terwyl konvensionele koppelvlakke analoog optiese tegnologie gebruik. Ten spyte van die toegevoegde kompleksiteit en hoë drywingsvereistes van die versyferingsproses, het die instrumentasie se veelsydigheid toegeneem tot die mate dat dit as 'n beter koppelvlak oplossing beskou word. Die instrumentasie het 'n bandwydte van ongeveer 6 MHz, met 'n opsionele teen-vou filter by 1 MHz.

Die ondersteuningstruktuur is van besondere belang aangesien enige ongebalanseerde lekweerstand na grond afwykings in die frekwensieweergawe sal veroorsaak aan die lae frekwensie kant. Lekweerstand van 100 MΩ sal die frekwensieweergawe beïvloed tot by ongeveer 1 kHz.

Uitgebreide simulasies is gedoen om kwalitatiewe en kwantitatiewe insig in die differensiële sensor topologie en die geassosieerde elektriese velde te verkry. Die verbetering van 'n differensiële parallel plaat sensor in vergelyking met die tradisionele enkel element plaat sensor is demonstreer met twee-dimensionele simulasies. Verdere simulasies met 'n drie-dimensionele pakket het gewys dat die twee- dimensionele simulasies onvoldoende is aangesien grensvoorwaardes en randeffekte 'n groot invloed het op die kalibrasiefaktor van die sensor.

Uitgebreide laboratorium toetse is ook gedoen om die sensor topologie sowel as die effekte van die koppelvlak instrumentasie en lekweerstand na grond te evalueer. Uitstekende korrelasie is gevind tussen gemete en voorspelde golfvorms, in beide die tyd- en frekwensie gebied met betrekking tot die kalibrasie faktor sowel as die toegevoegde pole en zeros by lae frekwensies. Die gevolgtrekking is dus dat 'n geldige stroombaanmodel voorgestel is vir die sensor topologieë vir die frekwensie bereik van 10 Hz to 1 MHz.

Sleutelwoorde: Kapasitiewe sensors, Ope-lug spanningsensors

Acknowledgements

Many people were directly and indirectly involved in this project. I would like to thank the following people and institutions:

- Dr. Vermeulen for his ideas and support of the project. The support encompassed more than enthusiasm about the concept, but also arranging funding for the sensor and instrumentation, my survival and the opportunity to present the research overseas.

- Pietro Petzer, André Swart and the rest of the workshop team. Without their effort and help, the practical aspects of this project would have been impossible. The construction of the prototype sensors and the measuring arrangements were skillfully handled by Pietro and the team.

- My colleagues through my PhD years: Johann, Katinka, Faatima, Francois, Theo and Thinus. Thank you for ideas, support and friendship. Francois and Theo in particular helped with the "muscle" work involved with the practical aspects of the project.

- Neil, Petrus and Wilhelm who manned the HV laboratory and advised on practical aspects as well as spending evenings at work so that I can finish the measurements.

- The NRF for financial support as well as Eskom for the TESP funds that were used for development of the sensor and interface instrumentation.

- Dr. Holtzhausen for the use of the simulation packages, Electro and Coulomb. His comments on the use of numerical methods and packages were also very useful.

- Last, but definitely most importantly: my parents. Thank you for believing in me and providing opportunities. Thank you for being there in all aspects of life, even when what I do seems unintelligible.

"If the facts don't fit the theory, change the facts"

Albert Einstein
1879-1955

Contents

List of Figures

List of Tables

List of Abbreviations

2D	-	Two-Dimensional
3D	-	Three-Dimensional
AC	-	Alternating Current
ADC	-	Analogue to Digital Converter
CT	-	Current Transformer
CVT	-	Capacitive Voltage Transformer
DAC	-	Digital to Analogue Converter
DC	-	Direct Current
D/I	-	Differentiating/Integrating (Principle)
EMC	-	ElectroMagnetic Compatibility
EMI	-	ElectroMagnetic Interference
EMTP	-	ElectroMagnetic Transients Program
EPLD	-	Erasable Programmable Logic Device
FACTS	-	Flexible AC Transmission System
GIS	-	Gas Insulated Switchgear
HV	-	High Voltage
HVDC	-	High Voltage Direct Current
LV	-	Low Voltage
MV	-	Medium Voltage
PD	-	Partial Discharge
PLC	-	Power Line Carrier
RMS	-	Root Mean Square
UHV	-	Ultra High Voltage
VFT	-	Very Fast Transient

List of Symbols

r_l -   Main line radius

h_l -   Main line height above ground

h_s -   Sensor height above ground

w_s -   Sensor width

d_s -   Thickness of dielectric separating the sensor plates

d_c -   Depth of faraday cage used to house the instrumentation

Φ -   Potential Distribution

v_i -   Measured input reference voltage during laboratory and practical measurements

v_m -   Measured sensor output voltage during laboratory and practical measurements

v_s -   Simulated output voltage using v_i and the system model

v_{mx} -   Maximum of v_m

v_{sx} -   Maximum of v_s

v_{mm} -   Mean around maximum of v_m

v_{sm} -   Mean around maximum of v_s

v_{m10} -   Subset of v_m: includes all samples larger than 10 % of v_{mx}

v_{s10} -   Subset of v_s: includes all samples larger than 10 % of v_{sx}

Chapter 1

Introduction

Many phenomena on high voltage lines generate high frequency signals. Examples range from low frequency harmonic distortion to high frequency noise generated by FACTS devices, switching-, lightning- and fault transients, partial discharges and corona noise. It is a known fact that standard substation equipment such as capacitive voltage transformers (CVTs), magnetic voltage transformers (MVTs) and current transformers (CTs) have limited bandwidth when used in the standard measuring configuration as they are designed and specified for 50 or 60 Hz operation. Therefore, they cannot be used to measure the high frequency waveforms accurately.

Furthermore this equipment is large and expensive due to the large amounts of insulation required at the high voltages. Therefore, the installations are usually fixed and at a limited number of locations, such as substation terminations. Future developments in harmonic penetration studies, lightning impulse studies, fault location and standing waves on long lines may require midline measurements. Further examples are insulation coordination under transient conditions and assessment of the nature and extent of overvoltages under dynamic conditions. Clearly there is a need for mobile equipment with very wide measuring bandwidths.

The lack of bandwidth in MVTs is discussed in detail by Douglass [1] and Malewski [2]. Bradley [3] concluded that it was not possible to create calibration curves for non-standard measurements with CVTs. Johns *et al* [4] discussed this limitation in the light of application of transient waveforms for fault location. Vermeulen *et al* [5] proposed a model for CVTs, which seems to work well into the harmonic frequency range. McKnight [6] mentioned the low bandwidth as support for the design of capacitive voltage sensors, especially when used in research laboratories.

Future studies are also planned on carrier propagation and standing waves. These studies may also include the effects of varying earth conductivity for long lines. Midline sensing or intersubstation measurement of waveforms will be required for these research projects, which is where a mobile

1

capacitive voltage sensor will be very useful. When these measurements are done further away from substations, the reflections caused by substation equipment may also be separated from the real transient waveforms.

The purpose of this research project is to evaluate possible non-intrusive, mobile, capacitive voltage sensors, which may fulfill the above requirements.

1.1 Project Motivation

Power systems are becoming more complex and tend to be operated closer to the stability limits. It is therefore important to locate and correct faults as fast as possible as well as to minimise the number of fault incidences. Fault location and analysis require accurate information of these fault-induced wideband transient waveforms, which cannot be measured using standard bandlimited voltage and current measuring equipment.

Harmonic distortion is a low frequency steady state phenomenon, but may have a significant influence on the network operation. FACTS devices are used to reduce harmonic distortion on the network, but in turn, they generate high frequency noise on the power network. The noise sources are the actual switching frequency of the semiconductor devices as well as the noise generated by the steep rise times of the voltage waveform.

Standard substation measuring equipment include CVTs, MVTs and CTs. It is possible to utilise these components in non-standard measuring topologies to obtain wider bandwidth measurements [7, 8, 9]. However, even in the transconductance topology, where the earth strap current is measured, the bandwidth is limited. Overall it can be said that conventional high-voltage measuring equipment such as CVTs, MVTs and CTs are bulky and expensive [7, 9, 10]. There is a need for affordable, easy-to-install or mobile wideband voltage transducers [6].

Alternative methods of measurement should definitely be investigated, which will reduce the size and increase the bandwidth. Cost of equipment will always be an issue for commercial companies, therefore, researchers should aim at cheaper technologies. Mobile units may also be a possibility to locate and solve problems involving inherent wide area phenomena.

Two possibilities may be mentioned: Voltage measurement using electro-optical effects or capacitive sensors, which utilise the "stray" capacitive coupling. The former is a rather expensive option as typical prices for a single crystal is on the order of US$ 6 000 and the polarising lenses on the order of US$ 1 000. At least one crystal and two lenses are required for a single-phase sensor. Capacitive sensors, as described in this project are much cheaper.

This research project therefore entailed a proper literature survey of the available sensors and establishing a design strategy for a suitable sensor. From available technology (see Chapter 2), it was found that there is scope for a new capacitive sensor using a differential topology.

Due to very high impedances involved and the harsh electromagnetic environment in which these sensors operate, a special interface between the sensor and measuring equipment had to be designed. This electronic circuitry had to be integrated with the sensor along with an optical fibre link, which provides galvanic isolation of the sensor and interference-free data transmission.

Long HVDC lines like the Cahora Bassa line usually runs along long stretches of uninhabited area, which complicates fault location. Along with the above-mentioned problem of ElectroMagnetic Interference (EMI), this provides an ideal situation to test a mobile, non-intrusive voltage sensor. One of the advantages of such a test site, is that this line is a monopolar line, i.e. a single sensor for a single phase voltage measurement is required, enabling thorough testing of a single unit.

Although travelling wave simulations and fault location algorithms may be a complete project on its own, some modelling of faults on the HVDC line has been done using EMTDC®. From this, typical waveforms were obtained, from which waveshape and frequency content could be derived. Most fault location algorithms require accurate timing of the fault transient measurement. For this reason, a separate project was initiated to develop a GPS receiver for integration with the sensor and sensor electronics [11].

The electrical environment below transmission lines (both AC and DC) has been an important research topic for a number of years for various reasons. The effect of power frequency electric and magnetic fields on the health of humans is a controversial issue. Knowledge of the maximum field strengths and potential distributions is also invaluable in future power system and substation design, especially when looking at higher voltages. A well designed capacitive voltage sensor may also be useful in such applications, due to close physical relationships between voltage sensing and electric field sensing using the capacitive coupling principle.

1.2 Project Description

This project comprised the design, analysis and evaluation of non-intrusive, open-air, capacitive voltage sensors in the simplified environment of a single line / single sensor topology in order to characterise the principles behind such sensor topologies properly. The sensor should be able to measure any transients with sufficient accuracy, where the accuracy is defined in terms of correct shape of the measured waveform. The calibration factor should be constant across the frequency

range of interest, but can be compensated for by comparative measurements. However, it is important to note at this point that most applications require predictable frequency-response characteristics, eg. a flat response, rather than an accurate prediction of the calibration or transformation constant. This reality is recognised throughout this investigation in that the frequency domain properties of the sensors are emphasised in the analysis.

Capacitive voltage sensors have been used on AC lines [12, 13, 14] to measure the voltage waveform on the overhead line. For three-phase lines, three or even more sensors should be used to be able to discriminate between the different phase voltages [12, 14]. It is therefore clear that decoupling is possible and if a suitable single phase sensor exists, the extension to multi-phase lines is fairly simple. The modelling and analysis presented in this dissertation, therefore, focus on sensors in a single line application. Extension of the work to multi-phase topologies is an exercise in superposition theory, which must be addressed in the recommendations for applications and future work.

Execution of the project comprised several steps, which may be summarised as follows:

- Compile a literature review of capacitive sensors in all areas of application with specific reference to types and topologies of sensors, design methodologies and construction aspects such as materials used and size of sensor. Calibration and accuracy of such sensors must also be addressed.

- Develop optically isolated, high speed interface instrumentation. The purpose of the instrumentation is to provide galvanic isolation of the sensor from the environment and reduce the effects of electromagnetic interference (EMI) on the measured signal.

- Develop equivalent circuit model topologies for open-air capacitive sensors under transmission lines. Thévenin's theorem may be used to simplify the model where possible. Contrary to expectations, this powerful approach has not received much attention to date.

- Model parameters must be obtained for the equivalent circuits. The capacitance parameters may be obtained from two- or three dimensional electromagnetic simulation packages. Field simulations should also be done to determine field distributions around typical capacitive sensors.

- Using the above-mentioned equivalent circuit models, determine the relationships between the different model parameters and the frequency response of the sensor. Equations for the circuit models should be derived as they may provide valuable insight into these relationships. Complimentary simulations should be done using PSpice® and Matlab®.

- Laboratory measurements should be done to obtain practical time and frequency domain responses for the prototype sensor. These must be compared with the simulated waveforms obtained earlier to evaluate the accuracy and validity of the equivalent circuit models.

- Estimation of circuit model parameters should be attempted using laboratory measurements and the defined circuit model.

- Field measurements underneath a monopolar line for final verification of the operation of the capacitive voltage sensor. This may be done under one pole of the Cahora Bassa HVDC transmission line. This line, which is located in the North-Eastern region of Southern Africa provides a suitable single phase transmission line to test a single sensor.

Most of the above objectives have been achieved. The exceptions are the field testing and parameter estimation exercise. The field testing could not be conducted due to operational constraints by the local utility, Eskom. However, the lack of field validation of the results was mitigated by a more extensive test program under laboratory conditions. The parameter estimation exercise yielded inconclusive, but promising results and was not completed mostly due to time constraints.

1.3 Dissertation Structure

The general background of the research project was briefly discussed in this chapter. A description of the requirements for the project was also given in section 1.2. The following comments give an overview of the structure of this dissertation:

- Chapter 2 provides the literature review on capacitive sensing techniques. The first section will be on small-signal applications of capacitive sensors, where the sensors are usually used as transducers of a mechanical input. Traditional voltage measurements are briefly discussed before continuing with capacitive voltage and electric field sensors. Some remarks on the construction of capacitive sensors are also given.

- The design aspects of a non-intrusive capacitive voltage sensor is discussed in Chapters 3 and 4. Chapter 3 starts with a field evaluation of the sensor topologies. Some remarks for numerical analysis and simplification of the sensing topology are also discussed. The following sections are devoted to derivation of the equivalent circuit model and the Thévenin simplification thereof. Four different types of sensors are analysed, single-, two- and three element parallel plate sensors and a single element coaxial sensor. The equations for these sensors are also discussed in order to provide more insight into the operation of such a sensor.

- The numerical analysis and simulations are discussed in Chapter 4. The equivalent models and equations are linked to the frequency domain response of the sensor using Matlab®. This step provides valuable insight into relative parameter sizes and other aspects, which should be kept in mind when designing such a sensor.

- It was found that galvanic isolation of the sensor is imperative for proper operation. Chapter 5 contains the design of optically isolated buffering instrumentation. A high-speed digital optical fibre is used to transmit data from a high input impedance buffer, which is integrated with the sensor, to the receiving circuitry, which interfaces with an oscilloscope or personal computer.

- Two sets of trial measurements were conducted during the design process. Valuable experience were obtained from these measurements, which are discussed in Chapter 6. The laboratory arrangement for the final measurements and the data processing algorithms are also discussed in Chapter 6.

- A prototype sensor was built using the design aspects from Chapter 4 and the instrumentation as discussed in Chapter 5. This sensor was tested in a shielded laboratory environment. The results of these laboratory tests and a discussion of the results are given in Chapter 7.

- The final conclusions and recommendations are given in Chapter 8.

Chapter 2

Literature Review: Capacitive Sensing Technology

2.1 Introduction

Capacitive sensors have been used for a long time to determine the electrical environment under power lines (both AC and DC) and to measure atmospheric electric field variations. Much research has also been done to evaluate the effectiveness of the relevant calibration procedures as well as the accuracy of the various electric field probes.

It was found, however, that most of the work proceeded in relative isolation, as most of the authors only reference their own work. One of the main reasons for this may be that the sensors are usually designed for a very specific purpose, e.g. DC electric field or voltage measurements, AC electric field or voltage measurements, partial discharges or corona measurements. A similar remark is made by Bassen & Smith [15] with regards to the development of electric field probes used for near-field measurements (i.e. small electric dipoles), where most probes are "custom-made" for a specific application.

The basic operation of these sensors are derived from electromagnetic field theory and good derivations of the sensor principles are available, albeit for limited applications. Examples are the work of Bassen & Smith [15] and Feser & Pfaff [16, 17, 18, 19].

Multiple aims for this chapter can be identified. Firstly it should serve as a reference for the completed work on capacitive sensors as well as background on other capacitive sensors and traditional voltage measurements. Secondly, the advantages and disadvantages of the existing measuring and sensing techniques should be discussed.

Section 2.2 contains a discussion of conventional substation voltage transducers. A brief description of the available technology as well as the shortcomings will be given. Section 2.3 contains information on capacitive sensing applications in all areas of engineering. The extension of these techniques and analyses to capacitive voltage sensing will be discussed. Section 2.4 gives a brief discussion of the calibration facilities available for capacitive voltage sensors.

DC measurements are discussed in section 2.5. This includes the different sensor types, namely space charge sensors, flat and cylindrical field mills and vibrating electrode sensors. Section 2.6 contains the discussion of the AC electric field and voltage sensors. Sensors for both open-air and gas-insulated-switchgear are discussed. The final conclusions for this chapter are given in section 2.7.

2.2 Conventional Substation Voltage Transducers

The main objective of this discussion is to review existing high voltage (HV) transducer principles and equipment and to critically appraise it in the context of wideband HV measuring applications. A good starting point for the discussion of HV measurements in power systems is to consider existing equipment and its shortcomings. A good discussion of conventional voltage transducers is given by amongst others Schwab [10], Kuffel & Zaengl [20] and Ryan [21]. The following voltage transducers are used in substations to measure AC waveforms:

- Resistive voltage dividers

- Capacitive voltage dividers

- Magnetic Voltage Transformers (MVTs)

- Capacitive Voltage Transformers (CVTs)

Most measuring techniques are extensions of low voltage methods and work fairly well up to approximately 100 kV. At higher voltages, the physical dimensions of the components are increased to prevent dielectric breakdown. With the increase in dimensions, the stray capacitances and leakage inductances are also increased - up to the point where these components may dominate the transfer function of the measuring system. Special constructional techniques are therefore required to minimise the stray components. Enough clearance should also be allowed between the measuring equipment and the environment, as this will further reduce the stray capacitive coupling.

Two configurations for resistive voltage measurements exist. The first method is to measure the current flowing through a high valued load resistor and find the input voltage from Ohm's law. The

second is to use voltage division of two series resistors and measure the voltage across the low voltage resistor. High valued resistors should be used to limit the loading effect on the network, i.e. the current through the resistors should be negligible to limit the intrusiveness of the measurement. Furthermore, it is impossible to construct a pure resistor that would mitigate the effects of the capacitive and inductive stray components. These stray components limit the high frequency response of both of the above-mentioned resistive voltage transducers.

Capacitive voltage division is achieved using series-connected capacitors. The measuring equipment is connected across the low-voltage capacitor. It is important that the input resistance of the measuring instrument is high enough so that distortion will be negligible. The input capacitance of the measuring instrument need to be taken into account, as it influences the dividing ratio of the divider.

The stray components mostly influence the high frequency behaviour of the voltage divider, but for 50 Hz measurements, the frequency response can be regarded as sufficient. The problem arises when fast rising impulses should be measured. Many researchers have developed mixed dividers, where the two impedances are matched in order to obtain maximum bandwidth. The matching of the low-voltage impedance should take into account as many of the stray components as possible. These dividers are, however, still sensitive to objects in close proximity, which will increase some stray capacitive components [10, 22, 23].

The magnetic voltage transformer (MVT) has been used extensively in earlier years. The MVT features a specially designed transformer, where the primary winding is connected to the high voltage to be measured and the secondary is connected to an AC voltmeter. Ideally, the measured HV signal is then equal to the measured LV signal multiplied by the transformer winding ratio.

Due to losses in the windings and transformer core, as well as loading effects of the measuring equipment, the output voltage may be larger or smaller than the expected transformed voltage. Several ratio taps are usually present on the secondary winding, to correct the ratio for these conditions. Apart from the losses, the transformer also has a low bandwidth, typically a few kHz, with a deteriorating response for higher voltage components.

A combination of the above two instruments is the capacitive voltage transformer (CVT), where the voltage is stepped down twice. First the voltage is stepped down to an intermediate level by standard series capacitive voltage division, while a transformer across the low voltage capacitor reduces the voltage even further. This arrangement is often used in transmission or distribution networks to monitor the line voltage and connect the power line communications to the HV line.

Bradley et al [3] attempted to obtain calibration curves for high frequency measurements with CVTs, but concluded that it was not possible. A wider bandwidth measuring system may be built

by measuring the current through a single high voltage capacitor. In power system applications, this may be achieved by measuring the current in the ground strap of a coupling capacitor [7]. The current is proportional to the time derivative of the high voltage and the voltage may be retrieved by integrating this current, using either hardware or software. The bandwidth for this arrangement is still limited.

Conventional substation voltage transducers, such as resistive and capacitive voltage dividers, MVTs, CVTs and CTs have the following drawbacks:

- The equipment is large and bulky

- The transducers have very limited bandwidth when used in the standard configurations

- All are intrusive as some form of impedance is connected to the high voltage electrode

The bandwidth of the measuring systems may be increased in two ways, namely by proper compensation or by using alternative configurations. These methods have, however, had limited success or are still under development.

2.3 General Application Transducers [24]

Baxter gives a review of the use of capacitive sensors in everyday applications in his book on capacitive sensors [24]. It is a developing field, where capacitive sensing replaces many of the old technologies, e.g. inductive sensors in traffic sensing. Many new applications also appear.

Typical applications of capacitive sensors can be categorised as follows:

- Proximity sensors [24]

- Measurement of displacement [24, 25, 26]

- Measurement of angle [24, 26]

- Touch-sensitive switches [24]

- Communications (capacitive isolation vs. optical isolation) [24]

- Computer graphic input (instead of a mouse) [24]

- Measurement of dielectric properties [27]

- Capacitive strain gauges [28]

All these methods basically amount to the measurement of a change in capacitance as either the dielectric constant or physical relationships between different electrodes change.

Guard gaps are used to stabilise the capacitance in varying conditions as mentioned by Goad & Wintle [27] when determining dielectric properties of materials. The principle of guarding is to provide alternative paths for stray fields and current caused by these stray fields in order to accurately measure the capacitive coupling between two electrodes. Guard electrodes for capacitive sensing applications in position or angle determination is discussed by Li *et al* [25, 26]. Heerens [28] also gives a detailed discussion of guarding and extends the modelling to 3-dimensional cases. Generic equations for different capacitance topologies are given together with a review of possible applications. It is the most comprehensive single reference found on capacitive sensors for general applications [28].

Baxter [24] also discussed the signal to noise ratios for different amplifier topologies. The measured capacitances may be very small and good amplifier circuit design and PC board lay-out principles are important. For applications where the ratio of capacitances are measured, correct circuit design will eliminate the need for very precise components and the effect of other component variations may also be cancelled. The use of multiple electrodes also increase the stability of these sensors, therefore it is advised to use such configurations. This aspect will be revisited when the final conclusions and recommendations are presented.

Environmental effects, like humidity and temperature may influence the accuracy of the measuring capacitor, while age may also influence the physical construction. The envisaged working environment of the sensor should, therefore, also be taken into account when designing a system dependent on a capacitive sensor.

Many of the above-mentioned aspects regarding sensor and amplifier design is important for capacitive voltage sensing as well. Differential voltage sensors have multiple electrodes and involve the indirect measurement of ratios of capacitances. Such sensors will, therefore, be less sensitive to environmental variations. For a sensor constructed from PCB (printed circuit board), humidity may affect the sensor response as the dielectric constant may change by 10-30 % due to absorption of water [24]. This variation has not been found under normal laboratory conditions, but for sensors constructed from PCB material and operated in the field, a proper sealant should be applied.

2.4 General Remarks on Calibration Facilities

Before moving on to a discussion of capacitive voltage sensors, the calibration facilities should be investigated. Most electric field sensors are calibrated inside parallel plate capacitors, where uniform fields can be produced. Takuma *et al* calculated the electric field inside two parallel plate topologies and showed for which circumstances a uniform field may be assumed [29]. It was found that their results showed a good correlation with IEEE Std 644-1979 and the recommendations from this standard could be deduced from Takuma *et al*'s findings.

Misakian developed an apparatus to generate a DC electric field with controllable amounts of space charge [30]. This was the first time where tests of DC electric field meters were done when the space charge current was known. For previous and many later tests, the researchers introduced some corona-generated ion current, without knowing the amplitude, to give a generalised result for the performance of the electric field sensors in the presence of space charge.

2.5 Field Meters for DC or Slowly Varying Fields

Although a discussion of literature on DC field measurements may seem irrelevant for the subject of this dissertation, many aspects of this field of study contains valuable clues for the design of wideband AC voltage sensors. These include the following:

- The performance and interaction of capacitive sensors in the presence of DC fields and space-charge; note that long DC lines are one of the applications of the technology discussed in this document

- Possible use of some of the calibration procedures

- Aspects of construction, particularly the electric and dielectric properties of the materials used

- Instrumentation design, particularly with reference to minimise the stray effects of measuring instrumentation

Moving electrode sensors are mainly used for DC field or voltage measurements, although slowly varying entities may also be measured. The developments in this kind of sensor proceeded in two disciplines, namely the measurement of the earth's atmospheric electric field and in power industry applications.

The field mill exists in two forms, namely a flat, rotating plate, which is usually mounted flush with the ground, and a rotating cylinder, which may be used at any height above ground. These two will be referred to as the flat or cylindrical field mill respectively. As with the other sensors, much research is done to eliminate the influence of space charge on the electric field measurement.

Wolzak [31, 32] developed two high voltage DC sensors, one stationary, selectively shielded, high voltage element and a vibrating electrode sensor. The former, called the knight due to the shielding electrode that looks like a knight's visor, can be used to measure DC, AC and impulse voltages. The knight's LV electrode is exposed to the HV electrode for several minutes, during which the low-drift integrator should give a steady reading indicating the high voltage. When space charge is present, eg. caused by corona, there will be a fast increase in output so that this error may be picked up easily.

2.5.1 Space charge and Ion current meters

As mentioned in section 2.4, space charge is present when measuring DC fields, but is difficult to quantify. Several sensors have been developed specifically for space- and surface charge and ion current measurements. Meek & Collins [33] developed a small probe to measure the influence of space charge on the electric field during the initial stages of spark breakdown in rod-plane gaps. The probe was mounted flush with the grounded electrode to measure the electric field at this grounded electrode and is terminated by a capacitor so that the output voltage is proportional to the field. Stassinopoulos [34] used two of these sensors, one at the grounded electrode and the other at the HV electrode for research on the initiation and growth of discharges in rod-plane gaps. The high voltage electrode's output was measured using an isolated oscilloscope inside a faraday cage, all at the high potential.

There are applications where it is desired to know both the electric field and the ion current. The above-mentioned probe gives an output proportional to the sum of the two quantities. Tassicker [35] used the probe exclusively to measure the ion current during corona situations by measuring the series current from the probe to ground. An improved probe by Tassicker [36] was biased by a DC voltage, in order to divert the ion current and measure only the field at the electrode. Selim & Waters [37] also commented on these probes and derived new equations for the fields due to the biasing voltages. According to Tassicker, it was possible to "over-bias" the probe leading to incorrect measurements, but Selim & Waters derived the proper equations for the response of the probe under these conditions [37].

Further developments by Stark, Selim & Waters led to the design of 'field-filter' probes [38]. Two forms were developed for bipolar ion fields so that the basic capacitive divider technique may be

used to measure the actual electric field at the probe location. This required a shielding grid or grids biased both positively and negatively in order to dispel the ion current charges. Two sets of grids may be used: one is a single layer of wires excited alternately by a positive or negative bias voltage, while the other consists of two perforated plates, which shield the sensing plate. One of these grids are biased positively, while the other is biased negatively.

Davies [39] devised a capacitive probe system to measure the charge accumulation on dielectric substrates in order to investigate the electrical properties of dielectrics. It is based on the principle that surface charge is equivalent to a voltage on that surface. Jing *et al* [40] used similar probes to determine the charge accumulation on insulators and spacers in DC Gas-Insulated-Switchgear (GIS) systems. This accumulation of surface charge presents problems with flashover inside the GIS system.

Jing *et al* [40] continued to discuss a procedure to measure the calibration factor of such sensors. Ootera & Nakanishi [41] proposed numerical methods and equivalent circuits to predict the response from these probes, also for use in DC GIS. The calibration factors of the sensors may, therefore, be determined from measurement, numerical or analytical methods. The above sensors were designed for use with well-defined geometries and reference potentials, which simplifies the calibration procedures.

2.5.2 Flat field mill

Most of the earlier work found in open literature on field mills, were done in conjunction with the measurement of the atmospheric electric field. Mapleson & Whitlock give a thorough discussion of the development of field mills up to 1955 and also include a description of the original "mechanical collector" [42]. This collector was moved between a grounded, "charge-collecting" position and a shielded, "charge-dumping" position. The charge-dumping was done either into an electrometer or galvanometer, where the amount of charge collected gave an indication of the applied field.

The flat field mill consists of two circular plates mounted on top of each other and separated by a thin isolating layer. The two plates are usually constructed as negatives of each other: the bottom plate has metal sectors, where the top plate has similar sectors cut out. As one of the plates is rotated, the result is that the bottom plate is alternately fully exposed or fully shielded from the applied electric field. The output voltage is usually a sinusoid with the amplitude proportional to the applied DC electric field.

The main reason for Mapleson & Whitlock's [42] new designs was to improve the accuracy obtainable with field mills. The need for operation during rain conditions was also stated, where

charge may be transferred to the pick-up electrode by the rain drops. In modern applications, for both HVDC field and the atmospheric electric field measurements, this problem is overcome by inverting and lifting the sensors so that the open side "looks" at the grounded earth plate on which they are mounted [43, 44, 45]. The positioning and calibration of the inverted sensor is discussed by Comber & Johnson [43]: the sensor is still grounded, but if mounted at the correct height above ground, the same amount of field lines will terminate on the sensing plate as when the sensor was mounted the usual way.

Two papers describe a set of measurements done by various groups to determine the electric field and ion current below a test HVDC line. The first, written by Comber & Johnson [43], focuses on the results for the single- and multiconductor HVDC lines. The second, written by Comber, Kotter & McKnight [44], was aimed at evaluating the different sensors available for these kinds of measurements. The electric field measurements varied from 15 % to 45 % from the mean, which is not a specifically good result. The main reason for this is most probably problems with the ion current, which adds more charge at the collecting plates and therefore gives a higher field reading. Some of the field mills were biased similar to the sensors discussed in section 2.5.1 in order to prevent the additive effect of ion currents and space charge. The measurements from these instruments may, therefore, be regarded as the most accurate. Maruvada *et al* developed two field mills, a flat and cylindrical mill [46]. Equations for the current flow generated by the mills are derived and it was shown that, by adding a phase reference, it is possible to measure both the electric field and the ion current simultaneously.

Smiddy & Chalmers [47] and Gathman [48] used a feedback amplifier to bring the reference voltage of the field mill to space potential so that the mill may be used above ground level without distorting the field. Due to the finite size of the sensor, the measured variable is usually an average value across the volume of the sensor. Smiddy & Chalmers [47] also mentioned that certain field mills only measure the mean value of the potential gradient between the sensor height and ground. Therefore, it is important to keep such a sensor small.

2.5.3 Cylindrical field mill

A sensor of the cylindrical type was developed simultaneously with the flat field mill, where two semi-cylindrical conductors are mechanically joined to form a complete cylinder and rotated around its axis, which is kept perpendicular to the field to be measured. The output is a sine-wave proportional to the magnitude of the electric field. Modern applications of the cylindrical field mill, specifically for the measurement of electric fields under HVDC lines, is described by Maruvada *et al* [46] and Johnston & Kirkham [49].

Kirkpatrick & Miyake [50] used a cylindrical field mill in 1932 in a fixed arrangement for high-voltage DC measurements. The voltmeter arrangement consists of two spheres placed on opposite sides of a cylindrical field mill. A galvanometer is connected in series with the two half-cylinders of the field mill, which measures the current flowing between these halves, where this current is proportional to the field generated by the voltage applied to the spheres. The current for this design is given by:

$$I = 2CVn \tag{2.1}$$

where C is the capacitance between one sphere and the one half of field mill cylinder, V is the potential difference between the two spheres and n is the speed of the rotor in revolutions per second.

This arrangement may be considered a "true" voltmeter, as the fixed arrangement allows external connection of any voltage to the leads. The arrangement will be sensitive to other conducting objects (energised or grounded) in the surrounding environment, similar to conventional high voltage transducers, but this may be minimised by proper placement.

Another voltmeter application is recorded 60 years later by Feldman *et al* [51]. A single electrode voltmeter was required to determine the voltage on HVDC lines. They also used a cylindrical field mill, but now physical connection to ground or another reference was prohibited. From field simulations, they found certain "sweet spots" close to an HVDC line conductor, where the potential distribution stays virtually constant across a large area. The field mill could be placed in such a sweet spot for very accurate results. This meter was tested on a field test line and had an accuracy of 7 % and better w.r.t. the predicted values.

The Kirkpatrick & Miyake cylindrical field mill is operated at ground potential, which is mainly for safety issues, as no current needs to flow to ground [50]. It cannot distort the field, as a balanced voltage is applied to the spheres, which results in a balanced field around a virtual ground plane where the field mill is placed. Maruvada *et al* also operated their cylindrical field mill at ground potential, but this distorted the field significantly [46]. It was found that operating the field at space potential would lead to less sensitivity, which is undesirable. A novelty about this sensor is that two sets of rotating plates were used so that the electric field and the ion current can be measured simultaneously. The phase reference of the rotation is required to extract the electric field and ion current variables.

Two other cylindrical field mills were designed to operate at space potential in order not to disturb the field. The one by Feldman *et al* has already been discussed [51]. Johnston & Kirkham also developed a small cylindrical field mill for minimal field perturbation and operated it at space potential [49]. The smaller probe also enables better spatial resolution of the measurements. Their

conclusion was that it is a working prototype, but several adaptations should be made for a commercial unit. One of the problems was the leakage current flowing along the handle, which influenced the measurements negatively. A better insulator should therefore, be found for the handle.

A last fieldmeter to be considered was developed by Kato and Takeuchi [52]. This meter used a combination of a field mill and standard capacitive sensor in order to obtain a response from DC right through to a few MHz. The frequency multiplication effect of the field mill required compensation to be added to avoid frequency peaking around the rotational frequency of the mill. This was implemented using feedback. The high frequency signal is filtered by a high-pass filter and fed back to a compensation electrode, which causes a biasing field cancelling the frequency peaks.

2.5.4   Vibrating electrode sensors

Although discussions of the design of vibrating plate sensors in literature are limited, many references to the uses there-off exist. Wolzak investigated the use of piezo-electric vibrating elements for the measurement of DC electric fields [31]. This sensor is also mounted flush with the ground plane. According to Misakian, a vertical displacement of approximately 1 mm of a vibrating sensor may lead to errors of several percent in the electric field reading, but the dimensions of the test arrangement for which this is true is not mentioned [30]. Misakian developed a controlled DC electric field intensity and space charge environment for the testing of DC field sensors. It was found that the vibrating type sensor is more sensitive to space charge than the field mill and gave consistently wrong readings when space charge is introduced into the measured region [30].

Six commercial vibrating plate sensors were tested by Comber, Kotter & McKnight [44]. From the results, it seems that these sensors are as accurate as the field mills also used in these tests. The field measurements ranged between 15 % to 45 % percent around the mean. The error distribution for these and the flat field mill sensors tested simultaneously is very similar. In contrast with Misakian's [30] results, these two types of sensors seem equally susceptible to ion current errors. This is attributed to the fact that Misakian's field mills were designed to reject the ion current, while the average field mill tested by Comber, Kotter & McKnight did not.

2.6   AC Electric Field Strength and Voltage Sensors

Fixed electrode sensors may either be constructed as part of the high voltage equipment as in AC GIS applications or as separate units, also called open-air sensors. The open-air sensors may be

mobile or add-on constructions to the HV equipment. Open-air electric field strength sensors in the form of small electric field probes may also be used to measure high voltages.

The fixed electrode sensors can be subdivided into three sections, namely the GIS voltmeters, open-air voltage sensors and open-air electric field strength meters.

2.6.1 Gas insulated switchgear

The instruments designed for GIS applications were exclusively designed to measure voltage or partial discharges (PDs) and have bandwidths ranging from a few kHz to hundreds of MHz. Switching transients in GIS seem to be a larger problem than in conventional switchgear due to the steep electric field gradients [53]. Many of these sensors were, therefore, designed to have very high bandwidths so that breakdown of GIS equipment may be investigated and prevented. Special sensors with very high bandwidths were developed to detect very fast transients (VFTs) as well as PDs.

Tokoro *et al* [54] designed new, low-burden voltage and current transducers by the late 1970s for a new digital control system on the expanding Japanese power system. A capacitive voltage divider was realised by adding a detection electrode to the GIS structure. The distributed capacitance between this detection- and the busbar electrodes form the high-voltage capacitor, while a secondary capacitor is connected between the detector and ground forming the low-voltage capacitor of the divider. Shield plates were also added to the GIS structure to shield each sensing element from the other phases.

A more compact current transformer was also developed at the same time, which had a dynamic range of 400 A to 4000 A. Both sensors' outputs were digitised and transmitted to the control room via optical fibre [54]. Proper attention was given to the grounding and shielding of the equipment to further improve the electromagnetic compatibility (EMC) of the system. The initial system was designed and tested on a 77 kV GIS system. Despite the promising results, it seems this system has not yet been implemented commercially [55].

Van Heesch *et al* [56, 57] used switchgear with flat metal hoops already present in the GIS. The only change to the equipment was, therefore, the connection of the coaxial cable leading to the oscilloscope.

Van Deursen *et al* [58] constructed an integrated current and voltage sensor. This type of sensor would allow for accurate simultaneous voltage and current measurements at, for example, current injection in HV transformers. The current sensor is a single turn, air cored Rogowski coil, which is mounted around the high voltage lead. The Rogowski coil output is a voltage proportional to

the time derivative of the magnetic flux passing through the coil and hence the current in the high voltage lead as well. An integrator is necessary to obtain a copy of the original current waveform. The voltage sensing element is a ring shaped electrode embedded concentrically in the side of the current coil.

The differentiating/integrating (D/I) principle is the process where the measured quantity is first differentiated due to some physical process and then integrated again to recover the original waveform [57, 59]. The differentiated signal is transmitted via the coaxial cable, with or without additional noise suppressing components, and the integration process is done in a controlled environment. The integration process will average any noise that was induced into the differentiated signal and in this way improves the electromagnetic susceptibility of the measuring system. A low termination impedance for the capacitive voltage sensor results in the differentiation of the voltage signal so that the capacitive voltage measurements may also benefit from the D/I principle [56, 57]. This termination impedance is usually chosen equal to the characteristic impedance of the coaxial cable, which eliminates any reflections on the cable. The D/I measuring system obviates the need for optical coupling or isolation when EMC is an issue [57]. The D/I principle is also explained by Keller [59] for use in high voltage probes to obtain a flat response over a wide frequency range. The theoretical bandwidth for this probe was from 85 kHz to 1.2 GHz. Practical measurements could only verify that the bandwidth extended to 200 MHz.

More precautions may be taken to enhance the signal reliability. An EMC cabinet [57, 60] is used for housing of the integrators and data handling equipment. Special precautions are also taken with the specially constructed termination resistors of the data cables. Several parallel branches are mounted in star configuration to minimise magnetic field coupling into the instrumentation rack.

Similar sensors were also designed for the detection of PDs and VFTs. Albiez *et al* and Meppelink & Hofer constructed a sensor with a single detection plate in the one side of the GIS structure [53, 61]. In contrast to previously discussed sensors, this sensor is not symmetrical around the GIS bus bar. The high voltage capacitor comprises the coupling between the high voltage bus bar and the detection plate, while the low voltage capacitor consists of the stray coupling between the sensing plate and the instrumentation housing, which, it is assumed, also shields this sensing plate from other conductors.

A low ohmic termination for the PD sensor attenuates the power frequency significantly. The high frequency pole of this differentiator, where the transfer function levels, results in a flat response for the very high frequency signals of the partial discharges.

VFTs contain frequency components from approximately 10 Hz to 200 MHz. Albiez *et al* [61]

redesigned the termination of their PD sensor in order to measure the larger VFT signals. The role played by the termination impedance is evident from the discussion. Great care should be taken to get a flat frequency response across the desired frequency range.

Osmokrovic *et al* [62] developed a VFT sensor where the high voltage capacitor is formed by the stray coupling between the GIS bus bar and a ring sensor, which is symmetrical, similar to previously mentioned sensors. Several options for the construction of the low voltage capacitor was investigated. It was found that a completely integrated approach should be taken to prevent oscillations at the higher frequencies. These oscillations are mainly caused by the stray inductance of leads connecting resistors and capacitors together. The use of complicated equivalent circuits to describe the behaviour of the sensor at these and higher frequencies is mentioned, but not discussed.

Both the above authors reported excellent results across the desired bandwidth. Very accurate sensors may therefore be obtained using these methods, but special care must be taken with the construction of the low voltage capacitor and connections made to it.

The D/I principle is used by McKnight from the National Bureau of Standards as well [6]. McKnight developed a so-called E-dot sensor, which basically means that the output voltage is proportional to the time-derivative of the applied electric field. An equivalent circuit diagram for the sensor and integrator is given as well as a description of the operation. The bandwidth of the system is discussed in conjunction with the integrator time constant and oscilloscope loading effects. The sensor forms a part of the HV equipment, but an open geometry is also possible for non-intrusive measurements [6]. Proper termination, calibration and other measuring principles are emphasized for proper results.

Overall the capacitive sensors designed and tested for GIS show:

- Better bandwidth than conventional techniques [6, 53, 54, 56, 57, 58, 59, 61]

- Good EMC properties:
    - the sensors are well-contained and shielded
    - optical data transmission is used [54]
    - D/I principle easily implemented [56, 57, 58, 59]

- Small size [54]

- Low cost [56, 57]

- Simple construction:
  - existing, built-in electrodes can be used [56, 57]
  - specially designed sensors can be constructed easily [54, 58]

It is clear from the above discussions that capacitive sensors have yielded excellent results for wideband applications in GIS. However, a number of important differences exist between the GIS environment and open-air applications. These include the following:

- The physical environment where GIS sensors are implemented are well-defined and also confined to small spaces with well-defined ground references

- Connections to GIS sensors can be made as an integral part of the sensor topology due to the well-defined ground reference, which accounts for the excellent responses achieved with the D/I galvanic coupling

The above advantages unfortunately do not exist in open-air applications.

2.6.2 Open air applications

Van Heesch *et al* [12] placed metal plates underneath a three-phase transmission line and measured the induced voltages using the D/I principle. A fixed grid of non-intrusive capacitive sensors is placed underneath the transmission line, forming a three-phase capacitive divider, with capacitive coupling between all conductors and sensors. The emphasis was on low cost sensors, which are easy to install. Van Heesch *et al* used the low impedance resistive termination to implement the D/I principle. The sensors of van Heesch *et al* were constructed as a ring with a grounded centre plate. This plate diverts leakage current to the ceramic insulator, on which the sensors were mounted. This ensures that the electric field reading is not influenced by ion current.

Roberts & Hoch [13] used a similar array under a three-phase line at the incoming point of the 400 kV substation. The termination impedance of their sensors comprised extra secondary capacitors and high impedance optical probes to capture the measured signals [13]. The value of the terminating capacitor was chosen to give a flat frequency response down to 50 Hz.

Three of these sensors were used to measure the voltage on three-phase overhead lines. Each sensor picks up a combination of the three phase voltage components, which needs to be decoupled. A matrix of coupling capacitances can be defined and evaluated for a set geometry of phase conductors and sensors. Very good results were obtained by both van Heesch *et al* [12] and Roberts &

Hoch [13]. Roberts & Hoch had an additional three-phase line adjacent to the line-under-test. The influence of this line was first measured with the line-under-test de-energised, so that the interference signals could be subtracted from the final signal. The decoupling factors for the sensors were calculated from an energising transient and the decoupling done numerically.

Gerrard *et al* [14, 55] showed that at least six sensors are necessary to decouple a three-phase system's voltages. Intuitively, three sensors should be adequate, as demonstrated above, but in the presence of noise three more may be required. Gerrard had to measure to a very fine resolution, 2 % changes from nominal, which explains the required redundancy. Eight sensors were eventually used, which is the next power of 2 larger than 6 and leaves even more redundancy. In the event of some sensors stopping to function, it is still possible to deduce the actual conductor voltages [55]. This was demonstrated by Gerrard for his doctoral dissertation, where two sensors stopped working during the field tests, but accurate results could still be extracted from the remaining sensor data.

Differential voltage sensors were discussed by Shimada, Furukawa & Ohchi [63]. Two differential sensors were discussed, which were mounted on the conductor of a 6.6 kV test system used for training. The phase shift between the conductor voltage and measured voltage caused concern and detailed numerical simulations were performed to determine the expected phase shift for each of the sensors. According to Shimada, Furukawa & Ohchi, each sensor is supposed to detect only a single phase voltage. The authors may have neglected the cross-coupling, which may cause the phase shift. It was also found that the phase shift of the unbalanced sensor topology was worse than the balanced concentric circles. The concentric circles provide more shielding, supporting the above assumption regarding the cross-coupling. The Power-Donut^{TM} [64] is a similar device clamped around an HV conductor. This sensor is ring- or donut-shaped and transmits real-time line voltage, current and conductor temperature to a ground station.

All the open air voltmeters were designed for three-phase applications. Both hardware and software (numerical) decoupling has been proven to find the original phase voltages. One exception is the knight, which was designed by Wolzak [31] and used by Van Helvoort *et al* [65] for evaluation of surge arrestor switching waveforms. Very good agreement between simulations and practical waveforms were obtained for these applications as well.

Different methods of terminating the sensors are discussed and all seem to work very well if all constraints are taken into account. Usually the input impedance of an oscilloscope is assumed to be large, but 1-10 MΩ may be small when talking about capacitive sensors and may therefore cause unfavourable loading of the sensor. Once again the EMC properties of the measuring system is assured by using either the D/I principle or optical data transmission.

The single element sensors seem to work well, but the capacitive coupling parameters are very sensitive to the actual position of the ground level. A differential sensor, similar to those of Shimada *et al*, will be less sensitive to ground plane variations as the reference is less important in differential topologies. This will emerge as an important aspect of the approach followed in this dissertation.

2.6.3 Open-air AC electric field strength sensors

Feser, Pfaff and co-workers developed several versions of a spherical potential-free sensor for the measurement of the localised electric field [16, 17, 18, 19]. This sensor was developed specifically to measure electric field strength, but the voltage on a nearby HV electrode can also be determined [16]. The signal is transmitted via optical fiber both for isolation of the sensor and good EMC properties for the signal transmission. The basic principle once again is that of a capacitive probe [17], similar to the spherical dipoles discussed by Baum *et al* [66]. Several versions of the probe have been discussed over the years, where the bandwidth and dynamic range that can be achieved progressed with available electronics. The latest version has a -3dB bandwidth ranging from 20 Hz to 350 MHz [19]. The size of the sensor has also increased to house the instrumentation as well as the battery (from 40 mm initially to 85 mm).

The effect of the termination impedance is discussed in great detail by Pfaff [18]. The sensors may be configured as integrating or non-integrating, but specific applications for either configuration is not mentioned. Both 2- or 3-dimensional versions were developed, where each component of the field is measured separately.

A different application, not mentioned by the original authors, may be to use the different components of the field to distinguish between different excitations. If, for instance, two HV electrodes are present, which have different contributions to the x or y component of the E-field, the two outputs may be decoupled back to the individual voltages. This is similar to the three-phase decoupling implemented for open-air sensors.

2.7 Conclusions

It has been argued that conventional voltage transducers work very well for their intended functions when used in the standard configuration. Other applications exist where the limited bandwidth, size and intrusiveness of these transducers require new sensing equipment.

From the above survey, it is clear that capacitive sensors may be applied effectively in power system applications. Various applications exist, ranging from voltage measurement to determination of surface charge accumulation on insulators. These sensors fulfill the needs for smaller, cheaper equipment with wider bandwidths. The sensors can usually be implemented to be non-intrusive, i.e. negligible load current is drawn from the HV electrode. Many of the sensors, eg. the field mills for DC measurements and the spherical open air electric field strength meters are mobile as well.

Capacitive sensors are widely used in all areas of engineering. It was found that multiple electrode sensors, where the ratios of capacitances are measured are stable and that they simplify the design of the associated instrumentation. These principles may be extended to differential sensors for voltage measuring applications.

Two significant problems should be mentioned, namely space charge induced voltages and leakage currents. Space charge in the sensor environment may distort the field or cause ion current flow to the sensor, which will result in an incorrect reading. Leakage current, which is caused by the finite resistance of an isolating medium may reduce the charge available for the measurement. It was found that leakage cause distortion in the low-frequency range, extending as low as 50 Hz.

The question of space charge and charge build-up on capacitive plates is very important, especially if DC measurements are made. Mapleson & Whitlock earthed their sensor periodically to prevent too large errors from charge build-up [42].

On the other hand, the leakage resistance of support structures, like the handles of Johnston & Kirkham's cylindrical field mill may also be a problem [49]. The lower frequency response may be affected negatively by this loss of charge, leading to a possibly lower electric field reading. This issue will be shown to have important implications for the frequency responses of practical capacitive sensors.

Compared to DC field measurements, electric field applications and GIS research, it is clear that relatively few investigations have been conducted on open-air capacitive voltage sensing applications. This is possibly due to the difficulties introduced by stray effects and the lack of a solid reference potential. It is in this arena that this dissertation aims to make a contribution by introducing alternative differential topologies with integrated instrumentation, equivalent circuit modelling, novel instrumentation principles and frequency-domain analysis.

Chapter 3

Sensor Topologies and Equivalent Circuit Models

3.1 Introduction

The process of sensor design and analysis was done as an iterative process. The main reason for this is that a number of parameters, which were regarded as negligible at first, were shown to affect the overall transfer functions. The first prototype sensors were constructed and tested in order to determine which parameters are significant and to what extent such parameters should be included in the equivalent circuit models. This chapter is dedicated to a detailed analysis of the structure of the sensor topologies and the derivation of the equivalent circuit models. A mathematical discussion of the equivalent circuit models will also be presented.

Equivalent circuit models are derived by lumping the capacitive coupling between the transmission line and the different sensing elements, similar to the equivalent circuits of multiple transmission lines. The sensor is electrically small and therefore all inductive coupling is ignored. However, certain loss elements need to be included and these are added in parallel with the capacitive coupling elements where required.

Section 3.2 gives a general description of important aspects concerning capacitive sensor design, introducing the problems experienced during preliminary measurements and the design principles that emerged during this process. A discussion of the different sensor topologies analysed for this dissertation is also included in section 3.2. Section 3.3 contains the equivalent circuits for each topology discussed in section 3.2. The important aspects of the equivalent circuits will be summarised in section 3.4.

3.2 Overview of Sensor Topologies

Four structural categories of capacitive sensors can be defined from the literature reviewed in Chapter 2. Table 3.1 lists these categories along with the typical applications.

Table 3.1: Structural categories of capacitive sensors listed along with typical applications

Sensor structure	Typical applications
Plate-type structures	Open-air sensors [12, 13, 14]
	Surface charge sensors [33, 39]
	DC flat field mills [43, 44, 46]
Coaxial structures	Gas-insulated-switchgear [54, 56, 65]
	Differential sensors around live conductors [63]
Cylindrical sensors	Cylindrical field mills [46, 50, 51]
Spherical sensors	Electric field strength meters [16, 17, 18, 19]

Both coaxial and cylindrical sensors have a cylindrical shape - the distinction is therefore in the positioning. Coaxial sensors are mounted in a coaxial fashion around the live conductor, while the cylindrical sensors are usually placed reasonably far from the live conductors, measuring the remote electric field. From Table 3.1 two broad categories of sensor topologies are proposed for further investigation for open-air applications, namely plate sensors and coaxial sensors.

- **Plate sensors:** The plate sensors are placed underneath a transmission line, close to ground and parallel to the (ideal) ground plane and equipotential lines. The single plate sensor topology is very sensitive to changes in the virtual ground plane level as caused by ground conductivity changes or relative sensor height variations. For this reason differential parallel plate sensor topologies are suggested to decrease the effect of the ground conductivity changes on the sensor response.

- **Coaxial sensors:** Differential sensors mounted around the conductors of the transmission line remain in direct contact with the transmission line [63, 64]. This is undesirable, but the coaxial topology should not be discarded as very good results were obtained in GIS. Sensors in GIS have a similar topology and the well-defined geometries and ground references ensure good, repeatable results. From a safety point of view, a similar sensing element may be used around the earth conductor, where the geometry and ground reference are well-defined.

  The proposed coaxial sensor is a single sensing element mounted around an earth conductor above HV transmission lines, where the potential lines approximate concentric cylinders. In contrast with the single plate sensor topology, the coaxial sensor is less sensitive to changes in the ground plane for two reasons:

  - It is placed far from the ground plane

- The capacitance between the sensing element and the earth conductor reference is large with respect to the coupling between the sensor and physical ground

Before continuing a discussion of the different sensor topologies, three additional features should be discussed. The following aspects were found to be of great importance for open-air capacitive sensors in transmission line applications:

- **Galvanic isolation from ground and other conducting media:**

  Charge is induced by the HV conductors on the plate elements via the electrostatic induction process. The amount of induced charge is proportional to the voltage of the HV conductor and thus allows measurement of the voltage on the transmission line. The termination impedance and instrumentation provide a known path for the discharge current and the support structure should not add significantly to this. The support structure may influence the sensor environment in two ways, namely by distorting the field due to charge build-up on itself or by conducting charge away from the sensor. The support structure should therefore be designed to minimise both these effects.

  Another important aspect is the data cable connection. The interface instrumentation was designed with a fibre-optic link to maintain the galvanic isolation. The instrumentation transmitter circuitry is located inside a faraday cage.

- **High impedance interface instrumentation:**

  The input impedance of the buffer instrumentation constitutes the termination impedance of the sensor, which may load the sensor. This loading effect is undesirable for two reasons, namely:

  - The output voltage may become too small to be measured
  - The frequency response of the sensor is not flat across the frequency range of interest

  Therefore, it is desirable to have a very high input impedance with a flat frequency response, i.e. all poles and zeros should lie outside the frequency range of interest.

- **Measurement Reference:**

  Due to the relative small size of the capacitive sensor compared to the transmission line, the sensor output voltage will be proportional to the transmission line voltage with respect to the local ground or an equipotential plane in the vicinity of the measuring point. The local ground is important when looking at aspects such as insulation coordination as well as transient modelling of transmission lines and depends on properties such as soil resistivity. It is envisaged that this fact will allow the measurement of these localised earth properties.

  Similarly for the coaxial sensor structure, the sensor voltage will give an indication of the voltage between the earth- and HV conductors at the sensor position. It is possible that the

earth conductor is insulated from the towers, in which case the series impedance of the earth conductor must be added to the equivalent circuit model.

One of the important objectives of the research presented in this dissertation is to clarify the relationships between the transfer function characteristics of the sensors and the individual parameters defining the sensor topology. This is achieved by using equivalent circuit analysis, where the individual circuit elements may be referenced to the abovementioned sensor parameters.

The main properties, advantages and disadvantages of the following four sensor topologies will be reviewed in the following subsections:

(1) Single element plate sensor

(2) Differential parallel plate sensor (two-element parallel plate sensor)

(3) Differential parallel plate sensor with floating faraday cage (three-element parallel plate sensor)

(4) Single sensing element coaxial sensor

Figure 3.1 shows two-dimensional diagrams of the plate sensor topologies. The electric field lines indicated in Figure 3.1 show the idealised electric field lines close to the ground plane underneath a transmission line. Figure 3.2 shows a two-dimensional diagram of the single element coaxial sensor topology. The idealised electric field lines are shown on the left half of the figure only to leave space for the text, but follows the same pattern on the right hand side of the sensor. The ground plane reference is not shown in Figure 3.2 as the ground plane plays a negligible role in the transfer function of this sensor topology.

3.2.1 Single element plate sensor

The single element plate sensor topology is shown in Figure 3.1 (a). It is similar to the open-air sensors discussed in literature and seems to work well [12, 13, 14]. No indication of calibration factor calculation was given for this sensor topology, but calibration factors for practical measurements were obtained from energising transients.

The main disadvantage of this topology is that it is very sensitive to ground level variations, eg. caused by ground conductivity changes. It is difficult to model the effect of the soil conductivity using the numerical electric field solvers and therefore, the changes in ground level is modelled by varying the relative sensor height, i.e. the sensor height as a percentage of the transmission line height.
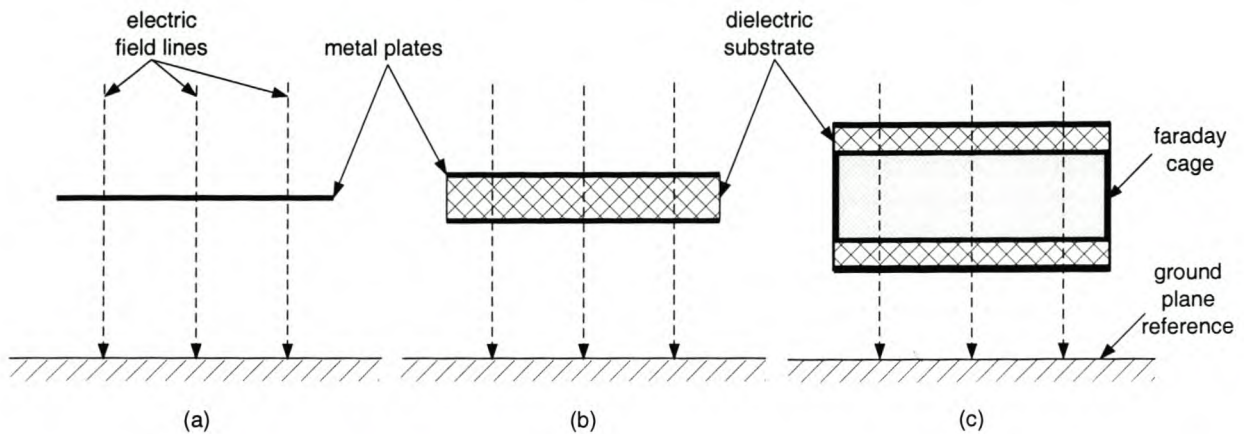
Figure 3.1: Different topologies for plate sensors: (a) single plate sensor (b) differential parallel plate sensor (two-element sensor) (c) differential parallel plate sensor with floating faraday cage (three-element sensor)
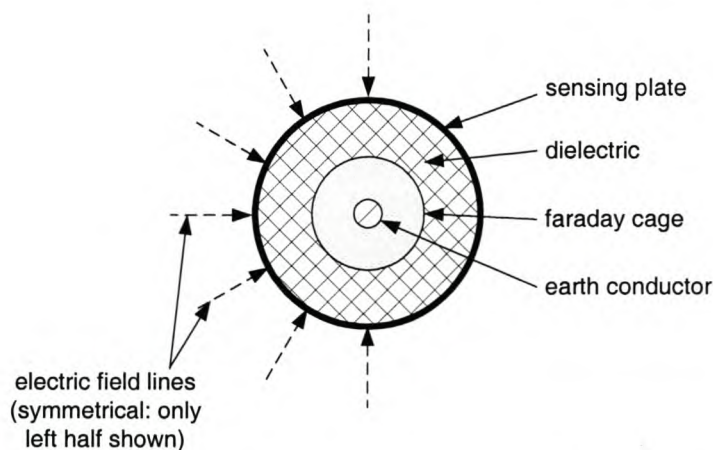
Figure 3.2: Diagram of single element coaxial sensor topology with faraday cage connected to earth conductor

3.2.2   Differential two-element parallel plate sensor

The differential two-element sensor is proposed for reduced sensitivity to ground level changes and is shown in Figure 3.1 (b). The common-mode voltage on the two differential sensing elements will approximate the behaviour of the single element plate sensor. In order to eliminate coupling between the common- and the differential mode voltage, galvanic isolation between the sensor and ground is of utmost importance.

Extensive simulation studies were performed using the 2D electric field solver to characterise this sensor and its surrounding electric field. According to these simulations, the sensor is less sensitive to variations in the ground level than expected. It was also found that galvanic contact between the sensor and ground influences the frequency response adversely.

The differential two-element parallel plate sensor is a preliminary design as the faraday cage is not inherently included in the design. For the initial tests a faraday cage for the interface instrumentation was connected to the top plate of the two-element sensor. The cage did not extend the whole length of the sensor as it was neglected in the 2D simulations and it was expected that this would only have a negligible influence on the sensor coupling parameters.

3.2.3   Differential three-element parallel plate sensor

Figure 3.1 (c) shows the three-element sensor with a separate, floating faraday cage for the interface instrumentation. The main disadvantage of the two-element parallel plate sensor is that a well-defined faraday cage was not included in the topology. It was therefore decided to include the faraday cage as an extra, floating element between the two sensing elements. This design is a balanced topology, where the faraday cage in essence provides a floating common mode reference voltage for the two differential elements.

The third element adds considerable complexity, but the faraday cage provides several benefits such as reduced sensitivity to leakage to ground. The differential sensor voltage is influenced negligibly by a galvanic connection between the faraday cage and ground, while connection to any of the sensing elements cause adverse effects similar to the two-element parallel plate sensor. The advantage of this fact is two-fold, namely that non-ideal support structures may be used if it is connected to the faraday cage and such a leakage path provide a suitable route for the removal of space-charge induced surface charge when measuring under DC conditions.

3.2.4   Single sensing element coaxial sensor

The single element coaxial sensor topology is shown in Figure 3.2. The potential distribution around a conductor above ground forms cylinders, which are almost concentric close to the conductor. It was considered a suitable position for a cylindrical or coaxial sensor around an earth wire. A cylindrical sensor around the live wire has been tested before [63]. A sensor around the ground wire is considered a better option, as the sensor is then very close to the ground reference, which makes it a safer option as well.

Ideally, the earth conductor provides a perfect ground reference and the induced voltage will correspond to the voltage on the transmission line. Significant series resistance and inductance exist in the path from the earth conductor to ground, which means that the reference voltage will rise along with the tower structure under transient conditions caused by eg. a lightning impulse. This

sensor topology will, however, give an accurate representation of the voltage across the insulator strings.

3.3   Derivation and Analysis of Equivalent Circuit Models

The sensor topologies were introduced in section 3.2. Equivalent circuits will now be derived and analysed for each topology. First the geometry of the transmission line sensor topology will be given for each topology, followed by the capacitive coupling elements in context of the geometry. From this the equivalent circuit model can easily be derived. The model is similar to the traditional transmission line circuit model, but with only the shunt elements included as the sensor is regarded as a point element.

Resistors are the only non-ideal elements, which are included in the model - no inductors were modelled. It was assumed that the sensor and all relevant elements are small/short enough, that the inductance could be neglected. Usually the shunt loss terms included in transmission line models are indicated as conductances. As only the shunt elements are used for the equivalent circuit models of the sensor topologies, resistance elements may be used without the risk of confusion.

Thévenin's theorem is used throughout to determine an equivalent voltage source and impedance to characterise the sensor topology. 1 V is assigned to the transmission line voltage so that the equivalent voltage source rather is a normalised Thévenin equivalent voltage. Any termination impedance can be connected to the Thévenin equivalent circuit to determine the overall output of the sensor topology. This termination impedance would typically be the input impedance of the interface instrumentation.

The output voltage of the sensor with any arbitrary termination impedance connected is given by equation 3.1:

$$V_{OUT} = V_{TH}\frac{Z_t}{Z_t + Z_{TH}}$$

(3.1)

where V_{OUT} is the output voltage, V_{TH} and Z_{TH} the Thévenin equivalent voltage and impedance respectively and Z_t the termination impedance.

The Thévenin equivalent voltage and impedance are both functions of frequency because of the resistance elements in the equivalent model circuits. If all the loss terms are neglected, the value of the high frequency asymptote for the normalised Thévenin equivalent voltage and a Thévenin equivalent capacitance are defined.

The Thévenin equivalent voltage together with the Thévenin equivalent capacitance allows for easy calculation of the high frequency division ratio or asymptote for any added termination. The

low-frequency cut-off caused by the resistive part of termination impedance can also be calculated easily from these equivalent circuit parameters.

3.3.1   Equivalent circuit for the single element plate sensor

Figure 3.3 shows a 2D diagram of the geometry of a single flat plate sensor above a ground plane underneath a transmission line. The letters in circles, namely l, s and g indicate the naming conventions of subscripts of element values and represent the transmission line, sensing plate and ground respectively. The dimensions for this sensor topology are defined as follows:

r_l Main line radius

h_l Main line height above ground

h_s Sensor height above ground

w_s Sensor width
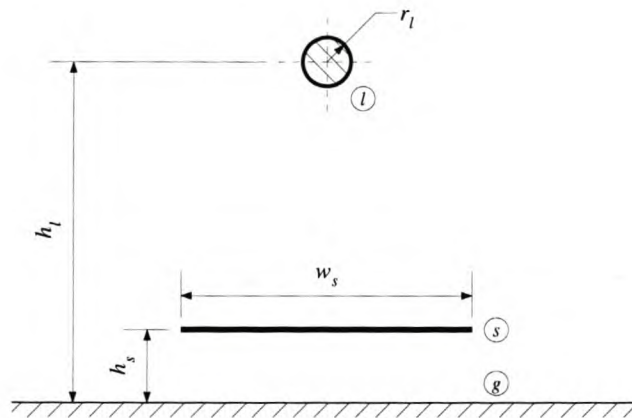
Figure 3.3: Two-dimensional view of transmission line and single plate sensor geometry

Figure 3.4 shows a 2D diagram of the capacitive coupling components of a single flat plate sensor above a ground plane underneath a transmission line. An equivalent circuit for the sensor geometry shown in Figure 3.4 can be deduced by arranging the capacitors in circuit format. The shunt loss terms from the traditional transmission line model should also be included in parallel with the capacitances. The main line capacitance to ground, C_{lg}, need not be included as the two systems are completely decoupled and the sensor is regarded as a point element. The resulting circuit is shown in Figure 3.5.

The capacitances and resistances in Figure 3.5 are defined as follows:

C_{ls}, R_{ls} Capacitance and resistance respectively between the main line and sensing plate

C_{sg}, R_{sg} Capacitance and resistance respectively between the sensing plate and ground
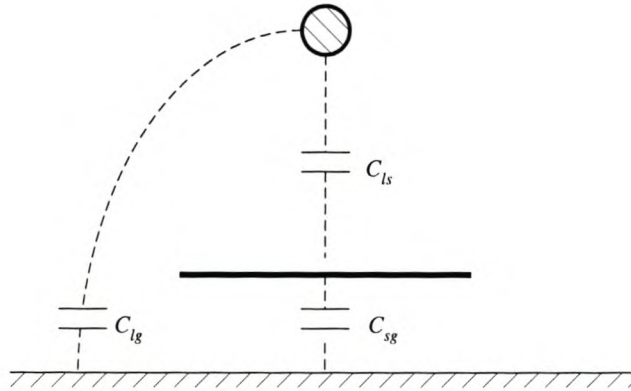
Figure 3.4: Two-dimensional view of transmission line and single plate sensor showing capacitive coupling
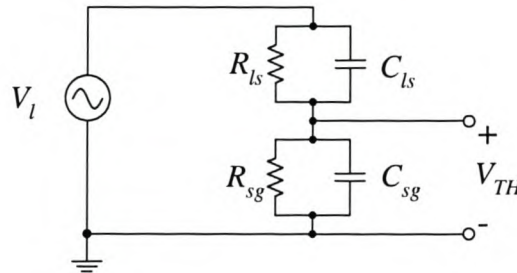
Figure 3.5: Equivalent circuit model for the single element plate sensor topology

The resistance between the main line and the sensing plate, R_{ls}, may be ignored as air is a very good insulator. Using the notation of Figure 3.4, the Thévenin equivalent voltage is given by the relationship:

$$V_{TH} = V_l \frac{sC_{ls}R_{sg}}{1 + sR_{sg}(C_{ls} + C_{sg})} \tag{3.2}$$

and the Thévenin equivalent impedance by the relationship:

$$Z_{TH} = \frac{R_{sg}}{1 + sR_{sg}(C_{ls} + C_{sg})} \tag{3.3}$$

where $s = j2\pi f$ is the complex frequency.

Under normal circumstances, it is expected that the resistance between the sensing plate and ground, R_{sg}, for this sensor topology is much larger than the value of the terminating resistor. Therefore, this resistor may also be neglected and the equivalent circuit comprises only capacitors as shown in Figure 3.6.
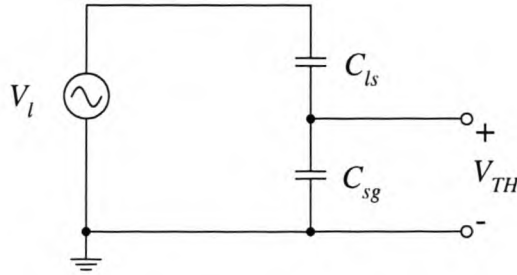
Figure 3.6: Simplified equivalent circuit model for the single element plate sensor topology

Using the notation of Figure 3.4, the high frequency asymptote Thévenin equivalent voltage is given by the relationship:

$$V_{TH} = V_l \frac{C_{ls}}{C_{ls} + C_{sg}} \qquad (3.4)$$

The Thévenin equivalent capacitance is given by the parallel combination of the capacitance between the transmission line and sensor plate and between the sensor plate and ground, i.e.

$$C_{TH} = C_{ls} + C_{sg} \qquad (3.5)$$

and the Thévenin equivalent impedance:

$$Z_{TH} = \frac{1}{s(C_{ls} + C_{sg})} \qquad (3.6)$$

If the sensor plate is close to ground relative to the transmission line height, the capacitance between the sensor and ground, C_{sg}, will dominate the transfer characteristics of the sensor topology. Small variations in this capacitance will, therefore, have an almost equal percentage change in the Thévenin equivalent voltage and impedance. One way to overcome this is to use a termination capacitance, C_t, that is much larger than C_{sg}, which will override small variations in C_{sg}. The single element plate sensor with the extra capacitance has been used before with good results [12, 13, 14].

The single element sensor is simple to analyse and construct. The main problem with this sensor is that it is very sensitive to the distance between the sensor and the virtual ground level. Inside a substation, this problem is limited by the earth mat providing a well-defined ground reference. However, the lack of a convenient ground plane under field conditions and the fact that the termination impedance of the interface instrumentation is not an integral part of the design, compromises the practical usefulness and accuracy of this topology. This is particularly true with reference to accurate determination of the voltage measuring calibration factor of the arrangement.

3.3.2   Equivalent circuit for the two element parallel plate sensor

The single plate sensor of section 3.3.1 is very sensitive to ground level variations. A differential sensor is suggested as an attempt to design a more robust sensor, which is less sensitive to outside influences.

Figure 3.7 shows a 2D diagram of the geometry of a two-element parallel plate sensor above a ground plane underneath a transmission line. The letters in circles, namely l, $s1$, $s2$ and g indicate the naming conventions of subscripts of element values and represent the transmission line, sensing elements and ground respectively. The dimensions for this sensor topology are defined as follows:

r_l	Main line radius
h_l	Main line height above ground
h_s	Sensor height above ground, measured to the bottom plate
w_s	Sensor width
d_s	Thickness of dielectric separating the sensor plates
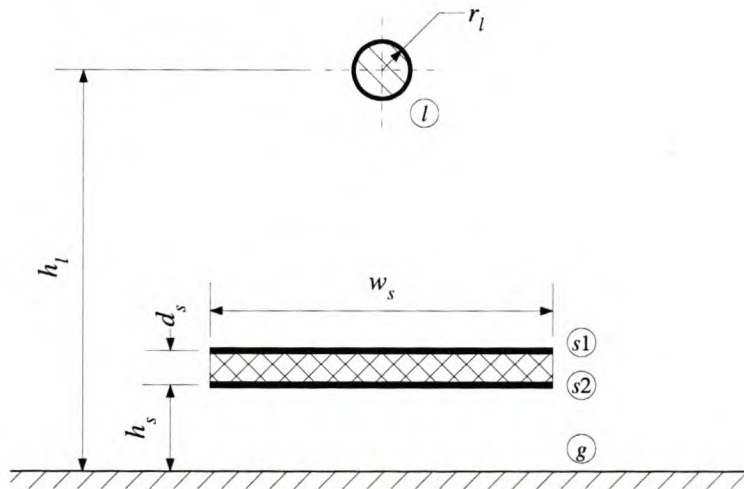
Figure 3.7: Two-dimensional view of transmission line and two-element parallel plate sensor geometry

Figure 3.8 shows a 2D diagram of the capacitive coupling components of a two-element parallel plate sensor above a ground plane underneath a transmission line. An equivalent circuit for the sensor geometry shown in Figure 3.8 can be deduced by arranging the capacitors in circuit format. The shunt loss terms from the traditional transmission line model should also be included in parallel with the capacitances. The main line capacitance to ground, C_{lg}, may be ignored in the equivalent circuit model as stated before. The resulting circuit is shown in Figure 3.9.
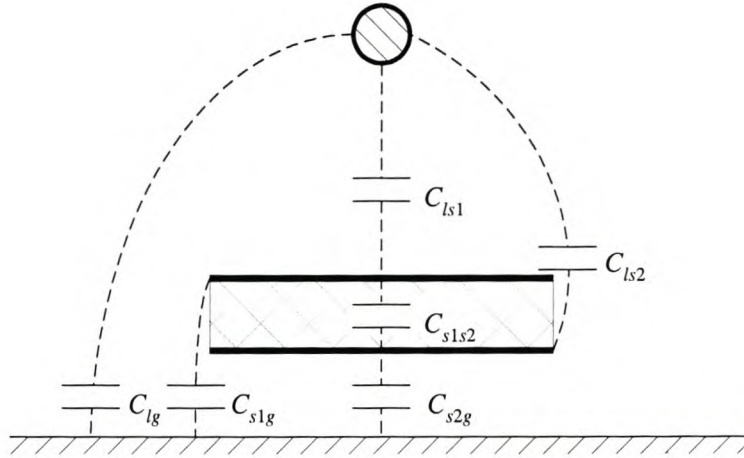
Figure 3.8: Two-dimensional view of transmission line and two-element parallel plate sensor showing capacitive coupling
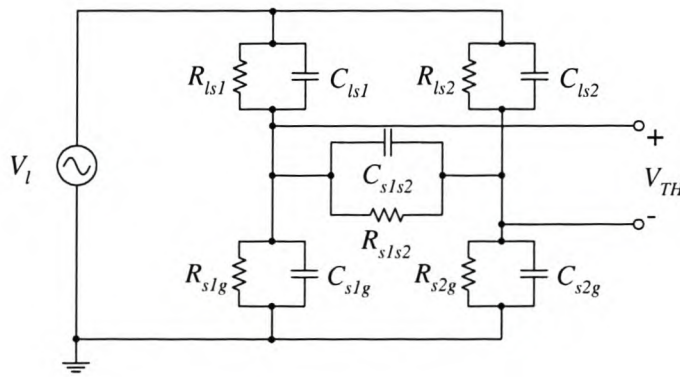
Figure 3.9: Equivalent circuit model for the two-element parallel plate sensor topology

The capacitances and resistances in Figure 3.9 are defined as follows:

C_{ls1}, R_{ls1}	Capacitance and resistance respectively between the main line and top sensor plate
C_{ls2}, R_{ls2}	Capacitance and resistance respectively between the main line and bottom sensor plate
C_{s1g}, R_{s1g}	Capacitance and resistance respectively between the top sensor plate and ground
C_{s2g}, R_{s2g}	Capacitance and resistance respectively between the bottom sensor plate and ground
C_{s1s2}, R_{s1s2}	Capacitance and resistance respectively between the top and bottom sensor plate

The equations for the Thévenin equivalent voltage and impedance are very complex and must be written in the following format:

$$V_{TH} = V_l \frac{V_{THn}}{DEN} \tag{3.7}$$

$$Z_{TH} = \frac{Z_{THn}}{DEN} \tag{3.8}$$

where

$$
\begin{aligned}
V_{THn} =\ & s^2 R_{ls1} R_{ls2} R_{s1g} R_{s2g} R_{s1s2}(C_{ls1}C_{s2g} - C_{ls2}C_{s1g}) + sR_{s1s2}\big(R_{ls1}R_{ls2}(C_{ls1}R_{s1g} - C_{ls2}R_{s2g}) + \\
& R_{s1g}R_{s2g}(C_{s2g}R_{ls2} - C_{s1g}R_{ls1})\big) + R_{s1s2}(R_{ls2}R_{s1g} - R_{ls1}R_{s2g}) \tag{3.9}
\end{aligned}
$$

$$Z_{THn} = sR_{ls1}R_{ls2}R_{s1g}R_{s2g}(C_c) + R_{s1s2}(R_{s1g}R_{s2g}(R_{ls1}+R_{ls2}) + R_{ls1}R_{ls2}(R_{s1g}+R_{s2g})) \tag{3.10}$$

$$
\begin{aligned}
DEN =\ & s^2 R_{ls1}R_{ls2}R_{s1g}R_{s2g}R_{s1s2}((C_a)(C_b) - C_{s1s2}^2) + \\
& s\big(R_{ls1}R_{ls2}R_{s1g}R_{s2g}(C_c) + R_{ls1}R_{s1g}R_{s1s2}(R_{ls2}+R_{s2g})(C_a) + R_{ls2}R_{s2g}R_{s1s2}(R_{ls1}+R_{s1g})(C_b)\big) + \\
& R_{s1s2}(R_{ls2}R_{s1g} + R_{ls1}R_{s2g}) + R_{ls1}R_{ls2}(R_{s1g}+R_{s2g}+R_{s1s2}) + R_{s1g}R_{s2g}(R_{ls1}+R_{ls2}+R_{s1s2}) \tag{3.11}
\end{aligned}
$$

with

$$C_a = C_{ls1} + C_{s1g} + C_{s1s2} \tag{3.12}$$

$$C_b = C_{ls2} + C_{s2g} + C_{s1s2} \tag{3.13}$$

$$C_c = C_{ls1} + C_{ls2} + C_{s1g} + C_{s2g} \tag{3.14}$$

However, these equations are of little practical value as two of the resistive elements, namely R_{ls1} and R_{ls2} represent the losses in air and can be neglected for most situations. The dielectric substrate separating the sensor plates cannot be regarded as a perfect insulator and R_{s1s2} must remain in the model. Unless the support structure consists of very good isolators, the resistive elements between the sensing plates and ground, namely R_{s1g} and R_{s2g} must also be included in the circuit model as shown in Figure 3.10.
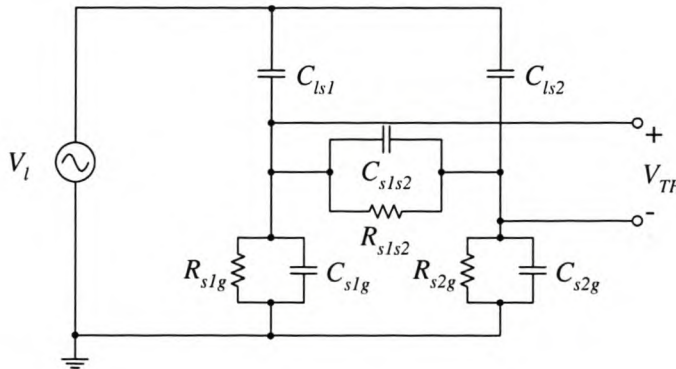
Figure 3.10: Simplified equivalent model for the two-element parallel plate sensor topology

In the derivation of the following equations, the resistance between the sensor plates, R_{s1s2}, will be neglected as well, because it is assumed that the termination resistor, R_t, is much smaller than

R_{s1s2}. R_t will therefore dominate the low-frequency behaviour of the sensor transfer function and R_{s1s2} may be ignored.

Four sets of equations representing practical cases will now be discussed. Three sets are for the different combinations of leakage paths that can be formed by the support structure and the last is the ideal case, when all loss terms can be neglected.

When the two resistors, R_{s1g} and R_{s2g}, are included in the model, equations 3.15 and 3.16 give the Thévenin equivalent voltage and impedance.

$$V_{TH} = V_l \frac{s^2 R_{s1g}R_{s2g}(C_{ls1}C_{s2g} - C_{s1g}C_{ls2}) + s(R_{s1g}C_{ls1} - R_{s2g}C_{ls2})}{s^2 R_{s1g}R_{s2g}(C_aC_b - C_{s1s2}^2) + s(R_{s1g}C_a + R_{s2g}C_b) + 1} \tag{3.15}$$

$$Z_{TH} = \frac{s(C_c)R_{s1g}R_{s2g} + R_{s2g} + R_{s1g}}{s^2 R_{s1g}R_{s2g}(C_aC_b - C_{s1s2}^2) + s(R_{s1g}C_a + R_{s2g}C_b) + 1} \tag{3.16}$$

where C_a, C_b and C_c have been defined before in equations 3.12, 3.13 and 3.14 respectively.

These equations correspond to the situation where both sensor plates are connected to the support structure. It has the advantage that the configuration is balanced and the differential voltage should not be influenced significantly. If, for example, the sensor rests on the support structure, the leakage from the top plate will become negligible and $R_{s1g} \to \infty$.

Now the Thévenin equivalent voltage and impedance are given by the relationships:

$$V_{TH} = V_l \frac{sR_{s2g}(C_{ls1}C_{s2g} - C_{s1g}C_{ls2}) + C_{ls1}}{sR_{s2g}((C_{ls1} + C_{s1g} + C_{s1s2})(C_{ls2} + C_{s2g} + C_{s1s2}) - C_{s1s2}^2) + C_{ls1} + C_{s1g} + C_{s1s2}} \tag{3.17}$$

$$Z_{TH} = \frac{sR_{s2g}(C_{ls1} + C_{ls2} + C_{s1g} + C_{s2g}) + 1}{s^2 R_{s2g}((C_{ls1} + C_{s1g} + C_{s1s2})(C_{ls2} + C_{s2g} + C_{s1s2}) - C_{s1s2}^2) + s(C_{ls1} + C_{s1g} + C_{s1s2})} \tag{3.18}$$

$$= \frac{sR_{s2g} + 1/C_c}{s^2 R_{s2g}C_{TH} + sC_a/C_c} \tag{3.19}$$

where C_a and C_c were defined in equations 3.12 and 3.14 and

$$C_{TH} = \frac{(C_{ls1} + C_{s1g} + C_{s1s2})(C_{ls2} + C_{s2g} + C_{s1s2}) - C_{s1s2}^2}{C_{ls1} + C_{s1g} + C_{ls2} + C_{s2g}} \tag{3.20}$$

C_{TH} is the Thévenin equivalent capacitance when all loss terms are neglected.

If the sensor is suspended from a support structure, the leakage from the bottom plate to ground will become negligible and $R_{s2g} \to \infty$.

Now the Thévenin equivalent voltage and impedance are given by the relationships:

$$V_{TH} = V_l \frac{sR_{s1g}(C_{ls1}C_{s2g} - C_{s1g}C_{ls2}) - C_{ls2}}{sR_{s1g}((C_{ls1} + C_{s1g} + C_{s1s2})(C_{ls2} + C_{s2g} + C_{s1s2}) - C_{s1s2}^2) + C_{ls2} + C_{s2g} + C_{s1s2}} \tag{3.21}$$

$$Z_{TH} = \frac{sR_{s1g}(C_{ls1} + C_{ls2} + C_{s1g} + C_{s2g}) + 1}{s^2 R_{s1g}((C_{ls1} + C_{s1g} + C_{s1s2})(C_{ls2} + C_{s2g} + C_{s1s2}) - C_{s1s2}^2) + s(C_{ls2} + C_{s2g} + C_{s1s2})} \qquad (3.22)$$

$$= \frac{sR_{s1g} + 1/C_c}{s^2 R_{s1g}C_{TH} + sC_b/C_c} \qquad (3.23)$$

where C_b, C_c and C_{TH} were defined in equations 3.13, 3.14 and 3.20.

The high frequency asymptotic value of the Thévenin equivalent voltage and impedance is found when all the loss terms are neglected and are given by the relationships:

$$V_{TH} = V_l \frac{C_{ls1}C_{s2g} - C_{ls2}C_{s1g}}{(C_{ls1} + C_{s1g} + C_{s1s2})(C_{ls2} + C_{s2g} + C_{s1s2}) - C_{s1s2}^2} \qquad (3.24)$$

$$Z_{TH} = \frac{C_{ls1} + C_{s1g} + C_{ls2} + C_{s2g}}{s((C_{ls1} + C_{s1g} + C_{s1s2})(C_{ls2} + C_{s2g} + C_{s1s2}) - C_{s1s2}^2)} \qquad (3.25)$$

From equation 3.25 it is clear that the Thévenin equivalent impedance for this approximation is a pure capacitor and it can be written as:

$$Z_{TH} = \frac{1}{sC_{TH}} \qquad (3.26)$$

where C_{TH} has already been defined in equation 3.20.

Equations 3.20 and 3.24 were used together with the electric field simulations to determine the Thévenin equivalent circuit in an attempt to obtain generic design curves for such a two-element sensor. From these simulations it could be shown that the Thévenin equivalent voltage is relatively independent to the sensor height above ground, if the sensor is placed close to ground. It therefore seems that the sensor is less sensitive to variations in ground level.

The preliminary measurements conducted with the two-element sensor indicated that this prototype sensor did not perform to expectations. This may be attributed amongst others the following:

- The limited accuracy that can be obtained with a two-dimensional simulation package, especially for taking boundary conditions and end effects into account

- A proper faraday cage does not exist for the interface instrumentation and the cage that was used was neglected in simulations

- Poor frequency response when a significant leakage path exist between either sensing plate and ground

3.3.3 Equivalent circuit for the three element parallel plate sensor

The faraday cage for this design was isolated from the two sensing plates in order to have a balanced design. In essence, the conducting body of the cage forms a floating common-mode reference for the differential sensor elements. It does, however, increase the complexity of the equivalent circuit and analytical equations.

Figure 3.11 shows a 2D diagram of the geometry of a three-element parallel plate sensor above a ground plane underneath a transmission line. The letters in circles, namely l, $s1$, $s2$, $s3$ and g indicate the naming conventions of subscripts of element values and represent the transmission line, sensing elements, faraday cage and ground respectively. The dimensions for this sensor topology are defined as follows:

r_l Main line radius

h_l Main line height above ground

h_s Sensor height above ground, measured to the bottom plate

w_s Sensor width

d_s Thickness of dielectric separating the sensor plates

d_c Depth of faraday cage used to house the instrumentation
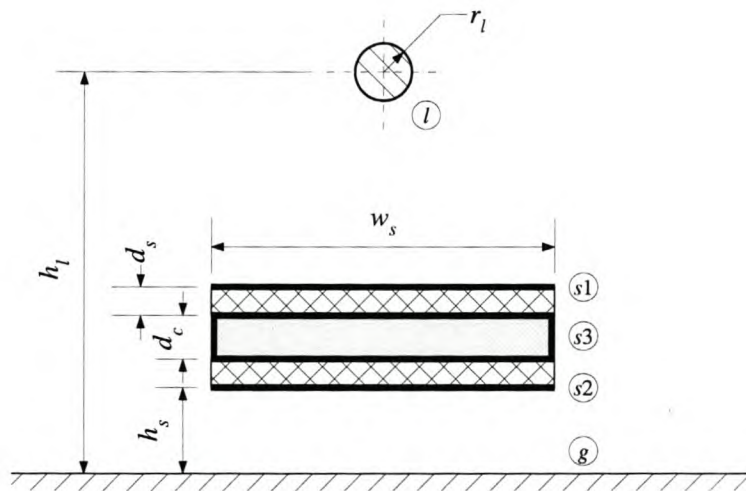
Figure 3.11: Two-dimensional view of transmission line and three-element parallel plate sensor geometry

The top and bottom dielectric have the same thickness, namely d_s, as a balanced design was required. However, this does not limit the validity of the circuit model in any way. The differential elements are still labelled $s1$ and $s2$, but the added faraday cage is labelled $s3$. As it is isolated

from the top and bottom sensor plates, it will assume a different voltage under excitation and must be solved for separately.

Figure 3.12 shows a 2D diagram of the capacitive coupling elements of a three-element parallel plate sensor above a ground plane underneath a transmission line. An equivalent circuit for the sensor geometry shown in Figure 3.12 can be deduced by arranging the capacitors in circuit format. The shunt loss terms from the traditional transmission line model should also be included in parallel with the capacitances. The main line capacitance to ground, C_{lg}, may be ignored in the equivalent circuit model as stated before. The resulting circuit is shown in Figure 3.13.
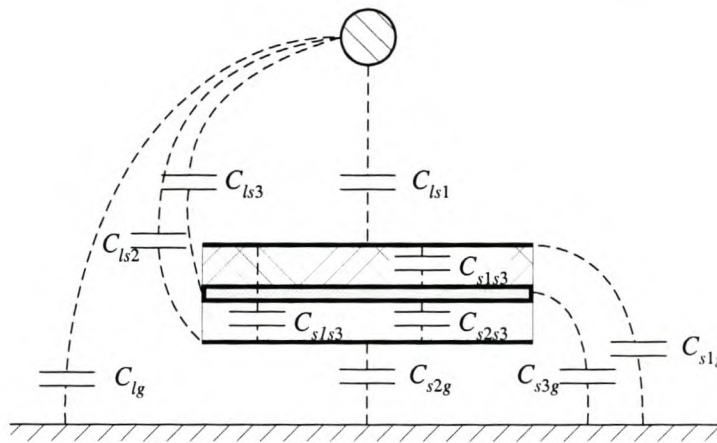
Figure 3.12: Two-dimensional view of transmission line and three-element parallel plate sensor showing capacitive coupling
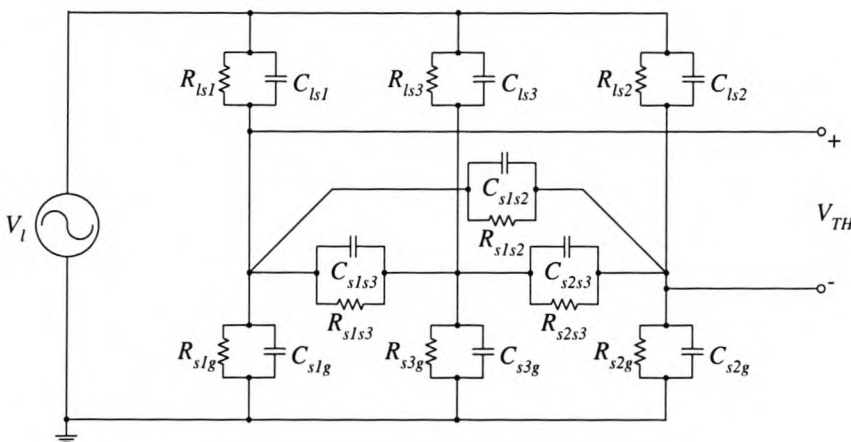
Figure 3.13: Three element sensor equivalent circuit taking all loss terms into account

The capacitances and resistances in Figure 3.13 are defined as follows:

C_{ls1}, R_{ls1}	Capacitance and resistance respectively between the main line and top sensor plate
C_{ls2}, R_{ls2}	Capacitance and resistance respectively between the main line and bottom sensor plate
C_{ls3}, R_{ls3}	Capacitance and resistance respectively between the main line and faraday cage
C_{s1g}, R_{s1g}	Capacitance and resistance respectively between the top sensor plate and ground
C_{s2g}, R_{s2g}	Capacitance and resistance respectively between the bottom sensor plate and ground
C_{s3g}, R_{s3g}	Capacitance and resistance respectively between the faraday cage and ground
C_{s1s2}, R_{s1s2}	Capacitance and resistance respectively between the top and bottom sensor plate
C_{s1s3}, R_{s1s3}	Capacitance and resistance respectively between the top sensor plate and faraday cage
C_{s2s3}, R_{s2s3}	Capacitance and resistance respectively between the bottom sensor plate and faraday cage

Equations for the Thévenin equivalent of the full circuit model as given in Figure 3.13 were not derived as the symbolic toolbox in Matlab® could not finish the manipulations. Any symbolic expression longer than 10 000 characters are truncated and cannot be used in further calculations. As the full circuit model does not represent a practical case, no further attempt was made to solve for the full circuit model Thévenin equivalent.

Once again the loss terms between the transmission line and the sensing elements, namely R_{ls1}, R_{ls2} and R_{ls3} may be ignored. Equations for this and other simplified circuits corresponding to the leakage models discussed in section 4.3.1 are given in Appendix C.

The equations for the high frequency asymptote of the three element sensor, when all loss terms are ignored, are given in a similar format as before. The Thévenin equivalent voltage is given by equation 3.27 and the Thévenin equivalent impedance has an extra $s = j2\pi f$ added in the denominator as given by equation 3.28.

$$V_{TH} = V_l \frac{V_{THn}}{DEN} \tag{3.27}$$

$$Z_{TH} = \frac{Z_{THn}}{s \cdot DEN} \tag{3.28}$$

The numerators and denominator, which should be substituted into equations 3.27 and 3.28 are given by equations 3.29 to 3.31.

$$
\begin{aligned}
V_{THn} =\ & C_{ls1}(C_{s2g}C_{s2s3} + C_{s2s3}C_{s3g} + C_{s2g}C_{s3g} + C_{s2g}C_{s1s3}) - C_{ls2}(C_{s1g}C_{s1s3} + C_{s1g}C_{s3g} + C_{s1g}C_{s2s3} + C_{s1s3}C_{s3g}) + \\
& C_{ls3}(C_{ls1}C_{s2g} + C_{s2g}C_{s1s3} - C_{s1g}C_{ls2} - C_{s1g}C_{s2s3}) \tag{3.29}
\end{aligned}
$$

$$Z_{THn} = (C_{s1s3} + C_{s2s3})(C_{ls1} + C_{ls2} + C_{ls3} + C_{s1g} + C_{s2g} + C_{s3g}) + (C_{ls3} + C_{s3g})(C_{ls1} + C_{ls2} + C_{s1g} + C_{s2g}) \tag{3.30}$$

$$DEN = (C_{ls1} + C_{ls2} + C_{ls3} + C_{s1g} + C_{s2g} + C_{s3g})(C_{s1s2}C_{s1s3} + C_{s1s2}C_{s2s3} + C_{s1s3}C_{s2s3}) +$$

$$(C_{ls1} + C_{ls2} + C_{ls3})(C_{s1g} + C_{s2g} + C_{s3g})(C_{s1s2} + C_{s1s3} + C_{s2s3}) +$$

$$C_{s1s2}(C_{ls1}C_{s3g} + C_{s2g}C_{ls3} + C_{ls2}C_{ls3} + C_{ls1}C_{ls3} + C_{s1g}C_{s3g} + C_{ls2}C_{s3g} + C_{s2g}C_{s3g} + C_{s1g}C_{ls3})$$

$$C_{s1s3}(C_{s2g}C_{ls3} + C_{ls2}C_{ls3} + C_{s1g}C_{s2g} + C_{s1g}C_{ls2} + C_{ls1}C_{s2g} + C_{ls2}C_{s3g} + C_{ls1}C_{ls2} + C_{s2g}C_{s3g})$$

$$C_{s2s3}(C_{s1g}C_{s3g} + C_{s1g}C_{ls3} + C_{ls1}C_{ls2} + C_{s1g}C_{s2g} + C_{s1g}C_{ls2} + C_{ls1}C_{s3g} + C_{ls1}C_{ls3} + C_{ls1}C_{s2g}) \qquad (3.31)$$

This represents the case when all loss terms are neglected. A Thévenin equivalent capacitance can be defined from this idealised case, namely:

$$C_{TH} = \frac{DEN}{Z_{THn}} \qquad (3.32)$$

The prototype three-element parallel plate sensor is expected to perform better than the two-element parallel plate sensor discussed in section 3.3.2. The conditions allowing the enhanced performance are ascribed to the following:

- Three-dimensional simulations were done for increased accuracy of the circuit model parameters

- The plate area was increased, thereby limiting the sensitivity of the sensing elements to leakage to ground

- A proper faraday cage was included in the sensor design and electric field simulation models

- This faraday cage exhibits negligible sensitivity to leakage to ground

3.3.4 Equivalent circuit for the single sensing element coaxial sensor

Figure 3.14 shows a 2D diagram of the geometry of a single element coaxial sensor around the earth conductor of a single phase transmission line. The letters in circles, namely l, s and g indicate the naming conventions of subscripts of element values and represent the transmission line, sensing element and ground respectively. The dimensions for this sensor topology are defined as follows:

r_l	Main line radius
h_l	Main line height above ground
h_s	Sensor height above ground, measured to the center of sensor
w_s	Horizontal distance between transmission line center and earth conductor center
r_s	Sensor cylinder outer radius
r_c	Faraday cage outer radius
r_g	Earth conductor radius
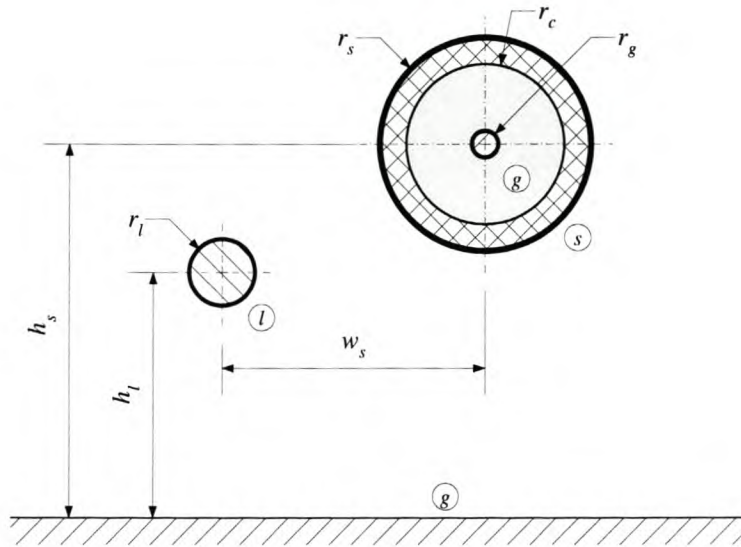
Figure 3.14: Two-dimensional view of transmission line and single element coaxial sensor around earth conductor geometry

Figure 3.15 shows a 2D diagram of the capacitive coupling components of a single element coaxial sensor around the earth conductor of a single phase transmission line. An equivalent circuit for the sensor geometry shown in Figure 3.15 can be deduced by arranging the capacitors in circuit format. The shunt loss terms from the traditional transmission line model should also be included in parallel with the capacitances. The main line capacitance to ground, C_{lg}, may be ignored in the equivalent circuit model as stated before. The capacitance between the sensing plate and the ground plane, C'_{sg}, is neglected in the equivalent circuit model because it is much smaller than the capacitance between the sensor plate and the earth conductor, C_{sg}. The resulting circuit is shown in Figure 3.16.

The capacitances and resistances in Figure 3.16 are defined as follows:

C_{ls}, R_{ls} Capacitance and resistance respectively between the main line and sensing plate

C_{sg}, R_{sg} Capacitance and resistance respectively between the sensing plate and the earth conductor

This circuit is the same as the equivalent circuit of the single plate sensor given in Figure 3.5. The resistance between the main line and the sensing plate, R_{ls}, may again be ignored as air is a very good insulator. Using the notation of Figure 3.15, the Thévenin equivalent voltage is given by the relationship:

$$V_{TH} \quad = \quad V_l \frac{sC_{ls}R_{sg}}{1 + sR_{sg}(C_{ls} + C_{sg})} \tag{3.33}$$
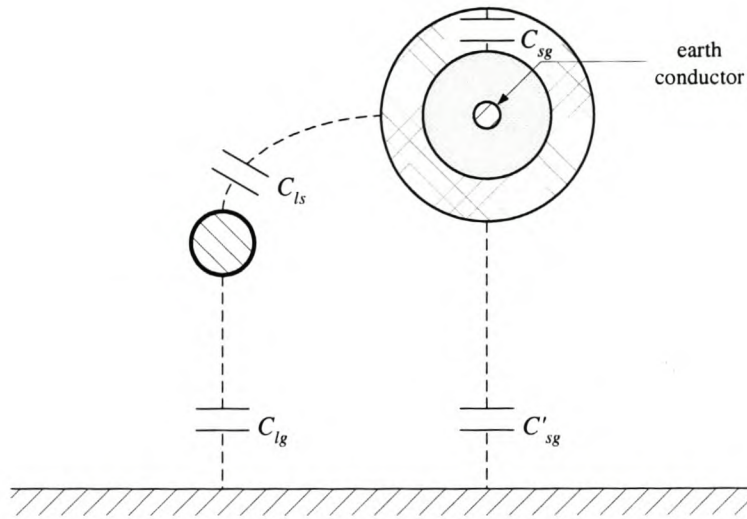
Figure 3.15: Two-dimensional view of transmission line and single element coaxial sensor around earth conductor showing capacitive coupling
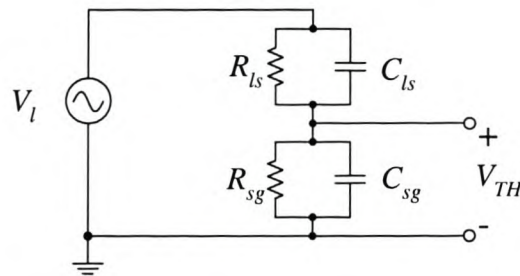
Figure 3.16: Equivalent circuit model for the single element coaxial sensor topology

and the Thévenin equivalent impedance by the relationship:

$$Z_{TH} = \frac{R_{sg}}{1 + sR_{sg}(C_{ls} + C_{sg})} \tag{3.34}$$

Under normal circumstances, it can be expected that the resistance of the dielectric substrate between the sensing plate and the faraday cage of the coaxial sensor, R_{sg}, for this sensor topology is much larger than the value of the terminating resistor. Therefore, this resistor may also be neglected and the equivalent circuit comprises only capacitors as shown in Figure 3.17.

Using the notation of Figure 3.15, the Thévenin equivalent voltage is equal to the induced voltage and is given by equation 3.35

$$V_{TH} = V_l \frac{C_{ls}}{C_{ls} + C_{sg}} \tag{3.35}$$
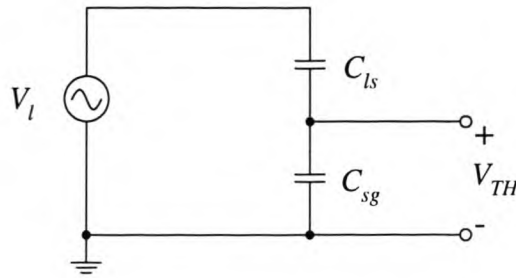
Figure 3.17: Simplified equivalent circuit model for the single element coaxial sensor topology

The Thévenin equivalent impedance is given by the parallel combination of the capacitance between the transmission line and sensor plate and between the sensor plate and ground, i.e.

$$Z_{TH} = \frac{1}{s(C_{ls} + C_{sg})} \qquad (3.36)$$

Despite the similarity in equivalent circuit structure and Thévenin equivalent voltage and impedance, it is important to note that the two sensors differ considerably. The main difference is that the single element coaxial sensor is much less sensitive to ground level changes than the single element plate sensor. The main reason is that the coaxial sensor is placed far from the ground plane and the transfer function of the coaxial sensor is dominated by the capacitance between the sensing element and the earth conductor and not the capacitance between the sensing element and the ground plane.

This sensor will therefore rather give a measure of the voltage difference between the live conductor and the earth conductor than between the live conductor and ground. This is useful as it is an accurate indication of the voltage across the insulator strings. The series inductance and resistance between the earth conductor and ground may cause high frequency resonances and losses and should be investigated further if the live conductor voltage with respect to ground is important.

3.4 Conclusions

Four different sensor topologies were proposed, analysed and modelled in this chapter, namely:

- Single element plate sensor

- Differential parallel plate sensor (two-element parallel plate sensor)

- Differential parallel plate sensor with floating faraday cage (three-element parallel plate sensor)

- Single sensing element coaxial sensor

The analysis and modelling of these sensors entailed the following steps:

- Development of equivalent circuit models

- Derivation of expressions for the Thévenin equivalent circuits for each of the above circuit models

The equivalent circuit models were derived for a 2D approximation of the sensor topology. It was also argued that the differential parallel plate sensor is superior to the single plate sensor that has been discussed in open literature. A single element coaxial sensor was suggested, with a simple equivalent circuit similar to the single plate sensor, which is more robust and less sensitive to amongst others, ground level changes. Another feature of these sensors is that they have inherent faraday cages for the interface instrumentation.

Further analysis of the sensors should now be performed using the equivalent circuit models. Typical parameter values should be obtained for the evaluation of the operation of these sensors.

Chapter 4

Numerical Modelling and Analysis

4.1 Introduction

The design process relied heavily on simulation tools and techniques. Electric field simulations were used to determine the capacitive coupling parameters of the sensing elements as well as the typical electric field distributions around the sensor. Equivalent circuit simulations were subsequently done to predict the time- and frequency domain response of the sensor in conjunction with the interface instrumentation. These simulations were combined to attempt to obtain generic design curves for a typical differential parallel plate sensor.

It is important to note that most of the analyses were done for a two-dimensional (2D) approximation of the system, where an infinitely long system is considered. It was also assumed that all height dimensions are constant across the infinite length. These assumptions are generally made for analyses of transmission line electromagnetic fields as mentioned by Olsen [67]. However, due to the short length of the sensor in comparison with the transmission line, these assumptions had to be tested and three-dimensional (3D) simulations were also conducted for comparison. These comparisons showed that 2D simulations are insufficient for the current application of electrically small capacitive voltage sensors.

Circuit parameter values were obtained from these electric field simulations. Section 4.2 contains a description of the 2D and 3D packages that were used to determine the capacitive coupling elements. The process followed towards generic design curves is also discussed in section 4.2. This process includes sensitivity analyses of the differential parallel plate sensor topologies to parameters such as relative sensor height, plate width and -separation.

Section 4.3 contains the time- and frequency domain simulations of the circuits that were discussed

in section 3.3. The effects of non-ideal elements, such as the termination resistance and leakage paths to ground are discussed in this section. A summary of the important aspects for selection of a sensor topology are given in section 4.4, with conclusions for this chapter following in section 4.5.

4.2   Numerical Analysis and Simulations

Two commercial packages were used to determine the capacitive coupling components as well as the field distribution around the sensor. Both are from the same company, *Integrated Engineering Software,* and uses the Boundary Element Method (BEM). The first, Electro©, is a two-dimensional solver, while Coulomb© is a three-dimensional solver.

This section contains a description of the simulation packages that were used to analyse the different sensor topologies, namely Electro© and Coulomb©. Then the different 2D and 3D simulations will be discussed together with the attempt to obtain the generic design curves.

4.2.1   Boundary Element Method (BEM) Packages

The Boundary Element Method (BEM) that is implemented by both Electro© and Coulomb© is based on the boundary integral equation formulation. The BEM is often called the Surface Charge Simulation Method (SCSM) [68] because the values of surface charges are calculated to match the boundary conditions. It corresponds to the Charge Simulation Method (CSM) as the CSM uses charges inside volumes to match the boundary conditions [69]. These methods are preferred for open boundary problems, as charges are only placed within boundaries or on the surface of boundaries and interfaces of different media.

Other popular numerical techniques, like the Finite Element Method (FEM), require elements in the whole space to be solved, while the BEM only solve for elements on conductor/material boundaries itself. The matrices generated for the BEM is slightly more complicated and larger for a certain amount of elements, but far fewer elements is required as only boundaries need to be discretised, not the entire simulation space.

Detailed discussions of the BEM formulation can be found in open literature [68, 69, 70]. It is therefore unnecessary to continue a discussion of the equations and implementation of the method.

One of the consequences of the BEM is that a floating boundary can only be defined if the boundary is surrounded by a single dielectric. This means that a plate that should be allowed to float

must be modelled with finite thickness. This increases the complexity of the model and simulation time considerably. The extra volume instead of a surface requires many more elements and consequently takes significantly longer to solve. Fortunately, this is unnecessary when calculating capacitances, as no floating boundary conditions are defined then.

4.2.2 Two-dimensional simulations for different parallel plate sensors

Extensive simulation studies were conducted for the two-element parallel plate sensor using the 2D Electro©. The simulation studies had the following objectives:

- To obtain qualitative and quantitative insight into the sensor topology and the associated electric field characteristics

- To attempt to generate a set of generic design curves

- To evaluate the error due to the 2D approximation

The following assumptions are made to permit the use of the Electro-Quasi-Static (EQS) 2D approximation:

- All structures are infinitely long

- Variations in height are neglected, i.e. average height is used

- Wavelength at maximum frequency must be longer than 10 times the actual length of the structure

The actual length of the structure is defined as the physical length of the structure, although this cannot be modelled in the 2 dimensions. As the program is two-dimensional, the parameters found from the simulations are given in units/m. The initial sensor, that was used, was 1 m long, therefore these parameters were used directly to characterise the sensor topology. The increase in capacitance between the transmission line and sensor elements due to fringing fields between the long line and short sensor was thus neglected.

The generic simulations were done for a two-element parallel plate sensor that would practically be built using PCB. The PCB that was commonly available have a dielectric with a relative permittivity of 5.8 and a thickness of 1.6 mm [71]. A single piece of double-sided PCB would then give two plates separated by 1.6 mm of dielectric. Thicker dielectric elements can be realised by using multiple layers of PCB, with single-sided PCB on the outsides.

Dimensions for the two-element sensor were defined in Figure 3.7, repeated here as Figure 4.1. All the dimensions listed in Figure 4.1 were varied for a sensitivity analysis. Table 4.1 list the ranges of parameter values for which the simulations were done. A few corresponding graphs will be included for the single element plate sensor to show the improvement in performance achieved by the differential parallel plate sensor.
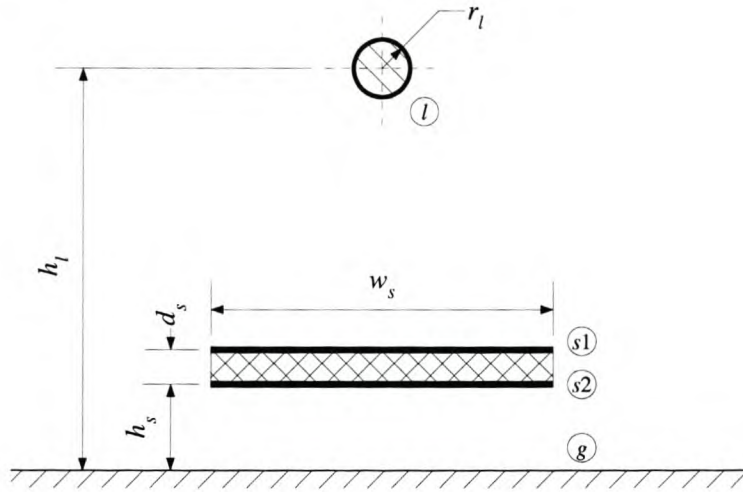
Figure 4.1: Two-dimensional view of transmission line and differential parallel plate sensor geometry

Table 4.1: Typical dimensions and ranges for single double sided PCB sensor simulations

Parameter	Typical value	Minimum value	Maximum value
r_l	10 mm	1 mm	1000 mm
h_l	10.0 m	5.0 m	15.0 m
h_s	1.0 m	0.1 m	2.5 m
w_s	0.5 m	0.1 m	2.5 m
d_s	1.6 mm	1.6 mm	16.0 mm

Provided that the sensor capacitance, C_{s1s2}, is much larger than the other capacitances, namely C_{ls1}, C_{ls2}, C_{s1g} and C_{s2g}, it can be shown theoretically that the Thévenin impedance is dominated by the sensor capacitance:

$$Z_{TH} \approx \frac{1}{sC_{s1s2}} \tag{4.1}$$

Practically, this implies that C_{s1s2} must be much larger than the smaller of the two sensor-to-ground capacitances, C_{s1g} or C_{s2g}, because the line-to-sensor capacitances, C_{ls1} and C_{ls2}, are significantly smaller than the C_{s1g} and C_{s2g} as it is desirable to keep the sensor height, h_s, much lower than the line height, h_l. From a geometry point of view, the separating distance, d_s, must be small with reference to the sensor height, h_s. This is also aided by a large relative permittivity of the dielectric substrate between the sensor plates.

The approximation was verified from the simulated values for the capacitance matrices as shown in Figure 4.2. The percentage difference between C_{TH} as defined by equation 3.20 and C_{s1s2} is shown in Figure 4.2. As expected the difference between the sensor capacitance, C_{s1s2}, and the Thévenin capacitance, C_{TH}, is the largest when C_{s1s2} is relatively small.

The coupling between the bottom sensor plate and ground, C_{s2g}, is the largest capacitor next to the sensor capacitance. The maximum difference between C_{TH} and C_{s1s2} is -0.99 % when C_{s2g} is approximately 2 % of C_{s1s2}.
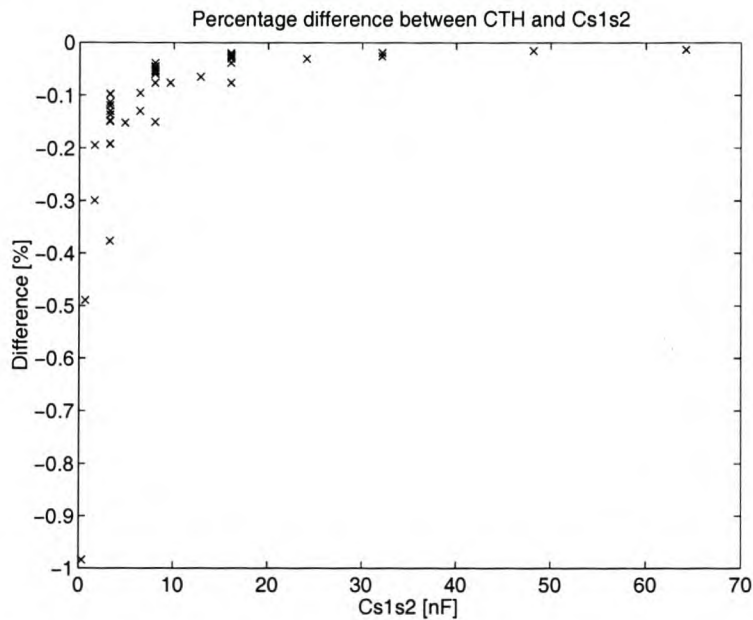
Figure 4.2: Percentage difference between C_{TH} (neglecting all loss terms) and C_{s1s2} as calculated by Electro©

As expected, the sensor parallel plate capacitance, C_{s1s2}, is approximated very well by the analytical equation for parallel plate capacitance as given by equation C.25 in Appendix C. Some of the arrangements included a small ratio between the width and separation of the plates and the fringing fields were also taken into account given by equation C.26. The maximum error between the simulated sensor capacitance from Electro© and the analytic capacitance using equation C.26 was less than 0.2 %. It is therefore unnecessary to discuss the Thévenin equivalent capacitance and impedance in terms of the geometrical parameters.

The variations in Thévenin equivalent voltage for the two-element parallel plate sensor compares well with expectations. The sensor dimensions, namely plate width and dielectric thickness or plate separation will be discussed first. The Thévenin equivalent voltage is directly proportional to the dielectric thickness, i.e. the further the plates are apart, the bigger the induced differential voltage. This is shown in Figure 4.3. The smooth curves in Figure 4.3 (b) are obtained by spline interpolation of the simulated data points, which are indicated as asterisks. It is, however, interesting

to note that the sensor plate width, w_s, does not have a very big influence on the induced voltage. This may be expected as the plates follow the equipotential lines when the sensor is placed close to ground level. However, this is not true for thin sensors as can be seen from the trace for w_s=0.1 m in Figure 4.3 (a) as well as the upward trend visible on all curves in Figure 4.3 (b). This is caused by the relative decrease in sensor capacitance, C_{s1s2}, when the plates become thin (w_s) with respect to the separation distance (d_s). This implies that the dividing ratio depends proportionally more on the other capacitances, C_{ls1}, C_{ls2}, C_{s1g} and C_{s2g}, for narrow plates than for wider plate widths.
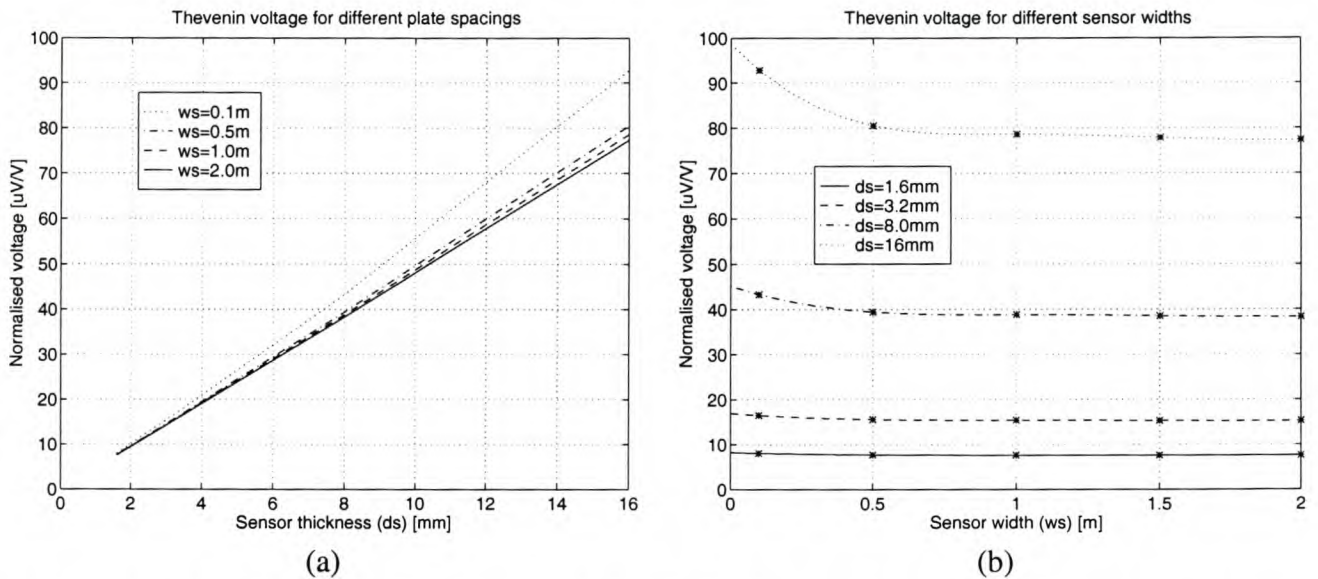
Figure 4.3: Equivalent Thévenin voltage for two-element parallel plate sensors (a) Equivalent Thévenin voltage for different plate widths (w_s) plot against the dielectric thickness (d_s) (b) Equivalent Thévenin voltage for different dielectric thicknesses (d_s) plot against the plate width (w_s)

Variations in the other parameters, namely, line and sensor height and radius of the main line also cause predictable results. The induced voltage is proportional to a function of the main line radius, r_l. The dependency of the voltage on the main line radius approaches a hyperbolic function as shown in Figure 4.4 (a). Figure 4.4 (b) shows the inverse normalised voltage of the sensor topology, i.e. the voltage required on the transmission line to induce one volt difference between the two plate elements.

The large increase in induced voltage when radius of the transmission line is increased, can be explained from physical aspects. If the line radius is increased, the HV surface moves closer to the ground plane, which means that the relative distance between the equipotential lines decreases, i.e. the electric field strength increases. The potential gradient will be larger, which means a larger differential voltage is induced onto the sensor.

Similar graphs are shown in Figure 4.5 for the single element plate sensor. As expected, a similar dependency exist for the single element plate sensor than for the two element plate sensor, because
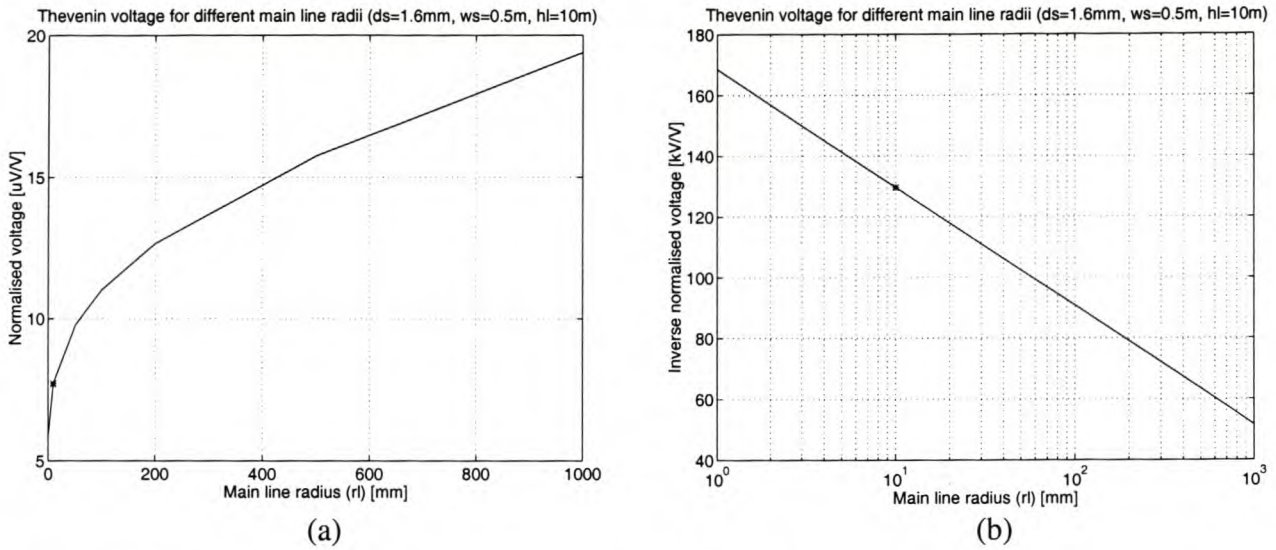
Figure 4.4: Thévenin equivalent voltage for two-element parallel plate sensor for variations in main line radius (r_l) (a) Thévenin equivalent voltage against main line radius on a linear scale (b) Inverse Thévenin equivalent voltage against main line radius on a logarithmic scale (the asterisk indicates the default simulation with r_l=10 mm)

the induced voltage is directly proportional to the electric field for both sensors.

Figure 4.6 shows the dependency of the Thévenin equivalent voltage for the two-element parallel plate sensor on the relative height of the sensor, where the relative height is defined as the sensor height as a percentage of the transmission line height. From Figure 4.6 (a) it is clear, however, that a region exists, namely below 10 % of the transmission line height, where the induced voltage is very insensitive to changes in height. The field in this area below 10 % of the line height is fairly uniform, analogous to the "sweet spots" that were used by Feldman et al [51].

When the transmission line height is changed, eg. under sag conditions, the Thévenin equivalent voltage does not show the same independence of relative sensor height as shown in Figure 4.6 (b). This is attributed to the relative variation in sensor width and transmission line radius, when either the sensor or the transmission line height is varied, amongst other possible causes. The main explanation for the difference between the graphs of Figure 4.6 (a) and (b) is the same as for the variation in main line radius, which was shown in Figure 4.4. When the transmission line height decreases, the electric field strength underneath the line is increased, including the field strength in the uniform field area. If the graphs of Figure 4.6 (a) and (b) are normalised with reference to the electric field strength just above ground level, the two graphs should have similar characteristics. It would thus be possible to get an indication of the transmission line sag when using a differential sensor as well, because the relationship shown in Figure 4.6 (b) is reasonably linear.
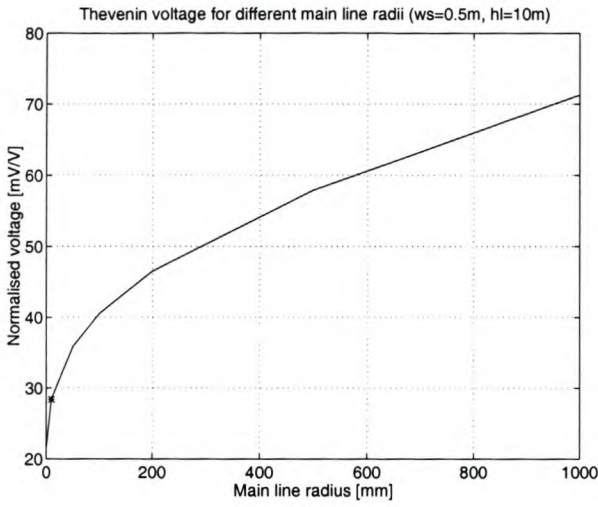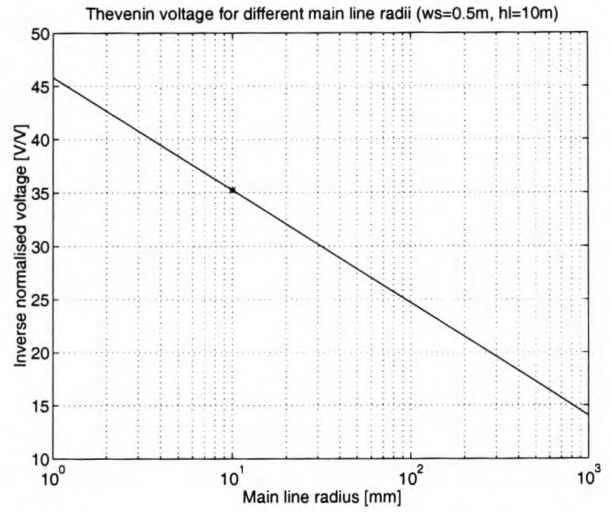
Figure 4.5: Thévenin equivalent voltage for a single element plate sensor for variations in main line radius (r_l) (a) Thévenin equivalent voltage against main line radius on a linear scale (b) Inverse Thévenin equivalent voltage against main line radius on a logarithmic scale (the asterisk indicates the default simulation with r_l=10 mm)
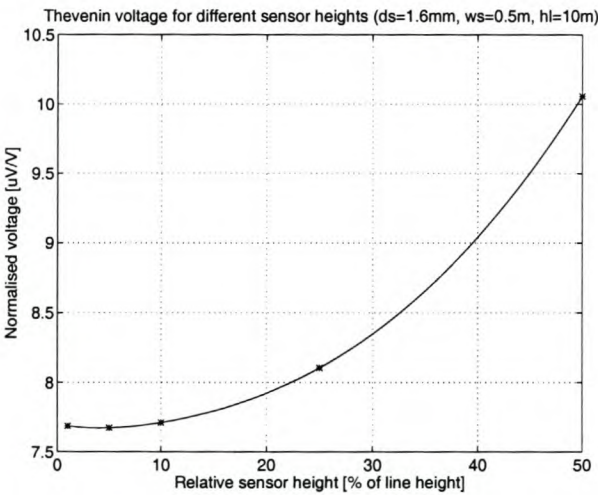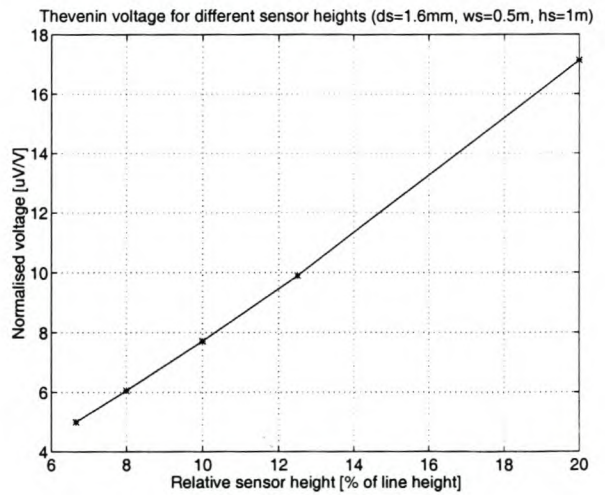
Figure 4.6: Thévenin equivalent voltage for two-element parallel plate sensor against ratio of sensor and transmission line heights ($h_s/h_l \times 100$) (a) Thévenin equivalent voltage against ratio of sensor and transmission line heights (sensor height varied) (b) Thévenin equivalent voltage against ratio of sensor and transmission line heights (transmission line height varied)

Figure 4.7 shows the main difference in operation between the single- and two element parallel plate sensors. The Thévenin equivalent voltage always depends on the relative height of the sensor and no uniform field area is available where the sensor may be moved around without a large difference in the output voltage.
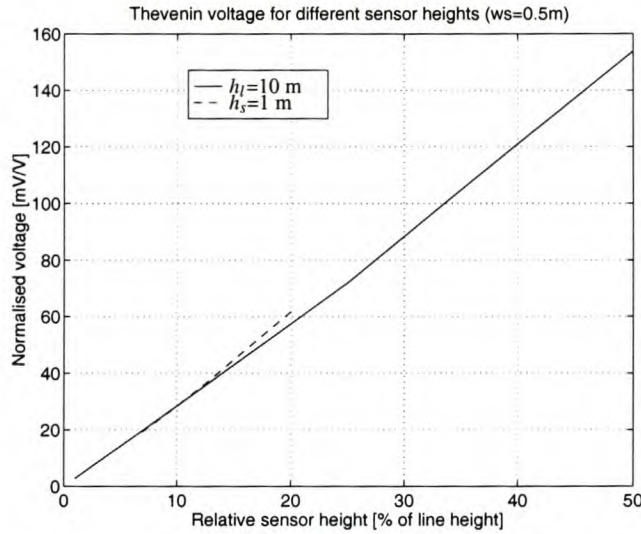
Figure 4.7: Thévenin equivalent voltage for single element plate sensor against ratio of sensor and transmission line heights ($h_s/h_l \times 100$) (Solid line $\rightarrow$ sensor height varied; dashed line $\rightarrow$ transmission line height varied)

Sensitivity sweeps were done by varying the different parameter values of the equivalent circuit model and noting the deviation caused in the Thévenin equivalent voltage and impedance. A sensitivity sweep of the Thévenin equivalent voltage versus $\pm 10\ \%$ variations in any of the capacitance parameters were also done. These simulations will show what should happen for small variations in geometric positioning as it is not always possible to position a sensor a 100 % accurately. Figure 4.8 shows that the Thévenin equivalent voltage changes by almost an equal percentage as the deviation in capacitance if the sensor capacitance is varied. This graph shows that the variation in induced voltage is almost directly proportional to the variation in the sensor capacitance. This specifies that it is imperative to know the value of the sensor capacitance. At this stage it is encouraging to note that the sensor capacitance is fixed for any specific sensor and should not influence measurements.

Figure 4.9 shows the dependency of the normalised Thévenin voltage in terms of variations in the line-to-sensor capacitances, C_{ls1} and C_{ls2}, and the sensor-to-ground capacitances, C_{s1g} and C_{s2g}. A graph for equal variation in either the line-to-sensor capacitances or the sensor-to-ground capacitances is included in both cases. Figure 4.9 (a) shows that the percentage change in the induced voltage is almost equal to the change in sensor-to-ground capacitances. If both these capacitances are varied by the same percentage then the change in the induced voltage is reduced
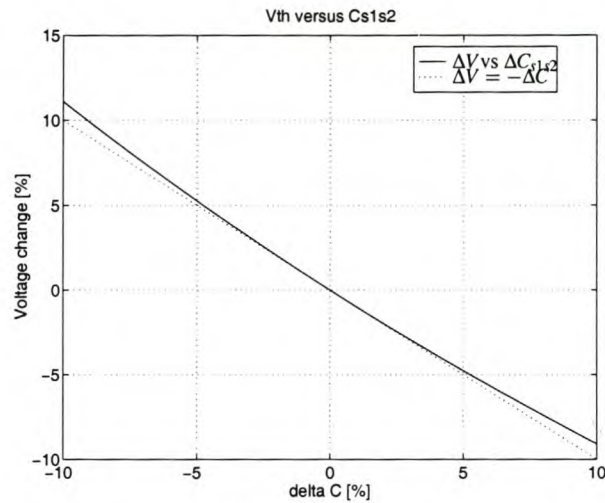
Figure 4.8: Graph showing sensitivity of Thévenin equivalent voltage to changes in the sensor capacitance along with the $\Delta V = -\Delta C$ line

to almost nothing. Comparisons of C_{s1g} and C_{s2g} for different geometric parameters have shown that the percentage change for these two capacitances are generally the same. The same argument applies for the line-to-sensor capacitances, namely C_{ls1} and C_{ls2}. Figure 4.9 (b) indicates that the Thévenin equivalent voltage is very sensitive to variations in C_{ls1} and to a lesser extent to variations in C_{ls2}. If both these parameters are varied by the same amount, the change in Thévenin equivalent voltage is almost equal to the change in the capacitive coupling elements. Figure 4.9 therefore shows that the output voltage depends mostly on variations in the line-to-sensor capacitance.

4.2.3   Three-dimensional simulations for two-element parallel plate sensors

Before simulating the other sensor topologies, the basic two-element parallel plate sensor topology was also simulated with the 3D equivalent of Electro©, namely Coulomb©. The objectives of these simulations were to compare the 2D and 3D simulations and determine the effects of the following approximations:

- To evaluate the influence of a sensor of finite length, i.e. end effects on the sensor response

- To evaluate the effect of the added faraday cage

- To evaluate the effect of sag of the transmission line

These comparisons were made for the sensor and measuring arrangement used for the second trial measurements. A two element differential sensor was constructed by using a single piece of double
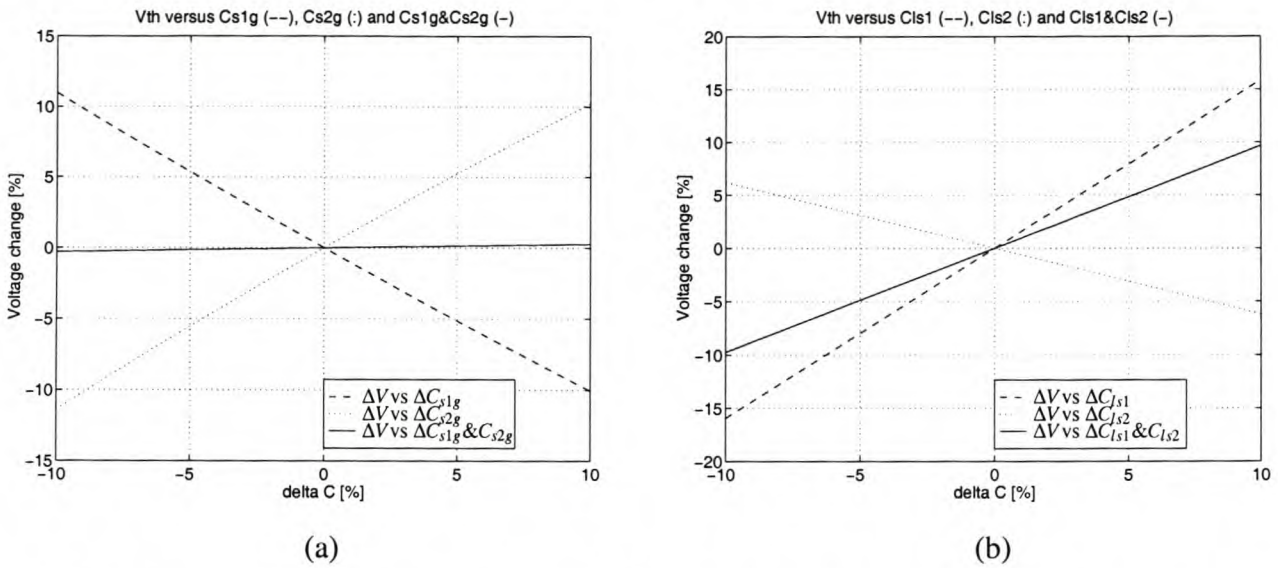
Figure 4.9: Thévenin equivalent voltage for two-element parallel plate sensor versus ±10 % variations in capacitive coupling elements (a) Thévenin equivalent voltage deviation versus ±10 % variation in sensor-to-ground capacitances (b) Thévenin equivalent voltage deviation versus ±10 % variation in line-to-sensor capacitances

sided PCB. The metal surfaces on either side of the PCB are then used as the differential input of the instrumentation.

A faraday cage must be included for integration of the sensor instrumentation. It will distort the field around the sensor, but this simple construction should be regarded as a first step in the sensor design, where different aspects of the process can be evaluated. Figure 4.10 shows a 2D view of such a double sided PCB sensor with faraday cage connected to the top plate. The faraday cage was neglected in the general 2D simulations. Therefore, the box did not extend the full length of the sensor in order to minimise its effect on the field, but local distortions are expected and may be a reason for poor measurements. Comparative simulations were done using both the 2D and 3D packages to evaluate the effect of the addition of the faraday cage and the length of the faraday cage. Furthermore, the degree of correlation between the 2D and 3D simulations would indicate whether 2D simulations can accurately predict the sensor response with or without the added faraday cage.

The dimensions for the scale model are given in Table 4.2. Table 4.2 (a) contains the parameter values that were defined in Figure 4.1, while the added parameters are given in Table 4.2 (b).

Figure 4.11 shows the side view of the two-element sensor with or without a faraday cage. Two possibilities exist, either having a faraday cage for the full length of the sensor, or making it just long enough to house the equipment. The latter option will be referred to as the short cage and should, theoretically, have a smaller influence on the surrounding field, but is more difficult to
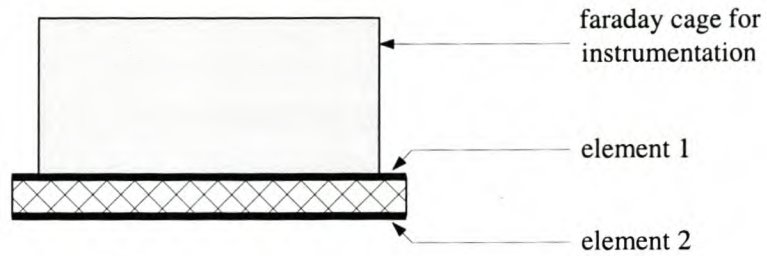
Figure 4.10: Diagram of differential parallel plate sensor with faraday cage connected to the top plate

Table 4.2: Dimensions for scale model for second trial measurements as used for the 2D and 3D comparative simulations

(a) Parameters defined in Figure 4.1		
Description	Parameter	Value
Main line radius	r_l	20 mm
Main line height above ground	h_l	1.5 m
Sensor height above ground, measured to the bottom plate	h_s	0.1 m
Sensor width	w_s	0.1 m
Thickness of dielectric separating the sensor plates	d_s	1.6 mm

(b) Parameters not defined in Figure 4.1	
Description	Value
Sensor length	1 m
Faraday cage height	3 cm
Faraday cage length (short)	25 cm
Faraday cage length (full)	1 m
Main line length	12 m
Ground plane length	12 m
Ground plane width	3.6 m

model, especially if only a 2D package is available.

The effect of sag on the capacitive coupling was also investigated during these simulation experiments. Figure 4.12 shows the side view of the two-element sensor underneath a transmission line simulated with three sections to approximate the sag of the scale model. The line height at the midpoint is now 1.42 m instead of 1.5 m.

A comparative table of the different simulations without a faraday cage is given in Table 4.3. As expected, the capacitive coupling between the transmission line and sensing elements, namely C_{ls1} and C_{ls2}, are influenced significantly when the line length is increased with respect to the sensor length. The percentage change in the Thévenin equivalent voltage, V_{TH}, is of the same order as the change in C_{ls1} as can be predicted from the sensitivity analysis graphed in Figure 4.9 (b). The change in the capacitive coupling between the sensor and ground, namely C_{s1g} and C_{s2g}, are almost
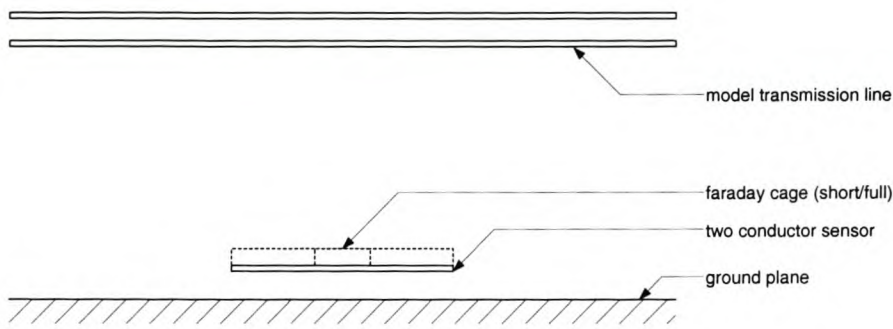
Figure 4.11: Side view of model transmission line and two conductor sensor topology (not drawn to scale)
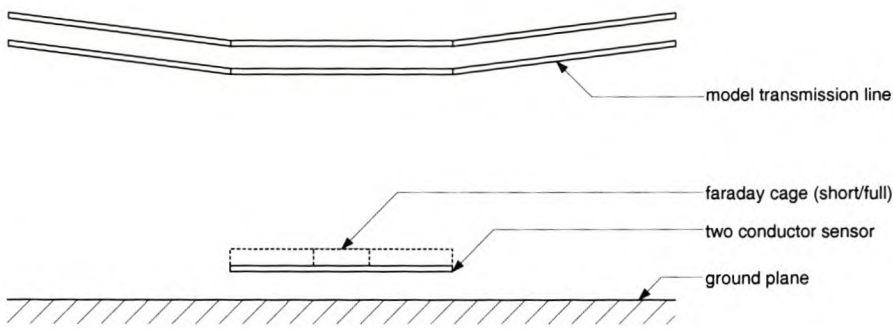
Figure 4.12: Side view of model transmission line and two conductor sensor topology with sag of the transmission line (not drawn to scale)

negligible as the sensor height is 10 times less than the sensor length. The percentage change in C_{s1s2} is almost zero, because the plate separation is significantly less than the other variables and is further supported by the increased dielectric constant of the PCB substrate. Equation 4.1 is applicable for this arrangement as well and therefore, the percentage change in the Thévenin equivalent impedance, Z_{TH}, is almost zero as well.

Table 4.3: Comparison of 2D and 3D simulations for the two-element parallel plate sensor when neglecting the faraday cage

Coupling element/ variable	2D simulation	3D simulation	Units	% difference
C_{ls1}	0.61	1.08	[pF]	78.18
C_{ls2}	0.18	0.22	[pF]	23.72
C_{s1g}	10.68	11.90	[pF]	11.36
C_{s2g}	15.25	14.86	[pF]	-2.61
C_{s1s2}	3.23	3.23	[nF]	0.16
Z_{TH}	49.25	49.16	[kΩ]	-0.17
V_{TH}	85.24	148.22	[μV/V]	73.89

The effects of transmission line sag is summarised in Table 4.4. The 5.3 % sag of the transmission line produced negligible changes in the capacitive coupling elements. The coupling between the

line and the sensing elements is influenced the most, but remains within 10 %, as does the change in Thévenin equivalent voltage. The influence of the sag may therefore be neglected for a first approximation.

Table 4.4: Comparison of 3D simulations for no sag or sag of the transmission line when neglecting the faraday cage

Coupling element/ variable	3D No sag	3D Sag	Units	% difference
C_{ls1}	1.08	1.16	[pF]	6.63
C_{ls2}	0.22	0.24	[pF]	9.28
C_{s1g}	11.90	11.75	[pF]	-1.26
C_{s2g}	14.86	14.86	[pF]	0.04
C_{s1s2}	3.23	3.23	[nF]	0.14
Z_{TH}	49.16	49.10	[kΩ]	-0.14
V_{TH}	148.22	157.82	[μV/V]	6.48

When including the faraday cage, the simulation results are summarised in Table 4.5. Table 4.5 (a) compares the 2D simulations with the added faraday cage to the 3D simulations with a full length faraday cage, i.e. 1 m long. The main difference between the two sets of simulations is visible mainly in the coupling elements between the transmission line and the sensing elements, namely C_{ls1} and C_{ls2}. The percentage difference is larger than for the case when the faraday cage is neglected (cfg. Table 4.3) and is attributed to the decrease in distance between the top plate (connected to the faraday cage) and the transmission line. The deviation of capacitive coupling elements between the different sensing elements and the sensing elements and ground respectively may be ignored.

It seems that when a short faraday cage is used, the top plate effective coupling area is decreased and the percentage difference between the coupling between the transmission line and the sensing elements is decreased significantly. This is clear from Table 4.5 (b) where the comparative 3D simulations were done for a 25 cm long faraday cage. It is interesting to note that the capacitive coupling between the top plate and ground has now decreased by a significant amount, namely 17 %. This is ascribed to the shorter cage with less coupling area to ground, than in the idealised 2D case or the previously compared full length faraday cage 3D simulations. This significant decrease in C_{s1g} caused an increase in the Thévenin equivalent voltage larger than the percentage increase in C_{ls1}. The overall deviation in the Thévenin equivalent voltage is, therefore, still significant.

The effect of sag is compared in Table 4.6 for the short faraday cage simulations. It seems that the transmission line to sensor capacitive coupling is dominated by the top surface of the faraday cage, providing the effective coupling area for C_{ls1}. This implies that the percentage variation for all the coupling elements and the Thévenin equivalent voltage and impedance is negligible for the short

Table 4.5: Comparison of 2D and 3D simulations for the two-element parallel plate sensor when including the faraday cage, either 1 m long or 25 cm long

(a) Comparison of 2D simulation with full faraday cage 3D simulation				
Coupling element/ variable	2D simulation	3D simulation 1 m long cage	Units	% difference 1 m cage
C_{ls1}	0.96	1.88	[pF]	96.28
C_{ls2}	0.10	0.05	[pF]	-47.69
C_{s1g}	15.59	17.21	[pF]	10.40
C_{s2g}	13.81	13.20	[pF]	-4.42
C_{s1s2}	3.23	3.23	[nF]	0.09
Z_{TH}	49.18	49.13	[kΩ]	-0.10
V_{TH}	118.03	228.10	[µV/V]	93.26
(b) Comparison of 2D simulation with short faraday cage 3D simulation				
Coupling element/ variable	2D simulation	3D simulation 25 cm long cage	Units	% difference 25 cm cage
C_{ls1}	0.96	1.32	[pF]	37.81
C_{ls2}	0.10	0.20	[pF]	95.64
C_{s1g}	15.59	12.93	[pF]	-17.07
C_{s2g}	13.81	14.45	[pF]	4.67
C_{s1s2}	3.23	3.23	[nF]	0.06
Z_{TH}	49.18	49.16	[kΩ]	-0.05
V_{TH}	118.03	176.26	[µV/V]	49.34

faraday cage under sag conditions. It therefore seems that it is desirable to have a faraday cage as short as possible for the current differential parallel plate sensor topology.

Table 4.6: Comparison of 3D simulations for no sag or sag of the transmission line when including the 25 cm long faraday cage

Coupling element/ variable	3D No sag	3D Sag	Units	% difference
C_{ls1}	1.32	1.31	[pF]	-1.05
C_{ls2}	0.20	0.20	[pF]	0.20
C_{s1g}	12.93	12.85	[pF]	-0.58
C_{s2g}	14.45	14.48	[pF]	0.20
C_{s1s2}	3.23	3.24	[nF]	0.14
Z_{TH}	49.16	49.09	[kΩ]	-0.14
V_{TH}	176.26	174.51	[µV/V]	-0.99

4.2.4   Three-dimensional simulations for three-element parallel plate sensors

Other sets of simulations were done to determine the influence of end effects on the Thévenin equivalent voltage and impedance. The basis simulation is a 2 m long section of a typical 2D simulation, with the geometry similar to the previous definition in Figure 3.11 given for the three-element parallel plate sensor.

Coulomb© allows for the use of symmetry planes to reduce the size and time required for the simulation. The first requirement is that the geometry and materials can be mirrored around any of the principal planes of the Cartesian coordinate system. If the boundary conditions can also be mirrored, then a symmetry condition applies. If the boundary conditions have identical magnitude, but opposite polarity, then an anti-symmetry condition applies. Two symmetry planes were defined for these simulations, namely the "xz" and "yz" planes.

Furthermore, these simulations were done for the three-element parallel plate sensor. Two pieces of double-sided PCB were connected to form a faraday cage 35 mm thick. PCB with standard FR4 dielectric with a permittivity of 5.8 was used. The values of the parameters that were defined in Figure 3.11 are given in Table 4.7.

Table 4.7: Parameter values used for generic simulations of a single transmission line and a three-element parallel plate sensor above ground

Description	Parameter	Value
Main line radius	r_l	0.2 m
Main line height above ground	h_l	15 m
Sensor height above ground	h_s	1 m
Sensor width	w_s	0.5 m
Thickness of dielectric	d_s	1.6 mm
Depth of faraday cage	d_c	35 mm

The ground plane width was not defined in Figure 3.11 as it was assumed infinite at that stage. For these simulations, the ground plane was 200 m wide, i.e. extending 100 m on either side of the transmission line in the 2D view.

A 3D view of the typical situation is shown in Figure 4.13. The '1/2 simulation length' as indicated in Figure 4.13 was varied from 1 m to 150 m. The origin for this arrangement was located at the back left corner of Figure 4.13, which shows a quarter of the actual arrangement that is modelled. Mirrors of this quarter should be added in the x and y direction ("yz" and "xz" planes) to complete the model. The full simulation length was varied from 2 m to 300 m using 8 steps, namely: 2 m, 4 m, 10 m, 20 m, 40 m, 100 m, 200 m, 300 m. The maximum of 300 m was chosen because it

is the typical inter-tower span for high voltage transmission lines, while the 2 m minimum results from the 2 m length of the prototype sensor.
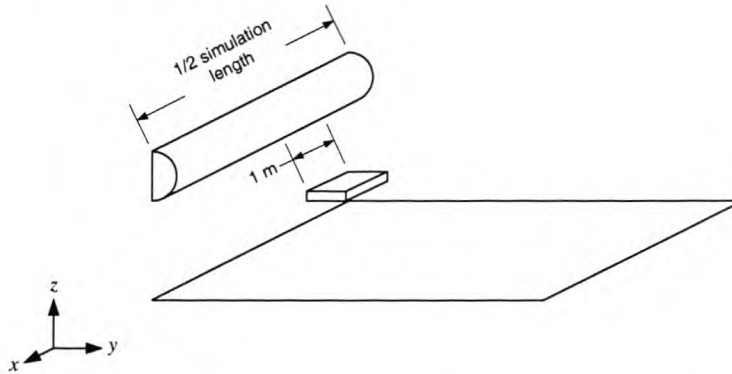
Figure 4.13: Generic drawing of 3D simulations to determine the influence of end effects

It should be noted that the shorter simulation length geometries that were simulated do not resemble any practical situation, but were conducted to obtain a geometry that will model the practical situation closely. The graphs for the different capacitive coupling elements, will indicate the amount of fringing fields present and therefore the minimum simulation length that will approximate practical arrangements. Spline interpolation was used to obtain smooth graphs.

Figure 4.14 shows the capacitance of the main transmission line to ground for different simulation lengths. The capacitance between the transmission line and ground, C_{lg}, approximates the theoretical value for the capacitance to within 10 % from 65 m simulation length and up as shown in Figure 4.14. Figure 4.15 plots the calculated Thévenin equivalent voltage for different simulation lengths. The Thévenin equivalent voltage approach the 10 % deviation already at 38.5 m simulation length, although a theoretical value is unavailable for the Thévenin equivalent voltage. The approximation is therefore with reference to the maximum value for V_{TH}, which occurs at a simulation length of 300 m.

A simulation length of 38.5 m, achieving 10 % accuracy for the Thévenin equivalent voltage amounts to a line length 2.57 times the height above the ground plane. For this purpose it is assumed that the ground plane is wide enough not to influence the accuracy of the above statement. For lower line heights, the 10 % accuracy length will therefore be shorter. This is demonstrated by the data in Table 4.8. It seems that the required ratio of line height to line length is approximately 2.7 for 10 % accuracy in the predicted Thévenin equivalent voltage. 1 % accuracy requires a line length approximately 8 times the line height.

The variation of the capacitive coupling elements versus the simulation length is shown in Figure 4.16. The capacitive coupling parameters are normalised with reference to the value obtained for a 300 m simulation length. The coupling between the transmission line and the sensing elements
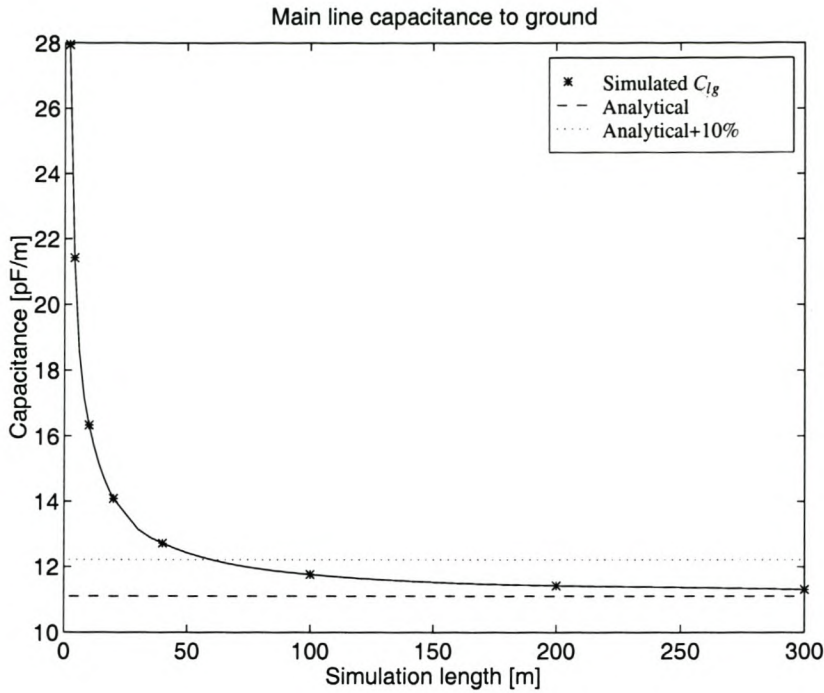
Figure 4.14: Main line capacitance to ground per meter length plot against simulation length compared with the theoretical capacitance for a single line above ground
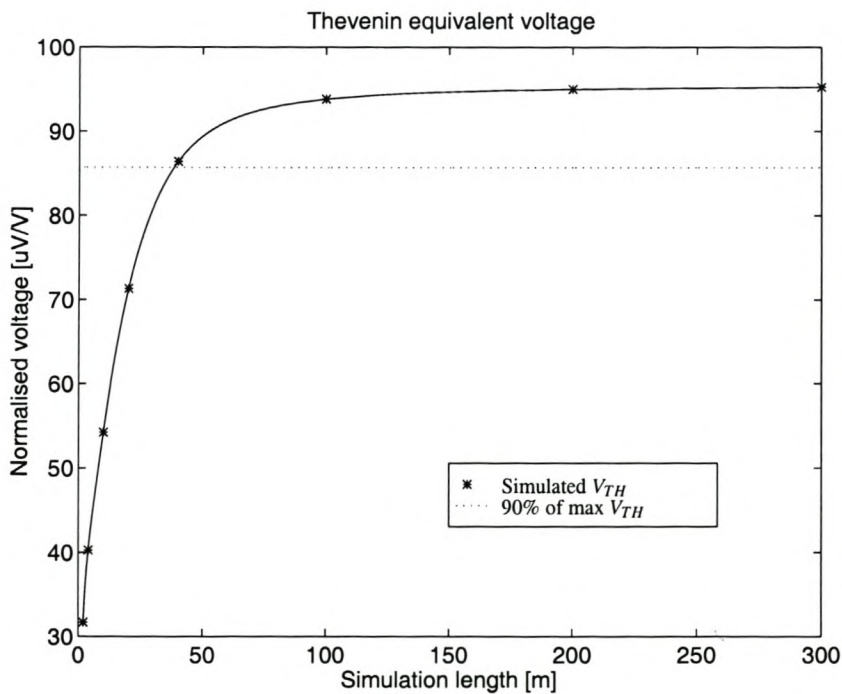
Figure 4.15: Normalised Thévenin equivalent voltage plot against simulation length compared with 90 % of the maximum value, i.e. V_{TH} for the 300 m simulation length

Table 4.8: Thévenin equivalent voltage deviation from the reference value at a 300 m simulation length

Line height (h_l)	Error at simulation length:		Simulation length for % deviation		Ratio of line length to height	
	40 m	100 m	10 %	1 %	10 %	1 %
8.0 m	-2.31 %	-0.08 %	21.5 m	50.0 m	2.69	6.25
11.27 m	-4.94 %	-0.52 %	28.5 m	74.0 m	2.53	6.57
15.0 m	-9.26 %	-1.50 %	38.5 m	120.0 m	2.57	8.00
20.0 m	-15.41 %	-2.98 %	52.5 m	149.0 m	2.63	7.45

shown in Figure 4.16 (a) approach the final value to within 10 % at approximately 40 m length, similarly to the Thévenin equivalent voltage, shown in Figure 4.15. The coupling between the sensing elements and ground is shown in Figure 4.16 (b) and is almost insensitive to the simulation length as the separation between the sensor and the ground plane is relatively small. The different coupling elements between the sensing elements, namely C_{s1s2}, C_{s2s3} and C_{s1s3} are not shown as the percentage change for these elements are negligible.

From the preceding paragraphs, it is clear that only the transmission line to ground capacitance require a fairly long simulation length to achieve 10 % accuracy. It is, therefore, deduced that the overall required length is at least 2.7 times the line height in order to achieve 10 % accuracy for the capacitive parameters of the sensor topology. The usual requirement to use the telegrapher's equations for transmission line analysis is that the line must be least 10 times as long as the height above ground. From the above discussion, it is clear that the 10 times ratio should result in an accuracy of at least 1 % for the Thévenin equivalent voltage and is regarded as a good approximation for the sensor topology as well.

4.2.5   3D simulations for the HV laboratory measurements

An extensive set of simulations were done using the three-dimensional Coulomb© for the test arrangement inside the HV laboratory. The arrangement differs from practical situations because the testing area is completely enclosed inside a faraday cage. The simulations were, therefore, done only to compare the laboratory tests with expected results as well as get an indication of a sensitivity analysis. These simulations will be discussed in section 6.4.
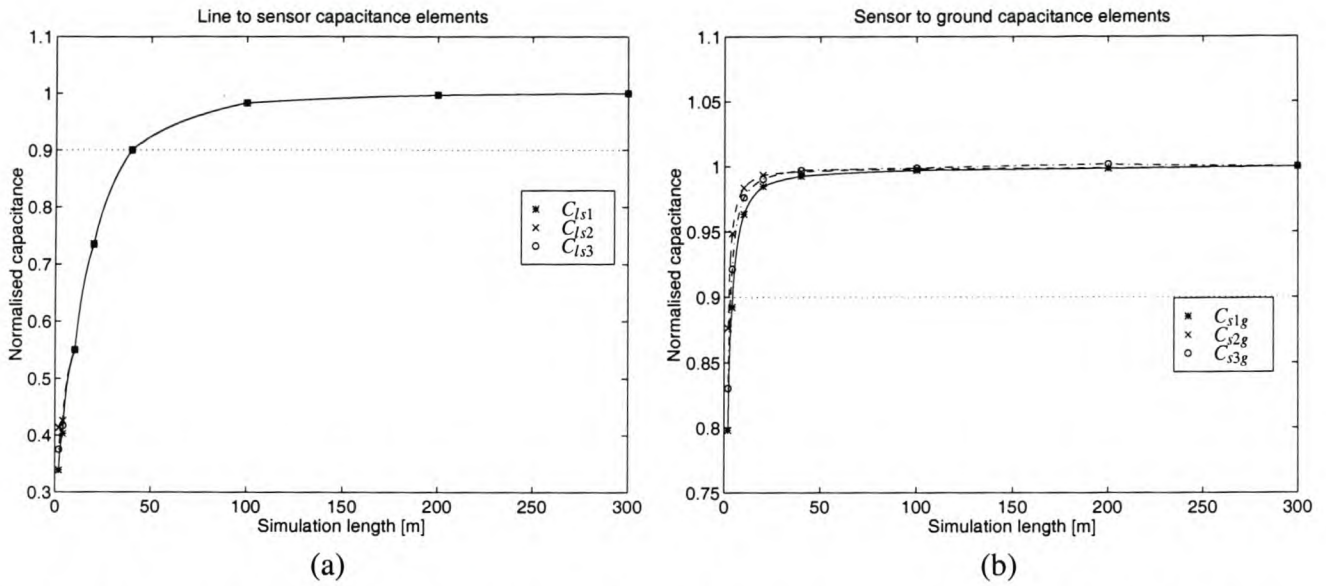
Figure 4.16: Normalised capacitance matrix element variation versus simulation length (a) Capacitance between transmission line and sensing elements (b) Capacitance between sensing elements and ground

4.3 Simulated Time- and Frequency Domain Responses

It has already been discussed that the differential parallel plate sensor provides a superior sensor topology and the addition of the separate faraday cage for the three-element parallel plate sensor increases the complexity but also the robustness of the sensor topology. The circuit models and Thévenin equivalent parameters derived in section 3.3.3 will be used to determine time- and frequency domain responses to characterise this topology completely. Matlab® from *The Mathworks, Inc.* was used to simulate the responses in both the time- and frequency domains.

Different excitation functions were used to determine the time domain response of the circuit, namely a step input and two practical impulse waveforms. The two impulse waveforms were the same as the impulse waveforms used for the excitation of the prototype sensor under laboratory test conditions. The fast impulse is the standard 1.2/50 μs lightning impulse, while the slow impulse has a 100 μs rise time and the voltage falls to half the peak value within approximately 1 ms. The frequency response of the sensor topology is given in terms of the predicted transfer function magnitude response.

It has been found that leakage to ground will negatively influence the response of the sensor topology. The aim of this section is to quantify the effects of the leakage elements. From the results, practical support structures may be proposed.
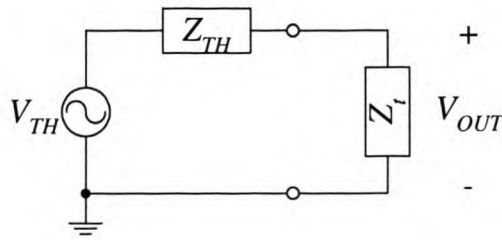
Figure 4.17: Thévenin equivalent circuit with arbitrary termination impedance

4.3.1 Modelling of leakage elements

The Thévenin equivalent voltage and impedance for the three-element parallel plate sensor has been discussed and derived in section 3.3.3. In order to find the output voltage, the termination impedance must be connected across the output of the Thévenin equivalent circuit as shown in Figure 4.17. Series voltage division across the Thévenin equivalent impedance and the termination impedance yields the following equation for the output voltage:

$$V_{OUT} = V_{TH}\frac{Z_t}{Z_t + Z_{TH}}$$
(4.2)

where Z_t is the termination impedance.

The termination impedance of the sensor is also the input impedance of the interface instrumentation. Both capacitance and resistance are inherent in the input impedance of any buffer or amplifier and is usually modelled as the parallel connection of the two components, namely R_t and C_t. Extra capacitance is added in parallel to increase the division ratio of the sensor topology and lower the pole formed by this parallel connection of R_t and C_t. All inductance terms are ignored as short lines are used as far as possible.

An ideal or default model is defined, where no loss terms are included except for the termination resistance, R_t. For this model it is assumed that all materials used for the support structure have ideal insulating properties, which is not realistic. Other models are defined by adding resistors to the default model, representing the different leakage components. Referring to Figure 3.13 in section 3.3.3, the following models may be defined apart from the termination resistance:

(1) Default model - only capacitances are included in the model

(2) R_{s1g} model - add a single resistor from the top plate to ground to the default model

(3) R_{s2g} model - add a single resistor from the bottom plate to ground to the default model

(4) R_{s3g} model - add a single resistor from the faraday cage to ground to the default model

(5) R_{s1g}/R_{s2g} model - add two resistors to the default model, one each from the top and bottom plate to ground

(6) R_{s1s3}/R_{s2s3} model - add two resistors to the default model, one each between the top and bottom plate and the faraday cage

(7) R_{sns}/R_{s3g} model - add three resistors to the default model, one each between the top and bottom plate and the faraday cage and one from the faraday cage to ground

(8) R_{sns}/R_{sg} model - add five resistors to the default model, one each between the top and bottom plate and the faraday cage and one from each sensing plate and the faraday cage to ground

These models are defined from a mathematical point of view. Practically the resistors represent leakage between the conductors referenced in the subscripts. The value used for the leakage between the sensor elements and ground is 100 MΩ , while 10 MΩ was used for the leakage between the different sensing elements and the faraday cage, i.e:

- R_{s1g}, R_{s2g} and R_{s3g} = 100 MΩ

- R_{s1s3} and R_{s2s3} = 10 MΩ

It is also assumed that R_{s1s2} is significantly larger than the termination resistor, R_t and R_{s1s2} is also ignored. The first model defines the ideal sensor topology, with the R_t the only loss term. R_t is included in the total circuit for all models defined above. Models 2-4 include one extra resistor representing the leakage between any of the sensor elements and ground. This implies that the sensor support structure, with relatively poor isolation properties, is connected to any one of the sensor elements.

Models 5 and 6 represent the case where the two sensing elements, s1 and s2, are connected in a balanced manner either to ground or the faraday cage, s3. Model 5 requires a perfect support structure, but allows for leakage across the substrate, which may be caused by pollution. Model 6 on the other hand, ignores the substrate leakage, but connects the sensor in a balanced manner to the support structure.

The last two models attempt to model practical support structure combinations. The resistors between the sensing plates and the faraday cage are included to fix the substrate losses for better predictable results and it is hoped that the leakage cause by pollution on the substrate will never exceed the fixed resistive values. It will be shown that unbalanced leakage affect the sensor response adversely and therefore a balanced support structure is proposed.

4.3.2 Frequency domain responses

The addition of the leakage elements is best described in terms of the poles and zeros caused by the resistor and capacitor combinations. It therefore makes sense to start the discussion from the frequency domain perspective.

Asymptotic responses are defined for the sensor when all loss terms, including the termination resistance, are ignored. This will correspond to the division ratio of the capacitive divider formed by the sensor at high frequencies. High frequencies are high enough so that the resistive terms do not affect the transfer function, while the frequency is low enough that inductive effects may be ignored as well.

The first loss term to be included in the simulations is the termination resistance, R_t. This parallel RC combination adds a zero, cutting of the low frequencies. The position of this zero is determined by the termination resistance and the parallel combination of the Thévenin equivalent capacitance and termination capacitance as given by equation 4.3.

$$f_c = \frac{1}{2\pi R_t (C_t + C_{TH})} \tag{4.3}$$

For accurate measurements down to 50 Hz, this pole should lie at or lower than 5 Hz. Therefore: $R_t \geq 1/2\pi f(C_t + C_{TH})$, where f is the frequency equal to 5 Hz.

The graph in Figure 4.18 shows the amplitude and phase response for the default model of the three-element parallel plate sensor in the enclosed HV laboratory. The amplitude response is normalised for the different arrangements, as the Thévenin equivalent capacitance is fixed for a certain sensor topology. The relative sensor height influences the voltage division ratio, but not the Thévenin equivalent impedance. The sensor response may therefore be normalised by the division ratio and 0 dB in Figure 4.18 indicates the high-frequency asymptote.

Graphs for three different termination impedance combinations are shown in Figure 4.18, namely 10 MΩ //30 nF, 10 MΩ //10 nF and 30 kΩ //10 nF. It is clear that the larger valued resistance and capacitance pairs cut off at a lower frequency than the low valued resistance termination. This emphasize the requirement for a high input impedance for the interface instrumentation.

Models 2, 3 and 4, which include one leakage element each are the R_{s1g}, R_{s2g} and R_{s3g} models. The R_{s1g} and R_{s2g} models present the practical cases where the sensor is either suspended from, or resting on the support structure. This means that either the top or bottom plate has unacceptably low leakage to ground. A third alternative is to connect the support structure to the faraday cage, which also result in a single leakage element added to the model. The faraday cage, $s3$, is not a sensing element as the Thévenin equivalent voltage is measured differentially between the top
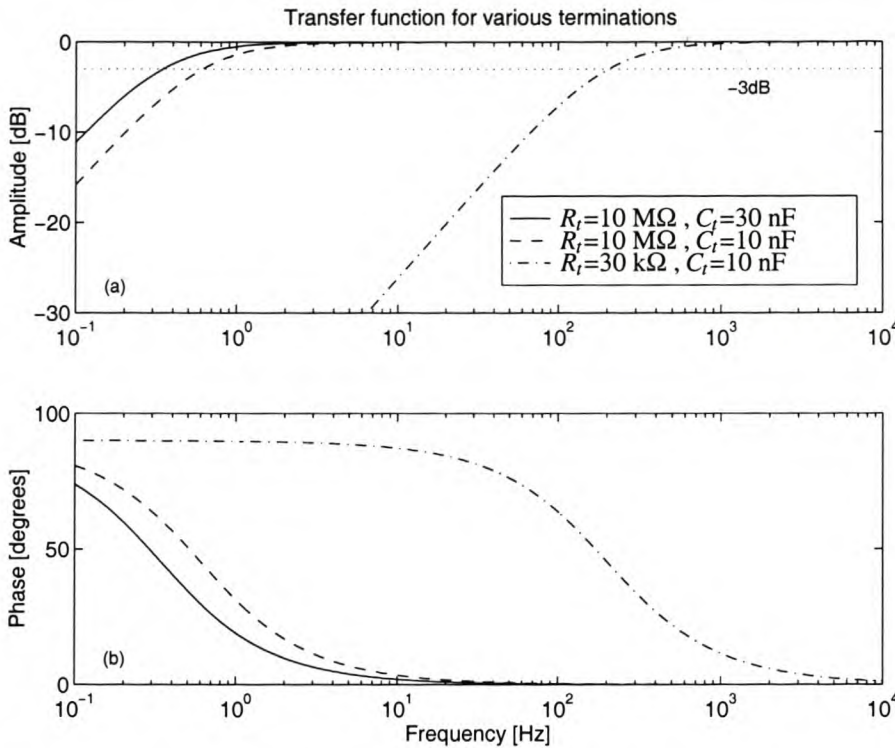
Figure 4.18: Normalised transfer function of transmission line and three element sensor topology for different termination impedances as listed in the legend (a) Amplitude response (b) Phase response

and bottom plates, $s1$ and $s2$, respectively. This provides an explanation why the transfer function for the R_{s3g} model is almost unaffected by the leakage, where-as the R_{s1g} and R_{s2g} models show unacceptable deviation from the default model. The transfer functions for these three cases are shown in Figure 4.19 together with the default model shown as a solid line. The termination impedance used for the default model, added as reference, was 10 MΩ //10 nF. It is clear that when a single sensing element, i.e. the top or bottom plate, of the sensor has significant leakage to ground, the deviation from the reference is unacceptable as the error is more than 10 dB at low frequencies. From the phase response of the R_{s1g} model, it is clear that the amount of charge conducted away from the top plate, $s1$, causes the top plate voltage to drop lower than the bottom plate voltage, i.e. the output is an inverted copy of the actual transmission line voltage.

The remaining models have more than one leakage element added. Figure 4.20 shows the situation where leakage exist between both the top and bottom plate and ground as well as when the PCBs have leakage across the substrate. Mathematically, these models are balanced with respect to the differential voltage across $s1$ and $s2$. Both these models also show negligible deviation from the default model, included as a solid line in Figure 4.20. The R_{s1s3}/R_{s2s3} model increase the cut-off frequency from approximately 0.6 Hz to approximately 0.9 Hz. The phase response is also influenced negligible and therefore, the leakage of the substrate is regarded as a minor problem. A
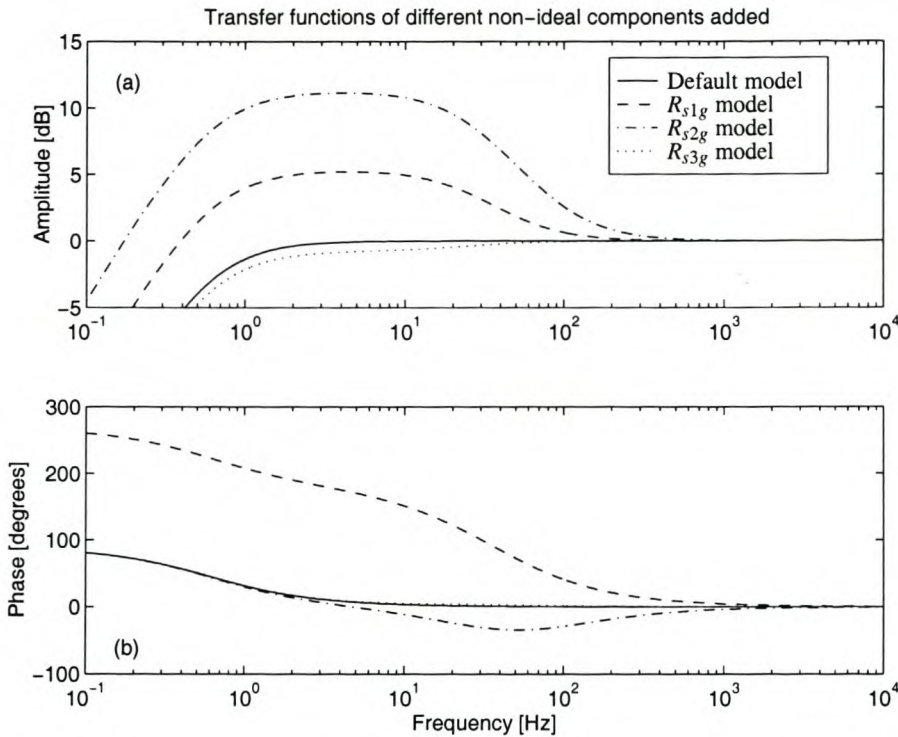
Figure 4.19: Transfer function with R_{s1g}, R_{s2g} or R_{s3g} added (a) Amplitude response (b) Phase response

lower limit for an acceptable -3 dB point is reached for the leakage at approximately 2 MΩ leakage resistance if the leakage remains balanced. The R_{s1g}/R_{s2g} model exhibit a slightly more complex response. There is a slight drop in the transfer function of approximately 1 dB between 50 Hz and 100 Hz. The -3 dB point, however, is located lower than for the R_{s1s3}/R_{s2s3} model.

The last two models, namely R_{sns}/R_{s3g} and R_{sns}/R_{sg}, represent two practical situations. Both these models exhibit similar behaviour to the R_{s1g}/R_{s2g} model, where the magnitude response drops in two stages as shown in Figure 4.20. The -3 dB point remains below 1 Hz and it is still regarded as acceptable. The influence on the phase response may be ignored in both cases as well.

4.3.3 Time domain responses

From section 4.3.2 it is clear that several models are available, where the effect of leakage remains negligible. Due to this only four models will be presented in the time domain, namely the following models:

- Default model

- R_{s1g} model
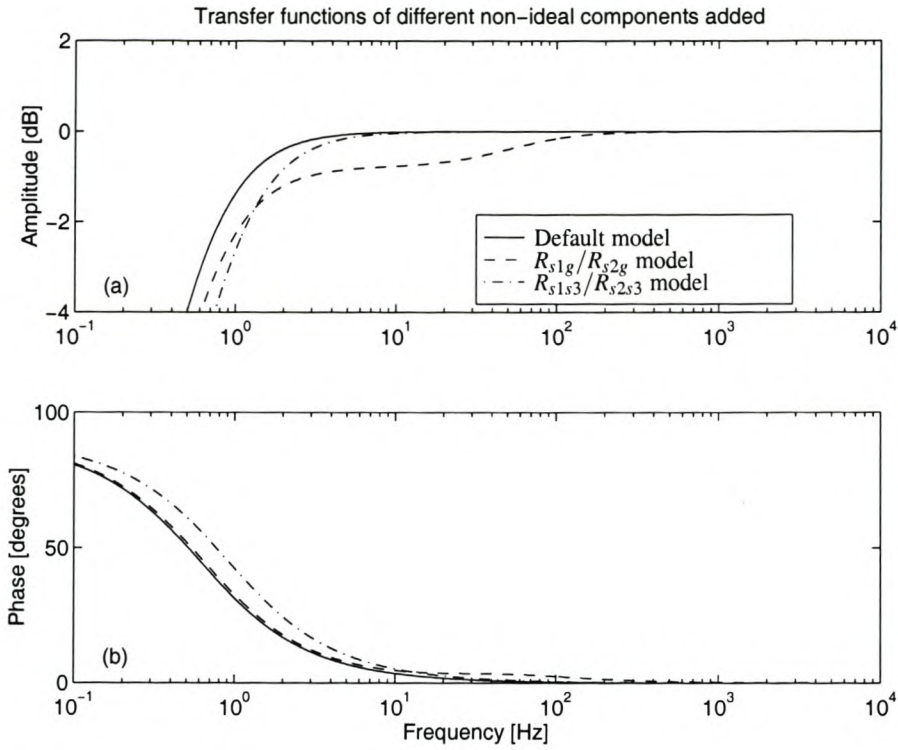
Figure 4.20: Transfer function with combinations of resistors added, namely the R_{s1g}/R_{s2g} or R_{s1s3}/R_{s2s3} model (a) Amplitude response (b) Phase response
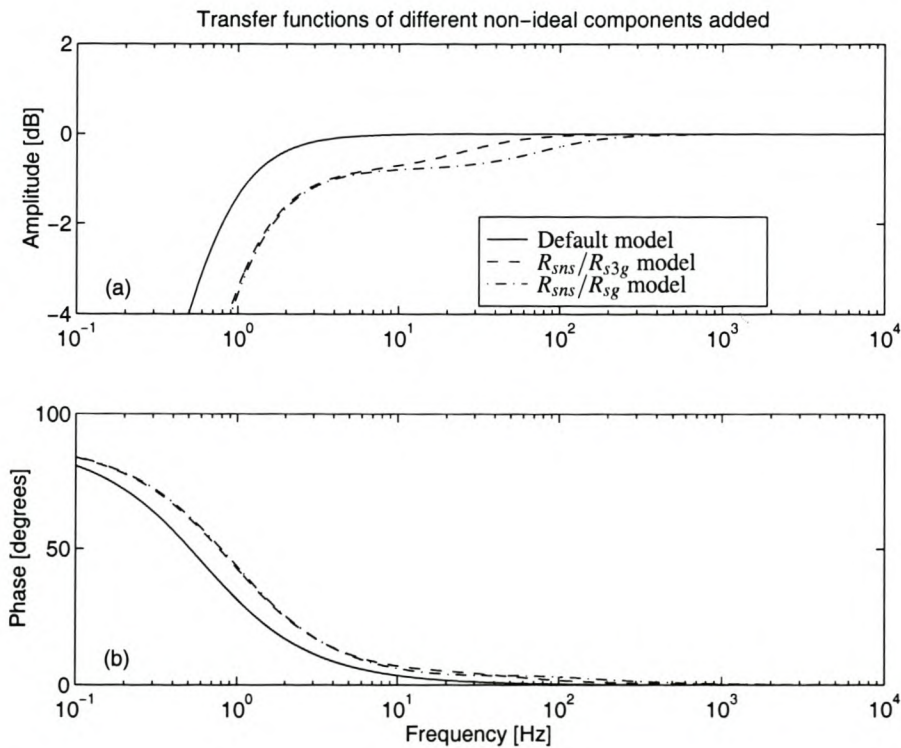
Figure 4.21: Transfer function for practical support structures (a) Amplitude response (b) Phase response

- R_{s2g} model

- R_{sns}/R_{s3g} model

It will be informative to show the time domain graphs for the R_{s1g} and R_{s2g} models along with the default model and a model for a practical support structure, namely the R_{sns}/R_{s3g} model.

The effect of the termination impedance on time domain signals is best illustrated using a step response as input for the default model as shown in Figure 4.22. The attenuation of low frequency information is clear, because all traces deviate from the flat part of the trace, i.e. DC is removed by the sensor topology. It is clear from the rising and falling edge of the step that high frequency information is transferred correctly.

The step waveforms in Figure 4.22 are normalised with respect to the voltage division ratio for a termination capacitance, C_t, of 10 nF. The 30 nF termination capacitance increases the voltage division ratio as can be seen from the peak value of the trace for the 30 nF termination. The low resistive termination, i.e. 30 kΩ //10 nF, removes information up to approximately 100 Hz and therefore, the step response decays to zero quickly. This decay is negligible for the 100 Hz square wave for a termination resistance of 10 MΩ .
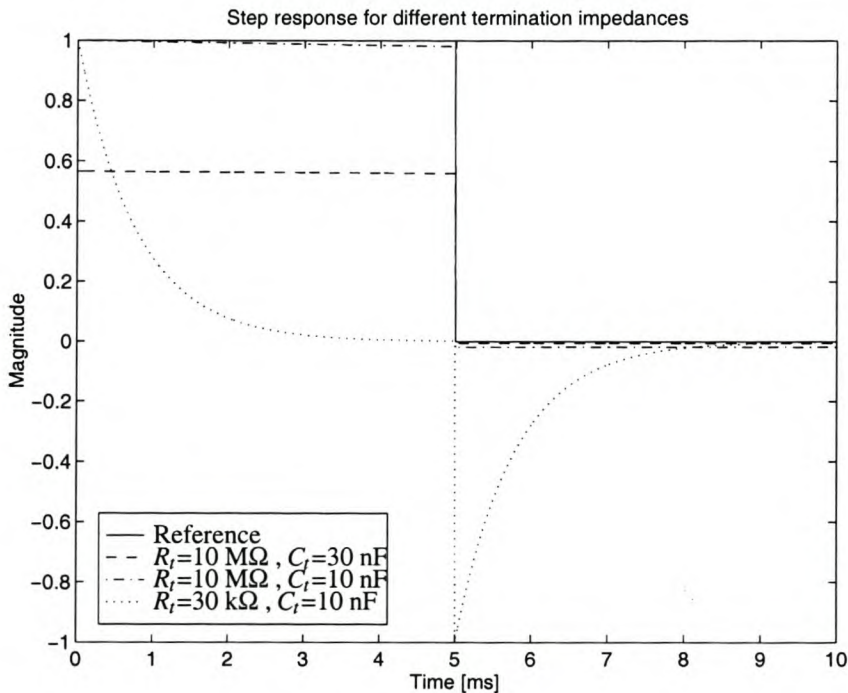
Figure 4.22: Step response of the three-element parallel plate sensor default model for different termination impedances

Figure 4.23 shows the step response of the three-element parallel plate sensor for three of the models listed in section 4.3.1. The impulse responses for these models are divided into a "slow" and "fast" impulse excitation and are given in Figures 4.24 and 4.25.

From Figures 4.23 to 4.25, it is clear that the R_{sns}/R_{s3g} model causes negligible deviation in the measured waveforms. As expected, the deviation for the R_{s1g} and R_{s2g} models is unacceptable and these situations should be avoided.
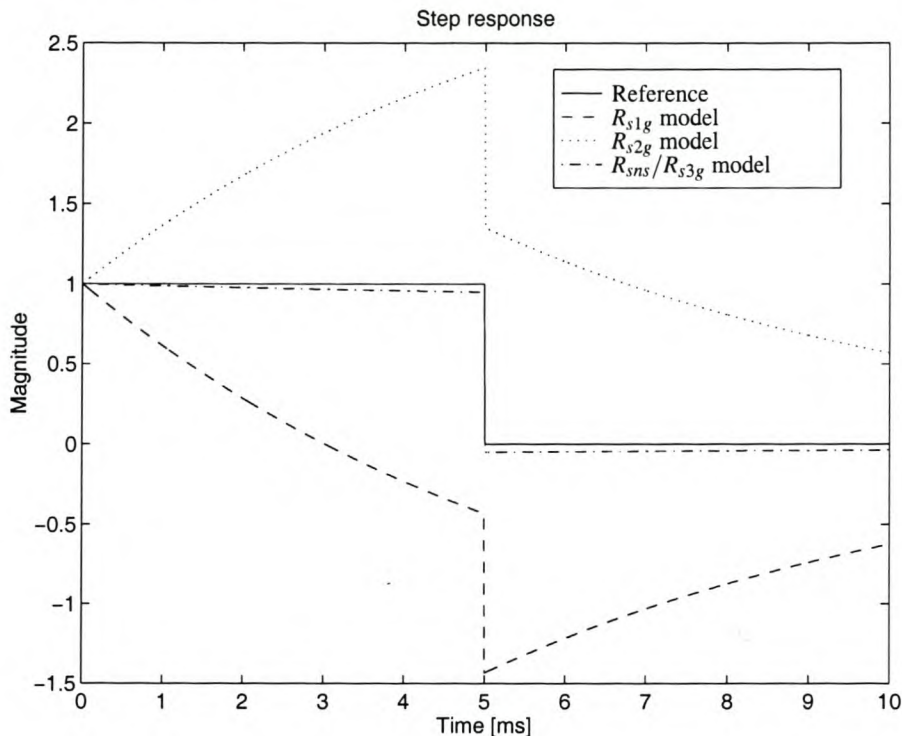
Figure 4.23: Step response of the three-element parallel plate sensor topology for different leakage models

The phase reversal at low frequencies, discussed for the R_{s1g} model is evident in Figures 4.24 and 4.25. At high frequencies, the output follows the input closely, but the lower frequencies present in the rising edge causes a negative peak for the R_{s1g} model response.

4.4 Design Strategy Discussion

The purpose of this chapter is to give the reader an overview of capacitive sensor parameters and which factors play a role in the operation of such sensors.

When a capacitive sensor is required for a certain application, the following main points should be considered first:
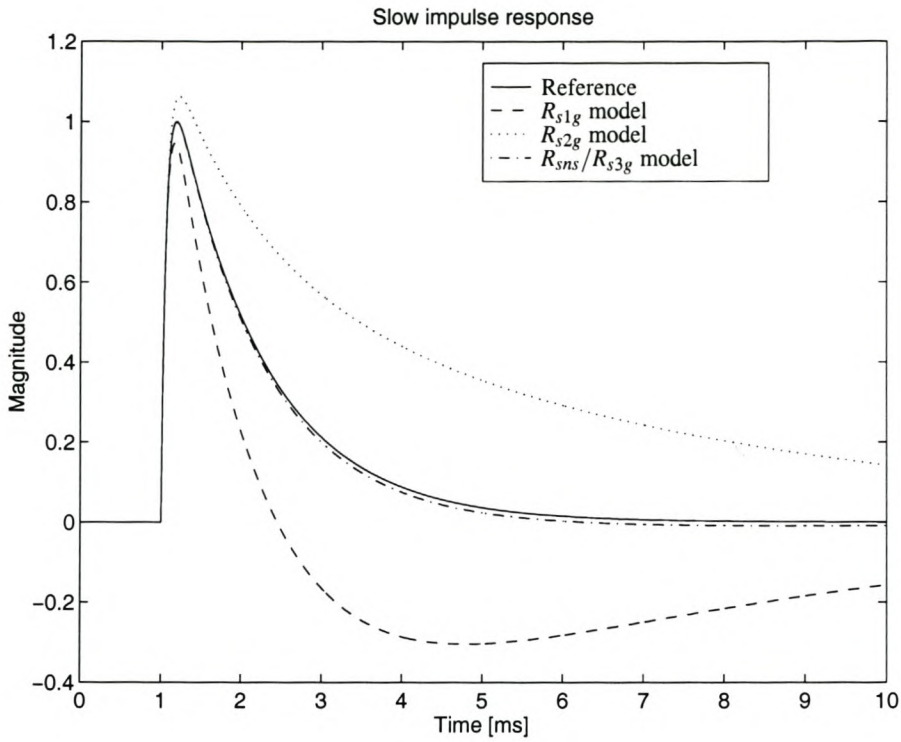
Figure 4.24: Slow impulse response of the three-element parallel plate sensor topology for different leakage models
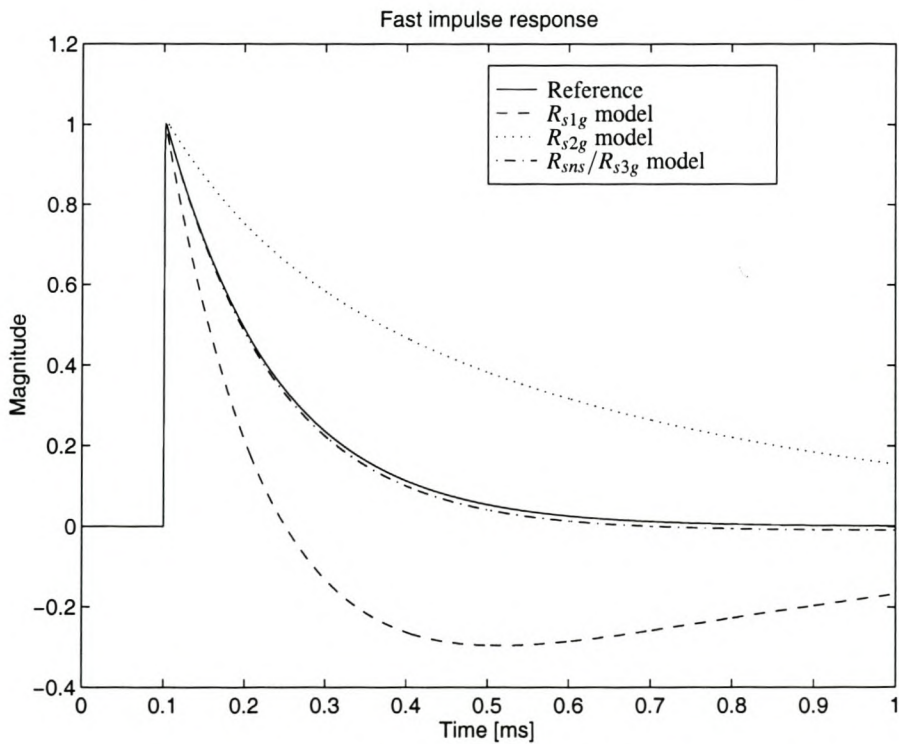
Figure 4.25: Fast impulse response of the three-element parallel plate sensor topology for different leakage models

- Application of sensor, i.e. how mobile or permanent will the installation be

- What are the restrictions on physical size

- What support structure is available or can be constructed

- What bandwidth is required

One of the main points emphasized in this dissertation, is that the sensor should remain galvanically isolated from the environment. This means that the instrumentation must be integrated with the sensor for proper operation.

The required bandwidth of the measuring arrangement will determine the requirements for the sensor instrumentation. It has been shown that the sensor approach infinite bandwidth under ideal conditions. The overall system bandwidth is therefore determined by the high frequency -3 dB point of the instrumentation and the low-frequency pole formed by the termination impedance and the sensor capacitance. Furthermore, the high frequency cut-off is determined by the size of the sensor and the test environment. It was assumed that the sensor, as well as the transmission line, is electrically short. It was assumed that the sensor's main dimension is shorter than one tenth of the wavelength. If this is not valid, then the equivalent circuits as derived in this dissertation are no longer valid either.

Three possible sensors are suggested at this stage, depending on the application. Two of the plate sensors, namely the two-element and the three-element parallel plate sensor are viable options as well as the single element coaxial sensor.

If a very mobile sensor is required, then the flat construction is advised. For a longer term installation, the coaxial sensor around the earth wire is suggested.

The coaxial sensor does not require a support structure, as it is mounted around the earth wire. One of the electrodes for the single-element coaxial sensor is earthed, which allows for power to be applied externally. This is also ideal for a longer term installation, as the frequent changing/charging of batteries may prove difficult for this sensor topology.

The plate sensor requires a support structure and as mentioned in this chapter, the leakage resistance to ground should approach infinity. Very good isolators are required between the sensor and ground. The differential parallel plate sensor is not very sensitive to changes in the actual ground level, which simplifies the calibration of the arrangement.

It is suggested that the instrumentation input impedance, or termination impedance of the sensor always be large enough that this pole lies at or below 5 Hz. The high frequency cut-off is determined either by the instrumentation bandwidth or the physical size of the sensor. If the termination

impedance and support structure approach the ideal situation, the frequency response of the sensor topology should be flat from 5 Hz to very high frequencies. This will allow the user to do 50 Hz measurements for calibration purposes.

Continuing the calibration issue: the Thévenin equivalent impedance, which is determined by the sensor capacitance, is also the main contributing factor to the output voltage magnitude. It is, therefore, very important to know the exact values of the sensor capacitance.

4.5 Conclusions

It was shown that the single element plate sensor is sensitive to ground level changes and is therefore not an attractive option to use. The single element coaxial sensor is more robust, but less mobile and may be used in more permanent installations. For a mobile sensor the differential topologies are suggested. The effect of variations in the sensor height above the ground plane is minimised by using a differential topology.

A faraday cage is required for proper integration of the instrumentation with the sensor. Two differential topologies were investigated, namely connecting the faraday cage to the top sensor plate of a differential sensor or having a separately floating faraday cage. The latter option was shown to be more robust as connections to the faraday cage does not have a significant influence on the transfer function of this topology. This means that a resistor may be connected between the faraday cage and ground to eliminate the effects of ion currents and space charge during field measurements.

Chapter 5

High Speed Optically Isolated Data Transmission System

5.1 Introduction

One of the main purposes for designing a capacitive sensor is to obtain a non-intrusive sensing device in the high voltage environment. It has been found that the sensor must be galvanically isolated from the environment so that the capacitive coupling of the sensor topology remains unaffected by the measuring instrumentation. A relatively high input impedance is also required so that very low frequency signals, where capacitive sensors exhibit a high Thévenin equivalent impedance, can be measured without distortion.

An alternative method, which has been used for low-noise measurements in HV environments, is the D/I principle [12, 31]. A very low resistive input impedance is used, resulting in differentiation of the measured quantity. The measured signal is then integrated to obtain a copy of the original waveform. The integration may be done using analogue instrumentation [12, 31] or digital methods [72]. This differentiator implemented by the termination resistor also imposes an upper frequency limit, which will determine the bandwidth of such a system.

For the current application, it was decided to use a high termination impedance in order to remain in the linear region. Special signal conditioning instrumentation was developed for the capacitive sensor as discussed in this dissertation. The purpose of this chapter is to describe the design and operation of this interface instrumentation used for the final measurements as presented in Chapter 7. The signal conditioning instrumentation and optical data transmitter is contained inside a faraday cage, which is designed and analysed as an integral part of the sensor topology. An optical receiver is also required to decode the data and interface with measuring instrumentation.

A general overview of the complete system is given in section 5.2. Section 5.3 contains a description of the transmitter subsystem. The optical link is discussed in conjunction with the digital subsystem of the transmitter. Section 5.4 contains the receiver subsystem's discussion. Conclusions and recommendations for future work are given in section 5.5.

5.2   Interface System Overview and Specifications

Figure 5.1 gives a block diagram overview of the complete instrumentation system. The system comprises two subsystems, namely the transmitter, which interfaces with the sensor and the receiver interfacing with the measuring instrumentation. These subsystems are interconnected via a fibre-optic cable.

The system topology given in Figure 5.1 represents a fairly unique approach in that conventional interfaces uses analogue optical technology [19]. The digitising approach facilitates improved versatility [72], linearity and controllability at the cost of power consumption and complexity. Overall, these features are expected to yield a superior sensor interface solution.
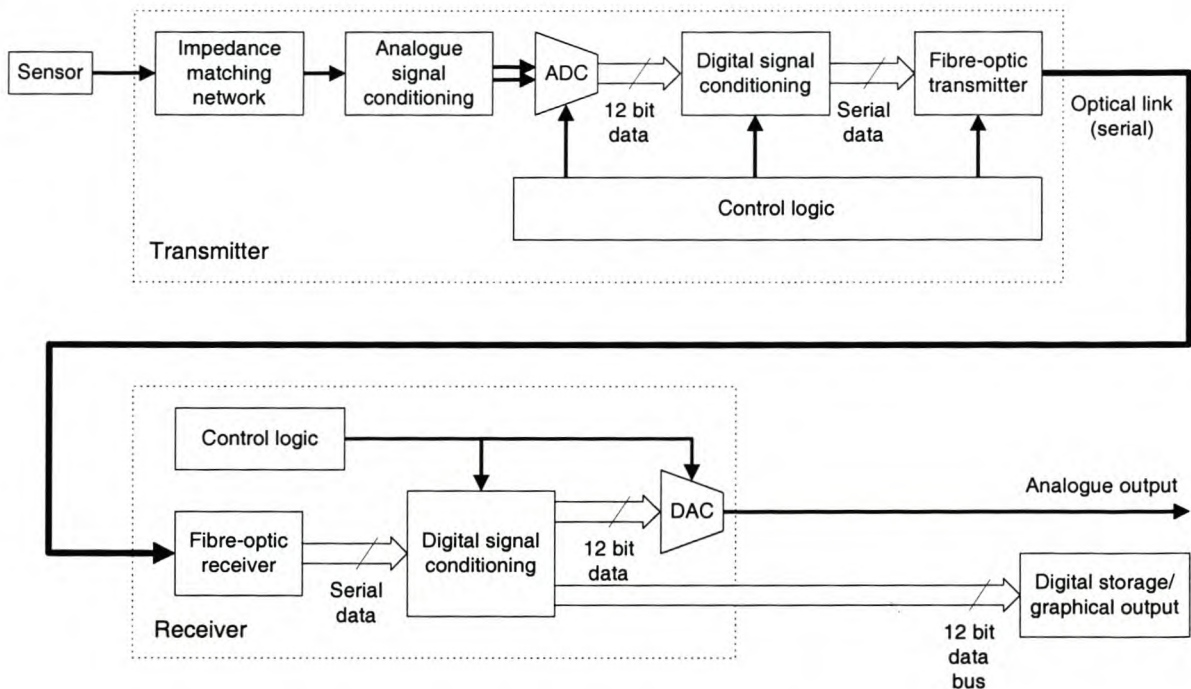
Figure 5.1: Block diagram of interface system

The analogue interface of the transmitter consists of the input impedance matching network and analogue signal conditioning circuitry, which scales and shifts the analogue signal to suitable levels for the Analog-to-Digital Converter (ADC). The digital data is encoded and serialised by the digital

signal conditioning, before it is transmitted serially by the fibre-optical transmitter. The control logic manages the analogue-to-digital conversion and encoding processes.

The receiver subsystem comprises the optical receiver, digital signal conditioning to convert the encoded serial data back to parallel and a Digital-to-Analogue Converter (DAC). Control logic is again required to manage the decoding and digital-to-analogue conversion processes.

The control logic for both subsystems are implemented in Erasable Programmable Logic Devices (EPLDs). Data can be transmitted using two modes, either 12 bit accurate at 5 MHz sampling frequency or 8 bit accurate at 10 MHz sampling frequency. The sampling frequency for either mode is limited by the serial transmission speed of the optical fibre link.

In the 8 bit mode, this enables the instrumentation to capture at least 10 data samples on the rising edge of a standard lightning impulse, which is considered adequate for good signal reproduction. The trade-off between resolution and speed was also considered acceptable for the 12 bit mode, where about 5 data samples will be measured on the rising edge of the standard lightning impulse.

The specifications, which were set and achieved for the instrumentation are listed below:

- 12 bit resolution at 5 MHz sampling speed or 8 bit resolution at 10 MHz sampling speed

- Bandwidth ranging from less than 1 Hz to 1 MHz with the anti-aliasing filter or up to approximately 6 MHz with the filter bypassed

- Gain variation of less than 2 % over the bandwidth range

- High input impedance, $\gg 10$ MΩ without termination resistor

- ± 1 V input range

- Galvanic isolation is maintained

5.3 Transmitter Design

5.3.1 Analogue signal conditioning and analogue-to-digital conversion

The transmitter shown in Figure 5.1 consists of the impedance matching network, analogue signal conditioning, ADC, the digital signal conditioning and an optical fibre transmitter. Figure 5.2
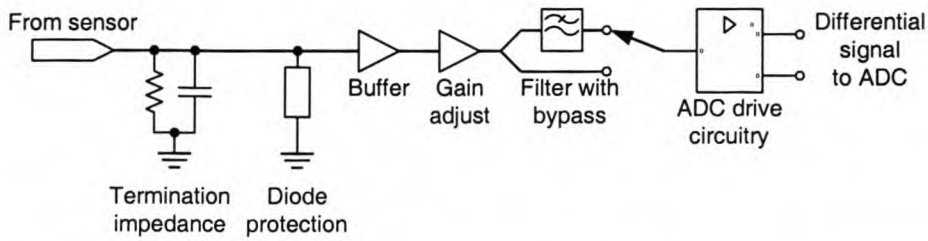
Figure 5.2: Diagram of impedance matching network and analogue signal conditioning components

shows a more detailed diagram of the impedance matching network and the analogue signal conditioning circuitry. The entire circuit is insulated with respect to the faraday cage in which it is housed and therefore it was not necessary to use a differential amplifier at the input stage.

The impedance matching network comprises the termination impedance as well as the input protection circuitry. The termination impedance consists of a parallel combination of a resistor and capacitor. The termination capacitor forms a capacitive voltage divider with the capacitive Thévenin equivalent impedance of the sensor. The value of the capacitor is therefore chosen to determine the voltage attenuation required for a specific sensor. The resistor value is chosen so that the low frequency pole formed by the parallel combination is low enough not to influence the frequency response of the sensor and instrumentation combination significantly.

In order to protect the input circuitry against excessive input voltages, several diodes are placed in anti-parallel as shown in Figure 5.3. Diodes with a very sharp 'knee' are used, i.e. the transition between "off" and "on" occurs across a very small variance in the applied voltage. This means that the input impedance will remain very high until the voltage across these diodes exceeds the on-state threshold, causing the diodes to start conducting. Eight diodes were used in total, 4 in each leg, resulting in a DC small-signal impedance of approximately 10 MΩ . This was considered adequate for use with most practical capacitive sensors. The effects of the diode protection circuit on the input impedance at high frequencies is, contrary to expectation, not a trivial issue and was the subject of extensive practical and theoretical investigations to find this particular solution. R_s is a small resistor in series with the input, which ensures that the protection scheme functions adequately even for an input source with a low output impedance.

The next stage is the buffer, which must provide a very high input impedance over the entire frequency range of interest, so that the overall input impedance is determined by the termination impedance. An N-channel JFET input operational amplifier with unity gain bandwidth of 16 MHz was used. The input impedance is specified as 10^{14} Ω //4 pF, which is more than adequate. Other components on the transmitter have much higher bandwidths so that the overall bandwidth of the system is limited by either the input buffer or the anti-aliasing filter.
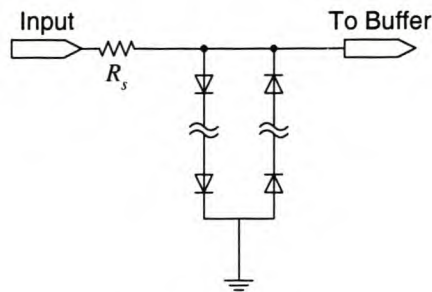
Figure 5.3: Generic configuration of anti-parallel diodes used for input protection of the transmitter

The buffer stage is followed by an adjustable gain stage. Jumper settings allow for three different gains to be selected, namely unity, 5 times or 10 times. Each of these gains can be calibrated separately.

The anti-aliasing filter was designed using a single Sallen-Key biquad section. The component values were chosen according to the Bessel-Thompson criterion. It is possible to bypass this filter for low-frequency applications, where aliasing will not take place.

The ADC requires a common mode voltage of 2.25 V at its differential inputs. Specific drive circuitry is used to achieve this offset and scale the input for maximum resolution. The configuration shown in Figure 5.4 is used to convert a single-ended signal to a differential signal with an offset of 2.25 V as required by the ADC. The common mode reference voltage supplied by the ADC is buffered via op-amp X_3 before adding to each leg of the instrumentation amplifier.

DC offset tuning was also incorporated into this section, which is used to calibrate the overall circuit's offsets.

The signal conditioning circuitry was simulated using PSpice®. Figure 5.5 shows a comparison of the measured and simulated transfer function of the analogue part, including the anti-aliasing filter, for the frequency range from 1 Hz to 2 MHz. These measurements were done with 1 V_{peak} and 0.5 V_{peak} inputs respectively. These voltages represent full- and half-scale input values and demonstrate that the transfer function does not depend on the voltage magnitude.

The maximum difference between the simulated transfer function and the measured transfer function occurs between 50 kHz and 500 kHz, but is always less than 1.7 %. This is of the same order as the accuracy of the measuring instrumentation that was used. The -3 dB point of the filter was designed for 1 MHz and is measured at 975 kHz. The dotted line indicates the -3 dB level. The mean deviation between the measured and simulated transfer functions is +0.5 %.

Figure 5.6 shows the measured and simulated transfer function of the analogue signal conditioning with the anti-aliasing filter bypassed. In this case, the ADC driving circuitry is connected directly
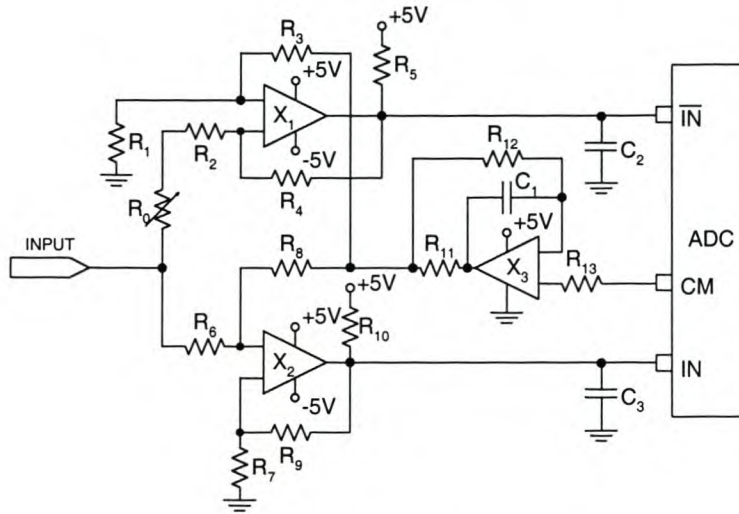
Figure 5.4: ADC driving circuitry [73]

to the gain adjust section. The input impedance of the ADC driving circuitry is lower than the input impedance of the anti-aliasing filter. This causes a drop in gain of approximately 0.9 dB when the filter is bypassed. This problem can be eliminated in future designs by introducing a buffer between the gain adjust- and ADC driving circuitry.

The simulated and measured transfer function compares very well, except at frequencies above 500 kHz. The output of the signal generator that was used, distorted significantly at the higher frequencies, which makes the measured transfer function in this region less accurate. The resonance peak is also steeper and located at a lower frequency than predicted. The deviation is attributed to the limited accuracy of the PSpice® models at higher frequencies.

5.3.2 Digital signal conditioning and fibre-optic link

Figure 5.7 shows the main functions of the digital signal conditioning subsection. Based on the mode selection, the digital signal conditioning controls the ADC clock speed, byte selection, data encoding and the conversion from parallel to serial data. The two modes used for data transmission influence the operation of the different blocks in Figure 5.7. Figure 5.8 shows the timing of 'DATA' at the input of the encoder and the SC/$\overline{D}$ (Special Character or Data) control signal for the two modes, namely the 8- and 12 bit mode.

The fibre-optic link is used in an asynchronous mode. The receiver requires an occasional synchronisation byte in order to accurately distinguish between the different bits. For the sake of simplicity, the synchronisation bytes are sent alternately with data. A multiplexer (MUX) is used
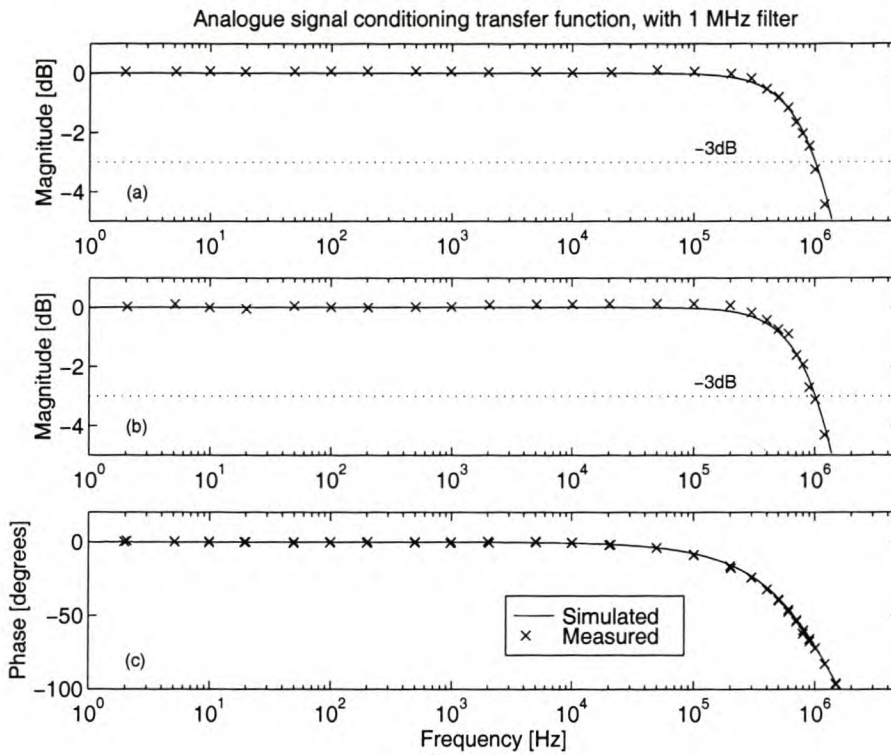
Figure 5.5: Measured and simulated transfer function for the analogue signal conditioning circuitry with the 1 MHz anti-aliasing filter inserted (a) Magnitude response for 1 V_{peak} input (b) Magnitude response for 0.5 V_{peak} input (c) Phase response

to select between the data and the synchronisation bytes.

For the 8 bit mode, the master clock of 20 MHz is divided by 2 so that the ADC may be clocked at 10 MHz. The main clock is a copy of the master clock and synchronises the transmission of the data and synchronisation bytes to the encoder and fibre-optic transmitter. The 8 most significant bits (MSBs) are selected by the 'Bit Selector' block for transmission and sent to the encoder alternately with the synchronisation byte. A special control line, namely SC/$\overline{D}$ is required by the encoder as data and special characters, of which the synchronisation byte is one, are encoded differently. The multiplexer alternately selects between the data from the ADC and the special character as is shown in Figure 5.8 (a).

The other two control lines are the enable line ($\overline{ENN}$) and the Built-In-Self-Test (BIST). $\overline{ENN}$ is active low to enable data encoding and transmission. BIST is used to test the fibre-optic link by transmitting a special series of data, which is recognised by the receiver on the receiver subsystem.

For the 12 bit mode, the master clock is divided by 4 so that the ADC may be clocked at 5 MHz. The main clock is still a copy of the master clock at 20 MHz. Now the 12 bit data must be divided into two bytes as only 8 bits can be encoded and transmitted at a time. The 8 MSBs are sent first and then the 4 least significant bits (LSBs) zero-padded to 8 bits. The sequence for the data
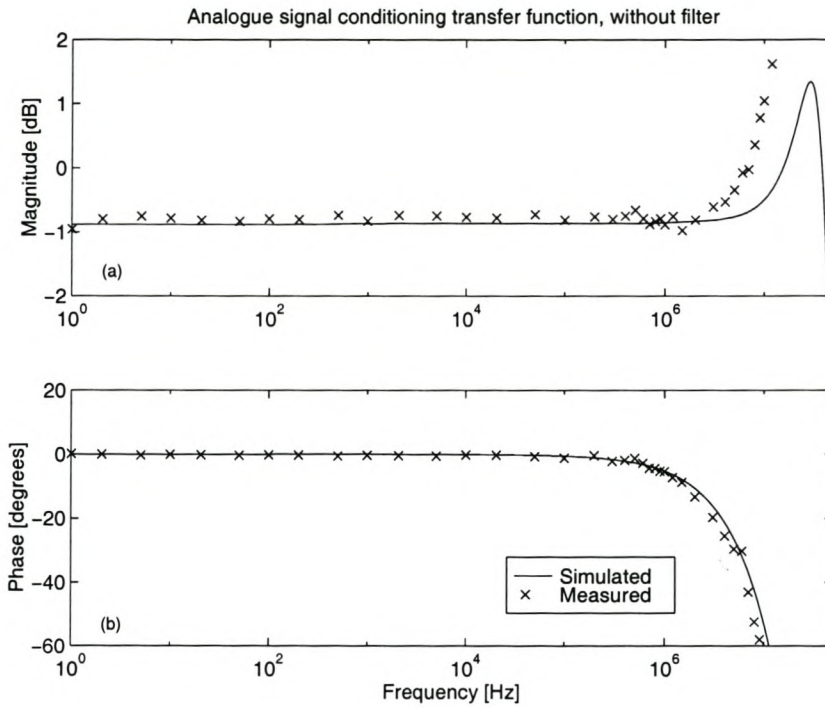
Figure 5.6: Measured and simulated transfer function for the analogue signal conditioning circuitry with the anti-aliasing filter bypassed (a) Magnitude response and (b) Phase response
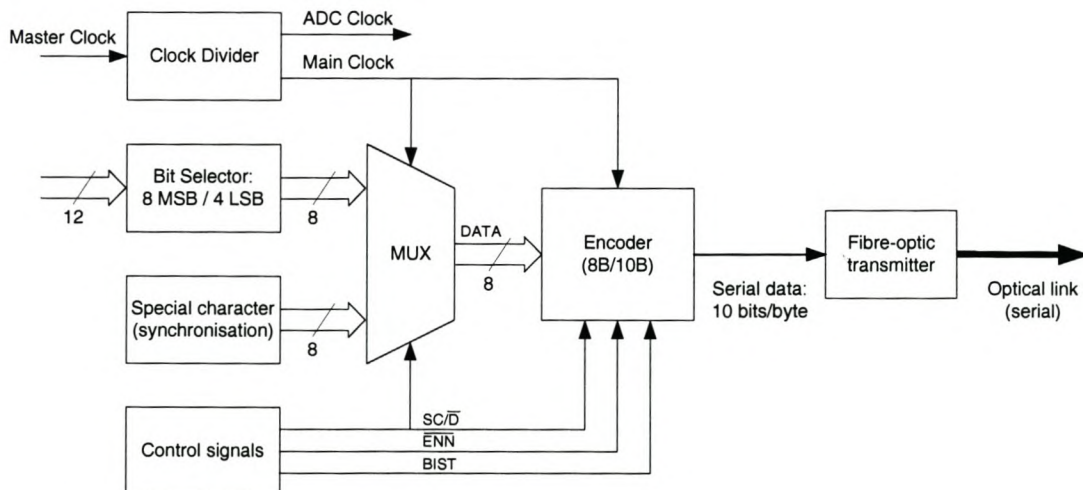
Figure 5.7: Main functions of digital signal conditioning subsection
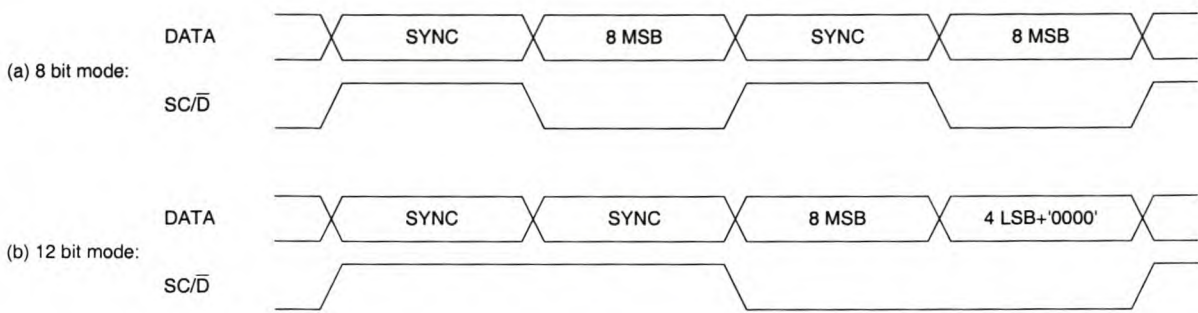
Figure 5.8: Timing diagrams of the 8 bit data at the encoder's input together with SC/$\overline{D}$ (special character or data) control line

transmission now starts with two synchronisation bytes and then the two data bytes as shown in Figure 5.8 (b). This enables the receiver to distinguish between the MSBs and LSBs of the 12 bit data.

A test mode is also available for testing of the complete digital conditioning subsystem and fibre-optic link. During this mode, the data from the ADC is ignored and a ramp signal generated internally for transmission in the same way as the ADC data is done otherwise.

The fibre-optical cable is a serial link and runs from components with a maximum speed of 266 Mbaud. Eight bits are sent across the link in packages constructed using the 8B/10B encoding scheme [74]. According to this scheme, the byte is mapped from 8 bits onto a 10 bit code and then serialised. The 8B/10B encoding scheme have two objectives, namely error correction and prevention of data-dependent jitter caused by baseline wander. Baseline wander occurs in AC-coupled signals, where the DC content of several consecutive '1s' or '0's prevents the receiver from distinguishing between consecutive bits when the series of '1s' or '0s' becomes too long. The 8B/10B encoding scheme ensures that no more than 5 consecutive '1s' or '0s' will be transmitted [74].

Due to the 8B/10B encoding, the byte speed of the link is 10 times lower than the bit speed of 266 Mbaud, which means the byte-speed of the link is 26.6 MHz. In the 8 bit mode, 2 bytes are transmitted for each data byte, which allow for 13.3 MHz data transmission and 4 bytes in the 12 bit mode allowing for 6.65 MHz data transmission.

The transmitter is powered from an alkaline battery pack and linear regulators. The high-speed digital components used in the transmitter are all high-power components. The total power consumption is on the order of 3 W, which is relatively high. This power supply is, therefore, only a temporary solution and not attractive for long-term operation. A switching power supply with rechargeable batteries should still be developed.

5.4 Receiver Design

The receiver shown in Figure 5.1 consists of the optical fibre receiver, the digital signal conditioning and a DAC. The data, which has been digitised and encoded by the transmitter, must now be decoded and converted back to analogue again by the receiver. Figure 5.9 shows a block diagram of the fibre-optic receiver and digital signal conditioning of the receiver subsystem.
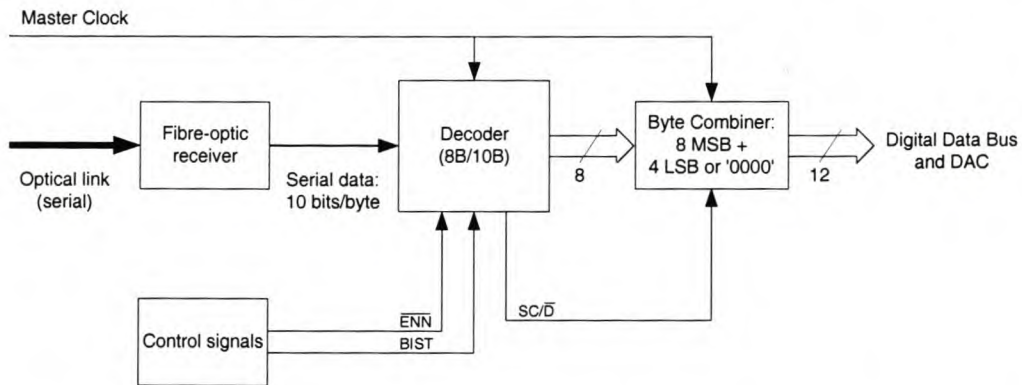
Figure 5.9: Block diagram overview of the optic receiver and digital signal conditioning of the receiver subsystem

The decoder receives the serial 10 bit data, decodes it according to the 8B/10B encoding scheme and outputs the 8 bit parallel data to the 'Byte Combiner' block. The SC/$\overline{\text{D}}$ signal is now generated by the decoder and thereby informs the combine block in which mode the system is running. If two synchronisation bytes were received consecutively, the next two bytes will contain first the 8 MSBs and then the 4 LSBs of the 12 bit data that is output to the digital data bus. The system is then running in the 12 bit mode. If only one synchronisation byte was received before the next data byte arrives, the system is operated in the 8 bit mode. These 8 MSBs are then zero-padded to 12 bits before being output to the digital data bus.

A 12 bit, 125 MSPS DAC is used and clocked by the processed clock from the control logic. It is a current output DAC, which requires a buffer to convert the current signal to a voltage signal. A wide bandwidth operational amplifier was used for this purpose. Provision has been made for calibration of the DAC/output buffer combination. This entails a zero-output from the EPLD for offset calibration and output of either +1 V or -1 V for calibration of the gain.

The control logic also communicates with the digital data bus, which may be used to combine several receivers for data download directly to a personal computer (PC).

As expected the overall transfer function is similar to that of the transmitter's analogue signal conditioning circuitry. Figure 5.10 shows a comparison between the measured transfer function for the analogue signal conditioning circuitry and the overall transfer function. The maximum

difference between the two measured transfer functions across the frequency range is less than 1.2 %.

There is a time delay of approximately 2.1 μs for signals processed by the transmitter and receiver due to the serial transmission process. This delay comprises the conversion time of the ADC and process time during the digital signal conditioning processes in the EPLDs of both the transmitter and receiver subsystems. Such a time delay manifests as a phase delay in the transfer function. Therefore, 2.1 μs was subtracted from the time difference of the overall transfer function, resulting in the phase response as shown in Figure 5.10 (b).
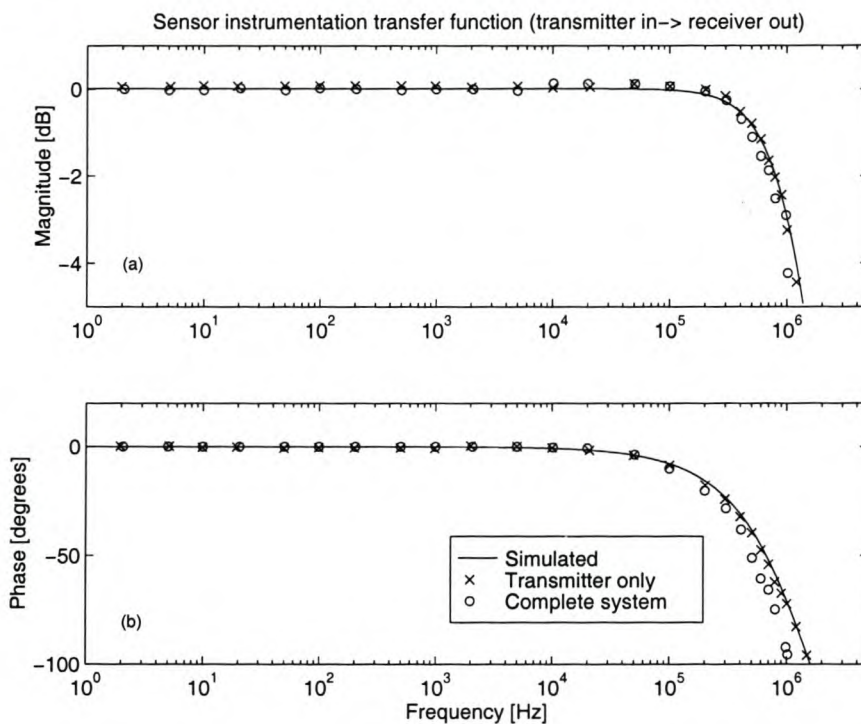
Figure 5.10: Overall transfer function of transmitter and receiver, (a) Magnitude response and (b) Phase response

5.5   Conclusions

This chapter has given a brief description of the optically isolated link, which was developed for use with the capacitive sensor. The instrumentation consists of a transmitter unit and a receiver unit, which are interconnected via a fibre-optical link. The transmitter located inside a faraday cage on the sensor has a high input impedance and transmits the digitised, encoded data via optical fibre. The receiver decodes the digital data and provides both an analogue and digital output.

Two modes of operation are available, namely a 12 bit, 5 MHz sampling mode and an 8 bit, 10 MHz sampling mode. The transmitter contains a removable anti-aliasing filter, which limits the analogue bandwidth to 1 MHz. If this filter is bypassed, an analogue bandwidth of 6 MHz is attained. The analogue signal conditioning circuitry on the transmitter ensures linear operation for half- and full-scale input voltages. The gain is flat to within 2 % across the entire bandwidth of the system.

The digitising and encoding approach is fairly unique and facilitates improved versatility, linearity and controllability for this interface instrumentation. Despite the increase in power consumption and complexity, the link provides a superior sensor interface solution.

Chapter 6

Sensor Evaluation: Arrangement and Procedures

6.1 Introduction

The modelling and analysis of four capacitive sensor topologies were discussed in Chapters 3 and 4, namely:

- The single element plate sensor

- The two-element parallel plate sensor

- The three-element parallel plate sensor

- The single element coaxial sensor

Equivalent circuit models were derived for each of these sensor topologies. Simulated time- and frequency domain responses were also generated for the three-element parallel plate sensor. The importance of galvanic isolation for proper operation of the sensors were stressed.

The following three different measuring arrangements were used during the course of the project:

- First trial measurements in a small enclosed HV area

- Second trial measurements in an open-air test site

- The final measurements for verification of the models and demonstration of the various design constraints in a large enclosed HV area

91

The problems experienced during trial measurements led to constraints being imposed on the final sensor and a suitable measurement area.

A background discussion of the initial tests and results will first be given in section 6.2. This section will also discuss the reasoning behind the subsequent adaptations to the interface instrumentation and sensor prototypes. The final measurement arrangement will be discussed in section 6.3 and is divided into three subsections discussing the laboratory geometry, excitation arrangement and the measuring instrumentation respectively. Section 6.4 gives a detailed analysis of the measurement uncertainties and their effects on the predicted sensor responses.

Section 6.5 contains a description of the procedures used to analyse and present the data. Different procedures are used for the time and frequency domain analysis and are discussed separately. Conclusions for the discussion on the trial measurements and final measurement arrangement will be given in section 6.6.

6.2 Preliminary Investigations

The initial measurements were all done with a two-element parallel plate capacitive sensor. A faraday cage for the instrumentation was added during the second initial measurements, but was neglected in the 2D numerical simulations. The three-element parallel plate sensor incorporates the faraday cage into the sensor in a balanced way and were simulated using the 3D software program.

6.2.1 First trial measurements

The literature review revealed a relative lack of information on the design, analysis and performance evaluation of open-air capacitive sensors for wideband transmission line voltage measuring applications. The project therefore commenced with measurements using a simple differential topology in a non-ideal test environment with the view to establish guidelines for a more sophisticated approach.

The first trial measurements were done in a relatively small space, where the floor area measured approximately 1.5×2.5 m. The scaled transmission line was 1.1 m above ground level and 2 m long. The differential sensor was a small piece of double-sided PCB; measuring 50×500 mm. A BNC connector was used to connect the sensor to a basic buffer amplifier. Tin foil was placed on the ground to form a ground plane measuring approximately 1.5×2.0 m. The sensor was placed on a cardboard structure approximately 100 mm high. Two-dimensional simulations were done for an approximation of expected results.

It is common practice to use scale models during testing and design processes in engineering [14, 75, 76]. Gerrard *et al* [14] has also shown that the electric field distribution remains the same if equal scaling is used for the size and voltages of a scale model. The objectives for this arrangement was:

- To verify whether the differential topology can work

- To determine the effect of the buffer instrumentation

- To find the sensitivity of the arrangement to parameters such as galvanic connections between the sensor and the environment involving the following:
    - Using different cables to connect the sensor and instrumentation, namely coaxial cable, twisted pair and shielded twisted pair
    - Varying the path traversed by the cable, namely arbitrarily hanging in the air or lying on the ground, as close to ground as possible or underneath the ground plane

- To evaluate the effect of boundary conditions

Variable frequency AC excitation was used to evaluate the voltage measuring characteristics of the sensor. All measured results exceeded predicted values, many by as much as 100 %. It was found that a large amount of coupling actually takes place to the cable itself. The cable also influenced the capacitive coupling between the transmission line and the different sensor elements, which would of course change the charge distribution on the sensor and hence the measured voltage. Two specifications for the instrumentation were derived from these results, namely that the sensor instrumentation should provide galvanic isolation of the sensor from the environment as well as that the input impedance must be very high so that the induced charge distribution on the plates is not disturbed too much.

The original simulations ignored any structures in the vicinity of the arrangement. Conductivity and permittivity parameters were unknown for these surrounding structures and therefore a conducting cage was built around the arrangement in order to have better defined boundary conditions. This improved the situation, but not to an acceptable level. Due to the fact that a relatively short transmission line was used, boundary conditions was found to have considerable effects.

The key conclusions from these measurements were:

- Dedicated optically isolated instrumentation had to be developed

- Instrumentation had to be integrated with the sensor inside a faraday cage

- A larger test area was necessary

Batteries would be used for the power supply and an optical fibre link to download the measured data to the measuring instrumentation at ground potential. Both these aspects are required to obtain galvanic isolation so that the capacitive coupling do not change from the ideal case. A larger test area would more closely approximate the two-dimensional case and boundary conditions would become less important.

6.2.2 Second trial measurements

The next set of measurements were done in an open-air test site using a ten times down-scaled version of the Cahora Bassa HVDC transmission line. The average height of 15 m was scaled down to 1.5 m and the line consisted of a bundle of 4 conductors, with 3 mm diameter, separated by 45 mm in a square formation. The test area and the transmission line was 12 m long. A 3.6 m wide ground plane was used. The closest wall to the arrangement was approximately 5 m away. A larger sensor was used as the instrumentation was larger. The single piece of double-sided PCB now measured 0.1×1 m. The faraday cage for the instrumentation was 35 mm high and connected to the top plate as shown in Figure 4.10. The sensor was now supported on 3 wooden blocks, also 100 mm high. Wood was chosen for its isolation properties, although this soon proved inadequate. Another problem with the wood was the non-unity relative permittivity there-of. This increased the capacitive coupling between the bottom sensor plate and ground.

Alternative support for the sensor was PVC tubes. The PVC had increased resistance and negligible effect on the capacitive coupling, but the surface areas attracted moisture and pollution, which lowered the resistance too much again. This was experienced in the early morning when condensation took place and caused water drops to form on the PVC surface. The measured frequency response of the sensor topology, therefore, changed as the day progressed.

The excitation for this arrangement was also variable frequency AC waveforms as well as impulse waveforms. Due to the above-mentioned aspects of support structures, these measurements were not repeatable and of questionable accuracy.

The following conclusions were derived from the results of these initial measurements:

- A three-dimensional package should be used for simulation as the two-dimensional package does not seem to give satisfactory accuracy

- A differential sensor with an integrated faraday cage should be used and the cage should be included in electric field simulations to test the added benefits as discussed in Chapter 4

- The effects of non-ideal elements, such as resistance between the bottom plate of the sensor and ground was highlighted and should be investigated under controlled conditions

- A suitable contained test area with well-defined boundary conditions were required

The final measurements as presented in this dissertation were evolved from the experiences described above. A controlled environment were selected for the final measurements, which could be simulated accurately using a three-dimensional package. The additional non-ideal components could also be added in a controlled manner to evaluate their exact influence on the sensor topology. The instrumentation remained unchanged as the original goal of galvanic isolation and very high input impedance had already been achieved.

6.3   Measurement Arrangement for Final Measurements

6.3.1   Laboratory Geometry

The final measurements as discussed in this dissertation, were done inside the high voltage laboratory. The floor dimensions of this laboratory is $12 \text{ m} \times 14 \text{ m}$ and the height is 18 m. A wire mesh is built into the walls and connected to ground, which forms a faraday cage for the laboratory. This cage provides shielding for electromagnetic noise entering as well as leaving the laboratory. The size of the mesh is unknown and, therefore, the frequencies, which may enter or leave the laboratory could not be determined.

Figure 6.1 shows a cut-away view of the arrangement inside the laboratory. The origin for distance measurement is indicated by the 'O' and axis indication in the center back wall. A typical transmission line structure was rotated through $90°$ so that the line was aligned vertically instead of horizontally, so that the z-direction indicates the height of the HV laboratory and the length dimension of the transmission line. The ground plane, sensor and transmission line are all centered in the laboratory at $y=0$.

Although not shown in Figure 6.1, the floor of the laboratory is very cluttered with equipment. A suitable space free of conducting objects were available from approximately 4 m above ground level and higher, which could be used for the final measurements. A well-defined ground plane was constructed from several strips of double-sided sisalation[1] and suspended 1.2 m in front of the back wall. The sisalation ground plane measured $8.72 \text{ m} \times 11.15 \text{ m}$. Weights along the bottom edge were used to smooth the ground plane as much as possible.

---

[1]Sisalation is a rough material with a layer of aluminium on either one or both sides.
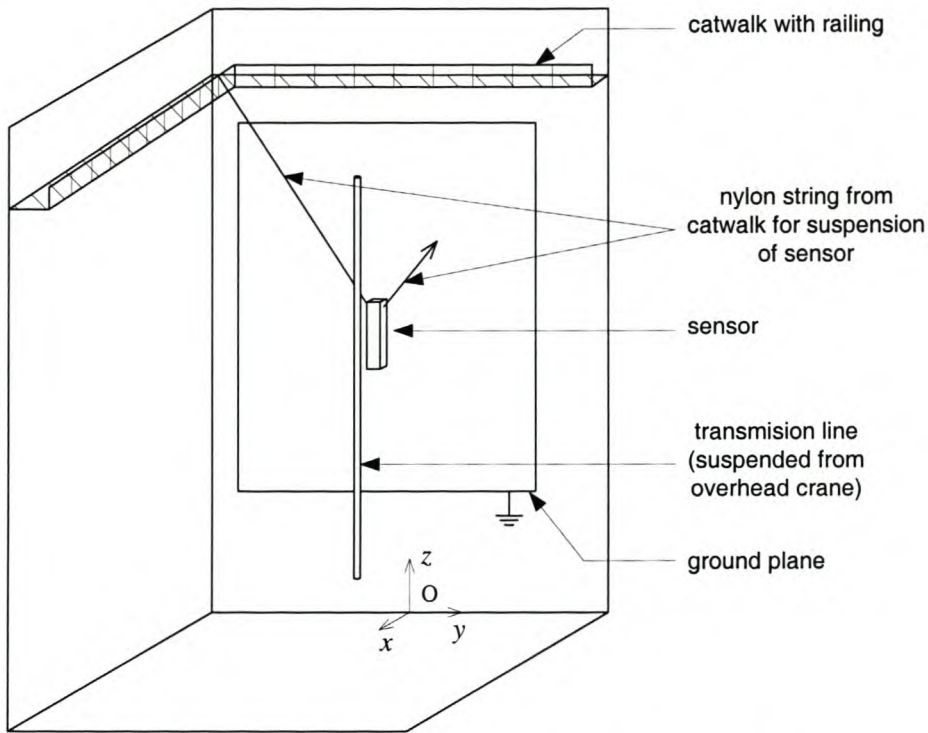
Figure 6.1: Cut-away view of measuring arrangement inside high voltage laboratory showing the ground plane, transmission line suspended from the overhead crane and the sensor suspended using nylon string from the catwalk

The transmission line bundle is the same as for the second trial measurements and was suspended from the overhead crane for easy adjustment of line distance from ground plane, i.e. in the x direction. The line was 12 m long and the distance from the ground plane varied between 1.5 m and 3.0 m. The conductors have 3 mm diameter and were arranged in a square of 45×45 mm and kept in place with spacers at 2 m intervals along the length of the line. The transmission line was excited using a high voltage construction kit, which can be used to generate both 50 Hz AC and different impulse signals.

The sensor, which was used, consists of two pieces of double-sided PCB. A faraday cage for the instrumentation was constructed between these PCBs plates using aluminium clad PMMA[2]. The aluminium connects the inner plates of the PCB together so that three different electrodes are formed, namely the top and bottom plates and the cage. The construction is shown in Figure 6.2. The sensor is suspended from the catwalk railing using nylon strings as shown in Figure 6.1 and was positioned 1 m in front of the ground plane.

---

[2]Polymethylmethacrylic. Commonly known as Perspex
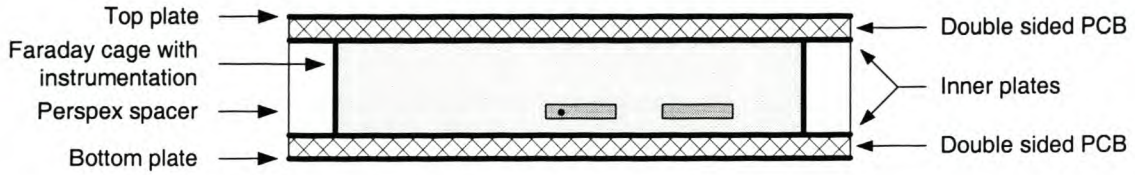
Figure 6.2: Sectional view of the three-element parallel plate sensor construction

6.3.2   Excitation Arrangement

Two types of impulses, namely fast and slow impulses, were used to excite the system. The basic circuit diagram for the impulse generation is shown in Figure 6.3.

R_m is a measuring resistor and is large enough not to load the transformer significantly. The series and parallel combination of C_{2a}, C_{2b} and C_{2t} forms capacitor C_2. The rising edge of the impulse is determined by the charging of capacitor C_2 (or parallel combination of C_{2a} and C_{2b}) through resistor R_1. The fall characteristics are determined by the discharge of C_2 through R_2.

The values of the circuit components used are listed in Table 6.1. The values listed in Table 6.1 gives a 10 %-90 % rise time for the slow impulse of approximately 90 μs, while the fast impulse is the standard 1.2/50 μs test impulse. The magnitude of the impulse is determined by the gap spacing, which is controlled by the operator.
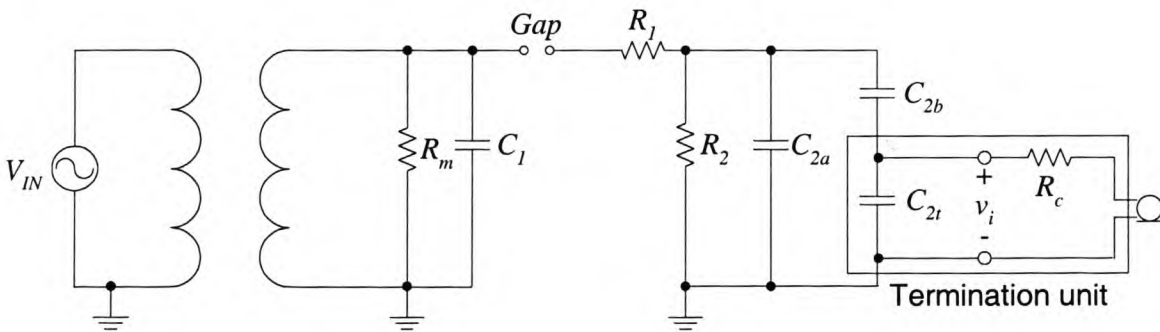
Figure 6.3: Circuit diagram of impulse source (R_c=75 Ω)

Resistor R_m is used to measure the magnitude of the rectified DC as well as to provide a discharge path for C_1. C_{2b} and C_{2t} forms a capacitive divider for the reference measurement of the impulse waveform with a division ratio of 100. The output of this divider can be connected to an oscilloscope to capture the impulse waveshape as the oscilloscope's input impedance is high enough not to load the divider significantly.

Simulated waveshapes for the slow and fast impulses respectively are shown in Figures 6.4 and 6.5.

Table 6.1: Component values for impulse generator

Component	Slow Impulse Value	Fast Impulse Value
R_m	140 MΩ	140 MΩ
R_1	50 kΩ	375 Ω
R_2	6100 Ω	6100 Ω
C_1	20 000 pF	20 000 pF
C_{2a}	10 000 pF	not used
C_{2b}	1 200 pF	1 200 pF

These graphs were obtained using the component values listed in Table 6.1 and were normalised with respect to the peak value. The graphs also include the simulated frequency content of each impulse, calculated using an FFT function. The -3 dB point of the amplitude spectrum is just above 100 Hz for the slow impulse and just above 1 kHz for the fast impulse.

6.3.3   Measuring Instrumentation

The measuring instrumentation comprise three components, namely the optical transmitter as integrated with the sensor, the receiver circuit and an oscilloscope.

The signal conditioning instrumentation and optical transmitter, which were incorporated with the sensor were discussed in Chapter 5. It consists of the following:

- An analogue amplifier with high input impedance ($\geq$ 10 MΩ)

- An anti-aliasing filter (with -3 dB frequency 1 MHz)

- Level-shifting circuitry and the analogue-to-digital converter (ADC)

- The optical transmitter

This instrumentation is housed inside the faraday cage of the sensor as shown in Figure 6.2. The prototype power supply is a battery pack with linear regulators, which is also placed inside the faraday cage. The buffer amplifier was used in the 12 bit/5 MHz mode as described in Chapter 5.

The receiver circuit consists mainly of the optical receiver and the digital-to-analogue converter (DAC). The data is available in both digital and analogue format, of which the analogue output was connected to the oscilloscope input. The receiver and oscilloscope was located inside an EMC cabinet close to the control panel of the high voltage construction kit.
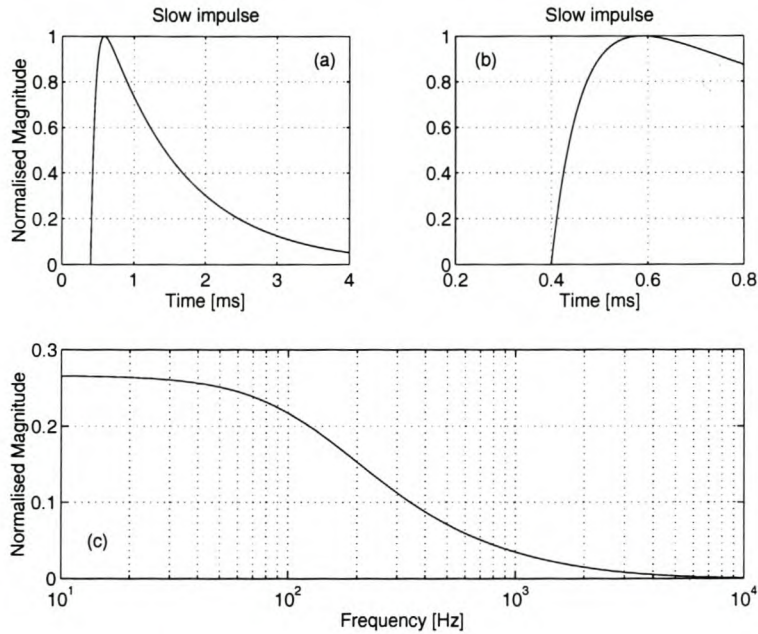
Figure 6.4: Slow impulse ideal time waveform and typical frequency content. (a) Slow impulse waveshape (b) Rising edge of slow impulse (c) Magnitude spectrum of slow impulse
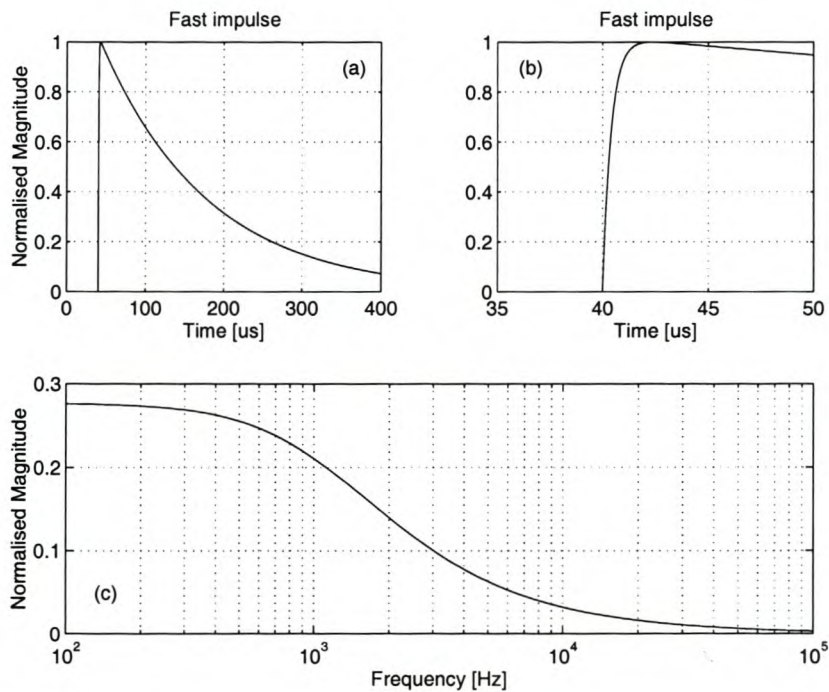
Figure 6.5: Fast impulse ideal time waveform and typical frequency content. (a) Fast impulse waveshape (b) Rising edge of fast impulse (c) Magnitude spectrum of fast impulse

The final measurements were done using a Tektronix TDS3032 digital oscilloscope. This oscilloscope has the following specifications:

- 9 bit sampling resolution

- 300 MHz analogue bandwidth

- Sampling frequency ≤ 2.5 GHz

- 10 000 data samples per trace per capture

The oscilloscope features two analogue filters that may be used to limit the bandwidth of the incoming signal, namely a 150 MHz or 20 MHz low-pass filter. All measurements were done with the 20 MHz filter inserted. All measurements were done on the DC coupling scale (i.e. any DC in the original signal will be displayed correctly). AC coupling adds a zero at a very low frequency, which may influence measured frequency components up to approximately 10 Hz. The oscilloscope's DC offset was calibrated before each set of measurements using the built-in function after the required 10 minute warm-up period.

6.3.4   Overview of test conditions

The final laboratory measurements were planned in order to demonstrate and quantify various effects found during the preliminary measurements. For this purpose several models were defined to model the effects of certain of the non-ideal loss terms. Figure 6.6 shows the equivalent circuit diagram for the three-element parallel plate sensor with the resistance between the transmission line and the sensing elements already ignored. The connection of the interface instrumentation is shown via the termination resistor, R_t and capacitor, C_t. The default model approaches the ideal case, where all resistors, except the termination resistor may be ignored. The single element coaxial sensor has a much simpler equivalent circuit. Therefore, the only non-ideal element is the termination resistor.

For the three-element parallel plate sensor, the resistance between the sensor elements and ground as well as between the different sensor elements themselves causes deviation from the ideal behaviour, especially for low frequency signals. The following models were defined to test the effect of each resistor:

(1) Default model - only capacitances are included in the model

(2) R_{s1g} model - add a single resistor from the top plate to ground to the default model
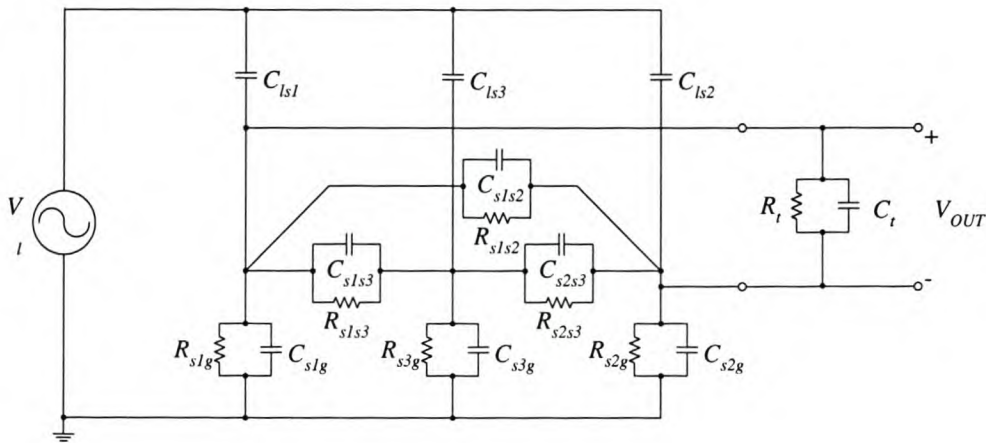
Figure 6.6: Three element sensor equivalent circuit with added termination resistor and capacitor parallel impedance

(3) R_{s2g} model - add a single resistor from the bottom plate to ground to the default model

(4) R_{s3g} model - add a single resistor from the faraday cage to ground to the default model

(5) R_{s1g}/R_{s2g} model - add two resistors to the default model, one each from the top and bottom plate to ground

(6) R_{s1s3}/R_{s2s3} model - add two resistors to the default model, one each between the top and bottom plate and the faraday cage

Measurements were done with all the models except model number 2, the R_{s1g} model. The resistors that were used consisted of a series connection of several resistors in order to obtain a graded resistance approximation of a support structure. It was hoped that the addition of these resistors with conducting sections would not influence the field underneath the sensor significantly.

Equations for the different models were developed in order to simulate the sensor topology's response for the different model groups. These equations were discussed in Chapter 3 and Appendix C and are functions of the complex frequency, s. The capacitance values used in the models were obtained from the 3D simulation package.

The termination resistor and capacitor pair causes the cut-off of the lower frequencies as were discussed in section 4.3. Three different termination combinations were used for the measurements and are listed in Table 6.2 together with the -3 dB frequencies caused by the specific termination components.

For both the cases where a 10 MΩ resistor is used the -3 dB frequency is low enough that all

Table 6.2: Termination impedances used for the different measurement sets

Resistor Value	Capacitor Value	-3 dB Frequency
10 MΩ	30 nF	0.5 Hz
10 MΩ	10 nF	1.6 Hz
30 kΩ	10 nF	530 Hz

impulse measurements should be unaffected by this zero. The 30 kΩ termination removes a significant amount of low-frequency data and together with the R_{s2g} model will prove very useful in frequency response/parameter estimation routines.

Furthermore, the transmission line height was changed for different measurement sets, i.e. it was moved in the x direction. All measurements included slow and fast impulse inputs in a mostly 50/50 relationship. Impulse voltages with different peak values were applied to confirm voltage independence of the sensor transfer function.

The single element coaxial sensor measurements were done for only one termination impedance, namely 10 MΩ //40 nF. No other non-ideal components were added as the circuit model is very simple and does not practically allow for extra resistors to be added.

The separation distance between the transmission line and the earth conductor were varied for the single element coaxial sensor. Both slow and fast impulses and 50 Hz AC voltages were also applied with various peak values for this coaxial sensor.

6.4 Test Geometry Uncertainties and Sensitivity Analysis

Various factors may influence the accuracy of the measured results. These factors include the type of measurement as well as the geometrical and instrumentation accuracies.

The instrumentation error may be subdivided into two areas, namely the sensor interface instrumentation itself and the oscilloscope. Any errors due to the sensor instrumentation should be fixed, i.e. gain error, except for the discretisation, which should be negligible as a 12 bit ADC was used. From the practical measurements, this was found to be less than 0.5 % and was verified by several sets of measurements of the gain of the amplifier section, which was given in Chapter 5. Other errors introduced by the sensor instrumentation is discretisation noise, but in the 12 bit mode this amounts to ±0.05 %, which is negligible in comparison with all other errors already mentioned. This error may increase up to about ±0.5 % if only 10 % of full scale is used, which was the case for some measurements, but is neglected in further discussions.

The oscilloscope's discretisation noise at 9 bit accuracy amounts to ± 0.39 %. The overall gain accuracy of the oscilloscope is specified as ± 2 % in the datasheets and the discretisation noise is also neglected in further discussions as full scale was used for the measurements as far as possible.

Inaccuracies attributed to measurement type may be categorised as follows:

- Rise and fall-time characteristics of the applied impulse (slow or fast)

- Termination impedance

- Modelling of non-ideal resistive components

- Nominal height of sensor and transmission line

Ideally, the transmission line to sensor transfer function should be flat from DC to very high frequencies. The zero caused by the termination impedance cuts off the low frequencies and DC. The other modelling resistors add more poles and zeros at predominantly low frequencies, which may increase as the resistor values decrease. The trajectories of the poles and zeros have been discussed in Chapter 4.

Compared to the fast impulses, the slow impulses have more low frequency components, which are influenced by the above-mentioned poles and zeros. The overall effect is that the slow impulse waveforms are less accurate, especially if the exact values of the resistive terms are not known.

Test simulations were done with purely numerical examples to find the sensitivity of the output voltage to the addition of the other modelling resistors, namely R_{s1g}, R_{s2g} or R_{s3g}. 'Reference' and 'sensor' voltages were generated using the values of Table 6.1. The capacitance matrix for the sensor topology was taken from the 3D simulation results of the HV laboratory arrangement for a nominal main line height of 2.0 m or 3.0 m.

The 'sensor' voltage was generated using resistance values 5 % smaller than the ideal values, while the comparison voltage was simulated using the ideal values for the resistors. All capacitor values were held at the ideal values. The comparison simulations were done for the six possible configurations or model groups as listed in the beginning of section 6.5. The different termination impedances as used for the practical laboratory measurements were also compared (cfg. Table 6.2).

The percentage error for the fast impulses were practically zero in all cases except for two cases, namely when only one plate was connected to ground via an extra resistor and when a low resistive termination impedance is used. The percentage difference between an ideally simulated impulse

waveform and the lower resistance values are summarised in Table 6.3. As expected, the termination impedance with the small resistive value caused significant errors, both for the slow and fast impulse waveforms. It is clear that the slow impulse is more sensitive to these non-idealities in the model than the fast impulse.

The absolute error of the slow impulse tests should therefore be larger than the error for the fast impulse tests, but in a negative direction. An error in the calibration factor, which causes a fairly large mean error will, therefore, result in a lower effective error for the slow impulse tests as will be shown in section 7.2.

If the results are to be divided according to model groups, the slow impulse errors should have a lower mean value for all model groups except for the R_{s2g} model group. This will also be verified in section 7.2. The positive error of the R_{s2g} model group may cause the slow impulse mean error for the first two termination columns to be higher than the fast impulse mean error as no measurements were done for the R_{s1g} model (which would have lowered the slow impulse mean error).

Table 6.3: Sensitivity in terms of percentage error caused by non-ideal resistive values for impulse tests

$Z_t = R_t / / C_t$	Slow impulse						Fast impulse		
	10 MΩ//30 nF		10 MΩ//10 nF		30 kΩ//10 nF		30 kΩ//10 nF		
Line Height	2.0 m	3.0 m	2.0 m	3.0 m	2.0 m	3.0 m	2.0 m	3.0 m	
Default model	-0.002	-0.002	-0.003	-0.003	-0.641	-0.641	-0.013	-0.013	[%]
R_{s1g} model	-0.273	-0.306	-0.274	-0.307	-0.805	-0.825	-0.017	-0.018	[%]
R_{s2g} model	0.344	0.387	0.342	0.385	-0.469	-0.450	-0.009	-0.008	[%]
R_{s1g}/R_{s2g} model	-0.011	-0.022	-0.013	-0.023	-0.647	-0.653	-0.013	-0.013	[%]
R_{s3g} model	-0.007	-0.012	-0.008	-0.013	-0.644	-0.647	-0.013	-0.013	[%]
R_{s1s3}/R_{s2s3} model	-0.002	-0.002	-0.004	-0.004	-0.642	-0.642	-0.013	-0.013	[%]

The R_{s1g}/R_{s2g} model is very sensitive to the relative size of the two resistors. This effect is demonstrated in Table 6.4, which shows the percentage difference for impulse tests done at a nominal height of 2.0 m. Once again the errors for the fast impulse tests are negligible except for the low-resistive termination, which is given as the last two columns of Table 6.4. If the unknown percentage of the two resistors is the same, the error remains of the same order than for the default- or R_{s3g} model. A 5 % unmodelled difference between R_{s1g} and R_{s2g} could increase or decrease the error to the same level as for the single resistor models, i.e. R_{s1g} model or R_{s2g} model.

The reason for the higher sensitivity for the case with a small resistive termination, namely 30 kΩ //10 nF, can be explained from the frequency transfer function. The low resistor causes the low-frequency zero to move high enough in frequency that some of the frequency components of the impulse is attenuated by this zero. This means that the effect of the two resistors from either plate to ground is mostly overshadowed by the termination resistor. Therefore, the difference between the

Table 6.4: Sensitivity in terms of percentage error caused by different values of the resistors between either plate and ground in the R_{s1g}/R_{s2g} model

$Z_t=R_t//C_t$		Slow impulse			Fast impulse	
		10 MΩ//30 nF	10 MΩ//10 nF	30 kΩ//10 nF	30 kΩ//10 nF	
$R_{s1g} \times 1$	$R_{s2g} \times 1$	-0.002	-0.003	-0.640	-0.013	[%]
$R_{s1g} \times 1$	$R_{s2g} \times 0.95$	0.293	0.291	-0.428	-0.009	[%]
$R_{s1g} \times 0.95$	$R_{s2g} \times 1$	-0.305	-0.306	-0.859	-0.017	[%]
$R_{s1g} \times 0.95$	$R_{s2g} \times 0.95$	-0.011	-0.013	-0.647	-0.013	[%]
$R_{s1g} \times 0.95$	$R_{s2g} \times 0.90$	0.315	0.314	-0.412	-0.009	[%]
$R_{s1g} \times 0.90$	$R_{s2g} \times 0.95$	-0.348	-0.349	-0.890	-0.018	[%]
$R_{s1g} \times 0.90$	$R_{s2g} \times 0.90$	-0.022	-0.023	-0.655	-0.013	[%]

default model error and the other models errors is smaller than for the higher resistive terminated sensor.

The errors for measurements at a nominal height of 3.0 m are spread over a wider range than the measurements at 2.0 m. The coupling capacitances from the transmission line to the sensor is smaller, namely C_{ls1}, C_{ls2} and C_{ls3}, while the added components' values remain the same. This means that the poles or zeros will move higher in the frequency band, which means percentage change in output voltage will be more than for the 2.0 m case.

Additionally, the accuracy of measurements at a higher transmission line height should increase as the absolute change of capacitances becomes relatively smaller as the nominal distances increase. This means that the geometrical positioning becomes less crucial at the higher transmission line heights. This is verified by the results of Tables 6.5 and 6.6.

The geometry accuracy is discussed for the following separate as well as combined positioning variations:

- Absolute position of sensor
  - Height above ground plane
  - Centering relative to ground plane and laboratory

- Absolute height of transmission line
  - Height above ground plane
  - Centering relative to ground plane and laboratory

- Movement of ground plane relative to stationary sensor and transmission line

The accuracy of the measured results may be quantified in terms of the instrumentation accuracy as well as the geometrical positioning accuracy. The influence of the dimensions of the measuring

arrangement can be found from Tables 6.5 and 6.6. These simulations were done for relatively big displacements to find the worst case scenario.

A few separate simulations were run to determine the sensitivity of the capacitance parameters to the geometry of the arrangement, e.g. the sensor or line height or even for movement of the ground plane. The differences are summarised in Tables 6.5 and 6.6. Row 1 lists the element. The other rows list the percentage change from nominal for specific changes in geometry. Rows 2 and 3 had the ground plane swinging around, i.e. the bottom edge moved either 10 cm forward or 10 cm backward, with the backward (further from sensor) values listed in row 2. For row 4 and 5 the sensor was moved 5 cm closer to the, now stationary, ground plane and 5 cm away from the ground plane respectively. Finally for rows 6 and 7 the transmission line was moved 5 cm closer to the sensor or 5 cm away from the sensor.

The values of C_{s1s3} and C_{s2s3} remain almost constant. The Thévenin equivalent impedance depends mostly on these two capacitances, therefore, the change in Z_{TH} is also 0 to two decimal places. These three elements are therefore, omitted in the above tables as all values are 0.00 %.

Table 6.5: Percentage change in capacitance parameters for the h_l=2.0 m arrangement with small variations in some of the geometry distances

Element	C_{ls1} [%]	C_{ls2} [%]	C_{ls3} [%]	C_{s1g} [%]	C_{s2g} [%]	C_{s3g} [%]	C_{s1s2} [%]	V_{OUT} [%]
Ground plane (10cm →)	0.84	3.55	1.74	-1.13	-1.86	-1.43	0.65	-1.40
Ground plane (10cm ←)	-0.89	-3.73	-1.83	1.23	2.08	1.57	-0.72	1.50
Sensor (5cm →)	-5.11	-6.36	-5.14	2.17	2.07	1.88	-0.45	-3.28
Sensor (5cm ←)	5.49	6.49	5.34	-2.09	-1.91	-1.83	0.35	3.63
Line (5cm →)	4.72	3.20	3.74	-1.08	-0.19	-0.49	-0.25	5.01
Line (5cm ←)	-4.32	-3.04	-3.51	1.02	0.21	0.44	0.22	-4.55
Ground & Line (← & →)	3.83	-0.60	1.88	0.15	1.89	1.07	-0.97	6.58
Ground & Line (→ & ←)	-3.48	0.44	-1.80	-0.12	-1.64	-0.98	0.88	-5.88
All variables (←, → & ←)	9.83	6.21	7.56	-2.09	-0.23	-0.86	-0.58	10.61
All variables (→, ← & →)	-8.20	-5.63	-6.64	1.91	0.24	0.77	0.48	-8.85

The sensor could be replaced in the same position very accurately, as it was suspended from the top balcony using nylon string. However, the absolute position of these strings may have differed from the ideal simulated case. The reason for this is that all measurements were done relative to each other and not relative to a single fixed reference point. For a 2 cm placement error of the sensor in the positive error direction, the anticipated error is approximately 1.45 % ($3.63 \times \frac{2}{5}$).

For a 5 cm deviation of the transmission line height, the error may vary by as much as ±5 %. The positioning of the transmission line was done with great care and time was allowed for the line to hang completely still after any displacement thereof. The accuracy of line height is, therefore,

Table 6.6: Percentage change in capacitance parameters for the h_l=3.0 m arrangement with small variations in some of the geometry distances

Element	C_{ls1} [%]	C_{ls2} [%]	C_{ls3} [%]	C_{s1g} [%]	C_{s2g} [%]	C_{s3g} [%]	C_{s1s2} [%]	V_{OUT} [%]
Ground plane (10cm →)	1.32	4.20	2.28	-1.02	-1.73	-1.29	0.70	-1.31
Ground plane (10cm ←)	-1.38	-4.37	-2.39	1.11	1.94	1.42	-0.78	1.38
Sensor (5cm →)	-3.75	-6.13	-4.49	1.42	1.86	1.53	-0.67	-1.45
Sensor (5cm ←)	3.85	6.22	4.56	-1.34	-1.72	-1.45	0.60	1.52
Line (5cm →)	2.65	2.33	2.46	-0.43	-0.12	-0.24	-0.04	2.79
Line (5cm ←)	-2.54	-2.25	-2.37	0.40	0.12	0.24	0.04	-2.65
Ground & Line (← & →)	1.24	-2.11	0.03	0.68	1.82	1.19	-0.82	4.22
Ground & Line (→ & ←)	-1.24	1.87	-0.13	-0.62	-1.60	-1.06	0.74	-3.92
All variables (←, → & ←)	5.27	4.33	4.79	-0.75	-0.10	-0.37	-0.15	5.78
All variables (→, ← & →)	-4.83	-4.05	-4.44	0.71	0.08	0.35	0.13	-5.31

expected to be on the order of 1 cm, which may introduce an error of not more than ±1 % for a nominal line height of 2.0 m.

It was found that the ground plane did swing around at times, most probably due to some wind entering the laboratory. The deviation was estimated to be approximately 10 cm to both sides. From Table 6.5, the possible deviation in measurement may amount roughly to ±1.5 %.

For a higher line, at for example a nominal height of 3.0 m, the expected deviation will be less. All values are approximately halved for the 3.0 m case from the 2.0 m case as can be seen when comparing Tables 6.5 and 6.6. The only exception is when only the ground plane is moving, where the percentage deviation is almost the same as for the 2.0 m case. The sensor, therefore, seems to be equally sensitive to ground level changes, regardless of the transmission line's height, for the sensor at a certain height, because the sensor was relatively high, i.e. h_s/h_l ¿ 10 %.

These errors are added together in order to get an error band indication as shown in Table 6.7. 5 % of the total error is subtracted from the average of the total error as listed in Table 6.7 as the error dependency of Tables 6.5 and 6.6 is not linear. The expected error for the 2.0 m line height measurements is therefore, 0.82 %±5.35 % and 0.36 %±4.47 % for the 3.0 m line height measurements. The average band between the 2.0 m and 3.0 m line height measurements is ±4.91 % and due to averaging of the mean errors, it is hoped that all errors will lie within this band from the overall mean error.

For any single measurement set, only the instrumentation errors and swinging of the ground plane need to be taken into account as all the other factors remain constant. Two exceptions to this statement exist, measurements using the R_{s2g} model and all measurements with the small resistive

Table 6.7: Possible peak measurement error percentages added together

Nominal Height [m]	Sensor Position [%]	Instrumentation		Ground Plane [%]	Line Height [%]	Total Error [%]
		Sensor [%]	Oscilloscope [%]			
2.0 m	+1.45	+0.50	+2	+1.50	+1.00	+6.45
		-0.50	-2	-1.40	-0.91	-4.81
3.0 m	+0.61	+0.50	+2	+1.38	+0.56	+5.05
		-0.50	-2	-1.31	-0.53	-4.34

termination (30 kΩ//10 nF). The increased error for these exceptions are caused by the unknown values of the added components, specifically R_t and R_{s2g}. The expected error limits per measurement set are listed in Table 6.8.

Table 6.8: Specific error limits for any given measurement set

Model/Termination	Line height [m]	Error bands [%]
All models	1.5	4.00
	2.0	3.95
	2.5	3.90
	3.0	3.85
R_{s2g} model	2.0	4.12
	3.0	4.15
30 kΩ //10 nF	2.0	4.28
	3.0	4.28

The three-element parallel plate sensor was built using undeveloped PCB. This has two drawbacks, namely that the dielectric substrate (FR4) may absorb moisture and become more conducting [24] and that the dielectric constant itself is not very predictable. A discussion for the lower resistivity of the dielectric substrate is implicit in the R_{s1s3}/R_{s2s3} model discussed above. A higher or lower dielectric constant than specified will cause a change in the sensor capacitance and hence the equivalent Thévenin impedance. The measured sensor capacitance, namely C_{s1s3} and C_{s2s3} is 28.25 nF.

The simulated value for C_{s1s3} and C_{s2s3} is 32.0 nF, which is 3.75 nF higher than the measured value. The mean error caused by this offset is tabulated in Table 6.9. It is clear that a higher termination capacitance lowers the sensitivity of the output voltage to such errors in sensor parallel plate capacitance. It is, therefore, desirable to add as much capacitance to the sensor as possible for an acceptable output voltage.

Two other factors also exist, which may influence the accuracy of the measurements, but were not quantified. The HV laboratory was not completely empty of other conducting objects and the main transmission line had a few kinks, remainders of being bent while stored.

Table 6.9: Mean error in output voltage caused by the parallel plate capacitance being 11.7 % too small

Termination capacitance	0 nF	10 nF	30 nF	50 nF
Error in output voltage	13.21	7.75	4.24	2.92

Simulations were done to test the addition of the horizontal bars in the laboratory used for hanging insulators etc. For these four floating metal objects, the influence is completely negligible. The expected scaling factor for the "ideal" case is 54.0499 μV/V, while the added bars change this scaling factor to 54.0547 μV/V; a difference of 0.01 %.

The effect of the twisted transmission line was not investigated. Both these factors may be investigated into more detail, but is neglected for further analysis in this dissertation.

6.5 Data Processing Algorithms

High voltage measurements typically suffer from problems such as induced noise, DC offsets introduced by the instrumentation, calibration problems, wide dynamic range and wide bandwidth requirements. It is also often not easy to define suitable criteria by which such measurement results can be qualified. This section therefore gives a detailed qualitative and quantitative description of how the measured results presented in this dissertation were processed and compared.

The raw waveforms were subjected to three basic processes before calculating the error or comparison criteria, namely the following:

- Removal of the residual DC offsets

- Removal of the delay introduced by the sensor interface instrumentation

- Removal of high frequency noise

Two waveforms were measured, namely the reference input voltage, which is denoted by v_i and the sensor voltage, which is denoted by v_m. A simulated sensor output voltage, labelled v_s, can be obtained from simulation of the system as described in Chapter 4 with the reference voltage as input signal. A reverse simulation is also possible to give v_l as comparison for the reference voltage, v_i.

Different types of comparisons between these signals were used in the time- and frequency domain to characterise the performance of the sensors.

6.5.1   Time domain analysis

Only capacitive dividers were used to measure the signals and therefore, any DC in the measured signals were added by the instrumentation. These DC offsets were minimised by calibrating all instruments carefully. Further DC calibration was performed for each set of measured waveforms using the following procedure:

- It was assumed that the pre-trigger flat part of the data is at zero potential

- The new waveforms were obtained by subtracting the average of this pre-trigger section from the original waveforms

Figure 6.7 shows the rising edges of a measured slow impulse before the DC offsets were removed. For some impulse measurements, an amount of trigger point noise was induced into the receiving circuitry as is visible in Figure 6.7. This noise, caused by the breakdown of the spark gap, is present on the sensor voltage as obtained from the instrumentation receiver circuitry, but is located before the above-mentioned time delay is over. It follows that it is induced into the receiver circuitry and will be ignored for further analyses. Figure 6.8 shows the rising edges and peak values of a fast impulse waveform after the DC offsets were removed. The definition for the peak error between the reference voltage, v_s and the measured sensor voltage, v_m is also indicated in Figure 6.8. The time delay of approximately 2.1 μs, which is caused by the interface instrumentation, is clearly visible.

This peak error is the percentage error between the absolute maxima, i.e. peak values, of the two waveforms and gives a first indication of the accuracy of the measurement and is defined as in equation 6.1:

$$e_p = \frac{v_{mp} - v_{sp}}{v_{sp}} \times 100 \tag{6.1}$$

where v_{mp} and v_{sp} denotes the peak values of v_m and v_s respectively.

A zoomed view of the reference and sensor voltages will show the amount of noise present, which may complicate the analysis of the data. A comparison between the amplitudes of the two impulse waveforms can be made if the amount of superimposed noise is the same for both of the measured signals.

Figure 6.9 shows a zoomed view of the measured impulse waveform peaks as well as the peaks of ideal impulse waveforms. These ideal impulse waveforms were calculated from the known component values and fit to the time and maxima of the measured signals. It is clear that there is a significant amount of noise present on the measured impulse waveforms. The percentage noise on the reference voltage, v_s, is approximately 1.5 %, while approximately 3 % noise is present on the
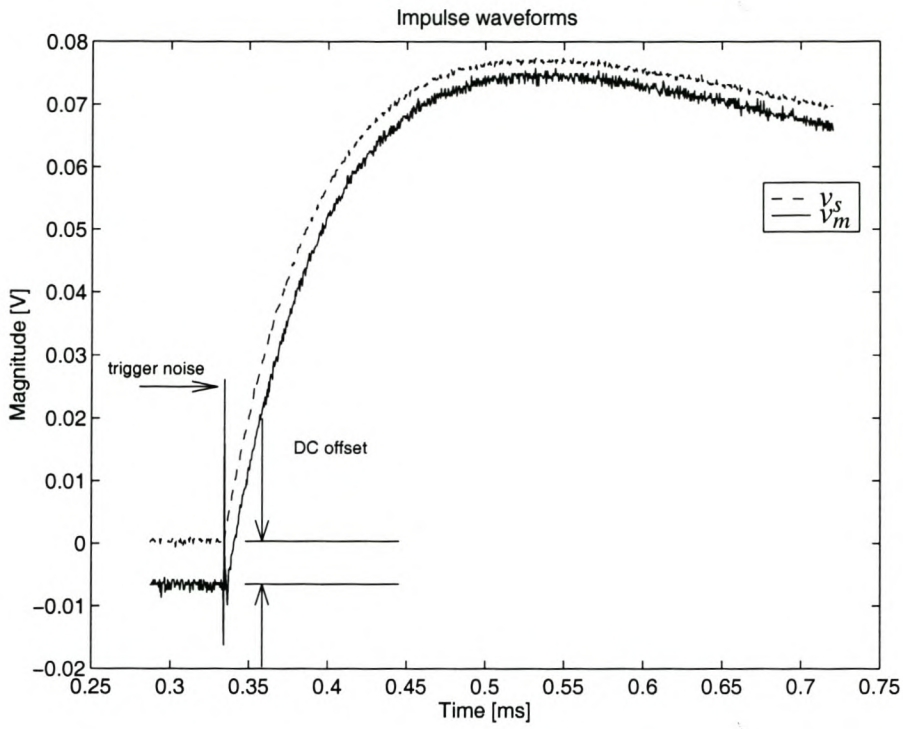
Figure 6.7: Figure showing the DC offset present in typical measured impulse waveforms as well as trigger point noise in the sensor output voltage
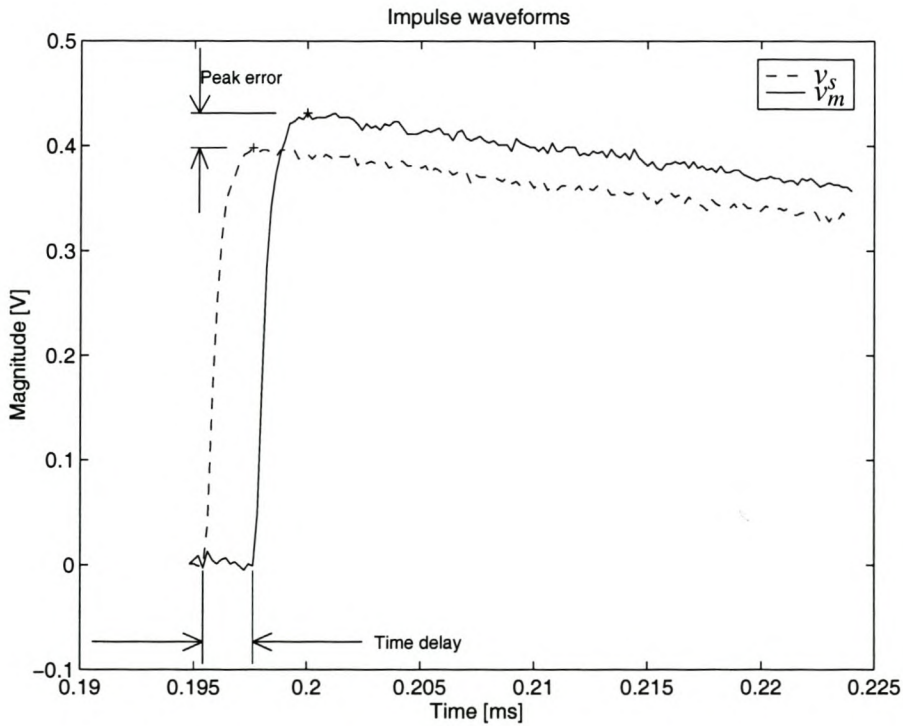
Figure 6.8: Graph of fast impulse showing magnitude error and time delay

measured sensor voltage, v_m. Waveform pairs exist where the noise percentage is approximately the same, but it cannot be assumed to be the same and therefore filtering is required for accurate comparison of the measured waveforms.
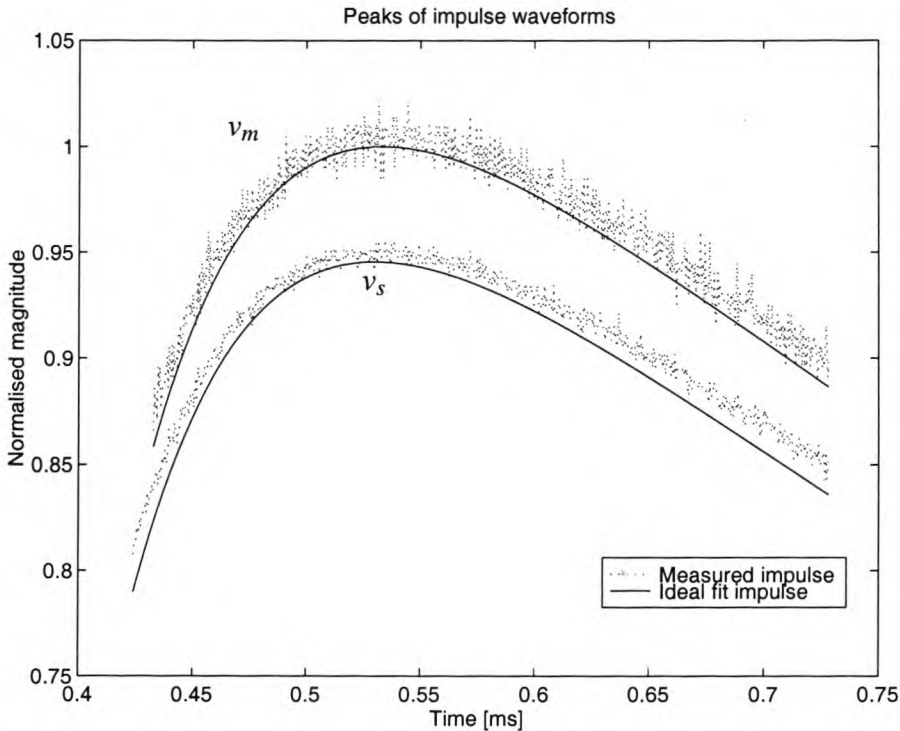
Figure 6.9: Graph of normalised measured waveforms and the expected ideal impulse waveforms

Two types of filters were used to attempt the removal of as much noise as possible. The two filters are a second order digital Butterworth filter and a moving average filter. The coefficients for the Butterworth filter was computed using Matlab®. The -3 dB frequency was chosen to remove noise, but very little of the frequency information of the signal itself. For the slow impulse waveforms, this meant a 100 kHz cut-off frequency while a 1 MHz cut-off frequency was used for the fast impulse waveforms. These frequencies were chosen to be well above the significant signal information as can be confirmed from Figures 6.4 and 6.5.

Figure 6.10 shows zoomed views of the peak of the measured sensor voltage and the two filtered waveforms. The dotted lines indicate the measured waveforms and the solid lines indicate the filtered waveform. The solid lines in Figure 6.10 (a) shows the measured sensor voltage and the waveform filtered using a 2nd order Butterworth filter. The second filter is a moving average filter, where the window length is chosen approximately equal to the rise time. The percentage error for the filtered waveforms is calculated in the same way as equation 6.1, where the maxima of the filtered waveforms are used. The moving average filter provides a much smoother filtered signal compared to the Butterworth filter. It is, therefore, expected that the moving average filtered signals will give the most accurate results.

The filtering of the fast impulse signals is less successful as shown in Figure 6.11. A window length of twice the rise time is required for adequate filtering as the noise and the rise time dynamics are of the same frequency order.
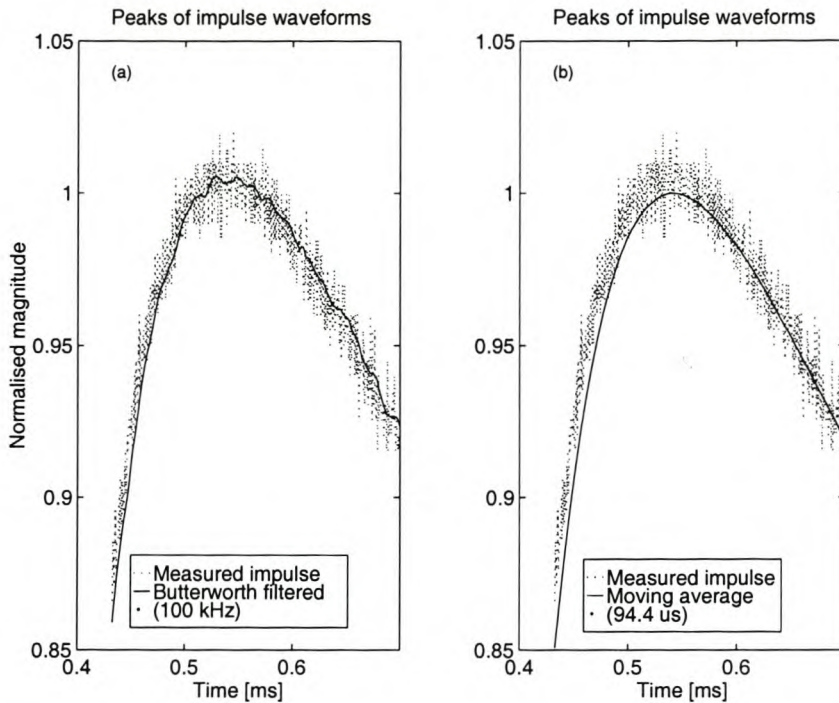
Figure 6.10: Figure showing peak of measured sensor impulse waveform together with filtered waveform (a) measured waveform and 2nd order low-pass Butterworth filtered waveform (b) measured waveform and moving average filtered waveform

Figure 6.12 shows a block diagram representation of the time domain data processing algorithms, where $G(s)$ is the predicted forward transfer function and $G^{-1}(s)$ the predicted reverse transfer function. The agreement between the measured sensor voltage, v_m, and the simulated sensor voltage, v_s, is defined in terms of the following:

- The peak error, namely e_{yp}

- The maximum error, namely e_{yx}

- The correlation coefficient when the signals are perfectly aligned, namely xc_y

The subscript y indicates how the signals were filtered according to the following legend:

- $y=u$ indicates that no filtering was used

- $y=b$ indicates that a Butterworth filter was used
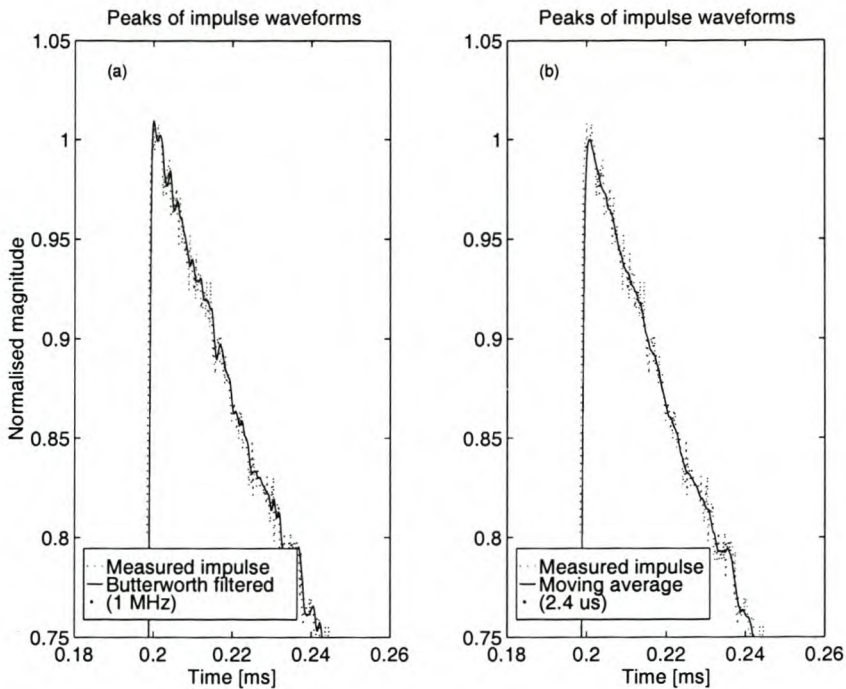
Figure 6.11: Figure showing peak of measured sensor impulse waveform together with filtered waveform (a) measured waveform and 2nd order low-pass Butterworth filtered waveform (b) measured waveform and moving average filtered waveform

- $y=m$ indicates that a moving average filter was used

Before continuing the discussion, it must be noted two situations exist, where the sensor voltage is an either completely or partially differentiated version of the reference voltage, i.e. a significant amount of DC is removed during the measurement process. These two situations are the low resistive termination, namely 30 kΩ //10 nF, and the R_{s2g} model. Impulse signals contain a significant DC component, which means that it is difficult to obtain the original waveform under these conditions. For this reason, the sensor voltages were compared using the forward simulation rather than the backward simulation.

The peak errors for the unfiltered and both filtered waveforms are calculated according to equation 6.1. An added subscript is used to differentiate between the waveform sets:

- e_{up} - peak error of unfiltered waveforms

- e_{bp} - peak error of Butterworth filtered waveforms

- e_{mp} - peak error of moving average filtered waveforms

The cross-correlation function can be used to obtain a numerical measure of the agreement between the two waveforms. The normalised cross-correlation function in Matlab® was used to compare
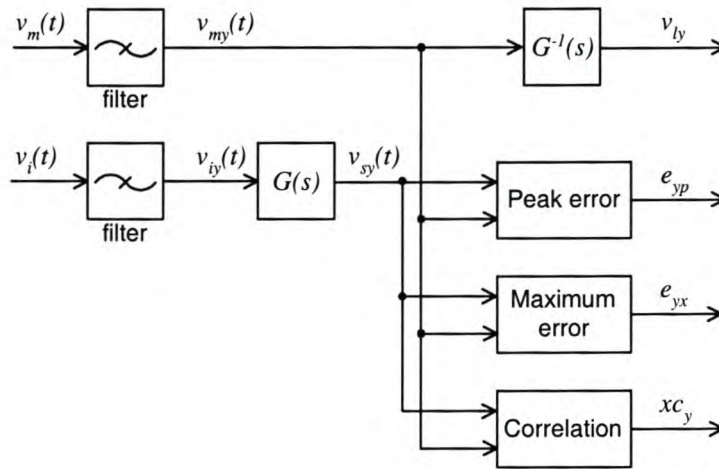
Figure 6.12: Block diagram representation of the time domain error calculation algorithms

the measured waveform, v_m, with the simulated waveform, v_s. The maximum value of the cross-correlation vector is called the correlation coefficient. According to Gerrard [55], a correlation coefficient of 90 % indicates a very good match between the two waveforms. The cross-correlation is indicated by xc_y, where the subscript $y = u, b$ or m indicates whether the unfiltered or filtered signals were compared.

Another useful feature of the cross-correlation function is that the maximum value gives an indication of the time delay between the two waveforms. This time delay was used to align the two waveforms in order to determine the maximum error between the two waveforms. The difference is referred to the simulated reference waveform peak value to get the error versus time as in equation 6.2:

$$e_y(t) = \frac{v_{my}(t) - v_{sy}(t)}{v_{syp}} \times 100 \qquad (6.2)$$

where y indicates which waveforms were used in the comparison and v_{syp} is the peak value of the simulated reference waveform.

The maximum of $e_y(t)$:

$$e_{yt} = max(e_y(t)) \qquad (6.3)$$

is the third measure of accuracy as defined in Figure 6.12.

It must be mentioned that the time delay is approximately 2.1 μs. In order to align the two waveforms accurately, the sampling interval must be equal to a factor of this time delay. The first available sampling frequency coinciding with such a factor is 10 MHz. The sensor interface instrumentation was used in the 5 MHz/12 bit mode, which means that the two waveforms can never be aligned perfectly and the maximum of the error versus time will always indicate an error that is too large. It is still regarded as a useful measure of the accuracy of the sensor measurement. It also shows the amount of noise present on the measured signals, as the unfiltered and both filtered

versions are compared. This aspect will be discussed further when the results are given in section 7.2.1.

It is expected that e_{up} will be the least accurate as none of the noise has been removed, while e_{mp} is expected to be the most accurate as the filtering provides a smooth output signal. The Butterworth filter -3 dB frequency was 1 MHz for the fast impulse waveforms, which is the same as the -3 dB frequency of the anti-aliasing filter on the sensor instrumentation. This causes a doubling of group delay for the sensor voltage, which may actually increase the error. It follows that e_{bp} is expected to be less accurate than the other error definitions. However, e_{bp} should be as accurate as e_{mp} for the slow impulse waveforms.

The cross-correlation gives a good indication of the match in shapes between the two waveforms. The peak error and maximum error versus time completes this by adding the absolute magnitude accuracy.

6.5.2   Frequency domain analysis

The transfer function of a system is defined as the ratio between the Laplace transform of the output to the Laplace transform of the input of a system under the assumption that all initial conditions are zero [77].

An estimate of the transfer function frequency response is obtained using three methods available in Matlab®, namely Spectral Analysis (SPA), Empirical Transfer Function Estimate (ETFE) and division of the fourier transforms, which will be called the Fast Fourier Transform (FFT) method. It was argued in Chapter 4 that the expected frequency response of the transmission line and sensor combination is flat, except for the cut-off at low frequencies caused by the termination impedance. When other resistances to ground are added in order to model the effects of support structure leakage, poles and zeroes are added in the low-frequency region as well. Therefore, it makes sense to determine the frequency response only at low frequencies, as it should remain constant at the high frequency asymptote where the capacitive coupling elements dominate.

Furthermore, estimation of the frequency responses is affected adversely by high frequency noise as this noise is mostly uncorrelated. Therefore, the input waveforms were filtered so that only low frequency information is available for the estimation routines. For the slow impulses, the filtering is almost unnecessary as very little excitation is present above 10 kHz except for noise, but the fast impulses required additional filtering. A 50 kHz, second order Butterworth low-pass filter was used to attenuate the noise present on all signals.

The process of filtering and frequency response calculation is shown by the block diagram in Figure 6.13. Both measured signals are filtered using the 2nd order Butterworth low-pass filter. Three

methods are used and will be discussed below in this section, namely the FFT method and the two standard functions available with Matlab®, namely SPA and ETFE. The frequency response errors are defined as the percentage difference of the estimated value of the high frequency asymptote, namely $G_f(s)$, $G_s(s)$ or $G_e(s)$ to the predicted value of the high frequency asymptote, namely $G_{pred}(s)$.
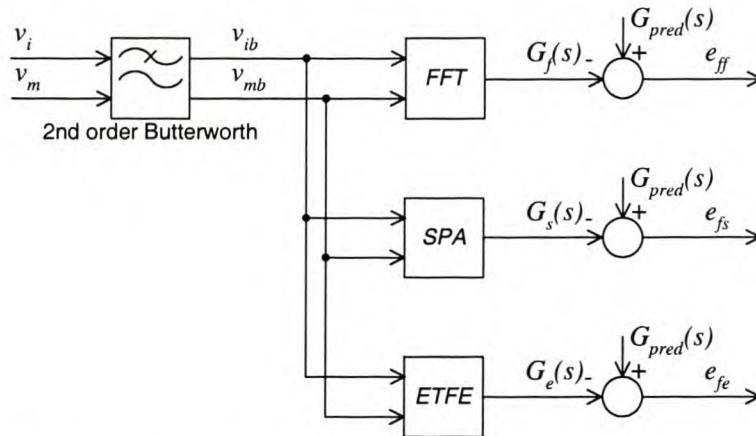
Figure 6.13: Block diagram representation of transfer function frequency response estimation

The low-frequency behaviour of the sensor topology is ignored in this comparison process as most waveforms were sampled too fast and contained too little low frequency information for accurate estimation in this frequency region. Only the low resistive termination had a pole at a high enough frequency to be recognised by the estimation routines. The low-frequency poles for the 10 MΩ //10 nF and 10 MΩ //30 nF terminations are too low to be estimated with the excitation signals used. The high frequency asymptote comparison gives the best indication of the capacitance matrix accuracy.

The simplest method to obtain the measured transfer function frequency response is to divide the FFTs of the two waveforms and is referred to as the FFT method. When looking at a graph of the frequency content of the impulse signal, eg. Figure 6.4, it is clear that the amplitude of the input signal becomes smaller at higher frequencies. The frequency response is calculated only at frequencies for which the input signal amplitude is more than 10 % of the maximum amplitude of the input signal. For the frequencies with amplitude less than 10 % of the maximum amplitude, the signal-to-noise ratio (SNR) has deteriorated too much for accurate estimation of the frequency response of the system. Figure 6.14 shows an estimated transfer function for frequencies where the amplitude is less than 10 % of the maximum amplitude. The asterisk indicate the 10 % excitation level. The ripple caused by the poor SNR is clearly visible for frequencies above this asterisk. Zero-padding is used to increase the frequency resolution, especially for the lower frequencies.

The other methods are Matlab® functions in the optimization toolbox. A discussion of both functions is available in the book by Ljung [78]. Both functions need a matrix consisting of the input
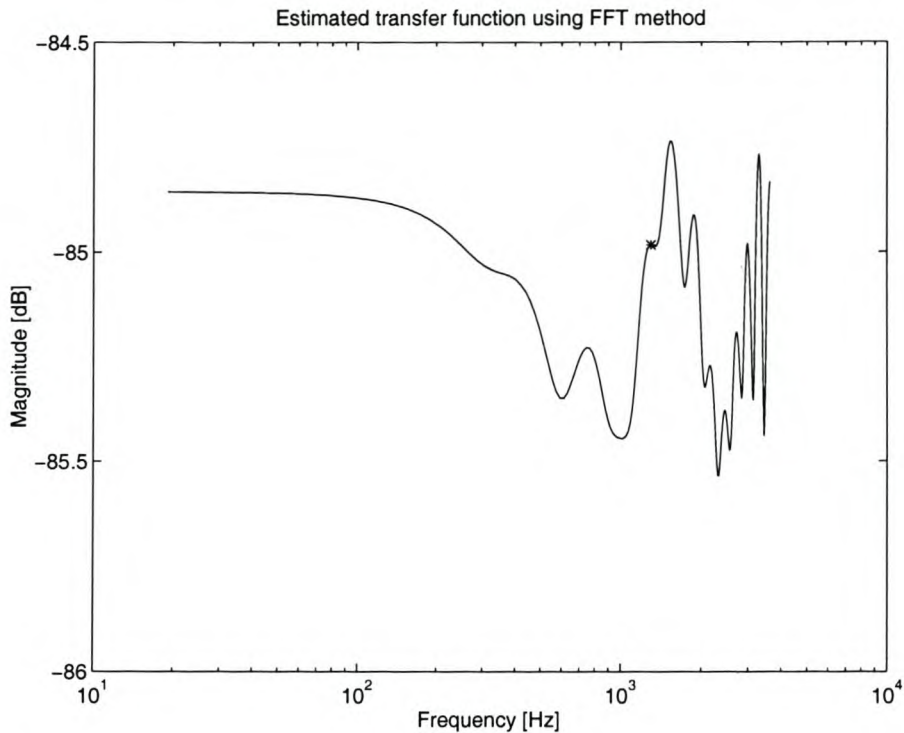
Figure 6.14: Graph showing estimated frequency responses when including frequencies where the input signal amplitude is less than 10 % of the maximum amplitude

and output data, with the possibility of specifying additional options. These options include the window length and the vector of frequencies where the frequency response must be calculated. The desired frequency vector may be supplied for SPA, while ETFE calculates a linearly spaced vector based on the number of frequencies at which the response need to be calculated. The frequency vector used by ETFE is the same as for an FFT for the same number of points. It is, therefore, very difficult to get an estimated frequency response at the low frequencies using ETFE as many points are required. SPA seems to work well in the range below 10 kHz and was mostly used across 3 decades in the frequency domain.

The window length determines the degree of smoothing of the estimated frequency response is. A smaller window length implies a wide window in the frequency domain, which results in a smooth estimated frequency response. A wider window applies less averaging in the frequency domain, which allows the user to find the variations in the frequency response, but also lets through more ripple, especially at the high frequency end. The effects of the window length will be discussed together with the results in section 7.2.1.

6.6 Conclusions

The main findings of the initial measurements were that galvanic isolation is essential for proper operation of capacitive sensors. It was also proven that the boundary conditions in small test areas have a significant effect on the output voltage of such a capacitive sensor and should be taken into account. It seems that the two-dimensional simulations are not adequate for the application, although this could not be proven decisively. It was shown, however, that the three-dimensional simulations for a well-defined measurement arrangement, are very accurate.

The final measurement arrangement in the HV laboratory was also discussed. The conventional arrangement of a transmission line above a ground plane was rotated through 90° so that the transmission line was aligned vertically instead of horizontally. A ground plane was suspended in front of the back wall of the laboratory. The sensor was suspended at a fixed distance of 1 m in front of the ground plane by nylon ropes connected to the catwalk railing. The transmission line was suspended from the overhead crane, allowing for easy and fast adjustment of the line distance (height) from the ground plane.

The capacitive coupling parameters for the three-element parallel plate sensor topology in HV laboratory arrangement was determined from 3D simulations. Extensive simulations were done for this arrangement to determine the influence of small variations in the physical arrangement on the measurement accuracy. Other unknown factors, such as leakage between the sensor elements and ground was also discussed in detail, providing a reference for the measured results presented in Chapter 7.

The data processing algorithms used to evaluate the accuracy of the above impulse measurements were discussed in detail. The time domain error parameters are defined as follows:

- The peak error is the percentage error between the peak values of the measured and reference impulse

- The maximum error is the maximum percentage error between the measured and reference impulse normalised with respect to the reference impulse peak value

- The correlation coefficient gives an indication of the match between the shapes of the measured and reference impulse waveforms

These error and correlation calculations were done for unfiltered and filtered waveforms. Two digital filters were employed, namely a 2nd order Butterworth filter and a moving average filter.

The frequency domain errors are defined as the percentage error between the estimated and predicted high frequency asymptote. Three methods were employed to estimate the transfer function frequency response, namely:

- Division of the FFTs of the measured and reference waveforms

- Spectral Analysis (SPA) function in Matlab®

- Empirical Transfer Function Estimate (ETFE) function in Matlab®

These processing algorithms were applied to the measured results, which are provided and discussed in Chapter 7.

Chapter 7

Sensor Evaluation: Results

7.1   Introduction

This chapter presents the results of the final measurements for both a three-element parallel plate sensor and a single element coaxial sensor. These results are discussed and correlated with the predicted behaviour, that were discussed in Chapter 4. The measurement arrangement and data processing algorithms were discussed in Chapter 6.

Section 7.2 contains the results for the three-element parallel plate sensor, while results for the single element coaxial sensor are discussed in section 7.3. The results are grouped together according to aspects such as rise- and fall time characteristics of applied impulses, transmission line height and non-ideal modelling aspects. The final conclusions for this chapter are given in section 7.4.

7.2   Experimental Results for the Three-Element Parallel Plate Sensor

A total of 311 impulse test results will now be discussed separately for the time- and frequency domains. This relatively large variety of test conditions were selected to allow for the following:

- **Different impulse peak values.**   This allows effects related to linearity with amplitude to be assessed.

- **Different transmission line heights.**   Since the relative dimensions of the test topology is an important factor in the sensor/line/ground plane topology, this allows biasing by their relative dimensions to be exposed.

- **Different impulse rise- and fall time characteristics.** This essentially allows emphasis on low- and high frequency effects respectively .

- **Different loss terms included in the sensor model.** These tests attempt to confirm the predicted responses modelled in Chapter 4, namely the relationships between the sensor equivalent circuit parameters such as termination impedance and support structure properties and the associated time- and frequency domain responses.

Table 7.1 contains a summary of the tests that were done. The first two columns list the tests according to the model group, different termination impedances or transmission line heights above ground. Then the breakdown is done according to fast and slow impulse tests, with an indication of the minimum and maximum peak input voltages that were used for each set of measurements. A more detailed breakdown can be found in Appendix A. It can be seen that the slow impulse tests have lower input voltage peaks than the fast impulse tests. The efficiency of the impulse generator circuit for the slow impulse tests was very low and therefore, large input voltages could not be generated.

The errors as discussed in this chapter are grouped in the first place according to the termination impedance that was used, i.e. the first 145 tests were done with the 10 MΩ //30 nF termination, the next 116 with the 30 kΩ //10 nF termination and the last 50 with the 10 MΩ //10 nF termination.

Table 7.1: Summary of number of tests and input voltage magnitude of all measurement sets

Grouping method	Group	Total # of tests	Fast impulse tests			Slow impulse tests		
			# of tests	min(V_p) [kV]	max(V_p) [kV]	# of tests	min(V_p) [kV]	max(V_p) [kV]
Termination impedance	10 MΩ //30 nF	145	70	6.15	30.25	75	2.40	5.15
	30 kΩ //10 nF	116	56	6.24	20.37	60	1.20	3.66
	10 MΩ //10 nF	50	25	7.70	18.66	25	1.12	4.75
Model	Default	100	47	6.24	16.58	53	1.20	4.10
	R_{s2g}	61	29	8.39	22.92	32	1.25	3.79
	R_{s1g}/R_{s2g}	64	32	8.74	27.53	32	1.25	3.33
	R_{s3g}	56	28	6.15	30.25	28	1.29	5.15
	R_{s1s3}/R_{s2s3}	30	15	7.70	16.08	15	1.12	4.75
Line height	1.5 m	18	9	8.210	8.410	9	3.12	3.21
	2.0 m	152	74	6.24	17.44	78	1.12	3.79
	2.5 m	12	4	9.640	9.720	8	2.72	2.75
	3.0 m	129	64	6.15	30.25	65	1.31	5.15

7.2.1   Time domain results

The time domain results are divided into the following three categories as defined in the block diagram of Figure 6.12:

- Peak error of filtered and unfiltered impulse waveforms (equation 6.1)

- Maximum error of filtered and unfiltered impulse waveforms (equation 6.3)

- Cross-correlation between filtered and unfiltered impulse waveforms

The initial comparisons were done using the simulated capacitance values obtained from the three-dimensional simulations. The mean errors for these simulations are listed in Table 7.2. The maximum deviations from the mean errors falls inside the 4.91 % error band as predicted in section 6.4 except for the Butterworth filtered signals, where the maximum deviation is the same as the limit. This is acceptable because the single test for which the error is 4.91 % is for a fast impulse at a nominal transmission line height of 2.0 m. Both the mean and the deviation are expected to be higher for the 2.0 m high transmission line than for a 3.0 m high line. The combined effect of the group delay of the filters for the fast impulses have been mentioned in section 6.4 and may also cause this deviation of a single sample for the Butterworth filtered signals.

The mean of the peak errors are, however, much larger than the expected mean error, which should ideally be 0. This indicates that there is a significant calibration error. As mentioned in section 6.4, the output voltage accuracy is very sensitive to the sensor capacitance. The relative permittivity of the PCB dielectric was taken as 5.8 for the results in Table 7.2 [71]. However, subsequent capacitance measurements indicated a value of approximately 5.2. There is, therefore, an 11.7 % error in the sensor capacitance as obtained from the original 3D simulations. The above comparisons were repeated with the corrected sensor capacitance, with much better results as shown in Table 7.3.

Table 7.2: Statistical parameters of peak error percentages for all impulse tests with original 3D simulated capacitance values (all values are given in percent [%])

Data set	Mean	Bounds		Standard Deviation	Maximum Deviation	Range
Peak errors: No filtering (e_{up})	7.10	+4.41	-4.27	1.59	4.41	8.68
Peak errors: Butterworth filter (e_{bp})	6.95	+4.91	-4.26	1.54	4.91	9.17
Peak errors: Moving average filter (e_{mp})	6.83	+4.61	-4.11	1.51	4.61	8.72

Apart from the lower mean of the peak errors, which fall within acceptable limits as discussed in section 6.4, the statistical decomposition of the peak errors looks better when the measured sensor capacitance is taken into account. The standard and maximum deviations are smaller in Table 7.3

Table 7.3: Statistical parameters of peak error percentages for all impulse tests with the corrected sensor capacitance (all values are given in percent [%])

Data set	Mean	Bounds		Standard Deviation	Maximum Deviation	Range
Peak errors: No filtering (e_{up})	0.46	+4.42	-3.44	1.43	4.42	7.86
Peak errors: Butterworth filter (e_{bp})	0.30	+3.30	-3.53	1.22	3.53	6.83
Peak errors: Moving average filter (e_{mp})	0.20	+3.02	-3.86	1.21	3.86	6.88

than the original comparisons given in Table 7.2. The corrected errors are shown graphically in Figures 7.1 and 7.2.

Figure 7.1 (a) shows theoretical gaussian plots for the peak errors of the unfiltered and two filtered waveform groups. The peak error is the percentage difference between the peak value of the measured sensor voltage and the simulated sensor voltage. Histograms for each peak error are drawn together with the gaussian approximation in Figure 7.1 (b)-(d). The gaussian approximation was calculated from the means and standard deviations as listed in Table 7.3. The gaussian variable is used to describe the uncertainty in scientific and engineering measurements. It is, therefore, expected that the agreement should be good as is the case in Figure 7.1. The distribution for the moving average filtered waveforms, i.e. Figure 7.1 (d), gives the closest approximation to the gaussian distribution.

Figure 7.2 shows plots of the impulse peak errors for all the tests as a function of the test index. The error bounds were calculated around the mean of all the errors using the limits given in Table 6.8. Errors falling outside the defined limits are indicated by asterisks. Figure 7.2 (a) shows the peak errors for the unfiltered signals and only the unfiltered signals have errors outside the defined limits. The peak errors of both the Butterworth filtered (Figure 7.2 (b)) and moving average filtered (Figure 7.2 (c)) signals fall within the limits of Table 6.8. It is clear that removal of the measurement noise by filtering reduces the observed error bounds.

Visually there is a significant correlation between the different errors as plot in Figure 7.2 (a)-(c). This confirms that the filtering processes do not remove significant information from the signals, as the peak error is not changed drastically by the filtering process. The normalised mathematical correlation coefficients for the different error graphs are given in Table 7.4.

Table 7.4: Correlation at zero lag between peak impulse errors (e_p)

Compared errors	Correlation coefficient [%]
Unfiltered and Butterworth filtered	83.06
Unfiltered and moving average filtered	80.74
Butterworth and moving average filtered	96.06
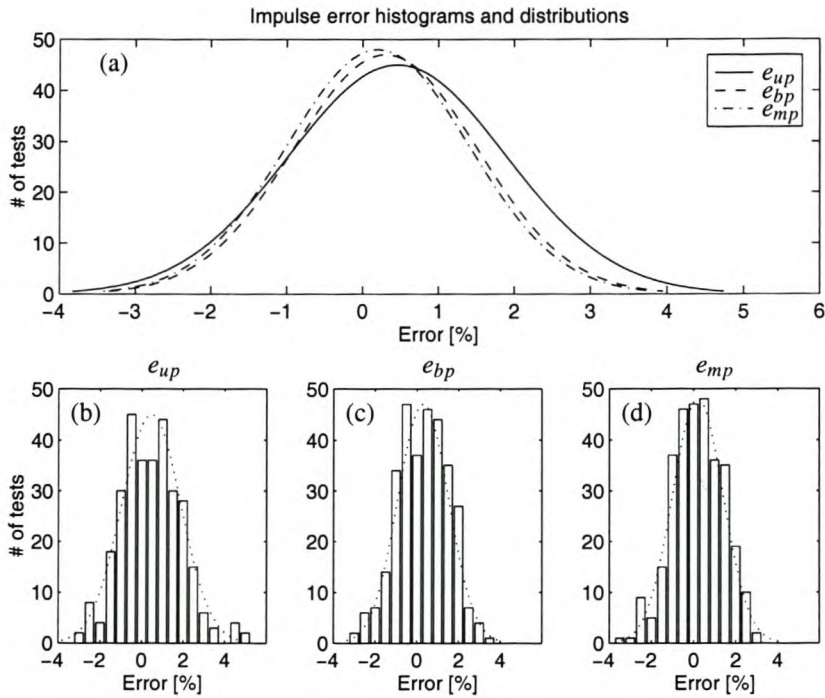
Figure 7.1: Figure showing the error histograms and correlation with gaussian error distribution: (a) Gaussian distributions (b) Peak error distribution of unfiltered waveforms (c) Peak error distribution of Butterworth filtered waveforms (d) Peak error distribution of moving average filtered waveforms
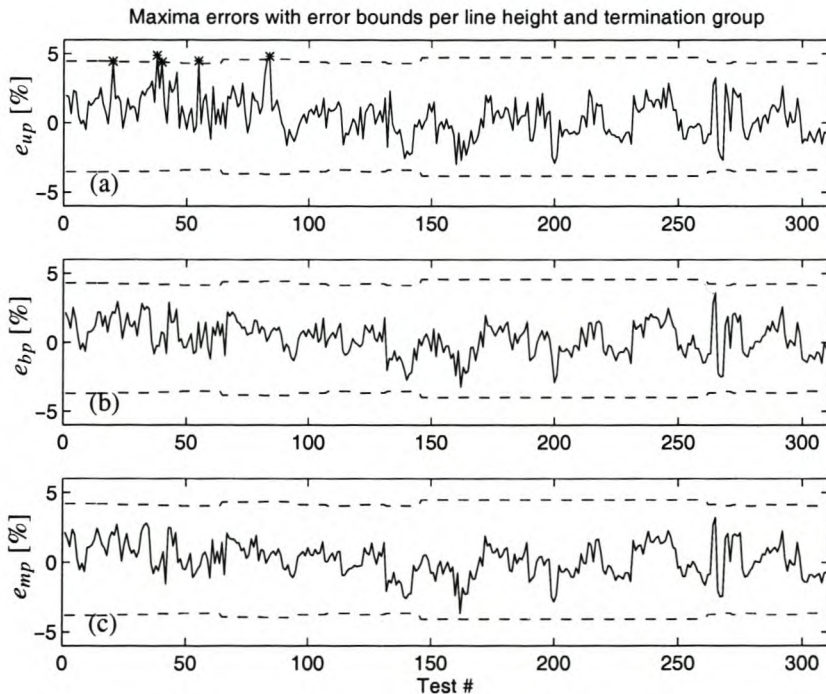
Figure 7.2: Impulse peak errors plot against test number with error limits as defined in Table 6.8 according to model group and termination impedance. (a) Peak errors of unfiltered signals (b) Peak errors of Butterworth filtered signals (c) Peak errors of moving average filtered signals

The maximum error, i.e. the maximum of the percentage difference between the measured and simulated sensor voltages, is shown in Figure 7.3. These differences are given as a percentage of the peak value of the simulated reference waveforms. Here the influence of noise on the perceived accuracy is again evident. The waveform filtered using the moving average filter have maximum errors within the mean +4.91 % error band. The other waveforms have significantly larger maximum errors.
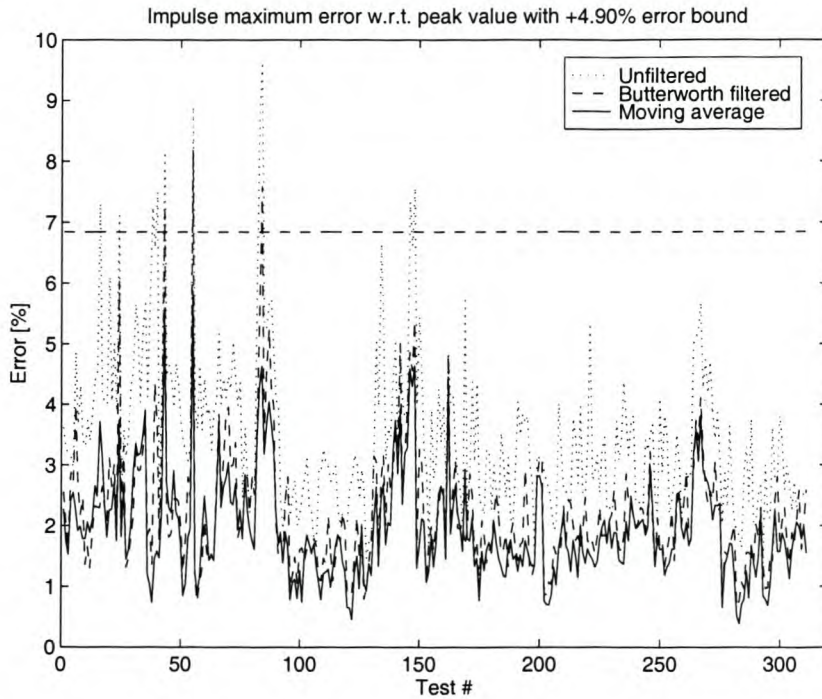
Figure 7.3: Maximum difference between predicted and measured sensor voltage, calculated with respect to the predicted peak voltage

Two types of errors have now been discussed, namely the peak errors and the maximum error at any time instant over the sampled time interval. In both cases, the errors were calculated with respect to the peak value of the simulated voltage and expressed in %. Both these errors indicate that the predicted and measured waveforms correlate very well. The mathematical correlation was also calculated for each predicted/measured waveform pair. The minimum cross-correlation is larger than 99 %, which represents an excellent match [55]. The cross-correlations are shown in Figure 7.4 (a). Figure 7.4 (b) shows the value of the final sample point of the impulse waveform that was used in the correlation procedure. Except for 6 slow impulse waveforms, the sampled impulse waveforms decayed to less than 10 % of the respective peak values during the sampling period. This means that significant portions of the impulse waveshapes had generally been compared.

Overall, the above confirms that the equivalent circuit model as discussed in Chapter 3 together with simulated capacitance values can be used to predict the response of the three-element parallel plate sensor reasonably accurately.
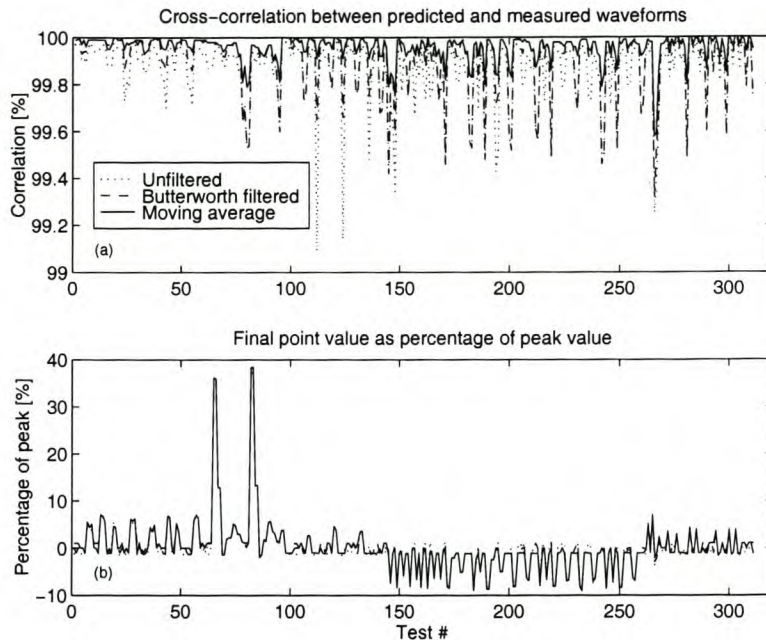
Figure 7.4: Cross-correlation between measured and predicted waveforms for all impulse tests: (a) Cross-correlation (b) Value of final sample point used in correlation procedure indicating what portions of the impulse waveforms were compared

Other interesting factors regarding the model discussed in section 6.4 will now be highlighted. The mean peak errors (cfg. equation 6.1) for the unfiltered and both filtered waveforms are listed in Table 7.5 together with the maximum error of the moving average filtered signal, namely e_{mt}. The measured data is subdivided according to the speed of the impulse, termination impedance, other non-ideal components added and transmission line height. Each of these groups are listed together with the overall mean at the top.

Table 7.5 lists the mean peak errors for all peak error definitions, in order to compare the actual data and the filtering process. There is a definite calibration error, which increased the mean error above 0 %. Several group mean errors, which are expected to be negative yielded positive values, which confirms the above conclusion.

With reference to the effects of the speed of the impulse, it is expected that the fast impulses will have more accurate results than the slow impulses. The mean error for the slow impulses is expected to be negative as discussed in section 6.4. This is due to the effects of the unknown resistive paths to ground, which primarily affects the low-frequency results.

For the filtered peak errors, the slow impulse tests exhibit lower mean values compared to the fast impulse tests given in Table 7.5 (b). A small calibration error is still present, because the mean errors are positive in both cases. It was difficult to generate slow impulse waveforms with large peak values, because of limitations of the impulse generator. The measured voltages for the slow

Table 7.5: Comparison of mean values of the peak errors of the unfiltered and both filtered wave-forms as well as the maximum error versus time for the moving average filtered waveforms (all values are given in percent [%])

Data set	# of Tests	Unfiltered peak error (e_{up})	Butterworth peak error (e_{bp})	Moving average peak error (e_{mp})	Moving average maximum error (e_{mt})
(a) No subdivision					
All tests	311	0.46	0.30	0.20	1.94
(b) Speed of impulse (slow/fast)					
Slow impulse tests	160	0.55	0.20	0.11	1.87
Fast impulse tests	151	0.36	0.40	0.30	2.02
(c) Sensor termination					
$Z_t = 10\ M\Omega//30\ nF$	145	0.89	0.56	0.46	2.11
$Z_t = 10\ M\Omega//10\ nF$	50	0.14	0.12	0.08	1.74
$Z_t = 30\ k\Omega//10\ nF$	116	0.06	0.06	-0.07	1.82
(d) Model group					
Default model	100	0.76	0.47	0.35	2.30
R_{s2g} model	61	0.71	0.49	0.35	2.14
R_{s1g}/R_{s2g} model	64	0.13	0.13	0.06	1.47
R_{s3g} model	56	0.27	0.13	0.07	1.92
R_{s1s3}/R_{s2s3} model	30	-0.01	0.04	-0.06	1.40
(e) Transmission line height					
2.0 m high	152	0.88	0.88	0.78	1.81
3.0 m high	129	-0.32	-0.53	-0.64	2.03

impulse tests were, therefore, relatively small, which means that noise due to discretisation and other induced noise is more pronounced. This effect of noise is confirmed to some degree by the fact that the mean error for the slow impulse tests for both filtered waveforms is lower than the mean error for the fast impulse tests in contrast with the unfiltered waveforms where this relation is reversed.

All tests are expected to have negative mean peak errors if the resistive components are smaller than the simulated values of 100 MΩ or 10 MΩ respectively, except for tests of the R_{s2g} model. This was shown in Table 6.3 in section 6.4. The tests conducted with a low resistive termination, namely 30 kΩ //10 nF, should have the lowest mean peak error and this is confirmed by the results given in Table 7.5 (c). The reason why the 10 MΩ //10 nF termination tests have a mean peak error comparable with the 30 kΩ //10 nF termination tests is because no tests with the R_{s2g} model are included in the 10 MΩ //10 nF termination group. This is the only model, which can increase the error above the mean and was included only for the 10 MΩ //30 nF and 30 kΩ //10 nF termination tests.

The mean errors of the different model groups are listed in Table 7.5 (d). All the model groups, except the R_{s2g} model are expected to have negative mean errors. The expected mean error of the R_{s2g} model group should be positive for the 10 MΩ //30 nF and 10 MΩ //10 nF terminations and negative for the 30 kΩ //10 nF termination. The tests for the R_{s2g} model contain an almost equal amount of tests for both the 10 MΩ //30 nF and 30 kΩ //10 nF termination and none for the 10 MΩ //10 nF termination. This means that the overall error for the R_{s2g} model group will approach the value dictated by the calibration error.

The mean error for the default model group, i.e. all resistors ignored, is very close to that of the R_{s2g} model. The expected mean error is less than 0 % or the calibration error. The range and standard deviation for the default model group is, however, larger than for the R_{s2g} model group as shown in Table 7.6 (c). Some of the tests for the default model and the R_{s1g}/R_{s2g} model were taken long before the rest of the tests. This means that the entire measurement arrangement had to be rebuilt, which leaves space for larger error distributions. The R_{s1g}/R_{s2g} model do not seem to suffer from this, but this is attributed to the fact that the expected mean error for this model group is lower than for the default model group.

The data comparisons for different transmission line heights are shown in Table 7.5 (e). The mean error for tests with a nominal line height of 2.0 m is higher than for the tests at 3.0 m line height. It is expected that the measurements at 3.0 m line height should be more accurate as positioning errors have less impact on the sensitivity factor of the sensor. It has, however, been shown in Table 6.3 in section 6.4 that the measurements for a line height of 3.0 m is more sensitive to the unknown resistive elements. If the actual resistance is lower than the simulated value, the error will be negative. This explains why the mean error for tests for a nominal line height of 3.0 m is lower than the calibration mean, while the tests for a nominal line height of 2.0 m is higher than the calibration mean.

The measured voltages are also smaller for the tests for 3.0 m line height than for 2.0 m height because of the larger separation between the transmission line and the sensor. This implies that induced noise influences the measurements for 3.0 m line height more than the measurements for 2.0 m line height. If the induced noise remains the same for both cases, this implies that the SNR for the 3.0 m line height is worse compared with the 2.0 m line height.

A statistical decomposition of the moving average peak errors are given in a similar format in Table 7.6. The results for the moving average filtered waveforms are shown in Table 7.6 as this data is expected to give the best approximation of the actual performance of the capacitive sensor.

The mean peak error of the moving average filtered signals was given and discussed together with Table 7.5. Table 7.6 lists the observed error bounds, standard and maximum deviations and range for the moving average filtered signals mean peak errors as well. From this it can be seen that all the error bounds are significantly less than the predicted error bound of ±4.91 % from section 6.4.

Table 7.6: Comparison of statistical parameters of the peak errors of the moving average filtered waveforms (e_{mp}) for all tests with e_{mp} for subsets of the data (all values are given in percent [%])

Data set	# of Tests	Mean	Bounds		Standard Deviation	Maximum Deviation	Range
(a) No subdivision							
All tests	311	0.20	3.02	-3.86	1.21	3.86	6.88
(b) Speed of impulse (slow/fast)							
Slow impulse tests	160	0.11	2.62	-3.77	1.18	3.77	6.39
Fast impulse tests	151	0.30	2.92	-3.13	1.23	3.13	6.05
(c) Sensor termination							
$Z_t = 10\ \text{M}\Omega//30\ \text{nF}$	145	0.46	2.36	-3.05	1.14	3.05	5.41
$Z_t = 10\ \text{M}\Omega//10\ \text{nF}$	50	0.08	3.14	-2.55	1.35	3.14	5.70
$Z_t = 30\ \text{k}\Omega//10\ \text{nF}$	116	-0.07	2.35	-3.59	1.16	3.59	5.94
(d) Model group							
Default model	100	0.35	2.87	-4.01	1.41	4.01	6.88
R_{s2g} model	61	0.35	1.75	-3.18	1.07	3.18	4.93
R_{s1g}/R_{s2g} model	64	0.06	2.08	-1.44	0.92	2.08	3.51
R_{s3g} model	56	0.07	2.21	-2.66	1.31	2.66	4.87
R_{s1s3}/R_{s2s3} model	30	-0.06	2.34	-1.40	0.98	2.34	3.74
(e) Transmission line height							
2.0 m high	152	0.78	2.44	-2.12	0.94	2.44	4.56
3.0 m high	129	-0.64	2.72	-3.02	0.98	3.02	5.73

7.2.2 Frequency Domain Results

The frequency domain results are divided into the following three categories as defined in the block diagram of Figure 6.13:

- The percentage error between the predicted and estimated high-frequency asymptote using the FFT method (e_{ff})

- The percentage error between the predicted and estimated high-frequency asymptote using the SPA method (e_{fs})

- The percentage error between the predicted and estimated high-frequency asymptote using the ETFE method (e_{fe})

A certain amount of ripple exists on the estimated frequency responses, which is inherent in the estimation routines. The window length determines the amount of smoothing in the estimated frequency response and is indicated by 'M' in the graphs. Figure 7.5 shows estimated frequency responses for slow impulses using both the SPA and ETFE functions with different window lengths.

Figure 7.5 (a) shows the SPA function comparison and Figure 7.5 (b) the ETFE frequency response comparison. Figure 7.6 shows identical plots for a fast impulse frequency response estimation. These plots concentrate on the low-frequency transition region of the expected sensor frequency response. Too much smoothing, i.e. a small 'M', disable the determination of the low-frequency poles caused by amongst others the termination impedance.

The following important aspects concerning the estimation process should be kept in mind:

- The estimated frequency response using a very short window, namely M=30, shows the effect of the averaging very clearly. In Figure 7.5 (a), the average frequency response is flat and lies somewhere between the high frequency asymptote and the low frequency amplification. The estimated frequency response for the fast impulse is flat, but very close to the high frequency asymptotic value as very little low frequency information is present in the time waveforms.

- If the low frequency behaviour needs to be estimated, a large M is required. Even if only the high frequency asymptote is estimated, too much low frequency information will lead to erroneous results if M is too small. An M of 5000, which is equal to half the number of samples, were used throughout. For the purpose of error calculation, it is assumed that the average value of this ripple approaches the magnitude of the frequency response HF asymptote.

- Any DC offset in either measured signal that was not removed properly, will influence the estimation at low frequencies. Otherwise it is also possible that the low-frequency pole, due to the termination impedance, is estimated too high, which cause a drop in the estimated frequency response towards the lower frequencies. Both the above-mentioned reasons may cause deviations in the average estimated frequency response in either increasing or decreasing direction and thereby increase the maximum deviations.

The initial comparisons were done using the simulated capacitance values from the 3D simulations. The mean errors for these simulations are listed in Table 7.7. The maximum deviation of the frequency response errors exceeds the 4.91 % error band predicted in section 6.4. This is attributed to the frequency response estimation and error calculation routines.

The comparisons were repeated with the corrected sensor capacitance, with lower mean errors as shown in Table 7.8. All the remaining error calculations were performed with the corrected sensor capacitance.

Figure 7.7 shows the error distributions for the different frequency domain errors. These error distributions also follow the gaussian distribution as did the time domain peak and maximum
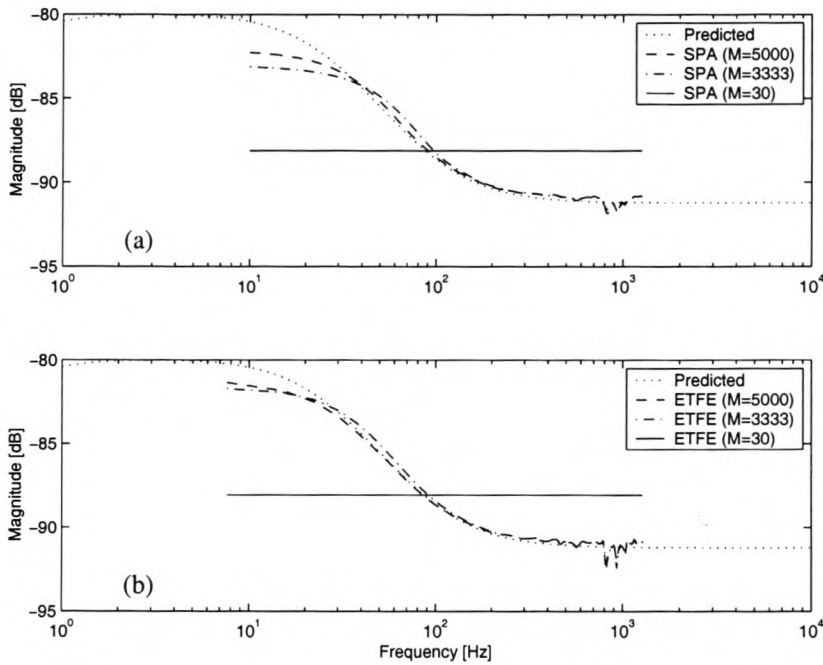
Figure 7.5: Comparison between different window lengths in the estimation process of a slow impulse for the low frequency transition region: (a) Estimation using the SPA function (b) Estimation using the ETFE function
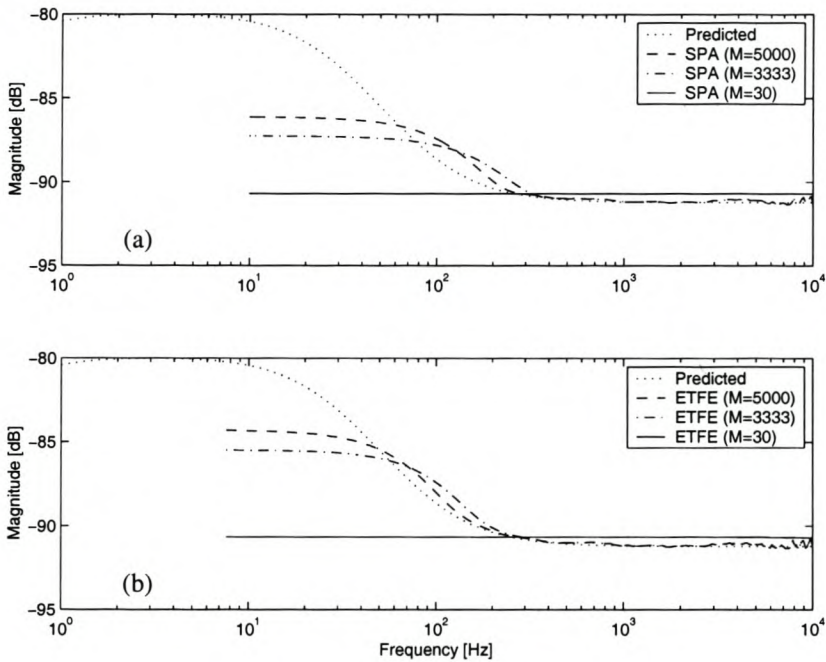
Figure 7.6: Comparison between different window lengths in the estimation process of a fast impulse for the low frequency transition region: (a) Estimation using the SPA function (b) Estimation using the ETFE function

Table 7.7: Statistical parameters of HF asymptote errors with original 3D simulated capacitance values (all values are given in percent [%])

Data set	Mean	Bounds		Standard Deviation	Maximum Deviation	Range
FFT method (e_{ff})	5.76	+4.70	-5.79	1.84	5.79	10.48
SPA estimate (e_{fs})	4.37	+7.73	-9.01	3.26	9.01	16.74
ETFE estimate (e_{fe})	5.79	+4.27	-6.28	1.90	6.28	10.54

Table 7.8: Statistical parameters of HF asymptote errors with the corrected sensor capacitance (all values are given in percent [%])

Data set	Mean	Bounds		Standard Deviation	Maximum Deviation	Range
FFT method (e_{ff})	-0.37	+4.81	-6.65	2.25	6.65	11.46
SPA estimate (e_{fs})	-1.09	+6.35	-9.01	3.33	9.01	15.36
ETFE estimate (e_{fe})	-0.39	+5.56	-7.24	2.49	7.24	12.80

errors. The correlation between the gaussian distribution and histograms of the frequency domain errors as shown in Figure 7.7 (b)-(d) is less than for the impulse peak errors. The SPA function estimation results shown in Figure 7.7 (c) appears to reflect the worst degree of correlation with the gaussian distribution.

A significant amount of errors calculated using the SPA function is less than the negative limit as indicated in Figure 7.8 (b). This is particularly true for test numbers 146-261, correlating with the low resistive termination measurements. An explanation can be made with reference to Figure 7.9. As the termination impedance has a relatively high frequency pole, the impulse waveforms contain enough information for the estimation routines to detect the pole. The slow impulse waveforms contain significant excitation only to approximately 1.5 kHz (cfg. Figure 6.4). The estimated frequency response, therefore, only just reaches the high frequency asymptote and some of the low frequency information will be included in the average estimated frequency response.

The frequency domain errors falling outside of the limits defined in Table 6.8 are shown with asterisks. The estimated frequency response using the FFT method has only one sample too small, while the ETFE method produced two errors smaller than the predicted limits. These three errors all come from the low termination measurements and they are explained as above. The errors estimated using the SPA function seem to be the least accurate.

The good visual correlation between the results from the FFT method and the ETFE function is confirmed by a correlation coefficient of 98.7 % as listed in Table 7.9. The correlation of the SPA estimation errors with the other two is less accurate and is caused by the overall low errors for estimation of the 30 kΩ //10 nF tests.
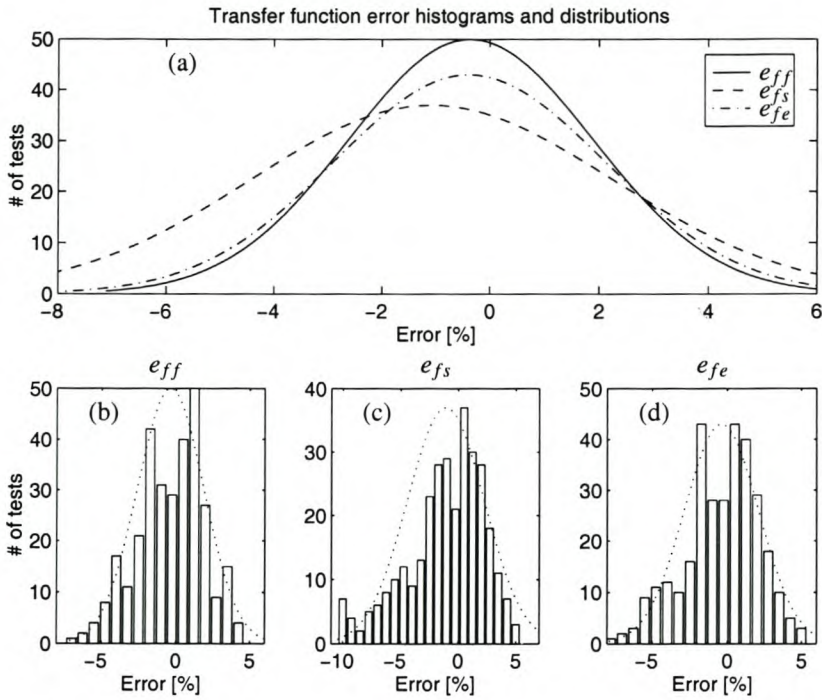
Figure 7.7: Frequency response estimation errors with gaussian error distribution: (a) Gaussian distributions (b) HF asymptote errors using FFT method (c) HF asymptote errors using SPA method (d) HF asymptote errors using ETFE method
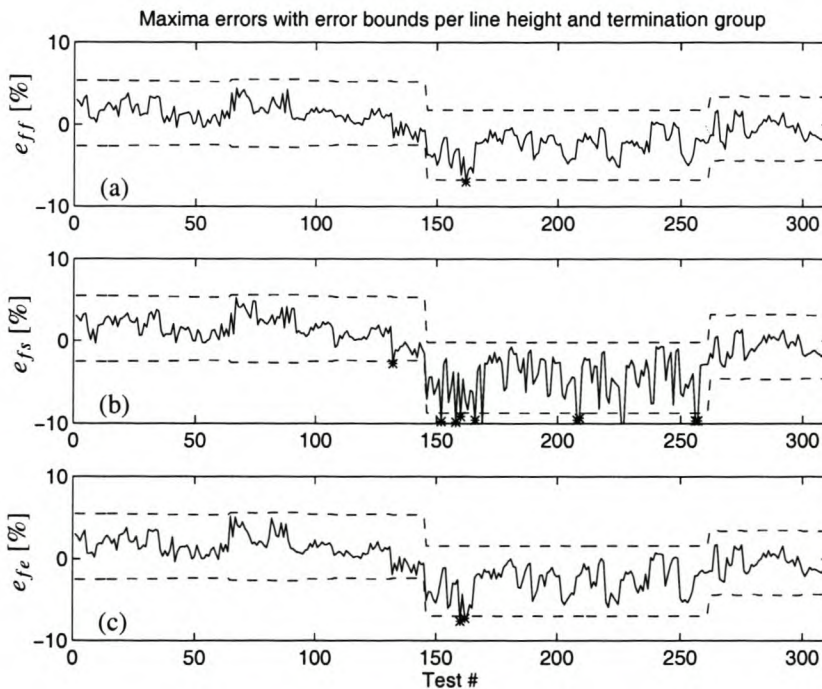
Figure 7.8: Frequency response estimation errors plot against test number with error limits as defined in Table 6.8 according to model group and termination impedance. (a) FFT method (b) SPA estimate (c) ETFE estimate
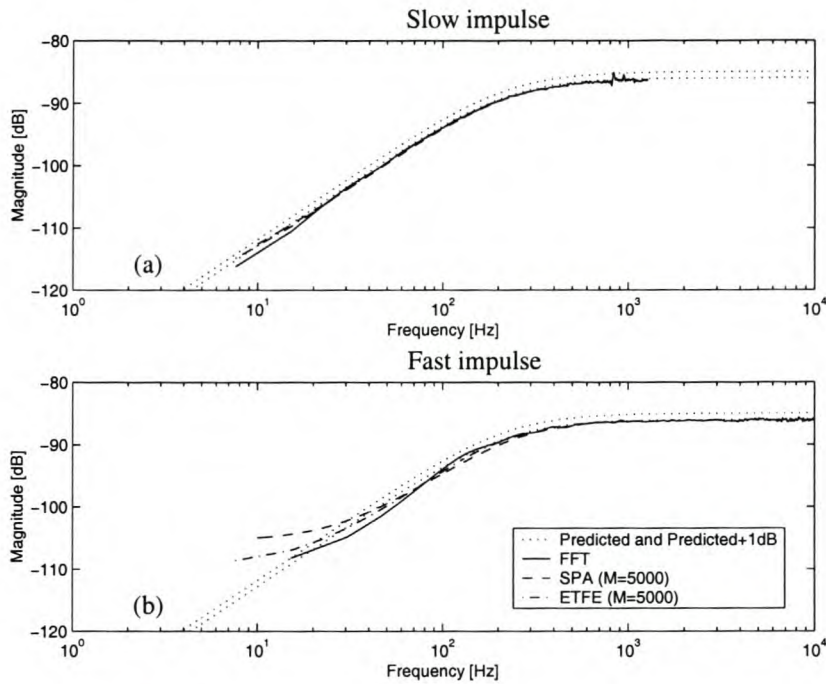
Figure 7.9: Estimated frequency responses for default model measurements with low resistive termination, namely 30 kΩ //10 nF, comparing the predicted frequency response with the three estimation methods discussed in the text (a) Slow impulse (b) Fast impulse

Table 7.9: Correlation at zero lag between frequency response estimation errors

Compared errors	Correlation coefficient [%]
FFT method versus ETFE	98.7
FFT method versus SPA	84.8
ETFE versus SPA	86.0

Frequency response estimates for the different model groups are shown in Figures 7.10 to 7.13. Here the predicted frequency response is shown together with estimates generated using FFTs, SPA or ETFE. Two plots are shown per figure, the top is the estimation using a slow impulse and the bottom plot an estimation using a fast impulse.

It can be seen that the theoretical estimation of the high frequency asymptotic value is accurate within 1 dB of the theoretical value at all times. The predicted frequency response as well as the predicted frequency response +1 dB is also plot using dotted lines on all the graphs for easier judgement of the error. The predicted transfer function ± 1 dB is plot for the R_{s2g} model estimation.

For all Figures 7.10 to 7.13 the slow impulse estimates seem to be more accurate, especially when picking up low frequency behaviour. Two reasons can be given, namely that the slow impulse contains more information at low frequencies, which can assist in the estimation procedure and secondly the slow impulse waveforms were sampled at lower sampling frequencies, which also provide more low frequency data to the estimation routines.
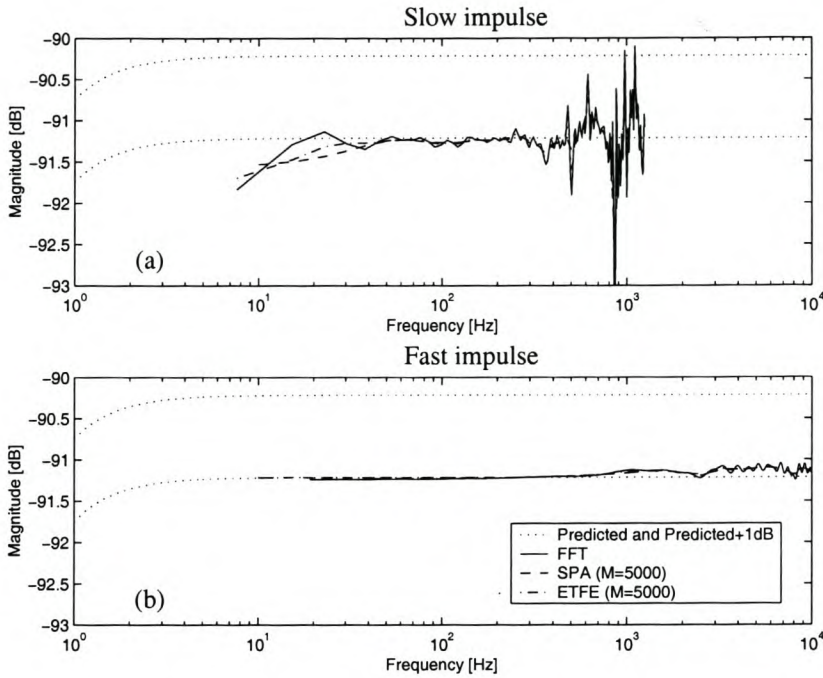
Figure 7.10: Estimated frequency responses for default model measurements, comparing the predicted frequency response with the three estimation methods discussed in the text (a) Slow impulse (b) Fast impulse
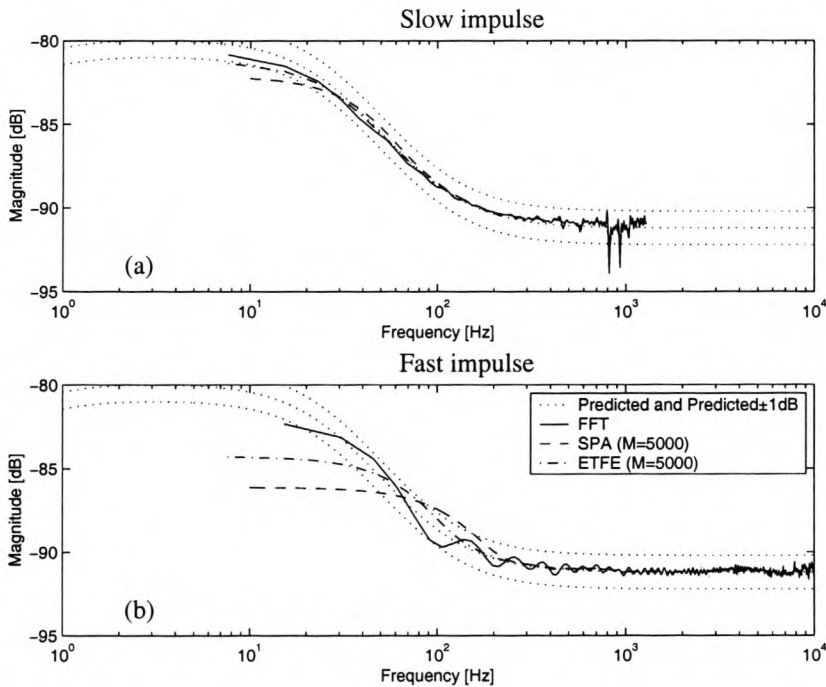
Figure 7.11: Estimated frequency responses for R_{s2g} model measurements, comparing the predicted frequency response with the three estimation methods discussed in the text (a) Slow impulse (b) Fast impulse
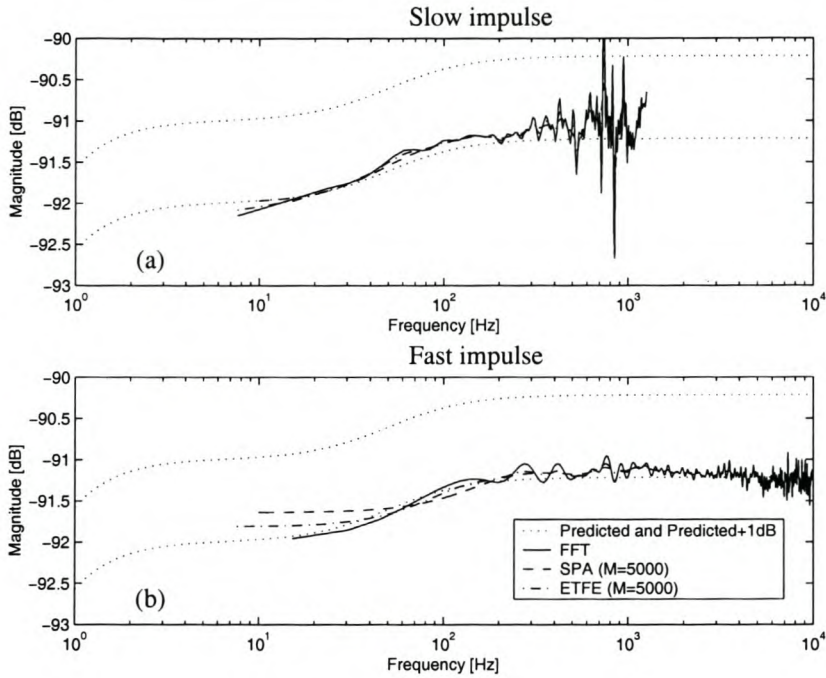
Figure 7.12: Estimated frequency responses for R_{s1g}/R_{s2g} model measurements, comparing the predicted frequency response with the three estimation methods discussed in the text (a) Slow impulse (b) Fast impulse
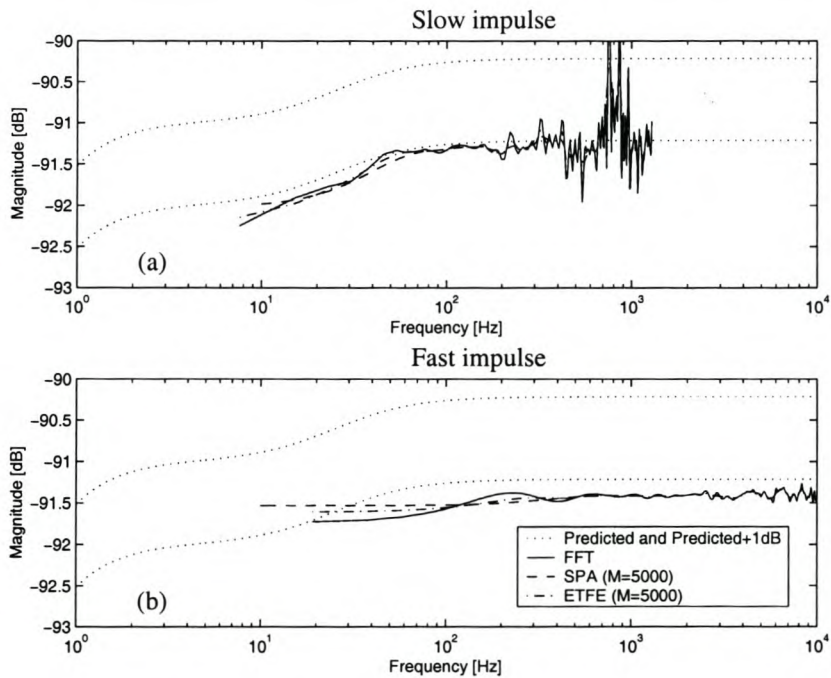
Figure 7.13: Estimated frequency responses for R_{s3g} model measurements, comparing the predicted frequency response with the three estimation methods discussed in the text (a) Slow impulse (b) Fast impulse

It was suggested that the R_{s3g} model, where the faraday cage is connected to ground portray a suitable support structure for a flat frequency response. It is required that 50 Hz AC signals be used for calibration of the sensor. For a 100 MΩ resistance between the faraday cage and ground, the deviation at 50 Hz from the high frequency asymptote is approximately -0.15 dB as could be seen from Figure 4.20. Figure 7.13 shows that the ripple on the estimated frequency response is more than 0.15 dB and it can safely be assumed that 50 Hz calibration measurements can be done for this situation.

For the higher termination impedances, i.e. the 10 MΩ //10 nF and 10 MΩ //30 nF, the low frequency poles is located below the lowest estimated frequency obtained with the estimators. However, in the case of the 30 kΩ //10 nF termination impedance, this pole shifted into the estimated frequency region. This was shown in Figure 7.9. It is clear that all methods predict the location of this pole quite accurately.

Overall it appears that the FFT method gives the most accurate results. No averaging is attempted in the frequency domain, which means that ripple due to noise in the time domain will come through, but fortunately this is limited to the high frequency band. Figure 7.14 shows two estimated frequency responses obtained with the FFT method for different amounts of zero padding. Eight and 15 times zero padding were used respectively, where the 15 times zero padding allows estimation to a lower frequency than the 8 times zero padding. The two traces are almost identical up to the low frequency point of the 8 times plot, i.e. they lie on top of each other.
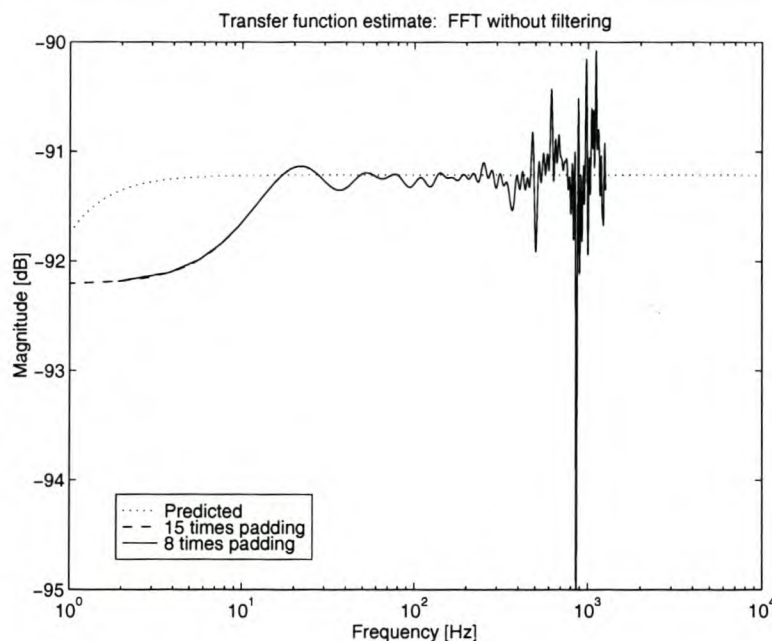
Figure 7.14: Estimated frequency responses using the FFT method with 8 and 15 times zero padding respectively

Table 7.10 lists the statistical parameters of the errors for the results obtained with the FFT method. These results are grouped according to speed of the impulses, termination impedance used, non-ideal components added and transmission line height.

Table 7.10: Comparison of statistical parameters of e_{ff} for all tests with e_{ff} for subsets of the data with C_{sns} accounted for

Data set	# of Tests	Mean	Bounds		Standard Deviation	Maximum Deviation	Range
(a) No subdivision							
All tests	311	-0.37	4.81	-6.65	2.25	6.65	11.46
(b) Speed of impulse							
Slow impulse tests	160	-0.68	5.12	-6.33	2.71	6.33	11.46
Fast impulse tests	151	-0.03	3.47	-2.95	1.57	3.47	6.41
(c) Termination impedance							
$Z_t = 10\ M\Omega//30\ nF$	145	1.38	3.06	-3.52	1.29	3.52	6.57
$Z_t = 10\ M\Omega//10\ nF$	50	-0.48	2.26	-2.53	1.18	2.53	4.79
$Z_t = 30\ k\Omega//10\ nF$	116	-2.50	2.89	-4.51	1.58	4.51	7.40
(d) Model group							
Default model	100	-0.02	3.85	-7.00	2.61	7.00	10.85
R_{s2g} model	61	0.29	4.15	-4.56	2.31	4.56	8.71
R_{s1g}/R_{s2g} model	64	-0.92	3.00	-4.30	2.17	4.30	7.30
R_{s3g} model	56	-0.99	3.00	-3.99	1.75	3.99	6.99
R_{s1s3}/R_{s2s3} model	30	-0.49	1.96	-1.56	0.98	1.96	3.51
(e) Transmission line height							
2.0 m high	152	-0.05	4.49	-5.27	2.26	5.27	9.76
3.0 m high	129	-1.19	5.46	-5.83	2.09	5.83	11.29

It was attempted to determine the error with which the HF asymptote could be estimated. This means that the effects of the resistive components on the mean errors should be eliminated. This seems not to be the case as the low resistive termination tests, namely 30 kΩ //10 nF definitely suffers from the resistive components' influence. The R_{s2g} model tests should show the same dependence on the value of R_{s2g}. The overall influence of these components seem to force the mean error distribution into the pattern discussed in section 6.4:

- The slow impulse errors have a lower mean error (more negative) than the fast impulse errors

- Tests done with the 30 kΩ //10 nF termination have the lowest mean error and those with the 10 MΩ //30 nF termination the highest mean error

- The R_{s2g} model has the only mean error bigger than the overall mean error

- The mean error for tests done with a transmission line height of 3.0 m is less than for the line height of 2.0 m

The range of the slow impulse errors is almost twice the range for the fast impulse tests. The excitation of the slow impulse tests was smaller than for the fast impulse tests, which implies that the slow impulse tests have a worse SNR. The same cut-off frequency was used for all tests during the frequency domain analysis, which means that the resultant slow impulse signals remained relatively noisy. As the frequency response estimation routines are influenced by noise, this probably explains the wider range of errors for the slow impulse tests.

7.3   Results for Single Element Coaxial Sensor

No model groups are defined for the coaxial sensor as only one termination was used and no other non-ideal components could be added. It does not make sense practically to add a finite resistor between the transmission line and the sensor on the earth wire, which is why this situation was not modelled. Furthermore, too few tests were done to justify the subdivision into slow and fast impulse tests.

In total 34 impulse tests and ten 50 Hz AC tests were done for the single element coaxial sensor. The tests were done for three different distances between the transmission line and sensor with three distinct applied peak voltages as listed in Table 7.11.

Table 7.11: Summary of tests conducted using the single element coaxial sensor

Distance between	# of tests		
line and sensor	Fast	Slow	AC
1.00 m	8	8	4
1.25 m	9	-	3
1.50 m	9	-	3

The accuracy of these impulse tests were calculated in the same way as defined in section 6.5. The time domain accuracy is defined in terms of the peak voltage error, the maximum error at any time instant across the sampled waveform and the correlation coefficients. The estimated frequency responses were calculated using the FFT method, the SPA estimate function and the ETFE estimate function.

7.3.1   Time domain results for the coaxial sensor

The measured signals from the coaxial sensor are very noisy. It is suspected that the EMC cabinet was used incorrectly for these measurements, namely that it was not earthed properly. This noise complicated the error calculations for the time domain analysis.

Figure 7.15 shows a typical example of the noisy sensor voltage. These spikes seem to be reflections of the initial trigger point noise. This trigger point noise exists in the output before the sensor voltage is available at the instrumentation receiver and, therefore, it is concluded that all these noise spikes are present only on the received signal, not on the actual sensor voltage. Filtering removes these spikes and Figure 7.16 shows the same voltages as in Figure 7.15 after passing through the moving average filter.
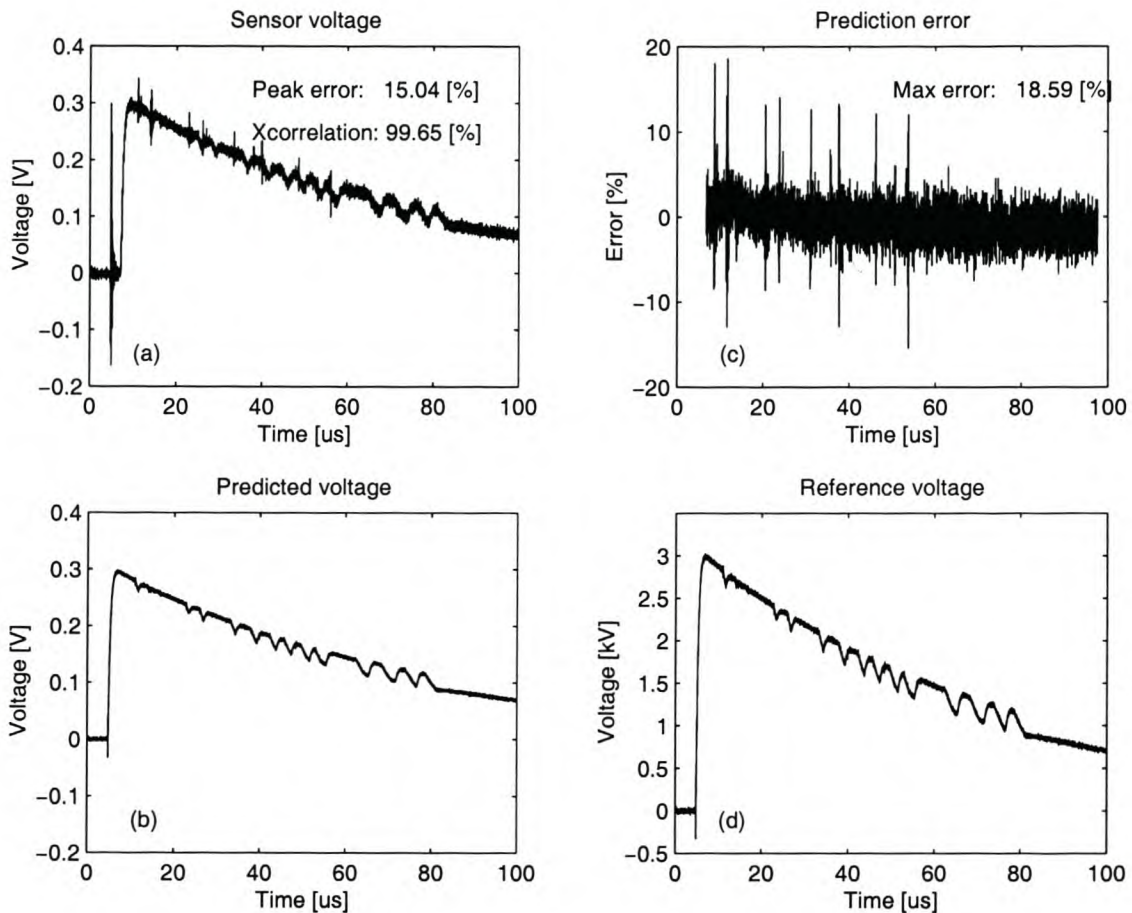
Figure 7.15: Graphs of typical reference and sensor voltages showing noise spikes in sensor voltage (a) Sensor voltage (b) Predicted voltage (c) Prediction error (d) Reference voltage

Furthermore, the error caused by these noise spikes increase as the sensor is moved away from transmission line. When the sensor is moved further away, the induced voltage decreases, but the induced noise remains the same. Due to the reduced SNR, the error increases when the voltage is decreased as is demonstrated in Table 7.12. This supports the above assumption that the noise spikes are induced on the instrumentation receiver side and not at the sensor.

The ripple visible on all the impulse waveforms, including the references, in Figures 7.15 and 7.16 is caused by the impulse generator. The spark gap does not flash over uniformly, i.e. the spark is quenched and reignites repetitively, when the voltage is this low. It does, however, provide extra
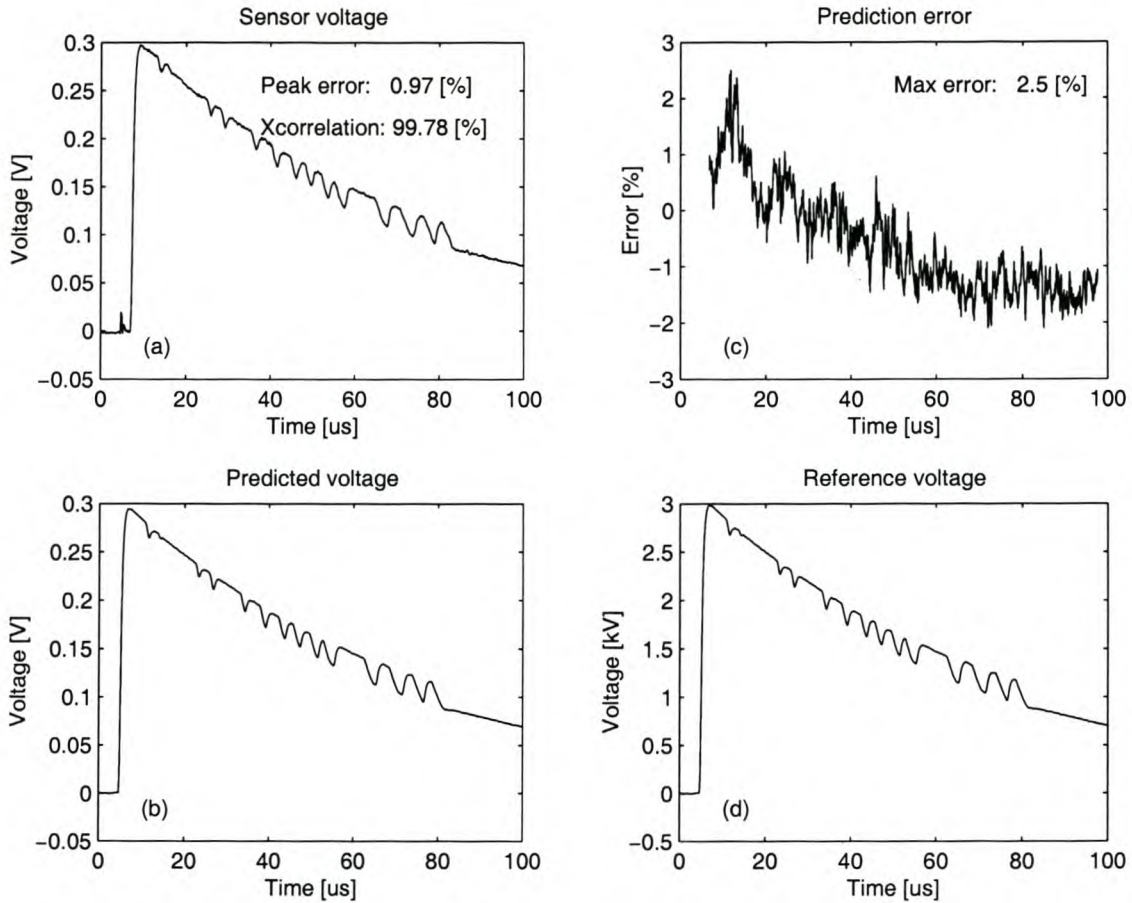
Figure 7.16: Graphs of filtered reference and sensor voltages showing reduction in noise (a) Sensor voltage (b) Predicted voltage (c) Prediction error (d) Reference voltage

wideband frequency information for correlation between the reference and sensor waveforms.

Table 7.13 lists the statistical parameters for the impulse peak voltage errors for the coaxial sensor in a similar format as before. Due to the large difference between the mean error for the unfiltered waveforms and the filtered waveforms, it seems that the peak error of the unfiltered signals is not representative of the actual sensor response.

Graphs of the impulse peak errors, as calculated using equation 6.1, versus test number are given in Figure 7.17. The error limits, which are shown, take only the instrumentation accuracy into account as was discussed in section 6.4. The asterisks shown in Figure 7.17 (a) indicate samples falling outside the expected accuracy limits. For the unfiltered results, almost all the samples fall outside, while the filtered versions have no samples outside the ± 2.5 % limits.

There is no obvious correlation between the unfiltered error graph and the filtered error graphs. This is not surprising as the noise spikes on the unfiltered waveforms do not correlate with the actual impulse peaks. The correlation coefficient between the two filtered versions is 84 %. Relatively few tests are available for the statistical analysis and, therefore, it is not possible to accurately

Table 7.12: Mean, standard deviation and range for coaxial sensor unfiltered peak errors (e_{up}) when grouped by sensor distance from transmission line (all values are given in percent [%])

Distance between line and sensor	Mean	Standard Deviation	Range
1.00 m	1.61	1.59	7.06
1.25 m	3.80	3.68	12.60
1.50 m	5.73	5.93	15.05

Table 7.13: Statistical parameters for coaxial sensor impulse test results (all values are given in percent [%])

Peak error data set	# of Tests	Mean	Bounds		Standard Deviation	Maximum Deviation	Range
No filtering (e_{up})	34	3.28	11.76	-4.12	4.00	11.76	15.88
Butterworth filter (e_{bp})	34	0.68	1.94	-1.19	0.75	1.94	3.13
Moving average filter (e_{mp})	34	0.90	1.74	-1.32	0.67	1.74	3.07

determine a correlation coefficient and the 84 % is regarded as acceptable. It may indicate that the two filtering processes behave very differently under very noisy conditions. However, it is not possible to say which filter is preferable from these results.

The maximum errors of the impulse versus time were calculated using equation 6.3 and are shown in Figure 7.18. The correlation between the two filtered error plots is clearly visible. From sample 9 to 34, the correlation coefficient is 98 %. The first 8 samples are the errors for slow impulse tests. For these tests, the digital Butterworth filter cut-off frequency was fixed at 1 MHz and the waveforms were, therefore, filtered too little to enable accurate error calculation.

Figure 7.19 shows the correlation coefficients versus test number for each predicted/measured impulse pair. The worst correlation coefficient is more than 99 %, which indicates a near perfect match. Figure 7.19 (b) shows the value of the last sample included in the correlation calculation as a percentage of the maximum value. This gives an indication of how far the sampled waveforms decayed with reference to the peak value for each case. From Figure 7.19 it is clear that the correlation drops if the impulse waveforms are chopped before they reach zero. The correlation coefficient is, however, so good that this is irrelevant.

7.3.2   Frequency domain results for the coaxial sensor

The frequency response estimates were determined in the same manner as was discussed for the three-element parallel plate sensor. The low frequency pole caused by the termination impedance for the coaxial sensor is situated at approximately 0.4 Hz. This pole is therefore, not reflected in the estimated frequency responses.
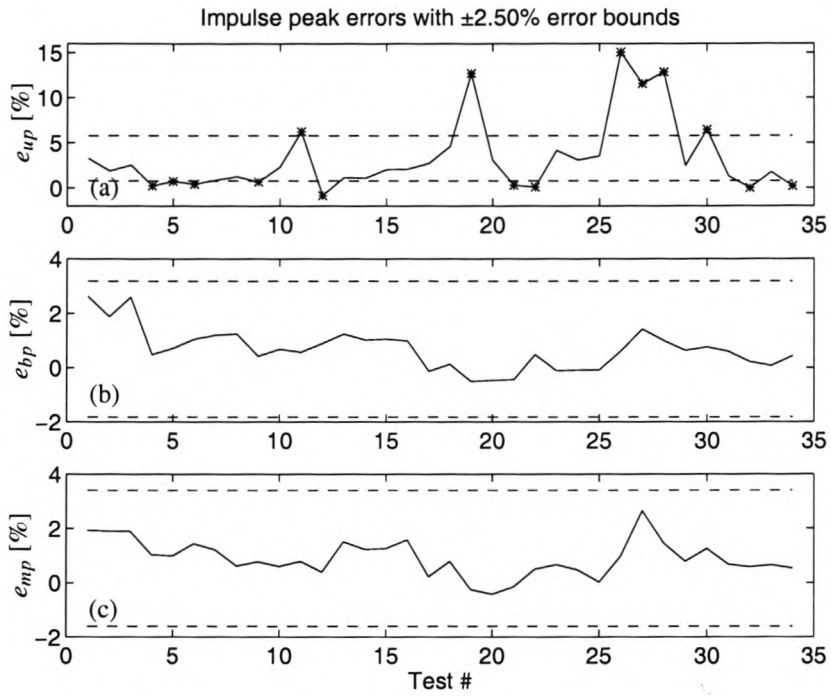
Figure 7.17: Impulse peak errors versus test number with ± 2.5 % error bounds showing the instrumentation accuracy limits (a) Unfiltered signals (b) Butterworth filtered signals (c) Moving average filtered signals
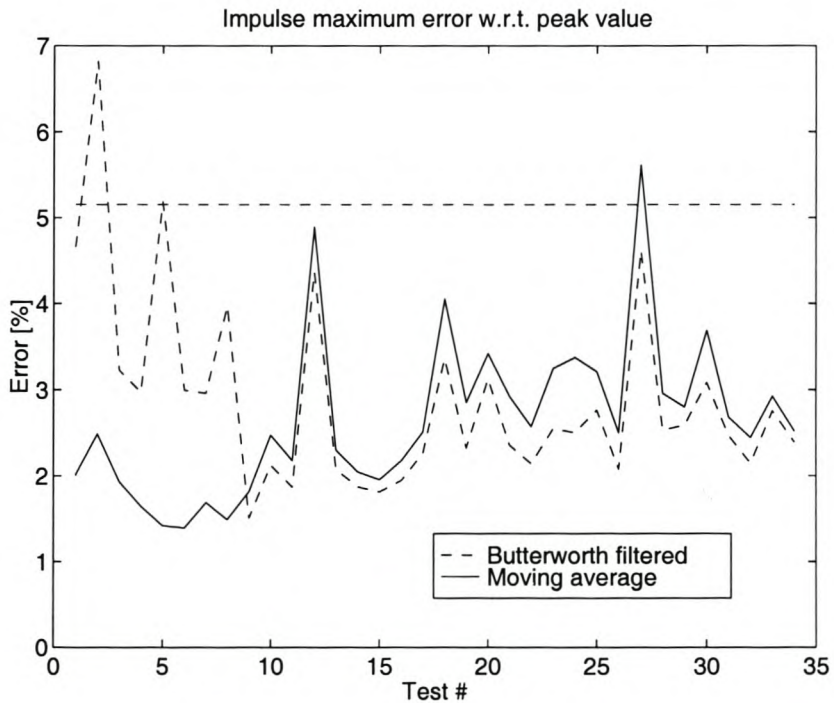
Figure 7.18: Impulse maximum errors versus test number with ± 2.5 % error bounds showing the instrumentation accuracy limits
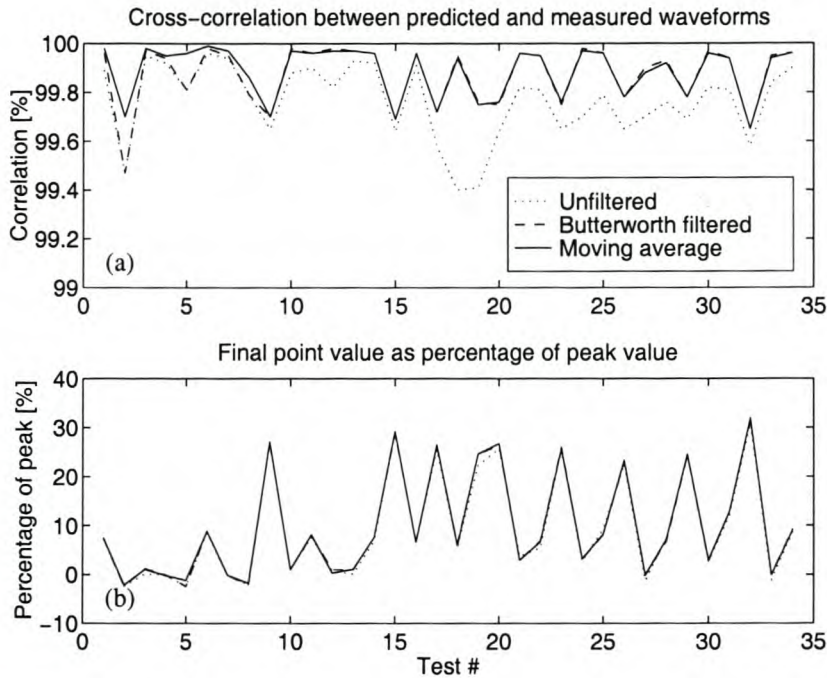
Figure 7.19: Correlation coefficients for coaxial sensor impulse measurements (a) Correlation coefficients (b) Final sample point value as percentage of peak value indicating how far the impulse have decayed

The errors listed in Table 7.14 is the comparison of the mean value of the estimated frequency response to the predicted value of the frequency response. All the errors have a mean value of approximately 1 % and the range is similar to the time domain impulse peak errors.

Table 7.14: Statistical parameters for coaxial sensor frequency response estimated errors (all values are given in percent [%])

Data set	# of Tests	Mean	Bounds		Standard Deviation	Maximum Deviation	Range
FFT method (e_{ff})	34	1.02	1.30	-0.85	0.52	1.30	2.15
SPA estimate (e_{fs})	34	1.07	2.36	-1.06	0.97	2.36	3.41
ETFE estimate (e_{fe})	34	1.26	1.67	-1.15	0.81	1.67	2.83

The estimated frequency response errors are also shown graphically in Figure 7.20. The errors fall inside the ±2.5 % accuracy limits of the instrumentation. The errors for time domain results differed for the slow and fast impulse tests (cfg. Figure 7.18), but this same distinction is not visible in the frequency domain.

A total of 10 steady-state 50 Hz AC tests were conducted in order to obtain an indication of the accuracy of the sensor as well as the flatness of the frequency response down to these frequencies. Figure 7.21 shows three plots of errors versus test number for the 50 Hz AC tests.

Figure 7.21 (a) is the percentage difference between the measured and predicted peak-to-peak
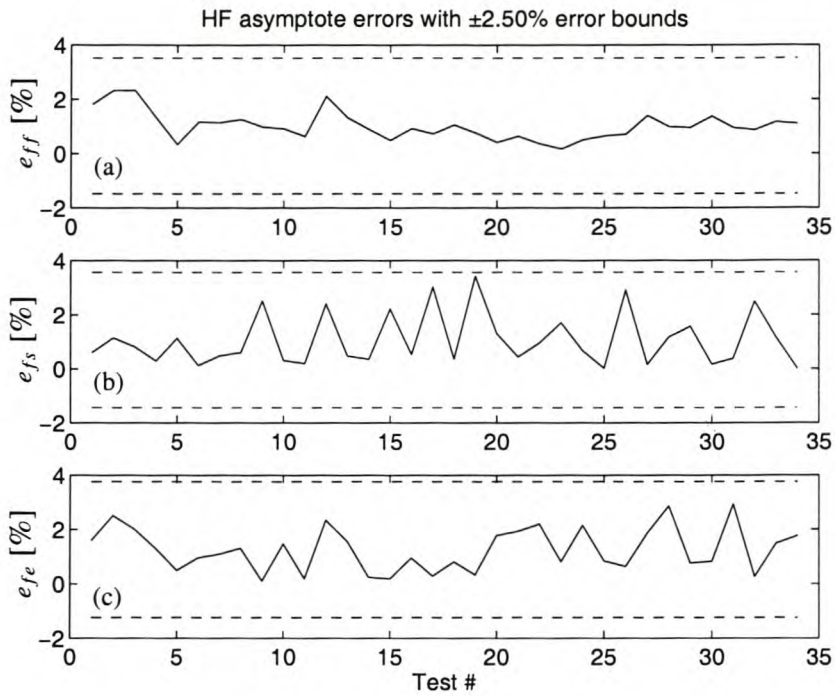
Figure 7.20: Error in estimated HF asymptote of coaxial sensor frequency response (a) FFT method (b) SPA estimate (c) ETFE estimate

voltage. The maximum error versus time is shown in Figure 7.21 (b). The output frequency spectrum at 50 Hz was divided by the input frequency spectrum at 50 Hz and compared with the HF asymptote value of the frequency response for the errors shown in Figure 7.21 (c).

The difference between the errors from the unfiltered waveforms and the errors from both filtered waveform versions indicate that the 50 Hz signals were also very noisy. The comparison of the 50 Hz components of the FFTs of the signals indicate that noise does not corrupt these comparisons as these error distributions are identical to an accuracy of two decimal digits.

The average errors for the 50 Hz tests are listed in Table 7.15. The mean errors are both negative. The mean value of the impulse peak errors were of the order of 0.75 % (cfg Table 7.13) and the mean error of the frequency response estimate for the impulse tests were of the order of 1.00 % (cfg Table 7.14). The corresponding errors for the steady-state tests are significantly smaller. This may be attributed to a lower termination resistance, which would move the low frequency cut-off pole to a frequency high enough to attenuate the 50 Hz signal. The range of errors obtained for the filtered 50 Hz tests are within the instrumentation accuracy of ± 2.5 %.
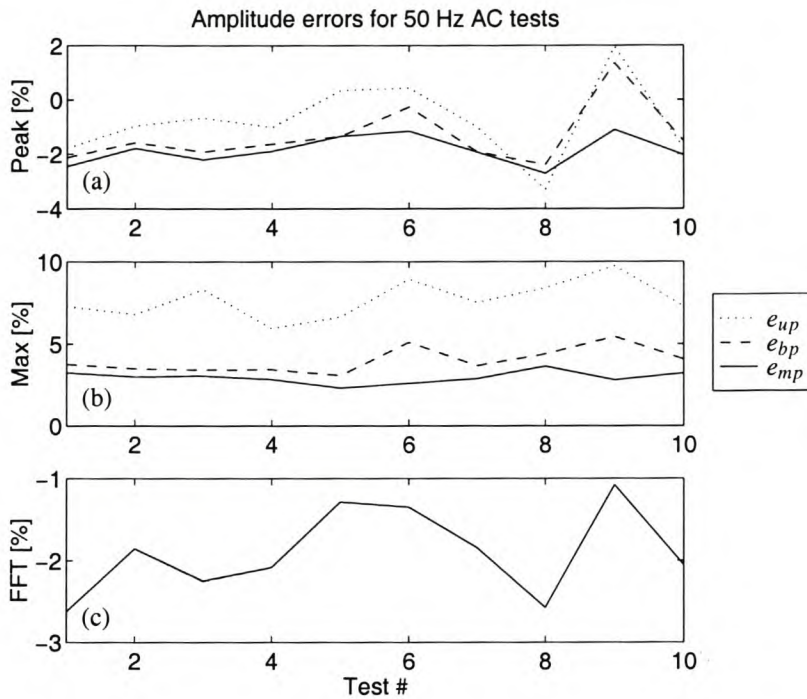
Figure 7.21: Errors between expected and measured response of the coaxial sensor for 50 Hz AC tests (a) Peak-to-peak voltage error (b) Maximum error for any time instant (c) FFT at 50 Hz

Table 7.15: Mean error percentage values and range for amplitude and FFT errors of the steady-state 50 Hz tests (all values are given in percent [%])

Comparison type	Unfiltered waveforms	Butterworth filtered waveforms	Moving average waveforms
Amplitude error mean	-0.78	-1.33	-1.86
Amplitude error range	5.26	3.74	1.61
FFT 50 Hz error mean	-1.90	-1.90	-1.90
FFT 50 Hz error range	1.54	1.54	1.55

7.4 Conclusions

Two types of sensors were evaluated during this project, namely the three-element parallel plate sensor and a single element coaxial sensor. Both produced very good results in the time- and frequency domains. The means and standard deviations of the impulse peak errors for both sensors in the time domain and the FFT method in the frequency domain are listed in Table 7.16.

From a calibration point of view the mean errors are very good. The largest absolute value for the mean error is 1.02 %. It was shown that all the measurement sets can be approximated by the gaussian distribution.

Table 7.16: Mean errors and standard deviations summarised for both the three-element parallel plate and single element coaxial sensor in both the time and frequency domain (all values are given in percent [%])

Sensor	Time Domain		Frequency Domain	
	Mean error	Standard deviation	Mean error	Standard deviation
Three-element parallel plate sensor	0.20	1.21	-0.37	2.25
Single element coaxial sensor	0.90	0.67	1.02	0.52

The standard deviation for the three-element parallel plate sensor is larger than the standard deviation of the coaxial sensor. The standard deviations for the coaxial sensor in both the time- and frequency domain are very similar, while the frequency domain standard deviation of the three-element parallel plate sensor is more than in the time domain. This is also attributed to the poor calibration accuracy obtained for the R_{s2g} model as was discussed in section 7.2.2. The results of the coaxial sensor included only one model and the resulting standard deviation is smaller in both the time- and frequency domains, explaining why the standard deviations for the coaxial sensor are less than for the three-element parallel plate sensor.

The influence of non-ideal values for the support structure and the termination impedance was tested under controlled conditions for the three-element parallel plate sensor. The results confirmed that these factors affect the responses considerably. It does seem, however, that the equivalent circuit models derived in Chapter 3 are adequate to predict the response of these sensors.

The results were subdivided into several groups according to termination used, the model inaccuracies added, height of transmission line and speed of impulse. The mean errors obtained for these groups agree very well with the predicted results discussed in section 6.4.

Chapter 8

Conclusions and Recommendations

8.1 Introduction

The purpose of this chapter is to summarise the main findings of this dissertation. These findings will be discussed with reference to the original objectives of the project. Recommendations for future work will also be given.

8.2 Conclusions with Reference to the Original Objectives

The steps that were followed during the execution of this research project may be divided into the following aspects:

- The compilation of a literature review of capacitive sensors in all areas of application with specific reference to sensor topologies, design methodologies, constructional aspects and calibration and accuracy of available sensors.

- The development of optically isolated, high speed interface instrumentation for use with the sensor in order to provide the necessary galvanic isolation of the sensor from the environment.

- The development of a modelling strategy for open-air capacitive sensors for voltage measurement on power systems and transmission lines. This involved the following components:
    - Selection of an appropriate sensor topology
    - Development of an equivalent circuit for the sensor topology

149

- Determination of the model parameters for the equivalent circuit from electric field simulations
- Using the above-mentioned equivalent circuit models and model parameters to predict the time- and frequency domain responses of the sensor topology

- Evaluation of the prototype sensors under laboratory conditions using impulses and 50 Hz AC excitation. This translates into the following:

  - Comparison of measured waveforms with the predicted time and frequency domain responses
  - Estimation of circuit model parameters from the laboratory measurements and equivalent circuit model.

The remainder of this section gives a critical appraisal of the achievements of the investigation, particularly with reference to the above objectives.

8.2.1   Important aspects from the literature review

Mobile, wide bandwidth voltage sensors are required to compliment standard substation equipment, such as CVTs, MVTs and CTs in specialised measurements, because the standard equipment have the following shortcomings:

- The equipment is bulky and expensive and can only be installed at a limited number of locations

- The transducers have very limited bandwidth when used in the standard configurations

- All transducers are intrusive as some form of impedance is connected to the high voltage electrode

Midline sensing or intersubstation measurement of high frequency voltage waveforms will be required for future studies such as carrier propagation, standing waves, harmonic penetration, fault location, lightning impulse studies, insulation coordination under transient conditions and effects of varying earth conductivity on long transmission lines.

It was found that capacitive sensing techniques have been used successfully for voltage measurements in power systems, where well-defined geometries and ground references exist, eg. in GIS. Open-air voltage sensors also showed promising results, however, the single plate sensors are very sensitive to changes in the ground level reference. A broad classification of capacitive sensors for voltage or electric field sensing in power systems is between sensors for DC- or AC waveforms.

DC require special sensors with moving electrodes, because a time variation in the charge distribution is required to induce a voltage. AC sensors must be stationary as the time variation of the induced charges is caused by the varying field. It was in fact shown that a rotating field meter in an AC field have resonant peaks in the transfer function at frequencies associated with the rotation speed of the sensing element [52].

All these sensors basically measure the electric field strength at the sensor position or between the sensor and the ground reference [47]. The output for which the specific sensor is calibrated, either voltage or electric field strength, determines the terminology.

Capacitive sensors for DC waveforms are divided as follows:

- Flat and cylindrical field mills

- Vibrating electrode sensors

- Ion current, space- and surface charge meters

The ion current is caused by the space charge, which in particular surrounds HVDC transmission lines. Separate sensors were developed to measure the ion current when investigating pre-breakdown electric field distributions in spark gaps. Ion current and space charge influence the DC voltage sensors specifically and special precautions with biasing voltages or grounding impedances are required for accurate measurements [35, 36, 37, 38].

Tests conducted underneath an HVDC test line indicated that similar instruments gave wide-ranging answers, varying from 15 % to 45 % from the mean value for any specific test. It is suspected that the space charge and ion current caused these large deviations and proper precautions for these phenomena should be taken when measuring underneath an HVDC line. One way of achieving this would be to provide a resistive path to ground for this ion current. Johnston & Kirkham [49] found that the leakage resistance of the handle of their cylindrical field mill caused erroneous measurements. It is, therefore, not a straightforward problem to solve and will be revisited in recommendations for future work.

It is clear from the literature on DC field measurements and the techniques employed for space-charge measurements that the capacitive voltage sensor topologies addressed in this investigation may suffer from the accumulation of charge under DC conditions. Field measurements would have shed more light on this and should be completed as part of future work to qualify the proposed topologies for HVDC applications. However, in order to mitigate the effects of charge collection, leakage paths to ground have to be deliberately introduced. This justifies the emphasis in the investigation on the effects of leakage introduced by the support structure.

Capacitive sensors for AC waveforms are divided as follows:

- Voltage sensors for gas-insulated-switchgear (GIS)

- Voltage sensors for open-air applications

- Electric field strength sensors for open-air applications

Despite the promising results obtained by Tokoro *et al* [54] for 60 Hz AC measurements in GIS, it seems it is not in commercial use yet [55]. The reason for this is unknown. Other sensors developed for use in GIS were developed for very fast transients or partial discharges for research into the steep rise-times of voltages and fields in GIS. For this reason very wide bandwidths were required, up to 200 MHz [61, 62, 53]. The accuracy of these sensors were discussed in terms of theoretical aspects and not verified by any other measurements.

The success of capacitive sensors in GIS topologies confirms that research into the use of capacitive sensors for open-air applications is justified. The important lesson from the GIS applications is that good results can be obtained provided that a well-defined physical topology with a good ground reference exists. For this reason, this investigation included the coaxial sensor with the earth wire as reference.

The open-air sensors also showed very good results. Van Heesch *et al* [12], Roberts & Hoch [13] and Gerrard *et al* [14, 55] used several single-element sensors underneath three-phase transmission lines. Only one instance of differential sensors were found, namely those discussed by Shimada *et al* [63]. The decoupling required when multiple sensors are used in the multi-phase environment was not discussed by Shimada *et al*, which may explain the phase error experienced at low frequencies.

Both van Heesch *et al* [12] and Roberts & Hoch [13] used the energising transients of their transmission line to determine the calibration and decoupling parameters. The results from the capacitive sensors agreed very well with the reference measurements in both cases. Gerrard *et al* [14, 55] measured the deviation of the voltage on each conductor from the long-term average, where this average is expected to be the nominal voltage of the transmission line. Gerrard *et al* used 8 sensors to increase the accuracy of the system and used simulations to find the decoupling parameters of the sensor outputs.

Impulse transients were used to qualify the sensors discussed in this dissertation. Special consideration were also given to the analysis of these transients with respect to accuracy and calibration factors.

The open-air electric field strength sensor that was developed by Feser, Pfaff and co-workers were also utilised for impulse voltage measurements [16]. This indicates the close relationship between voltage and electric field sensors. The calibration factor was of secondary importance for this test,

but the accurate representation of the waveshape is considered very good. The calibration procedures used by Feser *et al* was not discussed, but seemed to be in good agreement with reference measurements.

It is clear from the literature review that limited attention has been given to the concept of a differential open-air sensor. The modelling of capacitive sensors using equivalent circuit modelling and frequency-domain estimation were also not previously rigorously addressed. No references to a coaxial sensor located on the earth conductor have been found. The practice of using the system frequency to calibrate open-air sensors seems to be well established. This method will only work if the low-frequency cut-off frequency identified in this dissertation is located appropriately, thereby justifying the emphasis on this aspect in this investigation.

It is fair to conclude that serious consideration should be given to the termination of capacitive sensors and also the design of the support structure if the low frequency response is of importance.

8.2.2 High speed optically isolated data transmission system

In order to maintain the galvanic isolation of the capacitive sensor, high speed optically isolated buffer instrumentation was developed. The instrumentation consists of a transmitter- and receiver subsystem interconnected by a digital fibre-optical link.

The transmitter subsystem is integrated with the sensor and mounted inside a faraday cage. The transmitter comprises analogue signal conditioning circuitry, an analogue-to-digital converter, digital encoding and fibre-optic transmission of the serialised digital data. The receiver decodes this serial data and presents the data in digital and analogue format.

The specifications of the instrumentation may be listed as below:

- Two modes of data transmission
  - 12 bit resolution at 5 MHz sampling
  - 8 bit resolution at 10 MHz sampling
- Wide bandwidth ranging from 1 Hz to:
  - 6 MHz when bypassing the anti-aliasing filter
  - 1 MHz with the anti-aliasing filter in-line
- Gain variation of less than 2 % over the bandwidth frequency range
- High input impedance, $\gg 10\ \mathrm{M\Omega}$ without termination resistor

- ± 1 V input range

- Galvanic isolation is maintained

The optical isolation interfaces employed by other researchers use analogue transmission. The digitising topology used here represents a relatively novel approach. While it offers improved accuracy and versatility, it also introduces more complexity and high power supply requirements. The conceptual development did not form part of this project and a prototype was available. However, this investigation provided the first rigorous evaluation of this technology and substantial design changes, particularly to the embedded control program was performed. The application also required extensive redesign of the input circuitry to optimise the performance of this technology for use with capacitive sensors in high frequency applications. Due to the high output impedance of the Thévenin equivalent circuit at low frequencies, special attention should be given to the input impedance of the interface instrumentation for a flat response across the frequency range of interest. It is concluded that the design of the instrumentation input impedance must form an integral part of the overall sensor design, optical isolation is essential and that the digitising approach works well in practice, despite the troublesome delay factor.

The 12 bit mode at 5 MHz sampling with anti-aliasing filter was used for all the laboratory tests discussed in this dissertation. Higher bandwidths are not required at this stage, as the test waveforms did not contain significant information at frequencies above 1 MHz. Parameter and transfer function estimation were also attempted and these procedures do not work well in the presence of noise. The high frequency noise is therefore filtered before measuring, allowing for better estimation results.

8.2.3 Development of a Modelling Strategy

8.2.3.1 Selection of an appropriate sensor topology

Four possible sensor topologies were investigated and discussed in Chapter 3, namely

- Single-element plate sensor above ground

- Two-element differential parallel plate sensor above ground

- Three-element differential parallel plate sensor above ground

- Single-element coaxial sensor mounted around the earth conductor

The ground reference is not absolutely defined for the plate sensor as the earth conductivity is finite and in many cases unknown. It was shown from simulations that for the single-element plate sensor, the absolute position of the sensor above the ground plane is very important. Previous researchers added extra capacitance between the sensing plate and ground to provide more attenuation with the added effect of minimising the sensitivity of the output voltage on the ground parameters [12, 13].

As the ground reference is well defined for the single-element coaxial sensor, this sensor is a viable option. The problem with this topology is that the sensor is less mobile and installation may be difficult. The coaxial sensor is a good long-term possibility. From a mobility point of view, the plate sensor above ground is a much better option. It would be useful if the plate sensor could be changed to be less sensitive to the ground parameters.

This can be achieved by using multiple sensing elements and measuring differentially. In principle this agrees with the design recommendations of Baxter as given for general capacitive sensing applications, namely that multiple electrode sensors are better stabilised [24]. It was shown that the two-element plate sensor is almost insensitive to sensor height above ground if the sensor is placed lower than 10 % of the transmission line height above ground (cfg. Figure 4.6). Although a similar analysis was not done for the three-element sensor, it is assumed to have the same benefit.

It was found that the sensor capacitance has the biggest single influence on the voltage division ratio. A decrease in the sensor capacitance will lead to an increase in the division ratio. The width of the sensor has a negligible effect on the induced voltage, because the increase in sensor capacitance and the coupling capacitance between the transmission line and the sensor increased comparatively (cfg. section 4.2.2).

The faraday cage was included as a third conducting element in the three-element sensor. This is a balanced option, maintaining the benefits of the two-element sensor. It was also found that leakage between this floating faraday cage and ground will have a negligible effect on the frequency response of the sensor, even for a relatively small resistive value of 100 MΩ (cfg. Figure 4.19). It is, therefore, advised that the support structure be connected to this floating faraday cage in order to eliminate adverse effects caused by the support structure. This also provides a useful location for the deliberate introduction of a leakage path to ground to mitigate the effects of charge accumulation under DC conditions.

8.2.3.2 Development of an equivalent circuit for the sensor topology

The equivalent circuit derivation is based on the equivalent transmission line model. Only the shunt elements, namely capacitances and conductances are included in the equivalent circuit model as the

sensor is used at frequencies where it can be regarded as a point element. Usually the conductances are ignored for transmission line models, but it was shown that some of the conductance elements are necessary to complete the sensor model for all practical situations. Using these models, it could be shown that a support structure with finite leakage resistance to ground affects the transfer function of the sensor topology greatly, especially in the low-frequency region. It was also found that the amount of deviation caused by the leakage depends on which element has leakage to ground. If the leakage is balanced between the sensing elements or only from the faraday cage to ground, the influence of the leakage is negligible.

The loading effects of the sensor instrumentation could also be shown by adding a termination impedance across the differential output elements. The termination impedance consists of a parallel RC combination, where the capacitor, C_t, determines the voltage attenuation factor of the sensor and the resistor, R_t, determines the low-frequency pole.

The similarities between a standard capacitive voltage divider and the capacitive voltage sensor is clearly visible from the equivalent circuit for the single-element plate sensor. Unfortunately the low-voltage capacitance between the sensing plate and ground is not defined very well, but the added termination capacitance will improve the situation. The single-element coaxial sensor have a model identical to the single-element plate sensor if the earth wire is considered as the absolute ground reference.

The two- and three-element plate sensors have relatively complicated equivalent circuits. Thévenin equivalent circuits may be derived and prove very useful for these two sensor topologies. For the ideal case, where all resistors may be ignored, it was found that the Thévenin equivalent impedance consists of only a capacitive element. From the Thévenin equivalent circuit, the voltage division principle is again clear, where the high voltage capacitor is formed by the Thévenin equivalent capacitance and the low voltage capacitor by the termination capacitor added at the input of the buffer instrumentation.

It was also shown from the equations that the Thévenin equivalent capacitance may be approximated by the sensor capacitance, i.e. the capacitance between the differential sensing elements. For the two-element sensor this is simply the capacitor between $s1$ and $s2$,

$$C_{TH} \approx C_{s1s2} \tag{8.1}$$

as defined in Figure 3.7. For the three-element sensor it is a combination of series and parallel capacitances,

$$\begin{aligned} C_{TH} &\approx C_{s1s2} + C_{s1s3}//C_{s2s3} \\ &\approx C_{s1s2} + \frac{C_{s1s3}C_{s2s3}}{C_{s1s3} + C_{s2s3}} \end{aligned} \tag{8.2}$$

as defined in Figure 3.11.

These approximations are valuable when calculating the loading effects of the buffer instrumentation.

8.2.3.3 Determination of the model parameters for the equivalent circuit from electric field simulations

The original simulations were done using a 2-dimensional electric field solver. A wide range of simulations were done using this solver to determine the sensor response for the different geometrical parameters. This provided a good understanding of the basic dependencies of single element and differential capacitive voltage sensors. Trial measurements, as discussed in the dissertation, indicated that the 2D simulations gave inadequate answers as end effects are not properly modelled.

Further simulations were, therefore, done using a 3-dimensional electric field solver. All simulations for the final measurements, as recorded in Chapter 7 were done with the 3D package. Comparisons between 2D and 3D simulations showed how end effects influence the capacitance parameters. This was expected, but required quantitative computation as discussed in section 4.2.3.

Simulations were also done for small variations in some of the geometric parameters for the sensitivity analysis, which was presented in section 6.4. These simulations provided valuable insight into the expected accuracy obtainable from the sensor and current instrumentation. It was clear that the dependency on accurate positioning of the sensor reduces when the transmission line to sensor separation is increased. This prove positive for practical installations, where the transmission line to sensor separation will be significantly larger than the separation in the testing arrangement.

8.2.3.4 Time and frequency responses of the sensor topologies

For the ideal case, no resistors are taken into account in the above-mentioned model. The voltage division ratio of the ideal case is referred to as the high frequency asymptote for the sensing arrangement, as this is the value of the high frequency response of the sensor topology.

The important contribution from this approach is, however, that it provides a reference for the influence of certain non-ideal effects. It is easy to calculate the position of the low-frequency pole formed by the termination resistor. The equivalent parallel capacitor is the termination capacitor in parallel with the Thévenin equivalent capacitance of the ideal circuit. The pole is given by equation 8.3:

$$f_c = \frac{1}{2\pi R_t (C_t + C_{TH})} \tag{8.3}$$

The three-element sensor topology has a relatively complex equivalent circuit, as was shown in Chapter 3. The Thévenin equivalent capacitance can be approximated by the sensor capacitance, as discussed in Chapter 4 and equation 8.2 and the calculation of the above-mentioned low-frequency pole remains relatively straightforward. It was found that an input resistance of R_t=10 MΩ is adequate for the practical sensor topologies that were evaluated, locating the low-frequency -3 dB point below 5 Hz.

Problems arise when the support structure presents finite leakage resistance to ground. For this situation, the complete circuit model must be used with appropriate leakage paths added. The following models were defined to test the effects of several non-ideal element combinations:

- Default model - only capacitances are included in the model

- R_{s1g} model - add a single resistor from the top plate to ground to the default model

- R_{s2g} model - add a single resistor from the bottom plate to ground to the default model

- R_{s3g} model - add a single resistor from the faraday cage to ground to the default model

- R_{s1g}/R_{s2g} model - add two resistors to the default model, one each from the top and bottom plate to ground

- R_{s1s3}/R_{s2s3} model - add two resistors to the default model, one each between the top and bottom plates and the faraday cage

It was found that connecting a conducting path to one of the sensing plates, as were done for the R_{s1g} or R_{s2g} model, causes severe distortion in the low-frequency region. The transfer functions for these models with added 100 MΩ resistors are shown in Figure 8.1 (repetition of Figure 4.19).

The decrease of attenuation at the lower frequencies is attributed to the fact that charge is conducted away from one of the plates when a resistive path exists between that plate and ground. For the R_{s2g} model, this means that the bottom plate voltage is lowered with respect to the top plate voltage and the differential voltage is increased. For the R_{s1g} model, the top plate voltage is lowered with respect to the bottom plate voltage, which also explains the phase reversal as shown in Figure 8.1. For the R_{s3g} model, the same leakage of 100 MΩ has a negligible influence on the frequency response as shown in Figure 8.1.

This finding has important implications for sensors mounted on support structures, as is invariably the case. For long-term deployment, where support structures will inevitably develop conductive paths due to pollution, degradation of the low frequency responses can be expected. The same conclusions apply to single-plate sensors.
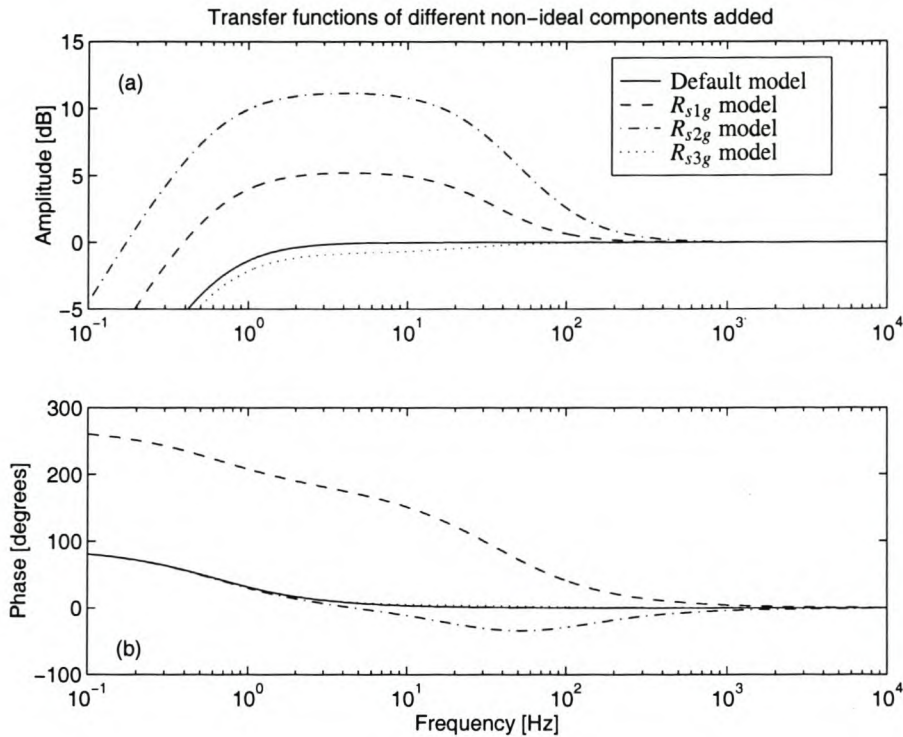
Figure 8.1: Frequency response of three-element plate sensor with R_{s1g}, R_{s2g} or R_{s3g} added

All the other models involve conducting paths from both sensing plates or from the faraday cage. For these models, the common mode voltage is influenced, but the differential voltage remains almost unaffected. The transfer function may be approximated by the default model with only the termination resistor added. It was shown in Figures 4.20 and 4.21 that the deviation in transfer function is negligible. One of these models are suggested for use when ion current may influence the measurement, eg. when measuring underneath HVDC lines.

This is an important finding, because it implies that calibration accuracy can be maintained by designing the support structure for the two- and three-element sensors appropriately. More specifically, if the support structure introduces earth leakage paths to all elements, or only to the faraday cage in the three-element case, good low frequency responses can be maintained.

8.2.4 Experimental evaluation of the prototype sensor under laboratory conditions

8.2.4.1 Comparison of measured waveforms with the predicted time and frequency domain responses

Initial measurements proceeded in parallel with sensor analysis and development. Important findings from the initial measurements include:

- Galvanic isolation is very important in the design of the sensor instrumentation and support structure in order to maintain good low frequency response

- 2D simulations are not adequate to predict the response of the sensor topology, because end effects are always significant

- A well-defined geometry is required for the measurement arrangement

Two sensors were evaluated, namely a single element coaxial sensor and a three-element differential plate sensor. Special measuring arrangements were assembled in the high voltage laboratory for the final measurements. Both sensors were tested using slow and fast impulse tests as well as 50 Hz AC tests for calibration purposes of the coaxial sensor. The measured results were compared both in the time- and frequency domain with the simulations obtained from the equivalent circuit models discussed in Chapter 3. It was found that filtering is required for all the impulse tests in order to effectively compare the waveforms.

Excellent correlation was found between the measured and simulated waveforms for both the sensors. No correlation coefficient value was less than 99 %, which for all practical purposes can be considered as a perfect match [55].

The impulse peak value comparisons for both sensors, as discussed in Chapter 7, indicated that a small mean error exist, which can be ascribed to calibration errors caused by the instrumentation and uncertainties in positioning. The deviation from this mean is within the expected ±4.9 % error bands discussed in section 6.4. The maximum errors versus time showed the same accuracy within the ±4.9 error band, but with a larger mean error.

Different models with different conducting paths to ground were also evaluated during the laboratory tests. The agreement between these tests and the predicted waveforms indicate that the proposed circuit models are valid in the frequency range of interest.

It can, therefore, be concluded that a suitable wideband sensor model was developed. The bandwidth of the sensing topology is limited by the instrumentation's high frequency cut-off. The low-frequency behaviour is limited by the resistive value of the termination impedance as well as conducting paths between the sensor and ground. Suitable circuit models were developed to predict the sensor's response both in the time and frequency domain.

For a properly designed sensor the following aspects are important:

- Multiple electrodes for differential voltage sensing

- High valued impedance termination

- Galvanically isolated interface instrumentation

- Proper knowledge of the capacitance parameters of the sensor, if the calibration constant must be predicted

- Balanced support structure to eliminate the adverse effects of leakage

It was shown that when the above criteria are met, a mobile, wide-bandwidth sensor with sufficient accuracy was designed.

8.2.4.2 Estimation of circuit model parameters from the laboratory measurements and equivalent circuit model

Parameter estimation was attempted using the laboratory measurements, but with limited success. Bounded estimation was used, which means that the estimated parameter values will be contained within the specified limits. The estimated circuit model parameters could be used for relatively accurate comparative simulations of similar arrangements. However, the actual circuit model parameters did not correlate with the values obtained from the 3D electric field solver. This is ascribed to the fact that the sensor amounts to the interconnection of several capacitive voltage dividers. This means that several capacitance ratios are estimated, but the actual value of any single capacitive coupling element cannot be estimated. Further work is thus required.

8.3 Summary of Main Conclusions and Contributions

8.3.1 Main Conclusions

The following main conclusions from the research discussed in this dissertation should be emphasized:

- Capacitive voltage sensors exhibit a predictable response if a well-defined topology and good ground reference exist

- Such well-defined topologies can be implemented using multiple electrodes and by measuring the differentially induced voltages

- The differential parallel plate topology is superior to the single- plate sensor topology

- Leakage elements to ground have an important influence on the time- and frequency responses of the sensor and should be included in the equivalent circuit models

- In order to mitigate the effects of charge collection when measuring under DC conditions, leakage paths to ground have to be deliberately introduced

8.3.2 Main Contributions

The following main contributions were made by the research discussed in this dissertation:

- Two novel capacitive sensing topologies for open-air high voltage transmission line applications were investigated, namely
  - Differential parallel plate sensor (with separate faraday cage)
  - Single element coaxial sensor mounted around the earth conductor

- Equivalent circuit models were derived for the analysis of the above sensor topologies

- Time- and frequency domain analysis of the sensor responses were calculated using the above equivalent circuit models and Matlab®. These simulations included:
  - Quantification of the effect of interface instrumentation on the sensor response in both the time- and frequency domain
  - Quantification of the effect of support structures and other leakage paths to ground in both the time- and frequency domain

- High speed, optically isolated, digital interface instrumentation was developed

8.4 Recommendations and Future Research

The investigation gives rise to several recommendations for future research and will be listed according to recommendations for the sensors and the interface instrumentation separately.

8.4.1 Sensor recommendations

8.4.1.1 Field measurements underneath a single-phase transmission line for final verification of the sensor's operation

One of the main recommendations is that the proposed sensor topologies should be evaluated under field conditions. A proper support structure with resistance approaching infinity was built and tested, which should allow very wide bandwidth measurements in the practical situation.

Two options exist at this stage: measurements underneath a DC line such as the Cahora Bassa HVDC line or measurements underneath a single-phase railway line. AC railway lines are available where the 50 Hz may be used for calibration purposes. Frequent transients are available for measurement as well, as a transient is initiated every time the train leaves or enters any specific section.

Provision was made for connection of a resistor with a known value between the faraday cage and ground in order to remove the effects of ion currents and space charge. This allows the effects of space-charge and ion current to be assessed.

8.4.1.2 Estimation of circuit model parameters from the laboratory or field measurements and equivalent circuit model

Parameter estimation was attempted using the laboratory measurements for the three-element plate sensor, but with limited success. Too many degrees of freedom exist in the circuit model of the three-element sensor topology. It may be necessary to derive an intermediate equivalent circuit and then estimate the different parameters in several steps. A recommendation is to regard the response of each sensing plate separately and interconnect the separate Thévenin equivalent circuits with the known sensor capacitances. If significant leakage elements exist, it is advisable to first estimate the capacitive components using the high frequency data and then use the low frequency data to estimate the leakage components.

No parameter estimation was attempted for the single-element coaxial sensor, but this should be

fairly easy, as only one element need to be estimated, namely the capacitance between the transmission line and the sensing plate. The capacitance between the sensing plate and the ground reference is dominated by the coaxial sensor capacitance and may be fixed at this value.

8.4.1.3 Estimation of transmission line sag from field measurements

It was argued in section 4.2.2 that sag of the transmission line can be determined using the differential plate sensor. It was found that the relationship between the induced voltage and the sensor height as a percentage of the line height is linear. The determination of the transmission line sag may be determined together with parameter estimation.

8.4.1.4 Addition of guarding elements for differential plate sensor

It was found that pollution influenced the conductivity between the sensing plates negatively, i.e. the leakage between the sensing plates and the faraday cage increased to unacceptable levels. This pollution forms on the exposed surface of the PCB substrate, which is also where the increased leakage current flows. A guard ring on the outer perimeter of each sensing plate and the faraday cage will as shown in Figure 8.2 will reduce the leakage between the sensing elements and the faraday cage.

sensing element
isolating strip
guarding element
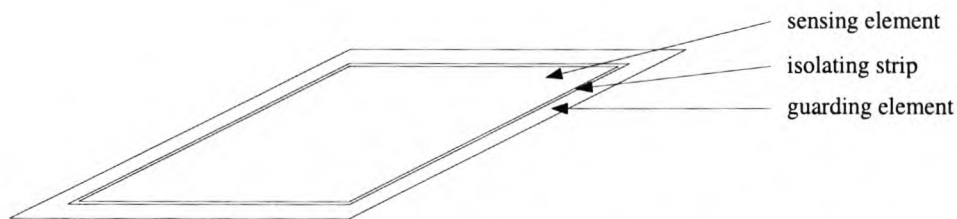
Figure 8.2: Guard ring proposal for sensing- and faraday cage elements of differential plate sensor

8.4.1.5 Field measurements underneath a three-phase transmission line using multiple sensors

If the sensor topology evaluation for a single phase transmission line is completed, the next logical extension would be to use three sensors underneath a three-phase line. The decoupling principle were discussed and proved by van Heesch *et al* [12] and Roberts & Hoch [13].

8.4.1.6 Midline sensing or intersubstation measurement possibilities

One of the main motivations for developing a mobile sensor with a wide bandwidth was to enable midline sensing of high frequency waveforms. Research on the following topics are now possible:

- Carrier propagation

- Standing waves

- Harmonic penetration

- Fault location

- Lightning impulse studies

- Insulation coordination under transient conditions

- Effects of varying earth conductivity of transmission on long lines

8.4.2 Instrumentation recommendations

8.4.2.1 Power supply

The digitising process and digital signal conditioning have high power requirements. A switching power supply with suitable rechargeable batteries should be developed.

8.4.2.2 Additional buffer between the gain adjust section and the ADC driving circuitry

Figure 5.6 in Chapter 5 showed that the ADC driving circuitry has a loading effect on the earlier gain adjust section when the anti-aliasing filter is bypassed. To prevent the drop in gain, the addition of a buffer between the gain adjust section and the ADC driving circuitry is advised when the filter is bypassed.

8.4.2.3 Instrumentation speed upgrade

It is proposed that the 12 bit mode of the instrumentation may be upgraded to run at 10 MHz. This will complicate the digital control logic significantly.

The proposed data transmission scheme is similar to the 8 bit mode, but now two bytes are transmitted between every synchronisation byte. The principle is shown in Figure 8.3. The extra 4 bits of two 12-bit data points, which are discarded in the 8 bit mode, are now combined into one byte so that three bytes are sent between every two synchronisation bytes.
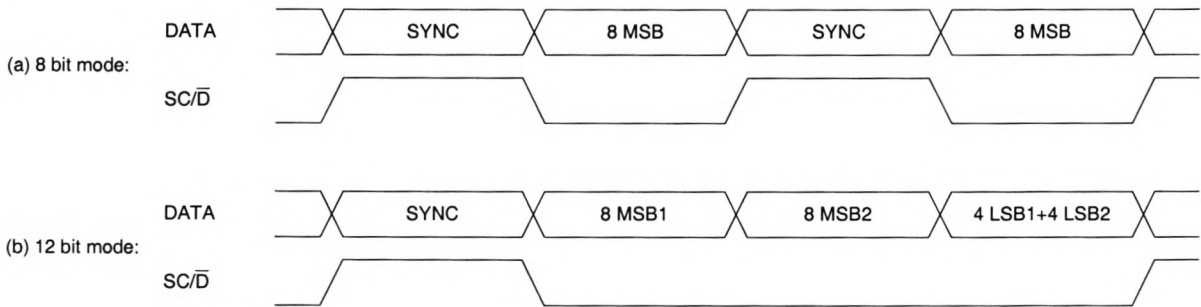
Figure 8.3: Possible timing diagrams for speed upgrade of sensor instrumentation

Appendix A

Practically Measured Values of Various Parameters

A.1 Introduction

One of the philosophies taught to the undergraduate students is: "To measure is to know". Apart from testing the hypotheses and equivalent circuit models proposed in this dissertation, certain parameters were determined or verified by measuring the actual values.

It was found that the true value of the sensor capacitance is very important. It is therefore imperative to determine this capacitance for the calibration of the sensor. Furthermore, the reference measurements are also obtained from a capacitive divider, which may have a voltage division ratio different from the specification.

This appendix is divided into two sections, namely:

- Measurement of the capacitive divider ratio for the reference measurements

- Summary of the measurements done using the three-element parallel plate sensor

A.2 Capacitive Divider for Impulse Reference Measurements

The capacitive divider used for the reference measurements consists of C_{2b} and C_{2t} of Figure 6.3, repeated here as Figure A.1.
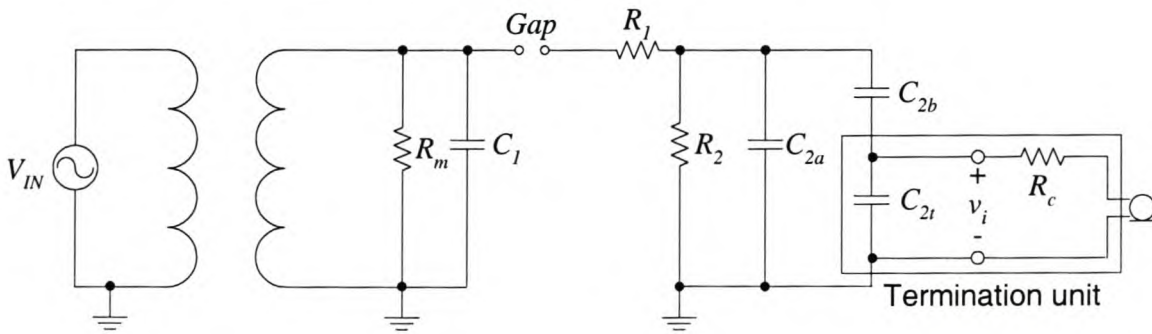
Figure A.1: Circuit diagram of impulse source (R_c=75 Ω)

C_{2b} has a nominal value of 1 200 pF and forms part of the standard component values for impulse generation etc. It may also be used in a measuring arrangement and therefore has an output port, which is either shorted or connected to the termination unit. Different units can be connected for different voltage division ratios, while compensating for the cable impedance of 75 Ω . The unit that was used has a maximum voltage rating of 75 kV and a nominal division ratio of 100.

The actual value of the 1 200 pF capacitor was measured using a Schering bridge by Mr. P Pieterse of the high voltage laboratory. The values were as follows:

- 1 252.2 pF at 20 kV

- 1 255.1 pF at 50 kV

An HP4260A measuring bridge was also used to measure the capacitance giving a value of 1 230 pF$\pm$ 22 pF. At the positive limit this agrees well with the value of 1 252.2 pF obtained from the Schering bridge.

The capacitance of the 75 kV terminator was measured using an HP4260A measurement bridge and an Escort ELC-131D digital LCR meter. The values for the capacitance of this unit is listed below:

- HP bridge $\rightarrow$ 121.5 nF$\pm$2.2 nF

- Escort meter $\rightarrow$ 121.9 nF, with no indication of accuracy

The values used for the calibration ratio of the divider are the measurements using the HP 4260A bridge, namely C_{2b}=1 230 pF and C_{2t}=121.5 nF. The ratio is given by equation A.1:

$$C_{ratio} = \frac{C_{HV}}{C_{HV} + C_{LV}} \qquad (A.1)$$

$$= \frac{1.230}{1.230 + 121.5}$$

$$= \frac{1}{99.8}$$

which is approximated by a ratio of 100 as mentioned in Chapter 6.

A.3 Three-Element Plate Sensor Measurements Summary

Table A.1: Summary of arrangement and excitation magnitude for measured results for three-element parallel plate sensor

Termination	Model Group	Line height [m]	Slow impulse tests			Fast impulse tests		
			# of tests	$\min(V_p)$ [kV]	$\max(V_p)$ [kV]	# of tests	$\min(V_p)$ [kV]	$\max(V_p)$ [kV]
10 MΩ //30 nF	Default model	1.5	9	3.12	3.21	9	8.21	8.41
		2.0	8	3.55	3.79	9	7.49	10.61
		2.5	8	2.72	2.75	4	9.64	9.72
		3.0	8	2.92	2.95	9	11.96	12.06
	R_{s2g} model	2.0	9	2.45	3.44	8	13.55	17.44
		3.0	8	2.93	3.79	6	22.35	22.92
	R_{s1g}/R_{s2g} model	2.0	6	2.77	2.81	6	11.32	11.60
		3.0	6	3.24	3.33	6	22.33	27.53
	R_{s3g} model	2.0	6	2.40	3.00	6	11.56	12.12
		3.0	7	2.47	5.15	7	6.15	30.25
10 MΩ //10 nF	Default model	2.0	2	3.32	3.34	2	8.96	9.00
		3.0	3	3.78	4.10	3	13.66	16.58
	R_{s1g}/R_{s2g} model	2.0	2	1.81	1.83	2	8.87	8.92
		3.0	3	2.81	2.84	3	18.63	18.66
	R_{s1s3}/R_{s2s3} model	2.0	6	1.86	2.77	6	7.70	9.69
		2.0	3	1.12	1.15	3	8.82	8.95
		3.0	6	2.74	4.75	6	14.23	16.08
30 kΩ //10 nF	Default model	2.0	6	2.76	3.66	3	6.24	6.34
		2.0	3	1.20	1.21	2	8.25	8.30
		3.0	6	2.91	2.95	6	6.29	8.65
	R_{s2g} model	2.0	6	1.31	2.61	6	8.39	8.48
		2.0	3	1.25	1.26	3	8.92	9.05
		3.0	6	1.31	2.88	6	13.03	20.37
	R_{s1g}/R_{s2g} model	2.0	6	2.90	2.95	6	8.78	8.91
		2.0	3	1.25	1.25	3	8.74	8.77
		3.0	6	3.01	3.10	6	12.33	12.64
	R_{s3g} model	2.0	6	1.30	2.72	6	8.39	8.53
		2.0	3	1.29	1.30	3	8.48	8.53
		3.0	6	3.03	3.08	6	12.68	12.84

Appendix B

Charge Simulation Method

Section B.1 reviews the basic mathematical relationships of the transmission line and line and plate sensors. The basic idea of charge induced on a nearby conductor is explored together with a brief discussion of the charge simulation method (CSM), which is commonly used to analyse 2D structures. The capacitive coupling between the different elements is refined to give an equivalent circuit diagram for the transmission line and sensor topology.

B.1 Field Analysis of Simple Sensor Topology

This section is included to describe the basis of the Charge Simulation Method (CSM). The CSM is very powerful and is often used in power system analysis. It is relatively simple to implement when using only line charge elements in a 2-dimensional analysis. The method also promotes insight into the field relations for certain simple geometries. The discussion that follows is by no means complete, but discus the use of the basic infinite line charge element and is applied specifically to the capacitive sensing problem. One or more conductors are therefore regarded as "floating" at a voltage that must be determined.

Section B.1.1 starts the discussion by giving the capacitance of a single transmission line above ground. Section B.1.2 gives the extension to multiple transmission lines. Sections B.1.3 and B.1.4 discuss how the induced voltage in secondary lines and plates may be calculated using the line charge approximation. A comparison between the CSM and results from Electro© is given at the end of section B.1.4. Electro© is a commercial electric field solver from *Integrated Engineering Software* utilising the Boundary Element Method (BEM). The BEM may be considered as a specialised form of the CSM [68].

B.1.1 Single transmission line above ground

The equations for a single transmission line above an infinite ground plane is well-known; a typical example of a derivation is given by Haus & Melcher [79]. A single line charge, λ_l, at a height a is used to model the conductor with finite radius, r_l, at height l as shown in Figure B.1. The equipotential contours around a single line charge above a perfect ground is circles, but not concentric. The outside surface of the conductor can, therefore, be fit to an equipotential line and the equivalent line charge determined from this.
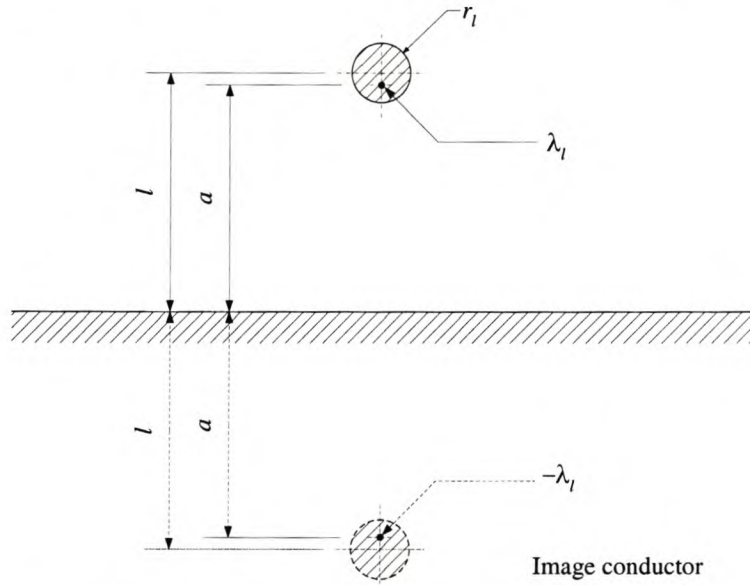
Figure B.1: Single conductor above infinite ground plane – dimensions for equation derivation

The height of the required line charge is given by equation B.1:

$$a = \sqrt{l^2 - r_l^2} \tag{B.1}$$

where l and r_l is defined as in Figure B.1. The magnitude of the line charge is given by equation B.2:

$$\lambda_l = \frac{2\pi\varepsilon_0 U}{\ln(\frac{l}{r_l} + \sqrt{(\frac{l}{r_l})^2 - 1})} \tag{B.2}$$

where U is the voltage on the line relative to ground potential and $\varepsilon_0 = 8.854 \times 10^{-12}$[F/m] is the permittivity of free space.

The capacitance between the line and ground per unit length is given by equation B.3:

$$C = \frac{2\pi\varepsilon_0}{\ln(\frac{l}{r_l} + \sqrt{(\frac{l}{r_l})^2 - 1})} \tag{B.3}$$

B.1.2 Multiple conductors above ground

For multiple conductors, the mutual and self capacitances for the arrangement need to be determined. The equations may be written in matrix form, as discussed by [80, 81, 82, 83]. The inverse of the capacitance matrix, or the potential matrix ($P = 1/C$), consists of the so-called Maxwell potential coefficients, which are used very often.

Multiple conductors' dimensions are defined in Figure B.2.
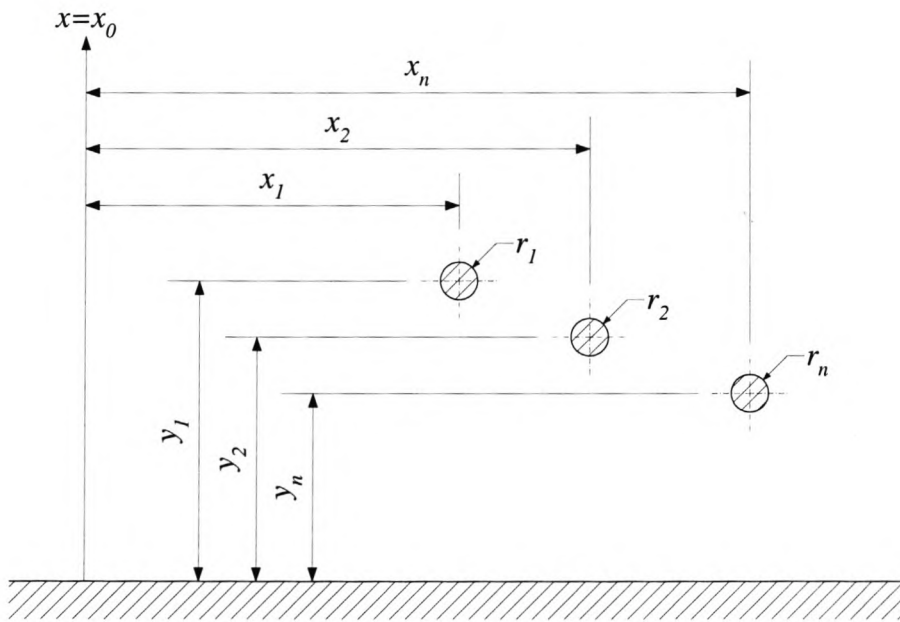
Figure B.2: Multi conductor transmission line dimensions

The potential coefficients are defined by [82, 83]:

$$p_{ij} = \frac{1}{2\pi\varepsilon_0} \ln \frac{\sqrt{(y_i + y_j)^2 + (x_i - x_j)^2}}{\sqrt{(y_i - y_j)^2 + (x_i - x_j)^2}} \tag{B.4}$$

The charge distribution and voltage on the different elements are related by the following matrix equation:

$$C = inv(P) \tag{B.5}$$

and

$$Q = CV \tag{B.6}$$

The capacitance of conductor i to ground is equal to the sum of row i's elements, i.e.

$$C_{ig} = \sum_{j=1}^{n} C_{ij} \tag{B.7}$$

for a system with n conductors.

B.1.3   Induced voltage onto secondary conductor above ground

Using basic voltage division, it is easy to find the induced voltage under static conditions on a secondary conductor parallel to the first conductor [84]. With the mutual capacitances as defined in Figure B.3, the induced voltage may be written as:

$$V_s = \frac{C_{ls}}{C_{ls} + C_{sg}} V_l \tag{B.8}$$

where V_l is the voltage on the top line and V_s the induced voltage on the bottom line due to V_l.
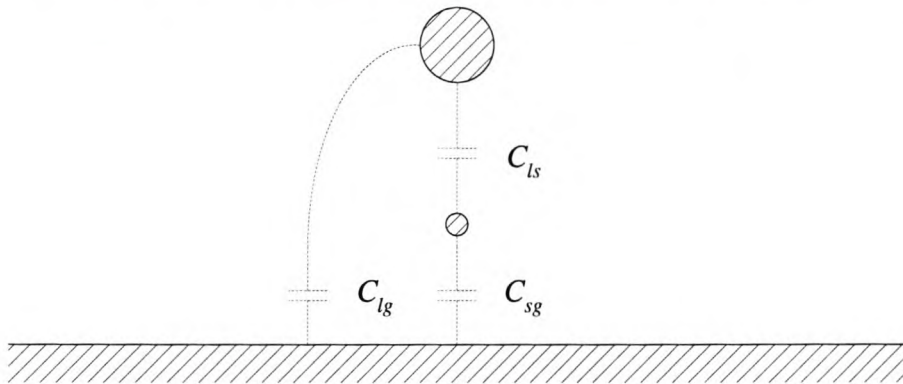
Figure B.3: Geometry of single transmission line with secondary line onto which a voltage may be induced

Using equation B.6, the matrix equation for the system would be:

$$\begin{bmatrix} Q_l \\ Q_s \end{bmatrix} = \begin{bmatrix} C_{ll} & -C_{ls} \\ -C_{sl} & C_{ss} \end{bmatrix} \begin{bmatrix} V_l \\ V_s \end{bmatrix} \tag{B.9}$$

where the subscripts l and s refers to the main transmission line and the secondary (induced) line respectively.

The capacitance matrix's non-diagonal elements are always negative. For the purpose of this discussion, the negative sign is added explicitly in the equations, so that the element numbering may be used directly in the circuit analysis.

If it is assumed that the bottom conductor is initially charge-free, Q_s is zero and the matrix equation can be solved for V_s:

$$V_s = \frac{C_{sl}}{C_{ss}} V_l \qquad (B.10)$$

where both C_{sl} and C_{ls} are negative and equal each other. By definition (cfg. equation B.7), the capacitance of the bottom line to ground is equal to the sum of $-C_{sl}$ and C_{ss}:

$$C_{sg} = -C_{sl} + C_{ss} \qquad (B.11)$$

or

$$C_{ss} = C_{sl} + C_{sg} \qquad (B.12)$$

and equations B.8 and B.10 give the same answer.

B.1.4 Induced voltage onto plate/plates underneath main conductor

The last derivation forms the basis for the charge simulation method (CSM). This method may be expanded to a single or double plate sensor by modelling the sensors with multiple thin lines next to each other. This concept is demonstrated in Figure B.4. If multiple lines are used for a plate in the sensing position, the sensor elements in equation B.9 are also matrices as given by equation B.13. The method is equivalent to the "method of spheres" developed and discussed by Tranen & Wilson [85] and Shih *et al* [86].
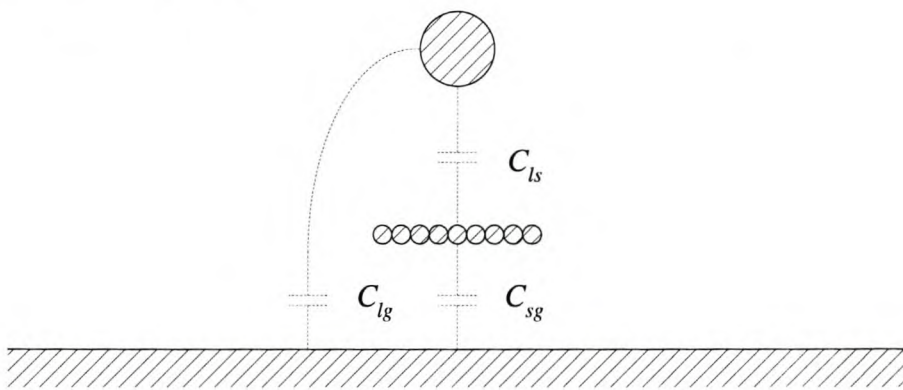
Figure B.4: Single overhead line and multiple lines to model a sensing plate inserted into the field

The equation has the same form as equation B.9 except that the elements defining the capacitance between the main line and the sensor 'line' are now matrices themselves.

$$\begin{bmatrix} Q_l \\ [Q_s] \end{bmatrix} = \begin{bmatrix} C_{ll} & -[C_{ls}] \\ -[C_{sl}] & [C_{ss}] \end{bmatrix} \begin{bmatrix} V_l \\ [V_s] \end{bmatrix} \qquad (B.13)$$

Zero charge is assumed on the sensing "lines", but now it is the sum of the charge on all the lines, i.e.

$$\sum Q_s = 0 \tag{B.14}$$

The induced voltage is then given by equation B.15

$$V_s = \frac{\sum C_{sl}}{\sum \sum C_{ss}} V_l \tag{B.15}$$

and now contain the sum of the separate matrix elements. The voltages on the sensing "lines" are all equal to V_s.

The single and double summation operators indicate that the capacitance matrix for the combined element can be simplified to a single number. This value should correspond to the actual capacitance to the order of approximation of the lines for a single plate.

Similar equations may be derived for multiple plate sensors. The diagram for a two-plate sensor similar to the original investigation of this dissertation is shown in Figure B.5.
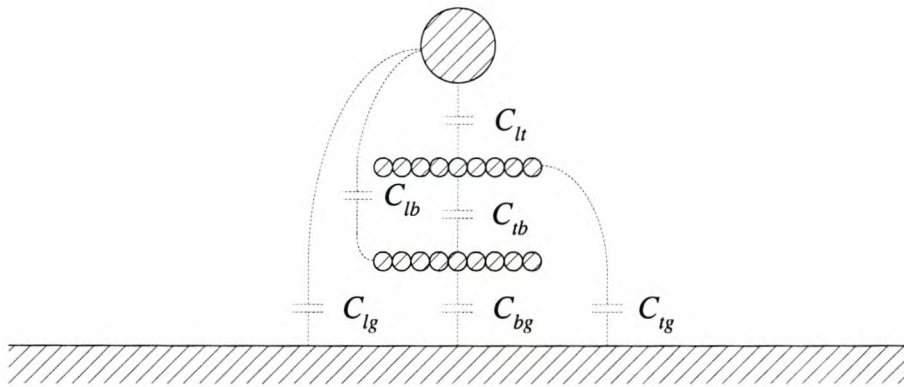
Figure B.5: Single overhead line and two sensing plates simulated using multiple lines

The matrix equation for this topology is given by equation B.16:

$$\begin{bmatrix} Q_l \\ [Q_t] \\ [Q_b] \end{bmatrix} = \begin{bmatrix} C_{ll} & -[C_{lt}] & -[C_{lb}] \\ -[C_{tl}] & [C_{tt}] & -[C_{tb}] \\ -[C_{bl}] & -[C_{bt}] & [C_{bb}] \end{bmatrix} \begin{bmatrix} V_l \\ [V_t] \\ [V_b] \end{bmatrix} \tag{B.16}$$

Now the sum of all elements of both Q_t and Q_b must equal zero and the voltages for all the lines of each plate are the same, either V_t or V_b.

$$V_t = \frac{\sum\sum C_{tb}\sum C_{bl} - \sum\sum C_{bb}\sum C_{tl}}{\sum\sum C_{bb}\sum\sum C_{tt} - \sum\sum C_{tb}\sum\sum C_{bt}}V_l \tag{B.17}$$

$$V_b = \frac{\sum\sum C_{bt}\sum C_{tl} - \sum\sum C_{tt}\sum C_{bl}}{\sum\sum C_{bb}\sum\sum C_{tt} - \sum\sum C_{tb}\sum\sum C_{bt}}V_l \tag{B.18}$$

where V_t is the induced voltage on the top plate and V_b the induced voltage on the bottom plate. No material properties are taken into account in these equations. In order to have two materials in the same problem, a more complex method will be required, and it is not possible to use these equations. The extension to include more materials is discussed by various authors, amongst others Malik [82] and Singer *et al* [83].

A sample model simulation are compared using equations B.17 and B.18 and a commercial boundary element method (BEM) package. The 2D parameters for this simulation are:

Transmission line height:	1.5	[m]
Sensor height:	0.1	[m]
Sensor width:	0.1	[m]
Distance between sensor plates:	1.6	[mm]
Dielectric constant of substrate between sensor plates:	5.8	

The capacitance matrix values are compared in Table B.1. The CSM solution matrix consisted of 820 elements. (4 elements for the main line, which is actually a bundle of 4 conductors and 408 elements for each plate.)

All values are within 10 % of the more complicated program's values, which gives confidence in the simpler method. The BEM method included a dielectric separating the top and bottom plates. This was accounted for in the CSM solution by multiplying C_{tb} by the dielectric constant of 5.8.

Table B.1: Comparison of ELECTRO© and equations B.17 to B.18

Element	CSM		BEM		% difference
C_{lg}	10.4882	[pF]	10.0200	[pF]	-4.67
C_{lt}	0.5684	[pF]	0.6089	[pF]	6.64
C_{lb}	0.1724	[pF]	0.1803	[pF]	4.40
C_{tg}	10.8435	[pF]	10.6819	[pF]	-1.51
C_{bg}	15.5493	[pF]	15.2546	[pF]	-1.93
C_{tb}	3.0060	[nF]	3.2251	[nF]	6.80

Appendix C

Additional Equations Referenced in Main Text

C.1 Equations for Two-Element Parallel Plate Sensor

When five leakage elements are included in the model, the situation is more complex to the extent that the equations cannot be written in a single line. Generic equations may be written for this situation given by equations C.1 and C.2.

$$V_{TH} = V_l \frac{V_{THn}}{DEN} \tag{C.1}$$

$$Z_{TH} = \frac{Z_{THn}}{DEN} \tag{C.2}$$

$$V_{THn} = s^2 R_{ls1}R_{ls2}R_{s1g}R_{s2g}R_{s1s2}(C_{ls1}C_{s2g} - C_{ls2}C_{s1g}) + sR_{s1s2}\big(R_{ls1}R_{ls2}(C_{ls1}R_{s1g} - C_{ls2}R_{s2g}) +$$
$$R_{s1g}R_{s2g}(C_{s2g}R_{ls2} - C_{s1g}R_{ls1})\big) + R_{s1s2}(R_{ls2}R_{s1g} - R_{ls1}R_{s2g}) \tag{C.3}$$

$$Z_{THn} = sR_{ls1}R_{ls2}R_{s1g}R_{s2g}(C_{s1g} + C_{ls2} + C_{ls1} + C_{s2g}) + R_{s1s2}(R_{s1g}R_{s2g}(R_{ls1} + R_{ls2}) + R_{ls1}R_{ls2}(R_{s1g} + R_{s2g})) \tag{C.4}$$

$$DEN = s^2 R_{ls1}R_{ls2}R_{s1g}R_{s2g}R_{s1s2}(C_{ls2}C_{ls1} + C_{ls1}C_{s2g} + C_{ls1}C_{s1s2} + C_{ls2}C_{s1g} + C_{s1g}C_{s2g} + C_{s1g}C_{s1s2} + C_{ls2}C_{s1s2} + C_{s1s2}C_{s2g}) +$$
$$s(((((C_{ls2} + C_{s2g} + C_{s1s2})R_{ls2} + (C_{ls1} + C_{s1g} + C_{s1s2})R_{ls1})R_{s1g} + (C_{ls2} + C_{s2g} + C_{s1s2})R_{ls1}R_{ls2})R_{s2g} +$$
$$(C_{ls1} + C_{s1g} + C_{s1s2})R_{ls1}R_{ls2}R_{s1g})R_{s1s2} + (C_{s1g} + C_{ls2} + C_{ls1} + C_{s2g})R_{ls1}R_{ls2}R_{s1g}R_{s2g}) +$$
$$((R_{s1g} + R_{ls1})R_{s2g} + R_{ls1}R_{ls2} + R_{s1g}R_{ls2})R_{s1s2} + R_{ls1}R_{s1g}R_{ls2} + ((R_{ls2} + R_{ls1})R_{s1g} + R_{ls1}R_{ls2})R_{s2g} \tag{C.5}$$

where $s = j2\pi f$ is the complex frequency.

C.2 Equations for Three-Element Parallel Plate Sensor

The following equations were derived for the Thévenin equivalent voltage and impedance for the three-element parallel plate sensor for different leakage elements. The equations are written in the format used before, namely:

$$V_{TH} \;=\; V_l \frac{V_{THn}}{DEN} \tag{C.6}$$

$$Z_{TH} \;=\; \frac{Z_{THn}}{DEN} \tag{C.7}$$

When six leakage elements, namely R_{s1g}, R_{s2g}, R_{s3g}, R_{s1s2}, R_{s1s3} and R_{s2s3} are included in the model, the following equations hold:

$$
\begin{aligned}
V_{THn} \;=\; & s^3 R_{s1g}R_{s2g}R_{s3g}R_{s1s2}R_{s1s3}R_{s2s3}\Big(C_{ls1}\big(C_{s3g}(C_{s2s3}+C_{s2g})+C_{s2g}(C_{s1s3}+C_{s2s3})\big)- \\
& C_{ls2}\big(C_{s3g}(C_{s1s3}+C_{s1g})+C_{s1g}(C_{s1s3}+C_{s2s3})\big)+C_{ls3}\big(C_{s2g}(C_{ls1}+C_{s1s3})-C_{s1g}(C_{ls2}+C_{s2s3})\big)\Big)+ \\
& s^2 R_{s1s2}\Big(C_{ls1}R_{ls1}\big(R_{s2g}R_{s3g}(C_{s2g}R_{s1s3}+C_{s3g}R_{s1s3}+C_{s2g}R_{s2s3})+R_{s3g}R_{s1s3}R_{s2s3}(C_{ls3}+C_{s3g}+C_{s1s3}+C_{s2s3})+ \\
& R_{s2g}R_{s1s3}R_{s2s3}(C_{s2s3}+C_{s2g})\big)-C_{ls2}C_{s2g}\big(R_{s1g}R_{s3g}(C_{s3g}R_{s2s3}+C_{s1g}R_{s2s3}+C_{s1g}R_{s1s3})+ \\
& R_{s3g}R_{s1s3}R_{s2s3}(C_{ls3}+C_{s3g}+C_{s1s3}+C_{s2s3})+R_{s1g}R_{s1s3}R_{s2s3}(C_{s1s3}+C_{s1g})\big)+ \\
& C_{ls3}R_{s3g}\big(R_{s1g}R_{s2s3}(C_{s2g}R_{s2g}+C_{s1s3}R_{s1s3})-R_{s2g}R_{s1s3}(C_{s1g}R_{s1g}+C_{s2s3}R_{s2s3})\big)\Big)+ \\
& sR_{s1s2}\Big(C_{ls1}R_{s1g}\big(R_{s1s3}(R_{s2g}+R_{s3g})+R_{s2s3}(R_{s1s3}+R_{s3g})\big)- \\
& C_{ls2}R_{s2g}\big(R_{s2s3}(R_{s1g}+R_{s3g})+R_{s1s3}(R_{s2s3}+R_{s3g})\big)+C_{ls3}R_{s3g}\big(R_{s1g}R_{s2s3}-R_{s2g}R_{s1s3}\big)\Big) \tag{C.8}
\end{aligned}
$$

$$
\begin{aligned}
Z_{THn} \;=\; & s^2 R_{s1g}R_{s2g}R_{s3g}R_{s1s2}R_{s1s3}R_{s2s3}\big((C_{ls1}+C_{ls2}+C_{s1g}+C_{s2g})(C_{ls3}+C_{s3g}+C_{s1s3}+C_{s2s3})+ \\
& (C_{ls3}+C_{s3g})(C_{s1s3}+C_{s2s3})\big)+sR_{s1s2}\big(R_{s1g}R_{s2g}R_{s3g}(R_{s1s3}+R_{s2s3})(C_{ls1}+C_{ls2}+C_{ls3}+C_{s1g}+C_{s2g}+C_{s3g})+ \\
& R_{s1s3}R_{s2s3}R_{s1g}R_{s2g}(C_{ls1}+C_{ls2}+C_{s1g}+C_{s2g}+C_{s1s3}+C_{s2s3})+ \\
& R_{s1s3}R_{s2s3}R_{s2g}R_{s3g}(C_{ls3}+C_{s1s3}+C_{s2s3}+C_{s3g})+R_{s1s3}R_{s2s3}R_{s1g}R_{s3g}(C_{ls3}+C_{s1s3}+C_{s2s3}+C_{s3g})\big)+ \\
& R_{s1s2}\big((R_{s1s3}+R_{s2s3})(R_{s1g}R_{s2g}+R_{s1g}R_{s3g}+R_{s2g}R_{s3g})+R_{s1s3}R_{s2s3}(R_{s1g}+R_{s2g})\big) \tag{C.9}
\end{aligned}
$$

$$
\begin{aligned}
DEN \;=\; & s^3 R_{s1s2}R_{s1s3}R_{s2s3}R_{s1g}R_{s2g}R_{s3g}\big((C_{ls1}+C_{s1g}+C_{ls2}+C_{s2g}+C_{ls3}+C_{s3g})(C_{s1s2}C_{s1s3}+C_{s1s2}C_{s2s3}+ \\
& C_{s1s3}C_{s2s3})+(C_{ls1}+C_{s1g})(C_{ls2}+C_{s2g})(C_{ls3}+C_{s3g})+(C_{ls1}+C_{s1g})(C_{ls2}+C_{s2g})(C_{s1s3}+C_{s2s3})+ \\
& (C_{ls1}+C_{s1g})(C_{ls3}+C_{s3g})(C_{s1s2}+C_{s2s3})+(C_{ls2}+C_{s2g})(C_{ls3}+C_{s3g})(C_{s1s2}+C_{s1s3})\big)+ \\
& s^2\Big(R_{s1s3}R_{s2s3}R_{s1g}R_{s2g}R_{s3g}\big((C_{ls3}+C_{s3g})(C_{ls1}+C_{s1g}+C_{ls2}+C_{s2g})+ \\
& (C_{s1s3}+C_{s2s3})(C_{ls1}+C_{s1g}+C_{ls2}+C_{s2g}+C_{ls3}+C_{s3g})\big)+ \\
& R_{s1s2}R_{s2s3}R_{s1g}R_{s2g}R_{s3g}\big((C_{ls2}+C_{s2g})(C_{ls1}+C_{s1g}+C_{ls3}+C_{s3g})+
\end{aligned}
$$

$$(C_{s1s2} + C_{s2s3})(C_{ls1} + C_{s1g} + C_{ls2} + C_{s2g} + C_{ls3} + C_{s3g})) +$$

$$R_{s1s2}R_{s1s3}R_{s1g}R_{s2g}R_{s3g}\big((C_{ls1} + C_{s1g})(C_{ls2} + C_{s2g} + C_{ls3} + C_{s3g}) +$$

$$(C_{s1s2} + C_{s1s3})(C_{ls1} + C_{s1g} + C_{ls2} + C_{s2g} + C_{ls3} + C_{s3g})) +$$

$$R_{s1s2}R_{s1s3}R_{s2s3}R_{s2g}R_{s3g}\big((C_{ls2} + C_{s2g} + C_{s1s2} + C_{s2s3})(C_{ls3} + C_{s3g} + C_{s1s3} + C_{s2s3}) - C_{s2s3}^2) +$$

$$R_{s1s2}R_{s1s3}R_{s2s3}R_{s2g}R_{s3g}\big((C_{ls1} + C_{s1g} + C_{s1s2} + C_{s1s3})(C_{ls2} + C_{s3g} + C_{s1s3} + C_{s2s3}) - C_{s1s3}^2) +$$

$$R_{s1s2}R_{s1s3}R_{s2s3}R_{s2g}R_{s3g}\big((C_{ls1} + C_{s1g} + C_{s1s2} + C_{s1s3})(C_{ls2} + C_{s2g} + C_{s1s2} + C_{s2s3}) - C_{s1s2}^2)\big) +$$

$$s\Big(R_{s1g}R_{s2g}R_{s3g}(R_{s1s2} + R_{s1s3} + R_{s2s3})(C_{ls1} + C_{s1g} + C_{ls2} + C_{s2g} + C_{ls3} + C_{s3g}) +$$

$$R_{s1s2}R_{s1s3}R_{s2s3}\big(R_{s1g}(C_{ls1} + C_{s1g} + C_{s1s2} + C_{s1s3}) + R_{s2g}(C_{ls2} + C_{s2g} + C_{s1s2} + C_{s2s3}) +$$

$$R_{s3g}(C_{ls3} + C_{s3g} + C_{s1s3} + C_{s2s3})\big) + R_{s1s2}R_{s1s3}\big((R_{s1g}R_{s2g} + R_{s1g}R_{s3g})(C_{ls1} + C_{s1g} + C_{s1s2} + C_{s1s3}) +$$

$$R_{s2g}R_{s3g}(C_{ls2} + C_{s2g} + C_{ls3} + C_{s3g} + C_{s1s2} + C_{s1s3})\big) +$$

$$R_{s1s2}R_{s2s3}\big((R_{s1g}R_{s2g} + R_{s2g}R_{s3g})(C_{ls2} + C_{s2g} + C_{s1s2} + C_{s2s3}) +$$

$$R_{s1g}R_{s3g}(C_{ls1} + C_{s1g} + C_{ls3} + C_{s3g} + C_{s1s2} + C_{s2s3})\big) +$$

$$R_{s1s3}R_{s2s3}\big((R_{s1g}R_{s3g} + R_{s2g}R_{s3g})(C_{ls3} + C_{s3g} + C_{s1s3} + C_{s2s3}) +$$

$$R_{s1g}R_{s2g}(C_{ls1} + C_{s1g} + C_{ls2} + C_{s2g} + C_{s1s3} + C_{s2s3})\big)\Big) +$$

$$\big(R_{s1s2}R_{s1s3}R_{s2s3} + (R_{s1g}R_{s2g} + R_{s1g}R_{s3g} + R_{s2g}R_{s3g})(R_{s1s2} + R_{s1s3} + R_{s2s3}) +$$

$$R_{s1s2}R_{s1s3}(R_{s2g} + R_{s3g}) + R_{s1s3}R_{s2s3}(R_{s1g} + R_{s2g}) + R_{s1s2}R_{s2s3}(R_{s1g} + R_{s3g})\big) \tag{C.10}$$

This is the most complicated model that will ever be required for the three-element parallel plate sensor, as the conductivity of air may be ignored in all practical situations. The equations for 4 other practical models that were modelled in the main text, will also be given here for the sake of completeness. These equations are significantly shorter and are easier to interpret. Some simplifications were attempted for this presentation, but is still uncomplete.

For the R_{s1g}/R_{s2g} model:

$$
\begin{aligned}
V_{THn} &= s^2 R_{s1g}R_{s2g}\big((C_{ls1}C_{s2g} - C_{ls2}C_{s1g})(C_{ls3} + C_{s3g} + C_{s1s3} + C_{s2s3}) + \\
&\quad C_{ls1}C_{s2s3}C_{s3g} + C_{ls3}C_{s2g}C_{s1s3} - C_{ls2}C_{s1g}C_{s1s3} - C_{ls3}C_{s1g}C_{s2s3}\big) - \\
&\quad s\big(R_{2g}(C_{12}(C_{14} + C_{4g} + C_{24} + C_{34}) + C_{14}C_{24}) - \\
&\quad R_{3g}(C_{13}(C_{14} + C_{4g} + C_{24} + C_{34}) + C_{14}C_{34})\big) \tag{C.11}
\end{aligned}
$$

$$
\begin{aligned}
Z_{THn} &= sR_{s1g}R_{s2g}\big((C_{ls1} + C_{ls2} + C_{s1g} + C_{s2g})(C_{ls3} + C_{s3g} + C_{s1s3} + C_{s2s3}) + \\
&\quad (C_{ls3} + C_{s3g})(C_{s1s3} + C_{s2s3})\big) + (R_{2g} + R_{3g})(C_{ls3} + C_{s3g} + C_{s1s3} + C_{s2s3}) \tag{C.12}
\end{aligned}
$$

$$
\begin{aligned}
DEN &= s^2 R_{s1g}R_{s2g}\big((C_{ls1} + C_{s1g} + C_{ls2} + C_{s2g} + C_{ls3} + C_{s3g})(C_{s1s2}C_{s1s3} + C_{s1s2}C_{s2s3} + C_{s1s3}C_{s2s3}) + \\
&\quad (C_{ls1} + C_{s1g})(C_{ls2} + C_{s2g})(C_{ls3} + C_{s3g}) + (C_{ls1} + C_{s1g})(C_{ls2} + C_{s2g})(C_{s1s3} + C_{s2s3}) + \\
&\quad (C_{ls1} + C_{s1g})(C_{ls3} + C_{s3g})(C_{s1s2} + C_{s2s3}) + (C_{ls2} + C_{s2g})(C_{ls3} + C_{s3g})(C_{s1s2} + C_{s1s3})\big) +
\end{aligned}
$$

$$s\big(R_{3g}((C_{13}+C_{3g}+C_{23}+C_{34})(C_{14}+C_{4g}+C_{24}+C_{34})-C_{34}^2+)$$

$$R_{2g}((C_{12}+C_{2g}+C_{23}+C_{24})(C_{14}+C_{4g}+C_{24}+C_{34})-C_{24}^2)+$$

$$(C_{ls3}+C_{s3g}+C_{s1s3}+C_{s2s3})$$ (C.13)

The equations for the R_{s1g}, R_{s2g} or R_{s3g} models are given by:

$$V_{TH} = V_l \frac{V_{THn}}{DEN}$$ (C.14)

$$Z_{TH} = \frac{Z_{THn}}{s \cdot DEN}$$ (C.15)

For the R_{s1g} model:

$$V_{THn} = sR_{s1g}\big((C_{ls1}C_{s2g}-C_{ls2}C_{s1g})(C_{ls3}+C_{s3g}+C_{s1s3}+C_{s2s3})+$$

$$C_{ls1}C_{s2s3}C_{s3g}+C_{ls3}C_{s2g}C_{s1s3}-C_{ls2}C_{s1g}C_{s1s3}-C_{ls3}C_{s1g}C_{s2s3}\big)-$$

$$(C_{ls2}C_{s3g}+C_{ls2}C_{s1s3}+C_{s2s3}C_{ls3}+C_{ls2}C_{ls3}+C_{ls2}C_{s2s3})$$ (C.16)

$$Z_{THn} = sR_{s1g}\big((C_{ls1}+C_{ls2}+C_{s1g}+C_{s2g})(C_{ls3}+C_{s3g}+C_{s1s3}+C_{s2s3})+$$

$$(C_{ls3}+C_{s3g})(C_{s1s3}+C_{s2s3})\big)+(C_{ls3}+C_{s3g}+C_{s1s3}+C_{s2s3})$$ (C.17)

$$DEN = sR_{s1g}\big((C_{ls1}+C_{s1g}+C_{ls2}+C_{s2g}+C_{ls3}+C_{s3g})(C_{s1s2}C_{s1s3}+C_{s1s2}C_{s2s3}+C_{s1s3}C_{s2s3})+$$

$$(C_{ls1}+C_{s1g})(C_{ls2}+C_{s2g})(C_{ls3}+C_{s3g})+(C_{ls1}+C_{s1g})(C_{ls2}+C_{s2g})(C_{s1s3}+C_{s2s3})+$$

$$(C_{ls1}+C_{s1g})(C_{ls3}+C_{s3g})(C_{s1s2}+C_{s2s3})+(C_{ls2}+C_{s2g})(C_{ls3}+C_{s3g})(C_{s1s2}+C_{s1s3})\big)+$$

$$((C_{ls2}+C_{s2g}+C_{s1s2}+C_{s2s3})(C_{ls3}+C_{s3g}+C_{s1s3}+C_{s2s3})-C_{s2s3}^2)$$ (C.18)

For the R_{s2g} model:

$$V_{THn} = sR_{s2g}\big((C_{ls1}C_{s2g}-C_{ls2}C_{s1g})(C_{ls3}+C_{s3g}+C_{s1s3}+C_{s2s3})+$$

$$C_{ls1}C_{s2s3}C_{s3g}+C_{ls3}C_{s2g}C_{s1s3}-C_{ls2}C_{s1g}C_{s1s3}-C_{ls3}C_{s1g}C_{s2s3}\big)-$$

$$(C_{ls1}C_{s2s3}+C_{ls1}C_{ls3}+C_{ls1}C_{s3g}+C_{ls1}C_{s1s3}+C_{s1s3}C_{ls3})$$ (C.19)

$$Z_{THn} = sR_{s2g}\big((C_{ls1}+C_{ls2}+C_{s1g}+C_{s2g})(C_{ls3}+C_{s3g}+C_{s1s3}+C_{s2s3})+$$

$$(C_{ls3}+C_{s3g})(C_{s1s3}+C_{s2s3})\big)+(C_{ls3}+C_{s3g}+C_{s1s3}+C_{s2s3})$$ (C.20)

$$DEN = sR_{s2g}\big((C_{ls1}+C_{s1g}+C_{ls2}+C_{s2g}+C_{ls3}+C_{s3g})(C_{s1s2}C_{s1s3}+C_{s1s2}C_{s2s3}+C_{s1s3}C_{s2s3})+$$

$$(C_{ls1}+C_{s1g})(C_{ls2}+C_{s2g})(C_{ls3}+C_{s3g})+(C_{ls1}+C_{s1g})(C_{ls2}+C_{s2g})(C_{s1s3}+C_{s2s3})+$$

$$(C_{ls1}+C_{s1g})(C_{ls3}+C_{s3g})(C_{s1s2}+C_{s2s3})+(C_{ls2}+C_{s2g})(C_{ls3}+C_{s3g})(C_{s1s2}+C_{s1s3})\big)+$$

$$((C_{ls1}+C_{s1g}+C_{s1s2}+C_{s1s3})(C_{ls3}+C_{s3g}+C_{s1s3}+C_{s2s3})-C_{s1s3}^2)$$ (C.21)

For the R_{s3g} model:

$$
\begin{aligned}
V_{THn} &= sR_{s3g}\big((C_{ls1}C_{s2g} - C_{ls2}C_{s1g})(C_{ls3} + C_{s3g} + C_{s1s3} + C_{s2s3}) + \\
&\quad C_{ls1}C_{s2s3}C_{s3g} + C_{ls3}C_{s2g}C_{s1s3} - C_{ls2}C_{s1g}C_{s1s3} - C_{ls3}C_{s1g}C_{s2s3}\big) - \\
&\quad \big(C_{ls1}(C_{s2g} + C_{s2s3}) - C_{ls2}(C_{s1g} + C_{s1s3})\big) \tag{C.22}
\end{aligned}
$$

$$
\begin{aligned}
Z_{THn} &= sR_{s3g}\big((C_{ls1} + C_{ls2} + C_{s1g} + C_{s2g})(C_{ls3} + C_{s3g} + C_{s1s3} + C_{s2s3}) + \\
&\quad (C_{ls3} + C_{s3g})(C_{s1s3} + C_{s2s3})\big) + (C_{ls1} + C_{s1g} + C_{ls2} + C_{s2g} + C_{s1s3} + C_{s2s3}) \tag{C.23}
\end{aligned}
$$

$$
\begin{aligned}
DEN &= sR_{s3g}\big((C_{ls1} + C_{s1g} + C_{ls2} + C_{s2g} + C_{ls3} + C_{s3g})(C_{s1s2}C_{s1s3} + C_{s1s2}C_{s2s3} + C_{s1s3}C_{s2s3}) + \\
&\quad (C_{ls1} + C_{s1g})(C_{ls2} + C_{s2g})(C_{ls3} + C_{s3g}) + (C_{ls1} + C_{s1g})(C_{ls2} + C_{s2g})(C_{s1s3} + C_{s2s3}) + \\
&\quad (C_{ls1} + C_{s1g})(C_{ls3} + C_{s3g})(C_{s1s2} + C_{s2s3}) + (C_{ls2} + C_{s2g})(C_{ls3} + C_{s3g})(C_{s1s2} + C_{s1s3})\big) + \\
&\quad \big((C_{ls1} + C_{s1g} + C_{s1s2} + C_{s1s3})(C_{ls2} + C_{s2g} + C_{s1s2} + C_{s2s3}) - C_{s1s2}^2\big) \tag{C.24}
\end{aligned}
$$

C.3   General Capacitance Equations

The equation for parallel plate capacitance per unit length is given by:

$$
C = \frac{\varepsilon_0 \varepsilon_r w}{d} \tag{C.25}
$$

where w is the area of the plates per meter length, d is the separation between the plates, ε_0 is the permittivity of free space and ε_r is the relative permittivity of the dielectric substrate. If fringing fields need to be taken into account, when the area to separation ratio becomes small, the equation can be adjusted to the following:

$$
C = \frac{\varepsilon_0(\varepsilon_r w + d)}{d} \tag{C.26}
$$

This implies that fringing in the length dimension is ignored, which is how Electro calculates the capacitance.

Appendix D

Testing of Operation of Coulomb©

D.1   Introduction

Before using the three-dimensional package Coulomb©, several simulations of analytically known situations were completed to compare with the analytic values. This promotes confidence in the program and results, while it provides the user with the opportunity to become familiar with the product and methods.

Three analytic situations were modelled and will be discussed separately in this appendix. The three geometries are the following:

- Single transmission line above ground

- Multiple transmission lines above ground (two/three)

- Parallel plate capacitance

D.2   Single Transmission Line Above Ground

Figure D.1 shows the sectional view of the geometry of a single transmission line above a 200 m wide ground plane (w_g). The simulations discussed in this section were done for a 200 m long section of this geometry, with no variations in the other coordinate directions. The analytical equations were derived for an infinite ground plane and an infinitely long transmission line. As none of the simulations were done for lines higher than 10 m, it was assumed that the analytic condition is approximated sufficiently accurately.
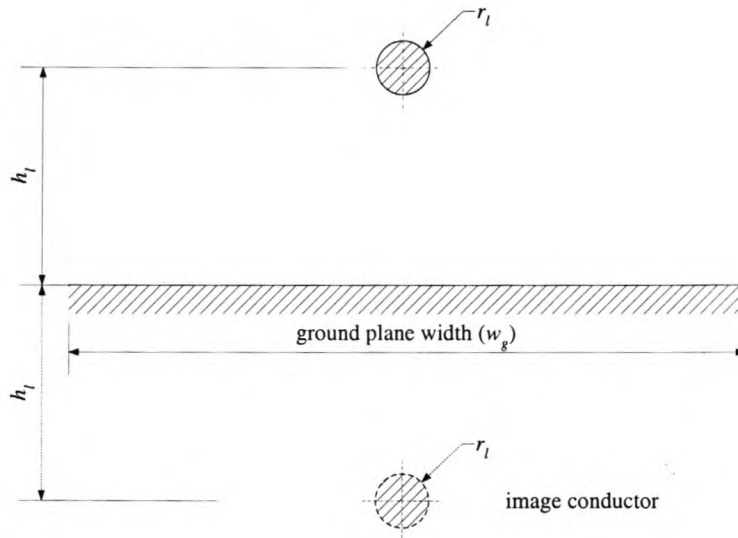
Figure D.1: Single conductor above ground plane for single transmission line simulations

The analytic equation for the capacitance of a single transmission line to ground is given by equation D.1 [79, 81]:

$$C_{lg} = \frac{2\pi\varepsilon_0}{\ln(\frac{h_l}{r_l} + \sqrt{(\frac{h_l}{r_l})^2 - 1})} \tag{D.1}$$

where h_l is the line height above ground and r_l is the line radius as defined in Figure D.1.

This may be simplified if the ratio of the line height, h_l, to the line radius, r_l, is large:

$$C_{lg} \approx \frac{2\pi\varepsilon_0}{\ln(2h_l/r_l)} \tag{D.2}$$

The method of images [79] is often used to simulate an infinite ground plane. The geometry above the ground plane is mirrored below the ground plane and excited with voltages of the opposite polarity. In principle this is equivalent to the use of symmetry planes in Coulomb©, designed to reduce simulation complexity and time. If the ground plane lies in the symmetry plane, as described above, this cannot be implemented in Coulomb© as no conductors may lie in the symmetry plane.

Two simulation geometries were therefore compared with the analytic equation D.2:

- Single transmission line above ground with mirror below the ground plane

- Single transmission line above ground plane with no mirror, i.e. the ground plane is assumed to approximate an infinite ground plane

For a ground plane measuring 200 m × 200 m and a line height of not more than 10 m, the single transmission line without images provides adequate accuracy. More simulations with different line

heights and line radii were therefore also compared with the analytical equation. The results from these simulations are all combined in Table D.1. The biggest error is 3.95 % for a 10 m high line with a 1 m radius. The smallest error is -0.64 % for a 1 m high line with a 0.1 m radius. A lower line with smaller radius is a better approximation for the infinite ground plane and consequently has more accurate results.

Table D.1: Comparison between Coulomb© simulations and analytic equation (cfg. eq. D.1) for a single transmission line above ground

Simulation type	Line dimensions		Capacitance value		Percentage difference [%]
	Height (h_l) [m]	Radius (r_l) [m]	Coulomb© [pF/m]	Analytic [pF/m]	
Mirror image below ground plane	10	1.0	19.30	18.57	3.95
	10	0.5	15.55	15.08	3.11
Single line above ground	10	1.0	19.30	18.57	3.95
	10	0.5	15.55	15.08	3.12
	5	0.5	18.95	18.57	2.04
	1	0.5	40.94	40.13	2.03
	10	0.1	10.71	10.50	2.02
	5	0.1	12.23	12.08	1.22
	1	0.1	18.45	18.57	-0.64

D.3 Multiple Transmission Lines Above Ground

Figure D.2 shows the sectional view of the geometry of a multiple transmission line above a 200 m wide ground plane. The heights and radii of the different conductors are also defined in Figure D.2.

For multiple transmission lines, the capacitance between the different lines and the lines and ground are defined by the potential matrix, P. The potential matrix coefficients are defined by [82, 83]:

$$p_{ij} = \frac{1}{2\pi\varepsilon_0} \ln \frac{\sqrt{(y_i + y_j)^2 + (x_i - x_j)^2}}{\sqrt{(y_i - y_j)^2 + (x_i - x_j)^2}}, i \neq j \tag{D.3}$$

$$p_{ij} = \frac{1}{2\pi\varepsilon_0} \ln \frac{2y_i}{r_i}, i = j \tag{D.4}$$

where x_i and y_i is the coordinates of line i and x_j and y_j the coordinates of line j respectively. The capacitance matrix equals the inverse of the potential matrix:

$$C = inv(P) \tag{D.5}$$
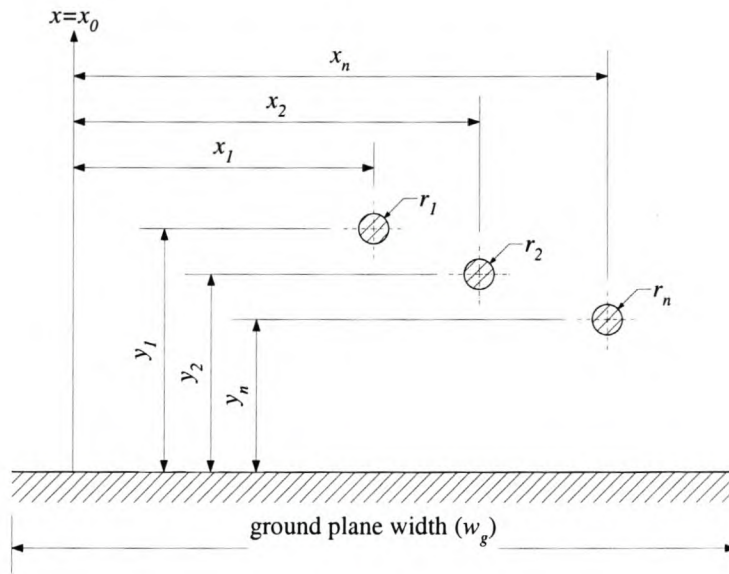
Figure D.2: Multiple conductors above ground plane for simulations

Four sets of simulations were done for 2 lines above a ground plane and two sets for 3 lines above a ground plane. All lines were 100 m long and the ground plane measured 100 m × 100 m. The length of the simulations were reduced to limit the number of elements and hence the simulation time. The dimensions for 2 line-simulations are listed in Table D.2.

Table D.2: Dimensions of simulations for two transmission lines above ground

Simulation #	x_1 [m]	y_1 [m]	r_1 [m]	x_2 [m]	y_2 [m]	r_2 [m]
1	0	10	1.0	0	5	1.0
2	0	10	0.5	0	5	0.5
3	0	5	0.5	0	2.5	0.5
4	1	5	0.5	-1	2.5	0.5

The results for the two-transmission line simulations are given in Table D.3. Except for the C_{1g} terms, all the capacitance values calculated by Coulomb© compare favourably with the analytical value. The large deviation in analytical and numerical capacitance values for C_{1g} is ascribed to:

- The shorter line length

- The finite ground plane

- The close proximity of the different transmission lines

The second transmission line seem to shield the top transmission line from the finite ground plane, thereby reducing the capacitive coupling as calculated by Coulomb©. When the two transmission

lines are offset with respect to each other or moved closer to the ground plane (i.e. the ground plane seems more infinite), the percentage error drops considerably to an acceptable value.

Table D.3: Results summary for two transmission lines above ground simulations

Simulation #	Capacitance [pF/m]						Percentage difference		
	Theoretical			Coulomb©					
	C_{12}	C_{1g}	C_{2g}	C_{12}	C_{1g}	C_{2g}	C_{12}	C_{1g}	C_{2g}
1	10.74	11.77	18.55	10.98	10.89	18.77	-2.25	7.49	-1.23
2	6.21	10.72	14.64	6.15	9.65	14.54	1.02	10.02	0.70
3	10.74	11.77	18.55	10.97	11.49	18.75	-2.16	2.39	-1.10
4	8.06	12.89	19.20	8.08	12.51	19.37	-0.23	2.97	-0.86

The dimensions for the 3 line simulations are listed in Table D.4 and the results in Table D.5. Note that 6 capacitive coupling elements are now compared.

Table D.4: Dimensions of simulations for three transmission lines above ground

Simulation #	x_1 [m]	y_1 [m]	r_1 [m]	x_2 [m]	y_2 [m]	r_2 [m]	x_3 [m]	y_3 [m]	r_3 [m]
5	0	10	0.5	0	7.5	0.5	0	5	0.5
6	0	10	0.5	1	7.5	0.5	-1	5	0.5

Table D.5: Results summary for three transmission lines above ground simulations

Simulation #	Capacitance or Percentage difference	Value					
		C_{12}	C_{13}	C_{23}	C_{1g}	C_{2g}	C_{3g}
5	Theoretical [pF/m]	11.61	1.73	10.86	8.38	5.67	12.45
	Coulomb© [pF/m]	11.79	2.16	11.04	7.34	5.86	12.34
	Percentage difference [%]	-1.59	-24.75	-1.62	12.48	-3.31	0.93
6	Theoretical [pF/m]	10.58	2.83	7.81	7.88	6.95	12.54
	Coulomb© [pF/m]	10.78	2.99	7.89	6.98	6.92	12.51
	Percentage difference [%]	-1.92	-5.78	-0.99	11.37	0.43	0.26

Once again the capacitive coupling calculated by Coulomb© seem very accurate, except where the conductors are shielded from "direct view" of each other or the ground plane. The offset conductors have a better overall accuracy, than for the three conductors in a straight vertical line.

D.4 Parallel Plate Capacitance

Figure D.3 shows a typical square parallel plate capacitor, with plate length l and separation d. The analytic capacitance for a parallel plate capacitor is given by equation D.6:

$$C = \frac{\varepsilon_r \varepsilon_0 A}{d} \tag{D.6}$$

where $A = l^2$ is the area of each of the square plates.
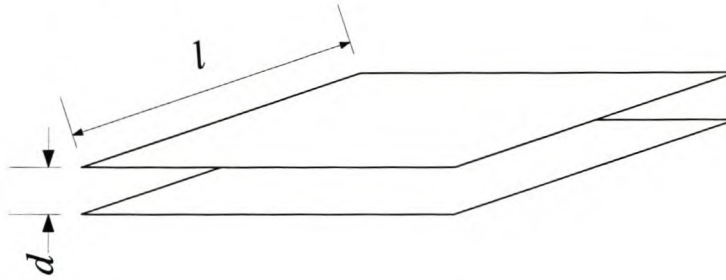
Figure D.3: Geometry of parallel plates for capacitance calculation

The capacitance as defined in equation D.6 was derived from two infinite parallel plates. Leakage of the flux between the plates occur at the edges and are called fringing. This leakage increase the effective area of the two plates. If the plate separation is small enough, the fringing field can be neglected. A_f in Figure D.4 indicates the area added to account for fringing, where the fringing area is the sum of all the small areas and is given by:

$$\begin{aligned} A_f &= 4\frac{ld}{2} + 4(\frac{d}{2})^2 \\ &= 2ld + d^2 \end{aligned} \quad \text{(D.7)}$$
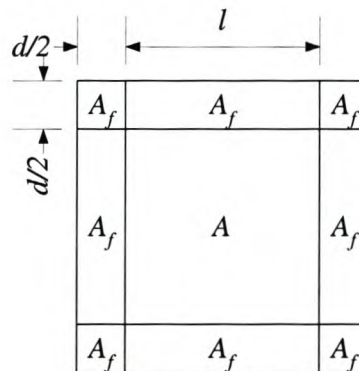
Figure D.4: Top view of the increased effective area for capacitance calculation when including the fringing fields

Half the plate separation, $d/2$ is added to all the edges of the plate to calculate the effective area. This means that the effective length of the plate is increased by the plate separation, d. For air dielectric the equation is as follows:

$$C = \frac{\varepsilon_0(A + A_f)}{d} \quad \text{(D.8)}$$

If the relative permittivity of the dielectric separating the plates differ from unity, the following

equation holds:

$$C = \frac{\varepsilon_r \varepsilon_0 A + \varepsilon_0 A_f}{d} \tag{D.9}$$

The fringing fields pass only through air and their effect on the capacitance is not multiplied by the relative permittivity.

Two sets of simulations were done for the parallel plate capacitors, namely:

- Varying the number of elements on a side in comparison with minimum suggested elements

- Varying the permittivity of the dielectric separating the two plates for an optimal number of elements

For plates with side length l and separation distance d, the suggested number of elements are given by:

$$n \leq \frac{l}{10d} \tag{D.10}$$

This is equivalent to saying that the ratio between the side lengths of an element may not exceed 10.

The minimum number of elements on a side is therefore 2, i.e. 4 elements per plate. Table D.6 lists the capacitance obtained from the Coulomb© simulations with the theoretical capacitance. When ignoring fringing the capacitance is 35.42 nF and when including the fringing it is 39.05 nF, a difference of 10 %.

Table D.6: Comparison of calculated capacitance with theoretical capacitance according to eq. D.6 when ignoring fringing and eq. D.8 when including fringing for different numbers of elements per side

# of elements	Coulomb© capacitance [nF]	Percentage deviation eq. D.6	eq. D.8
1	38.01	7.34	-2.64
2	38.27	8.05	-2.00
4	38.44	8.55	-1.54
8	38.66	9.16	-0.99
16	38.87	9.77	-0.44
32	39.00	10.24	-0.01
65	39.10	10.52	0.25

The voltages applied to the top and bottom plates were +1 V and -1 V respectively. Figure D.5 shows the calculated potential distribution along the top plate for six different element arrangements. From Table D.6 it was seen that fringing plays a smaller role in the calculated capacitance for the single element per plate capacitor than for the 65^2 elements per plate capacitor. This can be

explained when comparing Figure D.5 (a) to (f). The voltage along the edges of the single element per plate capacitor is approximately 0.4 V and the amount of fringing will be much less than when the voltage is close to unity as was applied.
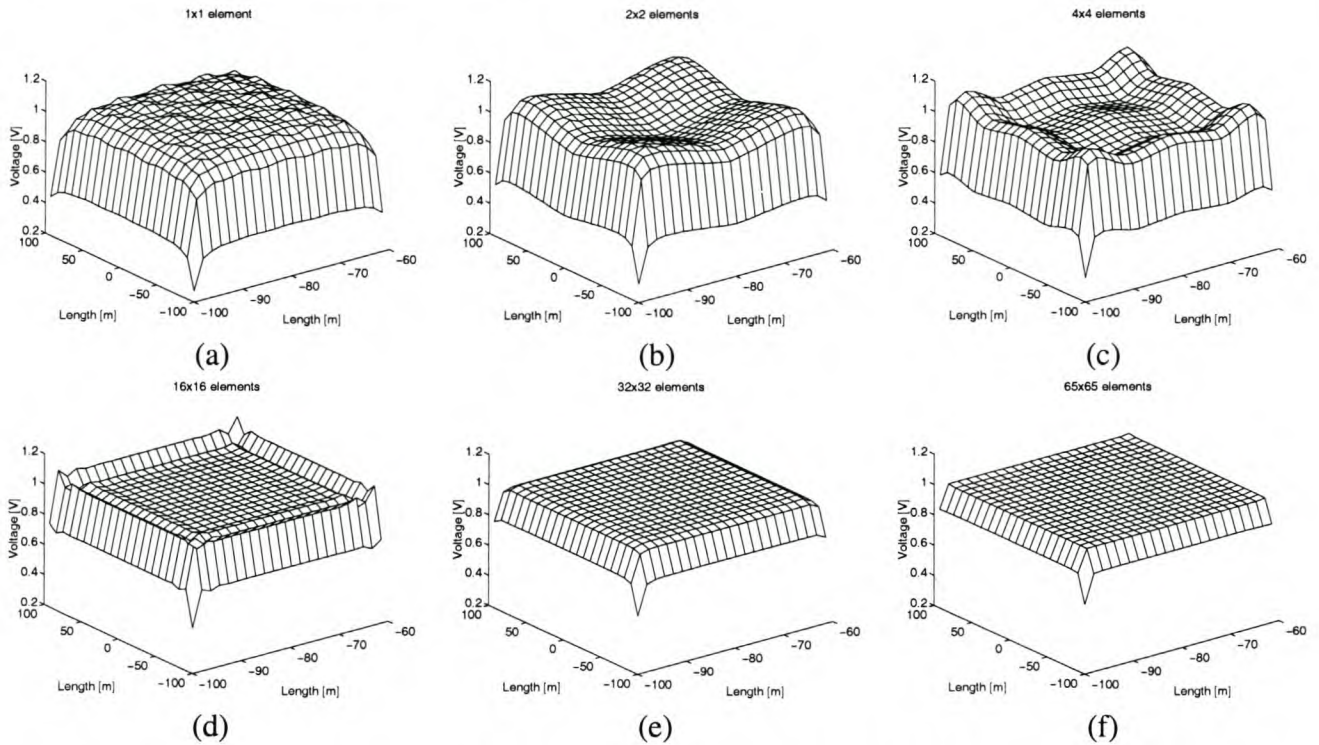
Figure D.5: Numerical potential distribution on top plate as solved by Coulomb© for a certain number of elements per side when the applied voltage is 1 V (a) Potential distribution for 1 element per side (b) Potential distribution for 2 elements per side (c) Potential distribution for 4 elements per side (d) Potential distribution for 16 elements per side (e) Potential distribution for 32 elements per side (f) Potential distribution for 65 elements per side

Table D.7 compares the capacitance calculated using either equation D.6 or D.8 with the Coulomb© answer for different dielectric substrates. 60 elements were used per side for each plate for these simulations, which should result in very accurate capacitance values. It is clear that the role of fringing decreases as the relative permittivity is increased because the main capacitance is increased together with the relative permittivity. The capacitance due to the fringing fields remains the same and thus becomes a smaller percentage of the overall capacitance.

From these results it can be said that the capacitive solver in Coulomb© can calculate the capacitance correctly for dielectric materials.

Table D.7: Comparison of calculated capacitance with analytical capacitance for different dielectric substrate properties

Relative permittivity (ε_r)	Capacitance [nF]			Percentage deviation	
	eq. D.6	eq. D.8	Coulomb©	eq. D.6	eq. D.8
1	35.42	39.05	39.14	10.50	0.23
1.5	53.12	56.72	56.93	7.16	0.35
2	70.83	74.42	74.70	5.46	0.38
3	106.25	109.82	110.22	3.73	0.36
4	141.66	145.23	145.72	2.86	0.34
5	177.08	180.64	181.21	2.33	0.32

Bibliography

[1] D. A. Douglass, "Potential transformer accuracy at 60 Hz voltages above and below rating and at frequencies above 60 Hz," *IEEE Transactions on Power Apparatus and Systems*, vol. PAS-100, pp. 1370–1375, March 1981.

[2] R. Malewski and J. Douville, "Measuring properties of voltage and current transformers for the higher harmonic frequencies," in *Canadian Communications and Power Conference*, pp. 327–329, 1976.

[3] D. A. Bradley, P. S. Bodger, and P. R. Hyland, "Harmonic response tests on voltage transducers for the new zealand power system," *IEEE Transactions on Power Apparatus and Systems*, vol. PAS-104, pp. 1750–1756, July 1985.

[4] A. T. Johns, Z. Bo, and R. K. Aggarwal, "A novel non-unit protection scheme based on fault generated high frequency noise on transmission lines," *IEE Symposium on Developments in Power System Protection*, vol. IEE Publication 368, pp. 65–68, 1993.

[5] H. J. Vermeulen, L. R. Dann, and J. van Rooijen, "Equivalent circuit modelling of a capacitive voltage transformer for power system harmonic frequencies," *IEEE Transactions on Power Delivery*, vol. 10, pp. 1743–1749, October 1995.

[6] R. H. McKnight, "Measuring fast-rise impulses by use of E-dot sensors," *5th International Symposium on High Voltage Engineering*, no. 32.07, 1987.

[7] H. J. Vermeulen, A. C. Britten, M. W. Roberts, and J. M. Strauss, "Frequency response of capacitive voltage transformers and insulated current transformers," in *Southern African Universities Power Engineering Conference*, (Stellenbosch, South Africa), pp. 81–84, 20-21 January 1998.

[8] H. J. Vermeulen, A. C. Britten, M. W. Roberts, and J. M. Strauss, "Impulse response of high voltage capacitive voltage transformers and insulated current transformers," in *Southern African Universities Power Engineering Conference*, (Stellenbosch, South Africa), pp. 85–88, 20-21 January 1998.

[9] H. J. Vermeulen, J. M. Strauss, A. C. Britten, and N. P. Tlhatlhetji, "Wideband voltage measurements using HV current transformers," in *Power and Energy Systems Conference* (M. H. Hamza, ed.), pp. 99–105, 19-22 September 2000.

[10] A. Schwab, *High Voltage Measurement Techniques*. Berlin, Heidelberg, New York: Springer-Verlag, english translation ed., 1972.

[11] H. J. Vermeulen and M. T. S. van As, "GPS based synchronisation module for data acquisition time-stamping and scheduling applications," in *Southern African Universities Power Engineering Conference*, (Vaal Triangle Technikon, Vanderbijlpark, South Africa), pp. 139–142, 30 January - 1 February 2002.

[12] E. J. M. van Heesch, R. Caspers, P. F. M. Gulickx, G. A. P. Jacobs, W. F. J. Kersten, and P. C. T. van der Laan, "Three phase voltage measurements with simple open air sensors," *7th International Symposium on High Voltage Engineering*, no. 63.08, pp. 165–169, 1991.

[13] M. Roberts and D. Hoch, "Non-intrusive measuring techniques," Tech. Rep. TRR/E/98/EL013, Eskom TRI, 1998.

[14] C. A. Gerrard, J. R. Gibson, G. R. Jones, L. Holt, and D. Simkin, "Measurement of power system voltages using remote electric field monitoring," *IEE Proceedings: Generation Transmission and Distribution*, vol. 145, pp. 217–224, May 1998.

[15] H. I. Bassen and G. S. Smith, "Electric field probes - a review," *IEEE Transactions on Antennas and Propagation*, vol. AP-31, pp. 710–718, September 1983.

[16] K. Feser, W. Pfaff, G. Weyreter, and E. Gockenbach, "Distortion-free measurement of high impulse voltages," *IEEE Transactions on Power Delivery*, vol. 3, pp. 857–866, July 1988.

[17] K. Feser and W. R. Pfaff, "A potential free spherical sensor for the measurement of transient electric fields," *IEEE Transactions on Power Apparatus and Systems*, vol. PAS-103, pp. 2904–2911, October 1984.

[18] W. R. Pfaff, "Accuracy of a spherical sensor for the measurement of threedimensional electric fields," *5th International Symposium on High Voltage Engineering*, no. 32.05, 1987.

[19] T. Krauß, W. Köhler, and K. Feser, "High bandwidth potential-free electric field probe for the measurement of threedimensional fields," *10th International Symposium on High Voltage Engineering*, 1997.

[20] E. Kuffel and W. S. Zaengl, *High Voltage Engineering: Fundamentals*. Pergamon Press, first ed., 1984.

[21] H. M. Ryan, ed., *High Voltage Engineering and Testing*. IEE Power Series, Peter Peregrinus Ltd., 1994.

[22] A. J. Schwab and J. H. W. Pagel, "Precision capacitive voltage divider for impulse voltage measurements," *IEEE Transactions on Power Apparatus and Systems*, vol. PAS-91, pp. 2376–2382, November/December 1972.

[23] T. J. Blalock, D. F. Bullock, W. S. Zaengl, and T.-W. Liao, "A capacitive voltage divider for uhv outdoor testing," *IEEE Transactions on Power Apparatus and Systems*, vol. PAS-89, pp. 1404–1412, September/October 1970.

[24] L. K. Baxter, *Capacitive Sensors: Design and Applications*. 445 Hoes Lane, P.O. Box 1331, Piscataway, NJ 08855 -1331: IEEE Press, 1997.

[25] X. Li, G. de Jong, and G. C. M. Meijer, "The influence of electric-field bending on the nonlinearity of capacitive sensors," *IEEE Transactions on Instrumentation and Measurement*, vol. 49, pp. 256–259, April 2000.

[26] X. Li, G. de Jong, and G. C. M. Meijer, "The application of the capacitor's physics to optimize capacitive angular-position sensors," *IEEE Transactions on Instrumentation and Measurement*, vol. 46, pp. 8–14, February 1997.

[27] D. G. W. Goad and H. J. Wintle, "Capacitance corrections for guard gaps," *IEE Proceedings: Measurement Science and Technology*, vol. 137, pp. 965–969, 1990.

[28] W. C. Heerens, "Application of capacitance techniques in sensor design," *Journal of Physics E: Scientific Instruments*, vol. 19, pp. 897–906, 1986.

[29] T. Takuma, T. Kawamoto, and Y. Sunaga, "Analysis of calibration arrangements for AC field strength meters," *IEEE Transactions on Power Apparatus and Systems*, vol. PAS-104, pp. 489–496, February 1985.

[30] M. Misakian, "Generation and measurement of DC electric fields with space charge," *Journal of Applied Physics*, vol. 53, pp. 3135–3144, May 1981.

[31] G. G. Wolzak, *The Development of High-Voltage Measuring Techniques*. PhD thesis, Eindhoven University of Technology, 1983.

[32] G. G. Wolzak, J. A. G. Bekkers, and P. C. T. van der Laan, "Capacitive measurement of high dc voltages," *Review of Scientific Instruments*, vol. 52, pp. 1572–1574, October 1981.

[33] J. M. Meek and M. M. C. Collins, "Measurement of electric fields at electrode surfaces," *Electronics Letters*, vol. 1, pp. 110–111, June 1965.

[34] C. A. Stassinopoulos, "Simultaneous electric-field measurements at both electrodes of a rod-plane gap," *Proceedings of the IEE*, vol. 115, pp. 1225–1226, August 1968.

[35] O. J. Tassicker, "Measurement of corona current density at an electrode boundary," *Electronics Letters*, vol. 5, pp. 285–286, June 1969.

[36] O. J. Tassicker, "Boundary probe for the measurement of current density and electric-field strength – with special reference to ionised gases," *Proceedings of the IEE*, vol. 121, pp. 213–220, March 1974.

[37] E. O. Selim and R. T. Waters, "Static probe for electrostatic field measurement in the presence of space charge," *IEEE Transactions on Industry Applications*, vol. IA-16, pp. 458–463, May/June 1980.

[38] W. B. Stark, E. O. Selim, and R. T. Waters, "Field-filter probes and the measurement of alternating-current corona," *IEEE Transactions on Industry Applications*, vol. IA-16, pp. 464–472, May/June 1980.

[39] D. K. Davies, "The examination of the electrical properties of insulators by surface charge measurement," *Journal of Scientific Instruments*, vol. 44, pp. 521–524, 1967.

[40] T. Jing, P. H. F. Morshuis, and F. H. Kreuger, "Experimental determination of capacitive parameters for calibration of surface charge measurement," *7th International Symposium on High Voltage Engineering*, no. 13.07, 1991.

[41] H. Ootera and K. Nakanishi, "Analytical method for evaluating surface charge distribution on a dielectric from capacitive probe measurement - application to a cone-type spacer in ±500 kV DC-GIS," *IEEE Transactions on Power Delivery*, vol. 3, pp. 165–172, January 1988.

[42] W. W. Mapleson and W. S. Whitlock, "Apparatus for the accurate and continuous measurement of the earth's electric field," *Journal of Atmospheric and Terrestrial Physics*, vol. 7, pp. 61–72, 1955.

[43] M. G. Comber and G. B. Johnson, "HVDC field and ion effects research at project UHV: Results of electric field and ion current measurements," *IEEE Transactions on Power Apparatus and Systems*, vol. 101, pp. 1998–2006, July 1982.

[44] M. G. Comber, R. Kotter, and R. McKnight, "Experimental evaluation of instruments for measuring DC transmission line electric fields and ion currents," *IEEE Transactions on Power Apparatus and Systems*, vol. 102, pp. 3549–3557, November 1983.

[45] Thunderstorm Technology. Internet web page, March 28, 1997. http://www.tstorm.com/index.html, e-mail: mfs@tstorm.com.

[46] P. S. Maruvada, R. D. Dallaire, and R. Pedneault, "Development of field-mill instruments for ground-level and above-ground electric field measurement under HVDC transmission lines," *IEEE Transactions on Power Apparatus and Systems*, vol. PAS-102, pp. 738–744, March 1983.

[47] M. Smiddy and J. A. Chalmers, "The double field-mill," *Journal of Atmospheric and Terrestrial Physics*, vol. 12, pp. 206–210, 1958.

[48] S. Gathman, "Guarded double field meter," *Review of Scientific Instruments*, vol. 39, pp. 43–47, January 1968.

[49] A. R. Johnston and H. Kirkham, "A miniaturized space-potential DC electric field meter," *IEEE Transactions on Power Delivery*, vol. 4, pp. 2153–1261, April 1989.

[50] P. Kirkpatrick and I. Miyake, "A generating voltmeter for the measurement of high potentials," *The Review of Scientific Instruments*, vol. 3, pp. 1–8, January 1932.

[51] J. M. Feldman, N. Reinhardt, K. Kuehn, J. M.Teixeira, and D. J. Pileggi, "A hotstick instrument for estimation of the potential of an HVDC conductor," *IEEE Transactions on Power Delivery*, vol. 7, pp. 1533–1541, July 1992.

[52] S. Kato and N. Takeuchi, "Development of fast electric fieldmeter," *5th International Symposium on High Voltage Engineering*, no. 32.06, 1987.

[53] J. Meppelink and P. Hofer, "Design and calibration of a high voltage divider for measurement of very fast transients in gas insulated switchgear," in *5th International Symposium on High Voltage Engineering*, (Braunschweig), p. 71.08, 24-28 August 1987.

[54] K. Tokoro, Y. Harumoto, H. Yamamoto, Y. Yoshida, H. Mukae, Y. Ohno, M. Shimada, and Y. Ida, "Development of electronic potential and current transducers suitable for gas insulated switchgear and adequate for application to substation digital control system," *IEEE Transactions on Power Apparatus and Systems*, vol. PAS-101, pp. 3967–3976, October 1982.

[55] C. A. Gerrard, *Remote Monitoring of Power System Conductor Voltages*. PhD thesis, University of Liverpool, 1996.

[56] E. J. M. van Heesch, J. N. A. M. van Rooij, R. G. Noij, and P. C. T. van der Laan, "A new current and voltage measuring system; tests in a 150 kV and 400 kV GIS," *5th International Symposium on High Voltage Engineering*, no. 73.06, 1987.

[57] E. J. M. van Heesch, A. P. J. van Deursen, M. A. van Houten, G. A. P. Jacobs, W. F. J. Kersten, and P. C. T. van der Laan, "Field tests and response of the D/I HV measuring system," *6th International Symposium on High Voltage Engineering*, no. 42.23, 1989.

[58] A. P. J. van Deursen, P. F. M. Gulickx, and P. C. T. van der Laan, "A current and voltage sensor combined in one unit," *8th International Symposium on High Voltage Engineering*, no. 56.02, pp. 463–466, 1993.

[59] R. Keller, "Wideband high voltage probe," *Review of Scientific Instruments*, vol. 35, pp. 1057–1060, August 1964.

[60] P. C. T. van der Laan, H. C. Reader, J. H. Cloete, and J. H. R. Enslin, *Electromagnetic Compatibility (EMC) for Industry, Short Course Notes*. Department of Electrical and Electronic Engineering, University of Stellenbosch, Stellenbosch, 1997.

[61] M. Albiez, W. Zaengl, K. J. Diederich, and J. Meppelink, "Design and calibration of an universal sensor for the measurement of partial discharges and very fast transients in GIS," *6th International Symposium on High Voltage Engineering*, no. 42.28, 1989.

[62] P. Osmokrovic, D. Petrokovic, O. Markovic, N. Kartalovic, and D. Vukic, "Measuring system for fast transients monitoring in gas-insulated substations," *European Transactions on Electrical Power Engineering*, vol. 7, pp. 165–172, May/June 1997.

[63] H. Shimada, T. Furukawa, and M. Ohchi, "Electric field analysis for a static induction type of voltage sensor in three-phase power distribution systems," *IEE Proceedings: Generation Transmission and Distribution*, vol. 145, pp. 437–443, July 1998.

[64] S. P. Walldorf, J. S. Engelhardt, and F. J. Hoppe, "The use of real-time monitoring and dynamic ratings for power delivery systems and the implications for dielectric materials," *IEEE Electrical Insulation Magazine*, vol. 15, pp. 28–33, September/October 1999.

[65] M. J. A. M. van Helvoort, E. J. M. van Heesch, and P. C. T. van der Laan, "Dynamic voltage and current measurements on substation components," *8th International Symposium on High Voltage Engineering*, no. 55.02, pp. 439–442, 1993.

[66] C. E. Baum, E. L. Breen, J. C. Giles, J. O'Neill, and G. D. Sower, "Sensors for electromagnetic pulse measurements both inside and away from nuclear source regions," *IEEE Transactions on Antennas and Propagation*, vol. AP-26, pp. 22–35, January 1978.

[67] R. G. Olsen, "Power-transmission electromagnetics," *IEEE Antennas and Propagation Magazine*, vol. 36, pp. 7–16, December 1994.

[68] T. Zhao and M. G. Comber, "Calculation of electric field and potential distribution along nonceramic insulators considering the effects of conductors and transmission towers," *IEEE Transactions on Power Delivery*, vol. 15, pp. 313–318, January 2000.

[69] D. Beatovic, P. L. Levin, S. Sadovic, and R. Hutnak, "A Galerkin formulation of the boundary element method for two-dimensional and axi-symmetric problems in electrostatics," *IEEE Transactions on Electrical Insulation*, vol. 27, pp. 135–143, February 1992.

[70] *Coulomb, Three dimensional electic field solver*. Winnipeg, Manitoba, Canada, 1997. Version 5.1.

[71] C. A. Harper, ed., *Handbook of Materials and Processes for Electronics*. McGraw-Hill, 1970.

[72] F. M. D. E. Agjee, H. J. Vermeulen, and K. Heunis, "A programmable signal conditioning system for high voltage transient measurements using a transconductance topology," in *33rd Universities Power Engineering Conference*, (Napier University, Edinburgh, UK), pp. 727–730, 6-8 September 1998.

[73] *Speed Plus 12-Bit, 10 MHz Sampling ANALOG-TO-DIGITAL CONVERTER*, September 1996.

[74] Cypress Semiconductor Corporation, *Cypress HOTLink User's Guide*, 1995.

[75] S. A. Sebo and R. Caldecott, "Scale model studies of AC substation electric fields," *IEEE Transactions on Power Apparatus and Systems*, vol. PAS-98, pp. 926–939, May/June 1979.

[76] S. A. Sebo, R. Caldecott, and D. G. Kasten, "Model study of HVDC electric field effects," *IEEE Transactions on Power Apparatus and Systems*, vol. PAS-101, pp. 1743–1751, June 1982.

[77] K. Ogata, *Modern Control Engineering*. Prentice-Hall International Editions, second ed., 1990.

[78] L. Ljung, *System identification : theory for the user*. Prentice-Hall information and system sciences series, Prentice-Hall, 1987.

[79] H. A. Haus and J. R. Melcher, *Electromagnetic fields and energy*. Prentice-Hall International Editions, first ed., 1989.

[80] D. E. Hedman, "Propagation on overhead transmission lines I - theory of modal analysis," *IEEE Transactions on Power Apparatus and Systems*, vol. PAS-84, pp. 200–205, March 1965.

[81] J. D. Glover and M. Sarma, *Power System Analysis and Design*. Boston: PWS Publishing Company, Second ed., 1994.

[82] N. H. Malik, "A review of the charge simulation method and its applications," *IEEE Transactions on Electrical Insulation*, vol. 24, pp. 3–20, February 1989.

[83] H. Singer, H. Steinbigler, and P. Weiss, "A charge simulation method for the calculation of high voltage fields," *IEEE Transactions on Power Apparatus and Systems*, vol. 93, pp. 1660–1668, 1974.

[84] H. R. J. Klewe, *Interference between power systems and telecommunications lines*. London: Edward Arnold (Publishers) Ltd., 1958.

[85] J. D. Tranen and G. L. Wilson, "Electrostatically induced voltages and currents on conducting objects under EHV transmission lines," *IEEE Transactions on Power Apparatus and Systems*, vol. PAS-90, pp. 768–775, March/April 1971.

[86] C. H. Shih, J. Di Placido, and B. J. Ware, "Analysis of parallel plate simulation of the transmission line electric field as related to biological effects laboratory studies," *IEEE Transactions on Power Apparatus and Systems*, vol. PAS-96, pp. 962–968, May/June 1977.